



HAL
open science

Quantum engineering of collective states in semiconductor nanostructures

Giulia Pegolotti

► **To cite this version:**

Giulia Pegolotti. Quantum engineering of collective states in semiconductor nanostructures. Quantum Physics [quant-ph]. Université Paris Diderot-Paris VII, 2014. English. NNT : . tel-01132396v2

HAL Id: tel-01132396

<https://theses.hal.science/tel-01132396v2>

Submitted on 27 Apr 2015

HAL is a multi-disciplinary open access archive for the deposit and dissemination of scientific research documents, whether they are published or not. The documents may come from teaching and research institutions in France or abroad, or from public or private research centers.

L'archive ouverte pluridisciplinaire **HAL**, est destinée au dépôt et à la diffusion de documents scientifiques de niveau recherche, publiés ou non, émanant des établissements d'enseignement et de recherche français ou étrangers, des laboratoires publics ou privés.

Université Paris Diderot - Paris 7
Sorbonne Paris Cité

ED 564: Physique en Île de France

Ph.D. in Physics

Quantum engineering of collective states in semiconductor nanostructures

Giulia PEGOLOTTI

Laboratoire Matériaux et Phénomènes Quantiques (MPQ)

December 18, 2014

Jury:

Reviewers: Jérôme FAIST
Lucia REINING
Examiners: Thomas COUDREAU
Patrice BERTET
Thierry GUILLET
Supervisors: Angela VASANELLI
Carlo SIRTORI

Abstract

This work focuses on the many-body properties of semiconductor nanostructures for quantum engineering of infrared optoelectronic devices. In particular, we theoretically investigate the optical response accounting for collective effects in systems of tunnel-coupled quantum wells. A clear manifestation of these effects appears in the optical spectrum of highly doped quantum wells, where the absorption peaks are at completely different energies with respect to the single-particle electronic transitions.

We calculate light-matter interaction in two steps. First, we consider the microscopic polarization associated with the electronic transitions between confined levels of the wells, which are all coupled by dipole-dipole Coulomb interaction. Then we calculate the interaction of the resulting collective states with the electromagnetic field. The absorption spectrum is finally expressed in terms of microscopic currents, describing the collective charge oscillations. The theoretical model is applied to a series of relevant systems, and its outcomes are compared with experimental results.

As the collective states are issued from the coherent superposition of several electronic excitations, they have the properties of superradiant states. They are thus a promising entity for the realization of efficient light emitters in the mid- and far-infrared frequency range.

Résumé

Ce travail de thèse est centré sur l'étude des effets multicorps dans des nanostructures semiconductrices pour l'ingénierie quantique de dispositifs optoelectroniques infrarouges. Plus particulièrement, nous étudions la réponse optique de gaz d'électrons confinés dans des puits quantiques couplés par effet tunnel, en incluant les effets collectifs. On peut trouver une manifestation de ces effets dans les spectres d'absorption de puits quantiques très dopés, qui présentent des résonances optiques à des énergies complètement différentes par rapport aux transitions électroniques.

L'interaction lumière-matière est calculée en deux étapes. Nous commençons par considérer les polarisations microscopiques associées aux transitions électroniques entre niveaux confinés des puits quantiques. Le couplage dipôle-dipôle entre polarisations électroniques donne lieu à des états collectifs, dont nous calculons successivement l'interaction avec le champ électromagnétique. Le spectre d'absorption est donc exprimé au travers de courants microscopiques, qui décrivent les oscillations collectives de charge. Le modèle théorique est appliqué à des systèmes pertinents et ses prédictions sont comparées aux résultats expérimentaux.

Comme les états collectifs sont issus de la superposition cohérente de plusieurs excitations électroniques, ils ont les propriétés d'états superradiants. Ils représentent ainsi un système prometteur pour la réalisation de sources lumineuses efficaces dans les régions spectrales du moyen et lointain infrarouge.

Remerciements

First of all, I would like to express my gratitude to my supervisors, Angela Vasanelli and Carlo Sirtori.

Angela has worked closely with me during these three years. I owe her much, not only because of her physical intuition and competence, but also because of her kindness, optimism, and steady support. I appreciate the great deal of time she has invested in helping me with this manuscript.

This work would not have been possible without Carlo, who included me in his ERC Adequate funding, and welcomed me in his group: for this I am very grateful. His scientific knowledge, vision, and enthusiasm have been essential to the project.

I have learnt a lot from both of them, and I am thankful for the energy they have dedicated to me and my work.

I would like to thank my referees, Lucia Reining and Jérôme Faist, for accepting the task of reviewing the thesis and for the interest they have shown in my work. I would also like to thank the rest of the jury, Patrice Bertet, Thierry Guillet and Thomas Coudreau, for taking the time to read the thesis and attending my defense.

A big thank you goes to Yanko Todorov, for many interesting discussions and his valuable contributions to this thesis (but also for his humour).

Part of this work has been possible thanks to the samples grown at LPN by Isabelle Sagnes et Grégoire Beaudoin, and to the post-growth measurements performed by Gilles Patriarche. I am also grateful to Giuliano Orso and Cristiano Ciuti, with whom I had useful discussions about the study of electron transport. Thank you to Anne Servouze and Jocelyne Moreau, for their helpfulness in the daily life of the lab.

It has been a pleasure to share this time with my QUAD mates, at the lab, during lunches, conferences and, last but not least, evenings at the Dupont. Grazie to Maria and Ariane for their experimental work on QCLs. Merci to Khalid, whose code I used at the beginning of my thesis, and to Baptiste, who performed the measurements to (eventually) confirm the theoretical model on absorption. Merci also to Benjamin, who contributed to these beautiful measurements, and has been a fun travel buddy to many

conferences, as well as Thibault (you can insert relevant song here) and Jean-Michel (Gianni Michele). Merci à Simon, who's doing a great job in continuing this project. Thank you to Anna for sharing with me many good moments of life in Paris. Grazie a Giulia for her smiles, I am happy that you joined our group. Merci à Margaux, especially for sharing the joys and the pains of the thesis writing (and for being patient with my French!). Merci aussi to all the other QUADs whose paths have crossed mine at some time or other, in random order: Daniele, Chérif, the three Pierres, Aymeric, Robert, Julien, Stefano, Djamal, Vishal, Hua, Pascal. Grazie a Silvia, who has always been present during these three(-ish) years, and to Benjamin who doesn't get angry even if I call him Bengiamino. Merci to Cécile, Guillaume, Claire, also for helping me with my pot de thèse.

Grazie alla mia famiglia italiana a Parigi, Valentina for having been a good friend for so many years now (wow), Jonny, Teresa, Pietro, Mina, Matty, Franca, Sponzy, Camilla, Anna, Picci. Thank you also to Giorgia and Walter, I was so happy to find you here after London. Thank you to my historical (meaning we're getting old) friends, Serena, Nicole, Claudia, Martina, Valentina. Grazie a Stefano, for being a close-long-distance friend when I need him.

Grazie alla mia famiglia, i miei genitori, i miei fratellini, nonna Mariú e Gipo: sono grata per il vostro supporto e per la fiducia che avete nelle mie scelte. Finally, thank you Elia, for always being loving and encouraging.

Contents

Introduction	1
1 Semiconductor quantum wells: single-particle electronic and optical properties	5
1.1 Band structure calculation	5
1.1.1 Bulk III-V semiconductors	5
1.1.2 Heterostructures and the envelope-function approximation	9
1.2 Effect of tunneling: extended and localized basis	13
1.2.1 Tight-binding approximation	16
1.3 Light-matter interaction: intersubband absorption	19
1.3.1 Lorentz model	19
1.3.2 Semiclassical model: Fermi's golden rule	20
1.4 Intersubband scattering processes	23
1.4.1 Intersubband and intrasubband scattering rates	23
1.4.2 Spontaneous emission	25
1.5 Quantum Cascade Lasers	26
1.5.1 Fundamentals of QCLs active regions	28
1.5.2 Rate equations for electronic transport	29
2 Many-body effects in the optical properties of a bidimensional electron gas	33
2.1 Intersubband absorption and collective effects	33
2.1.1 One occupied subband	34
2.1.2 Two occupied subbands	35
2.1.3 Several occupied subbands: cooperative regime	38
2.1.4 Intersubband transitions as polarizations: coupled oscillators model	41
2.2 Quantum model of multisubband plasmons	42
2.2.1 Light-matter interaction Hamiltonian in dipole representation	44
2.2.2 Second quantization: bosonized Hamiltonian	45
2.2.3 Microscopic expression of the polarization and microscopic current densities	46
2.2.4 From intersubband transitions to intersubband plasmons	52
2.2.5 From intersubband to multisubband plasmons	55

2.2.6	Multisubband plasmon current densities and absorption spectrum . . .	59
2.2.7	Extension to piecewise constant mass	61
2.3	Coupling between multisubband plasmons and a cavity mode	62
2.3.1	One multisubband plasmon coupled with light	63
2.4	Dielectric function and absorption spectrum	66
3	Absorption spectra of single and tunnel-coupled quantum wells	69
3.1	Single quantum well with several occupied subbands	70
3.1.1	Single-particle properties	70
3.1.2	Collective renormalization: bright multisubband plasmon and absorption spectrum	73
3.1.3	Electronic density and well width dependence	77
3.1.4	Relation to the semiclassical model	81
3.2	Tunnel-coupled quantum wells: tight-binding analysis	85
3.2.1	Tunnel contribution to plasmon-plasmon coupling	87
3.3	Two tunnel-coupled asymmetric quantum wells	92
3.3.1	Tight-binding analysis	92
3.3.2	Numerical results	95
3.3.3	Laser-free Autler-Townes effect	96
3.3.4	Variable external electric field	97
3.3.5	Comparison with the absorption spectrum in time-dependent perturbation theory	100
3.4	Tunnel coupling between multisubband plasmons	102
3.4.1	Two identical highly doped quantum wells	102
3.4.2	Coupling between active transitions	105
3.4.3	Increasing quantum well width	106
3.4.4	Comparison with the experimental spectrum	108
3.5	Symmetric step well	112
3.5.1	Comparison with the experimental spectrum	114
3.6	Coupling between a multisubband plasmon and a single-particle transition .	115
3.7	Ultra-strong coupling between a multisubband plasmon and a cavity mode .	118
4	Electron transport in MQWs: role of tunneling and Coulomb interaction	123
4.1	Coherent resonant tunneling in multiple quantum wells	124
4.1.1	One-dimensional transport in a weakly coupled superlattice	125
4.1.2	Application to a THz quantum cascade laser	130
4.2	Transport in the presence of Coulomb interaction	137
4.2.1	Observables and equations of motion	140
4.2.2	Single-particle density matrix	141
4.2.3	Cluster-expansion approach	144
	Conclusions and perspectives	149

A	Implementation details	153
A.1	Absorption spectrum calculation	153
A.1.1	Electron population distribution	154
A.2	Density matrix model for electron transport	156
B	Intersubband and intrasubband scattering times	159
B.1	Interface roughness	159
B.2	Alloy disorder	161
B.3	Electron-electron scattering	162
B.4	Inelastic scattering: LO phonon	162
B.5	Material parameters	164
C	Density matrix formalism for systems of multiple quantum wells	165
C.1	Pure and mixed states	165
C.1.1	Populations and coherences	167
C.2	Simplified density matrix model for mid- and far-infrared QCLs	168
C.2.1	Two-level system	168
C.2.2	Four-level system	170
C.2.3	N -level system	173
D	Mid-infrared QCLs: from TEM measurements to modeling	177
D.1	HAADF-STEM tomography measures	178
D.2	Modeling	178
	Bibliography	187

Introduction

Semiconductor structures with dimensions of a few tens of nanometers can be realized thanks to nanotechnology. In these systems, quantum effects naturally arise as a consequence of the reduced dimensions, and strongly affect electronic and optical properties of the matter. To bring these phenomena to the macroscopic world, it is necessary to create an interface capable to connect the realm of quantum with the sizeable effects. This interface is what we want from a quantum device [1]. The design of devices completely relying on quantum effects is called quantum engineering.

Quantum Cascade Lasers (QCLs) [2] are one example of this approach. In a QCL, laser emission takes place between confined levels (*subbands*) in tunnel-coupled semiconductor quantum wells. The emission wavelength does not depend on the material system, but on the thickness of the quantum wells. As a consequence, QCLs span a very wide frequency interval, from the mid- to the far-infrared. Since their first realization in 1994, these devices have seen impressive progresses [3]. Their maturity has allowed several industrial applications, especially in mid-infrared spectroscopy for sensing systems [4–6]. The operation of QCLs depends on a *bandstructure* and *lifetime engineering*, ingeniously combining quantum confinement and resonant tunneling. A QCL represents a fascinating macroscopic result of controlling quantum effects.

QCLs rely on quantum engineering to achieve stimulated emission and realize powerful mid- and far-infrared sources. On the other hand, in this frequency range spontaneous emission cannot be exploited to produce light-emitting structures as efficient as in the visible. This is due to the characteristic time for spontaneous emission τ_{sp} , which scales with ω^{-3} , ω being the emission frequency. In the mid- and far-infrared range, τ_{sp} is much longer than the non-radiative lifetime, giving rise to quantum efficiencies of the order of 10^{-6} .

The general context of this theoretical work is the possibility of modifying the characteristic time of light-matter interaction by introducing new coherences in a quantum system. An example of this phenomenon is the strong coupling between an intersubband excitation in a quantum well and a microcavity photon mode [7, 8]. In this case, the

interaction frequency is controlled by the electronic density in the well. Another possible way to modify light-matter interaction is to exploit the phenomenon of *superradiance*, already demonstrated in atomic physics [9, 10], occurring when a dense ensemble of two-level emitters is placed in a small volume. The spontaneous emission becomes in this case a cooperative effect, resulting in a dramatic increase of the spontaneous emission rate, depending on the number of emitters involved. The possibility of realizing solid-state devices based on superradiance is an open and challenging research field [11–13].

In this direction, it has been recently experimentally demonstrated [14] that it is possible to create a collective state with superradiant properties in a condensed-matter system. The structure considered in Ref. [14] is a large and highly doped quantum well, where the important density of charge makes many-body effects crucial. As a result, the measured absorption spectrum consists of a single resonance concentrating the whole interaction with light, at a higher energy than all the bare electronic transitions. This single resonance corresponds to the excitation of a collective mode of the system: the electron gas responds to the electromagnetic field in a cooperative way, with a giant dipole depending on the electronic density, as it is typical of superradiant states. With electronic densities achievable in semiconductor quantum wells, lifetimes of the order of 100 fs can be attained. This collective mode is thus a promising entity for the realization of efficient light emitters in the mid- and far-infrared [15].

Most of this work has been focused on the study of optical properties of dense electronic gases, confined by a one-dimensional potential. After theoretically demonstrating the emergence of collective modes from dipole-dipole Coulomb interaction, different confining potentials have been investigated. In these systems, two couplings are present: tunneling, which creates a coherence between electronic levels, and Coulomb interaction, which couples transitions involving a high density of electrons. Particular consideration has been devoted to the study of the interplay between the two effects. This analysis is a first step toward a novel engineering of quantum devices, based on many-body excitations, rather than on single-particle properties.

A further step in this direction would be the description of electron transport in the presence of tunnel and Coulomb coupling. A density matrix model accounting for coherent tunneling has been studied and applied to examples of THz and mid-IR QCLs. A preliminary analysis of the inclusion of collective effects in electron transport has also been performed.

The structure of the manuscript is the following.

Chapter 1 provides a general overview on the single-particle properties of semiconductor quantum wells, in particular regarding the calculation of electronic levels. A brief introduction to quantum cascade lasers is given, along with references for various concepts exploited in the rest of the work.

Chapter 2 presents a quantum model to calculate the optical response of high-density

electron gases confined by heterostructure potentials, where coherence induced by tunneling combines with the coherence induced by the high density of charge [16]. A description of the collective states, issued from the coherent oscillation of all the optically active dipoles in the system, is provided in terms of microscopic current densities.

Chapter 3 is devoted to applications of this quantum model to relevant examples. The starting point is the single heavily doped quantum well, for which the experimental results of Ref. [14] are recovered. The interplay between Coulomb interaction and tunneling is then systematically discussed in the case of tunnel-coupled quantum wells. An analytical tight-binding model to describe these systems in the limit of low doping and thick barriers is provided.

In Chapter 4, the effects of the two couplings on electron transport are investigated. First, a density matrix model accounting for coherent tunnelling is introduced, and applied to a quantum cascade laser operating in the THz range. The final part of the chapter represents a preliminary study of the inclusion of many-body effects due to Coulomb interaction. After considering a single-particle density matrix method, equations accounting for second-order correlations, following a cluster-expansion approach [17], are presented.

Some supplementary material has been included in appendices, with the intent of simplifying the flow of the main text. Appendix A presents the structure of the programs used for numerical calculations. Appendix B presents the details of intersubband and intrasubband scattering times calculations. Appendix C contains an introduction to the density matrix formalism used in Chapter 4, and describes the algorithm used to extend the calculation to an arbitrary number of levels. Finally, Appendix D reports the results of a post-growth study of a MOCVD- (MetalOrganic Chemical Vapour Deposition) grown mid-IR QCL, whose electrical and optical characteristics have been simulated with the technique introduced in Chapter 4.

Semiconductor quantum wells: single-particle electronic and optical properties

This first chapter is devoted to an introduction to the properties of semiconductor quantum wells in a single-particle picture, where interactions between electrons are neglected. We provide an overview on theoretical concepts that will be widely used in the rest of the work. Section §1.1 presents the basics of electronic levels (subbands) calculation in quantum wells. We discuss the choice of the basis to solve the wavefunctions eigenproblem in §1.2. Section §1.3 is dedicated to a brief review of intersubband absorption in a single-particle picture, in a classical and semiclassical framework. We introduce intersubband scattering processes in §1.4. Finally, we present Quantum Cascade Lasers (QCLs)[3], the major example of device based on intersubband transitions, in §1.5.

1.1. Band structure calculation

The semiconductor nanostructures that will be considered in this work are based on III-V semiconductor alloys. In this section, we briefly review the band structure calculations in these materials. We recall the $\mathbf{k} \cdot \mathbf{p}$ approximation and the Kane model.

1.1.1. Bulk III-V semiconductors

Bulk III-V semiconductors are compounds of materials of group III and materials of group V of the periodic table, like InAs, GaAs, and AlAs. They crystallize in the zinc-blende structure: two interpenetrating face-centered cubic Bravais lattices, displaced along the body diagonal of the cubic lattice with the two-point basis $\mathbf{0}$ and $\frac{a}{4}(\mathbf{x} + \mathbf{y} + \mathbf{z})$, with a lattice constant [see Fig. 1.1(a)]. In the zincblende structure there are two atoms in the elementary cell, one for each of the two different elements of the compound. The first Brillouin zone is a truncated octaedron, as shown in Fig. 1.1(b).

It is possible to find III-V semiconductors both with an indirect gap (for instance AlAs, BN, GaP) and a direct gap (e.g. GaAs, GaN, InAs). Figure 1.2 shows the band structure

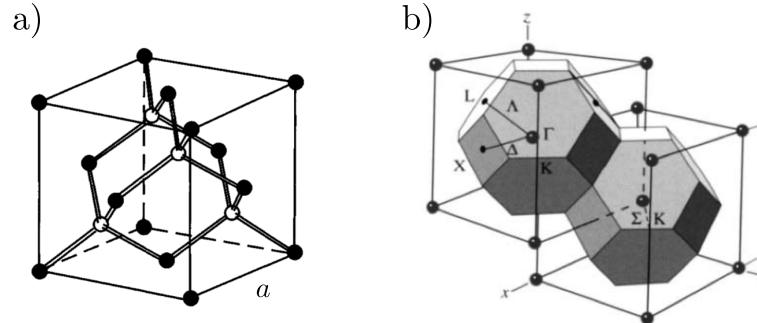


Figure 1.1: From Ref. [18]: a) Crystalline structure of III-V semiconductors (zinc-blende), with two types of atoms, represented in black and white. b) First Brillouin zone with high symmetry points.

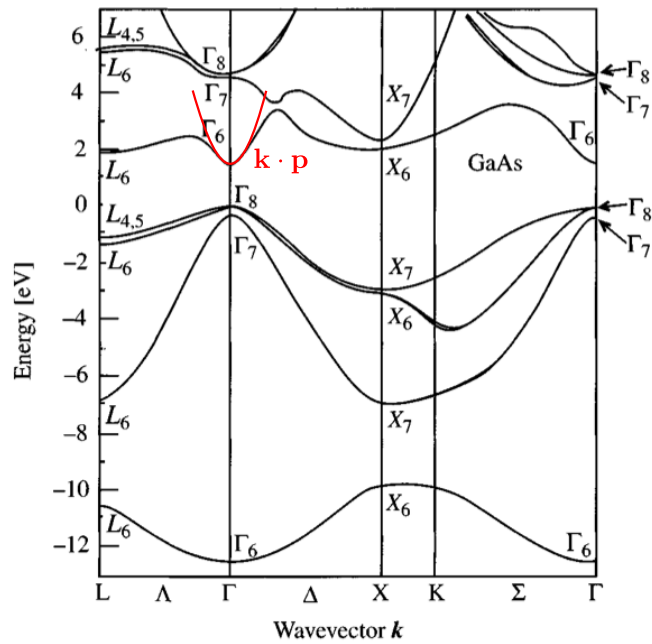


Figure 1.2: From Ref. [19]: Electronic band structure of bulk GaAs calculated by the pseudopotential technique [18]. At the Γ point, the parabolic energy dispersion approximated with the $k \cdot p$ is sketched in red.

in the case of GaAs, where both the minimum of the conduction band and the maximum of the valence band are located at the Γ point, center of the Brillouin zone.

$\mathbf{k} \cdot \mathbf{p}$ analysis and effective masses

The electronic states in a crystalline solid are determined by the time-independent Schrödinger equation

$$\left[\frac{\mathbf{p}^2}{2m_0} + V(\mathbf{r}) \right] \psi(\mathbf{r}) = E\psi(\mathbf{r}) \quad (1.1)$$

where $V(\mathbf{r})$ is the periodic potential due to the crystal structure, and m_0 is the mass of the electron. The periodicity of $V(\mathbf{r})$ is that of the crystal: $V(\mathbf{r} + \mathbf{R}) = V(\mathbf{r})$ where \mathbf{R} is in the Bravais lattice. Bloch Theorem [20] states that the eigenstates of the Hamiltonian (1.1) have the form

$$\psi_{n,\mathbf{k}}(\mathbf{r}) = \frac{e^{i\mathbf{k}\cdot\mathbf{r}}}{\sqrt{V}} u_{n,\mathbf{k}}(\mathbf{r}) \quad (1.2)$$

where V is the volume of the unit cell, n is the band index, and \mathbf{k} is a vector of the reciprocal space. $u_{n,\mathbf{k}}(\mathbf{r})$ are a set of functions with the same periodicity as the crystal structure: $u_{n,\mathbf{k}}(\mathbf{r} + \mathbf{R}) = u_{n,\mathbf{k}}(\mathbf{r})$. We see then that the eigenstates are expressed as the product of a plane wave and a periodic function. The quantity $\hbar\mathbf{k}$ is called crystal momentum. It is not the actual momentum of the electron, as $\psi_{n,\mathbf{k}}$ cannot be eigenfunction of \mathbf{p} and H at the same time.

We are not interested in the calculation of the full semiconductor band structure (which can be done using tight-binding or pseudopotential methods [18]), but rather we want to calculate the dispersion $E_{n\mathbf{k}}$ for a small range of \mathbf{k} values around the band extrema. Indeed, a local description of the extrema of the conduction band and valence band is often sufficient to describe the electronic and optical properties of semiconductors relevant for optoelectronic devices. The band structure near the $\mathbf{k} = 0$ point can be determined within the $\mathbf{k} \cdot \mathbf{p}$ method, which we summarize here briefly. For a complete discussion, see for example Refs. [18, 21].

If one inserts the wavefunction expression (1.2) in Schrödinger equation (1.1), a differential equation for the periodic functions $u_{n\mathbf{k}}(\mathbf{r})$ is obtained:

$$\left(\underbrace{\frac{p^2}{2m_0} + V(\mathbf{r})}_{H(\mathbf{k}=\mathbf{0})} + \underbrace{\frac{\hbar\mathbf{k} \cdot \mathbf{p}}{m_0} + \frac{\hbar^2 k^2}{2m_0}}_{W(\mathbf{k})} \right) u_{n\mathbf{k}}(\mathbf{r}) = E_{n\mathbf{k}} u_{n\mathbf{k}}$$

We can treat the \mathbf{k} -dependent terms as perturbations in k and calculate the band dispersion around a given point \mathbf{k}_0 . The fundamental idea of the $\mathbf{k} \cdot \mathbf{p}$ approximation is indeed to use the $u_{n\mathbf{0}}$ as a basis for the expansion of the wavefunctions and energies at finite \mathbf{k} value.

Let us assume that the band structure is non degenerate in $\mathbf{k} = \mathbf{0}$ and has an extremum at the energy $E_{n\mathbf{0}}$. It can be shown [18] that the $\mathbf{k} \cdot \mathbf{p}$ perturbation of non-degenerated

bands gives a parabolic energy dispersion in the vicinity of the Γ point (see red curve in Fig. 1.2). $E_{n\mathbf{k}}$ can be expressed in a free-electron form as

$$E_{n\mathbf{k}} = E_{n\mathbf{0}} + \frac{\hbar^2 \mathbf{k}^2}{2m^*} \quad (1.3)$$

where m^* is defined as the effective mass of the band, in general written as [20]¹

$$\frac{1}{m^*} = \frac{1}{\hbar^2} \frac{\partial^2 E_{n\mathbf{k}}}{\partial \mathbf{k}^2}$$

and in the $\mathbf{k} \cdot \mathbf{p}$ approximation reads [18]

$$\frac{1}{m^*} = \frac{1}{m_0} + \frac{2}{m_0^2 k^2} \sum_{n' \neq n} \frac{|\langle u_{n\mathbf{0}} | \mathbf{k} \cdot \mathbf{p} | u_{n'\mathbf{0}} \rangle|^2}{E_{n\mathbf{0}} - E_{n'\mathbf{0}}} \quad (1.4)$$

Equation (1.4) shows that an electron in a solid has a different mass from that of a free electron because of coupling between electronic states in different bands via the term $\mathbf{k} \cdot \mathbf{p}$. As an example, we may consider just two bands, conduction and valence, and write the conduction band energy as

$$E_{c\mathbf{k}} = E_{c\mathbf{0}} + \frac{\hbar^2 k^2}{2m_0} + \frac{\hbar^2 k^2}{m_0} \frac{|p_{cv}|^2}{E_g} = E_{c\mathbf{0}} + \frac{\hbar^2 k^2}{2m_0} \left(1 + \frac{E_P}{E_g} \right)$$

where $p_{cv} = \langle u_{c\mathbf{0}} | p | u_{v\mathbf{0}} \rangle$ is the isotropic interband momentum matrix element, and we have introduced the Kane energy $E_P = 2|p_{cv}|^2/m_0$ (≈ 20 eV in III-V semiconductors [3, 18]).

If the parabolic approximation is valid, the overall effects of the band structure on an electron (i.e. the fact that it experiences the periodic potential $V(\mathbf{r})$ instead of moving in the vacuum) are included in the use of the constant effective mass (1.4) instead of the free electron mass. The notion of effective mass is at the heart of the semiclassical description of carrier motion in semiconductors [20]. The carrier velocity in a Bloch state $|n\mathbf{k}\rangle$ in the parabolic approximation (1.3) is equal to

$$\mathbf{v} = \frac{1}{\hbar} \frac{\partial E_{n\mathbf{k}}}{\partial \mathbf{k}} = \frac{\hbar \mathbf{k}}{m^*}$$

which is reminiscent of the familiar relation $\mathbf{v} = \mathbf{p}/m_0$ for free particles in vacuum.

Beyond the quadratic dispersion relations: Kane model

For a given \mathbf{k} , the range of validity of the $\mathbf{k} \cdot \mathbf{p}$ approximation is dependent on the effective mass values: the parabolic approximation is less and less valid the lighter the effective mass. The reason for this is that the influence of valence bands closer to the conduction band becomes rapidly more important for smaller energy gaps, which vary proportionally

¹We neglect here the tensorial nature of m^* (see for example [21]), because the effective mass can be considered mostly isotropic in III-V compounds in the vicinity of $\mathbf{k} = 0$.

to effective masses [22].

A method to account for conduction band nonparabolicity was proposed by Kane [23], who applied it to InSb. In this compound, the topmost valence bands and the conduction bands are very close and well-separated from the other bands. The perturbation $W(\mathbf{k})$ can in this case be diagonalized exactly for this subset of bands, and the coupling with other remote bands considered as a second order perturbation.

The model considers then just the four states represented in Fig. 1.3: one state in the conduction band and three in the valence band (light holes, heavy holes and split-off). Note that in $\mathbf{k} = 0$ heavy and light hole bands are degenerate. Their separation with the split-off band is denoted Δ_{so} . In order to find the energy dispersions, one writes the Hamiltonian composed of the matrix elements of the perturbation $W(\mathbf{k})$ on the four states (with a factor of two due to spin). The energies $\varepsilon(\mathbf{k})$ are then given by the eigenvalues of this 8×8 matrix. An important result of this approach is that the dispersions $\varepsilon(\mathbf{k})$ are found to be no more parabolic, which can be reformulated with an energy dependence of the mass. We omit here the details of the procedure for bulk, which can be found in Ref. [21].

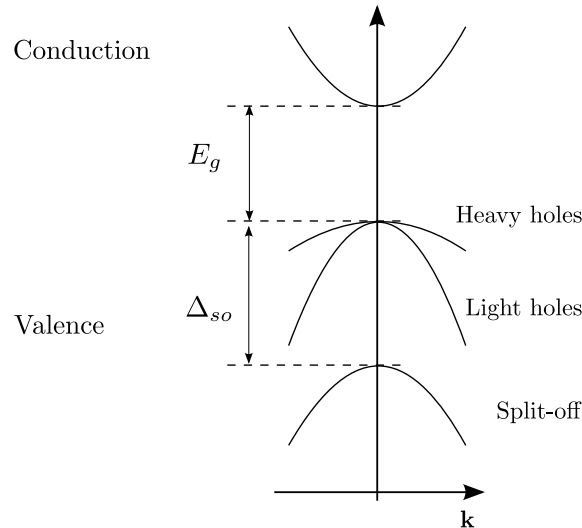


Figure 1.3: Schematic band structure of a direct gap III-V compound in the vicinity of the Γ point.

1.1.2. Heterostructures and the envelope-function approximation

We shall now consider the determination of eigenstates in heterostructures, artificial semiconductors composed of more than one material, with the same lattice constant but different energy gaps. In this case, the difference in energy gaps between the different materials is shared between valence and conduction bands, ultimately determining for the latter a profile $E_c(z)$ (see Fig. 1.4).

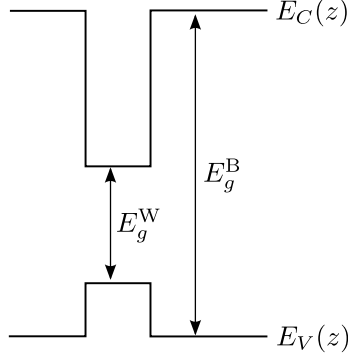


Figure 1.4: Conduction and valence band profiles in a type I heterostructure. W (well) denotes the smaller gap material and B (barrier) the greater gap material.

Even in this situation, it is possible to keep a description similar to the bulk semiconductor, where the electron wavefunction is expressed as the product of a function $u_{\mathbf{k}}(\mathbf{r})$ with the same periodicity as the crystal, and an envelope function $\chi_{i\mathbf{k}}(\mathbf{r})$ slowly varying on the scale of the lattice constant:

$$\varphi_{i,\mathbf{k}}(\mathbf{r}) = u_{\mathbf{k}}(\mathbf{r})\chi_{i\mathbf{k}}(\mathbf{r})$$

The envelope function $\chi_{i,\mathbf{k}}$ is determined by the potential profile $E_c(z)$ plus, if it is the case, an external contribution $V_{\text{ext}}(\mathbf{r})$ (for example an external electrical field applied to the structure, or the electrostatic potential due to electrons and ionized impurities). With this approach, it is possible to describe the electrons in the conduction band just with their envelope function, considering for them an effective mass m^* that includes the effects of the crystal potential, as above [21].

The Schrödinger equation for the envelope function reads:

$$\left[-\frac{\hbar^2}{2} \nabla \frac{1}{m^*(E_{i,\mathbf{k}}, z)} \nabla + E_c(z) + V_{\text{ext}}(\mathbf{r}) \right] \chi_{i,\mathbf{k}}(\mathbf{r}) = E_{i,\mathbf{k}} \chi_{i,\mathbf{k}}(\mathbf{r})$$

In the structures discussed in this manuscript, V_{ext} depends only on z . The problem can then be separated and the envelope function expressed as the product of a plane wave propagating in the layers plane and a function of the growth direction z :

$$\chi_{i\mathbf{k}}(\mathbf{r}) = \psi_i(z) \frac{e^{i\mathbf{k}_{\parallel} \cdot \mathbf{r}_{\parallel}}}{\sqrt{S}}$$

where S is the surface of the plane. The function $\psi_i(z)$ is then solution of the one-dimensional Schrödinger equation:

$$\left[-\frac{\hbar^2}{2} \frac{\partial}{\partial z} \frac{1}{m^*(E_i, z)} \frac{\partial}{\partial z} + E_c(z) + V_{\text{ext}}(z) \right] \psi_i(z) = E_i \psi_i(z) \quad (1.5)$$

The total energy $E_{i,\mathbf{k}}$ is then the sum of the eigenenergy E_i and the kinetic energy associated with the free movement in the plane of the layers.

Quantum wells

A quantum well can be obtained by sandwiching a semiconductor layer between two layers of another semiconductor with a greater gap, as schematized in Fig. 1.4. The discontinuity in the conduction band confines the movement of electrons in the growth direction, while leaving it free on the layer (parallel) plane. In this case, the confinement in the z direction makes the eigenenergies E_i of Eq. (1.5) discrete. If one considers also the kinetic contribution in the layer plane, the total energies are given by

$$E_{i\mathbf{k}} = E_i + \frac{\hbar^2 k_{\parallel}^2}{2m^*(E)}$$

The index i labels a set of states called *subbands*, whose dispersion on the plane (x, y) is parabolic if the effective mass does not depend on the energy (see Fig. 1.5). In this case, the energy separation between consecutive subbands is constant and independent of k_{\parallel} .

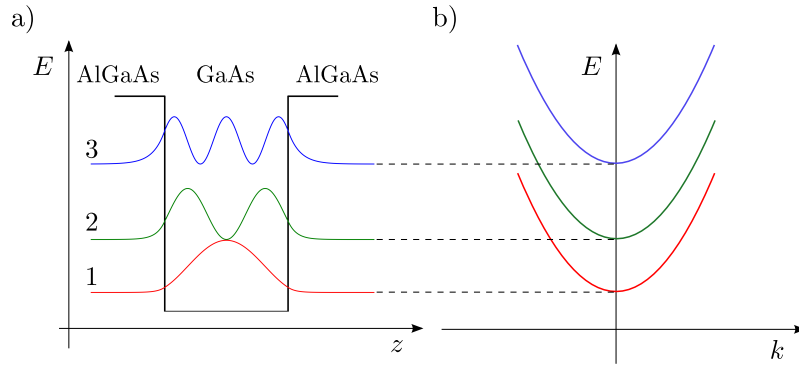


Figure 1.5: a) Schematization of a GaAs/AlGaAs quantum well: conduction band (in black) and square moduli of wavefunctions associated with three bound states (colored lines), represented at their respective energies. b) Dispersion curves on the parallel plane (parabolic approximation).

In the general case, Eq. (1.5) cannot be solved analytically, and electronic states must be obtained numerically. It is however instructive to consider the problem of an infinite quantum well of width L , with constant effective mass, for which the exact wavefunctions and eigenenergies can be calculated as [24, 25]:

$$\begin{aligned} \psi_i^{\text{infinite}}(z) &= \sqrt{\frac{2}{L}} \sin\left(\frac{i\pi z}{L}\right) \\ E_i^{\text{infinite}} &= \frac{\hbar^2 \pi^2 i^2}{2m^* L^2} \end{aligned} \quad (1.6)$$

We see from the above expression of the energies E_i that the separation between subbands depends on the width of the quantum well L . This remains true also in the case of finite potential, and is a fundamental feature in the design of devices based on intersubband transitions, i.e. transitions between different subbands.

Three-band Kane model in the envelope-function approximation

In a certain number of cases, for example InGaAs/AlInAs, the approximation of a constant effective mass (i.e. parabolic bands) is not sufficient for an accurate description of the system.

Band structure calculations in this work accounting for non parabolicity were performed following Ref. [26]. The approach used is the three-band Kane model in the envelope function approximation. In this model, the conduction states are coupled to the light-hole and spin-orbit valence states, as the heavy-hole state is decoupled from the original 4×4 Hamiltonian (8×8 reduced by spin degeneracy). The remaining 3×3 Hamiltonian in the Kane approximation reads:

$$\begin{pmatrix} E_c(z) & \sqrt{\frac{2}{3}} \frac{p_{cv}}{m_0} p_z & -\sqrt{\frac{1}{3}} \frac{p_{cv}}{m_0} p_z \\ -\sqrt{\frac{2}{3}} \frac{p_{cv}}{m_0} p_z & E_{lh} & 0 \\ \sqrt{\frac{1}{3}} \frac{p_{cv}}{m_0} p_z & 0 & E_{so} \end{pmatrix}$$

and it is acting on a three-dimensional vector of envelope functions:

$$H \begin{pmatrix} \Phi_c \\ \Phi_{lh} \\ \Phi_{so} \end{pmatrix} = E \begin{pmatrix} \Phi_c \\ \Phi_{lh} \\ \Phi_{so} \end{pmatrix} \quad (1.7)$$

where c , lh and so label conduction, light-hole and split-off position-dependent band edges (see also schematization in Fig. 1.3). As previously mentioned, the matrix element p_{cv} can be expressed in terms of the Kane energy E_P as $p_{cv} = i\sqrt{\frac{m_0 E_P}{2}}$.

Considering the eigenproblem (1.7), we get the valence band wavefunctions in terms of the conduction band wavefunction:

$$\begin{aligned} \Phi_{lh} &= -\frac{1}{E - E_{lh}} \sqrt{\frac{2}{3}} \frac{p_{cv}}{m_0} p_z \Phi_c \\ \Phi_{so} &= \frac{1}{E - E_{so}} \sqrt{\frac{1}{3}} \frac{p_{cv}}{m_0} p_z \Phi_c \end{aligned}$$

which combined with (1.7) give

$$(E_c - E)\Phi_c - \frac{E_p}{2m_0} p_z \left[\frac{2}{3} \frac{1}{E - E_{lh}} + \frac{1}{3} \frac{1}{E - E_{so}} \right] p_z \Phi_c = 0 \quad (1.8)$$

From Eq. (1.8) it is finally possible to define $m(E, z)$ as

$$\frac{1}{m(E, z)} = \frac{E_p}{m_0} \left[\frac{2}{3} \frac{1}{E - E_{lh}} + \frac{1}{3} \frac{1}{E - E_{so}} \right]$$

In the following, we will set the zero of the energy scale to the conduction band edge, so that $E_c = 0$. In this case, we express the energy-dependent mass as

$$\frac{1}{m(E, z)} = \frac{E_p}{m_0} \left[\frac{2}{3} \frac{1}{E + E_g} + \frac{1}{3} \frac{1}{E + \Delta_{so} + E_g} \right] \quad (1.9)$$

where we have adopted the same naming convention as Fig. 1.3, and used the relations

$$\begin{aligned} E_c - E_{lh} &= E_g \\ E_c - E_{so} &= E_g + \Delta_{so} \end{aligned}$$

Numerical resolution

The band structure calculations performed in this work are either based on the Kane model described above (for non-parabolic bands, namely in the case of GaInAs/AlInAs), or on a simplified one-band version where the coupling with valence bands is not considered. The latter approximation has been applied only to the case of AlGaAs/GaAs systems, where non-parabolicity does not play a crucial role.

The numerical method that implements the resolution of Schrödinger equation (1.5) is a shooting method [27, 28], an iterative method for the resolution of differential equations based on the calculation of the solutions point by point. This procedure makes it possible to solve the eigenproblem for arbitrary potentials, also in the case of nonzero applied electric fields.

1.2. Effect of tunneling: extended and localized basis

The heterostructure potentials considered in this work are often composed of more than one quantum well, separated by barriers thin enough for the wavefunctions to tunnel from one well to the other [25]. Figure 1.6 presents the example of a GaInAs/AlInAs structure observed with a Transmission Electron Microscope (upper panel), along with the corresponding conduction band profile (lower panel). The TEM image shows the abruptness of the interfaces between different semiconductors. Growth imperfections occur on the Å length scale, over one monolayer².

In structures consisting of multiple quantum wells, one has the choice of the basis to use in order to calculate the eigenstates of the system. An illustrative example of a three-well potential is shown in Fig. 1.7.

- If the calculation is applied to the whole potential, the resulting wavefunctions are the eigenstates of the potential considered as a unique quantum-mechanical system. These eigenstates include the effect of tunneling, and the wavefunctions are delocalized over the whole structure. In the following, we will refer to this as *extended basis* solution. As an example, see the upper panel of Fig. 1.7.
- Alternatively, one can choose to solve the problem on subsets of the whole potential, considered as isolated: this is a *localized basis* approach. In this way, the tunnel coupling between the localized regions is no more included in the calculated wavefunctions, and it has to be added as a coupling potential between states belonging

²This creates static scatterers that may diffuse electrons (see §B.1 for a discussion on interface roughness scattering).

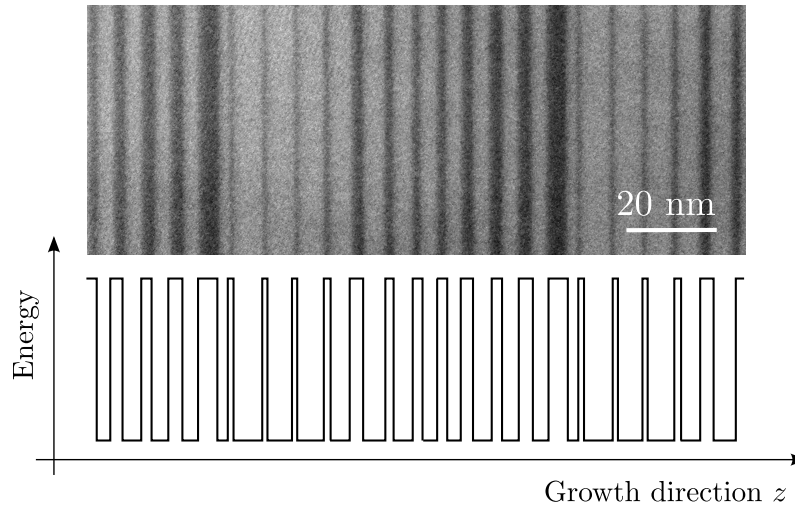


Figure 1.6: Upper panel: Transmission Electron Microscopy (TEM) image of a MOCVD-grown AlInAs/InGaAs quantum cascade laser (see §1.5) active region (courtesy of Isabelle Sagnes and Grégoire Beaudoin, Laboratoire de Photonique et de Nanostructures). Lower panel: schematization of the resulting conduction band profile, confining potential for electrons.

to different subsets. A possible method for achieving this is discussed in the next subsection.

The choice of the subsets is arbitrary (see lower panel of Fig. 1.7). The whole system could for instance be decomposed on zone (a)+(b), or on a single-well basis composed of regions (b)+(c)+(d), or using (c)+(d)+(e). It is usually reasonable to choose as limits of the localized regions the thicker barriers in the structure, therefore the last two solutions would normally be avoided.

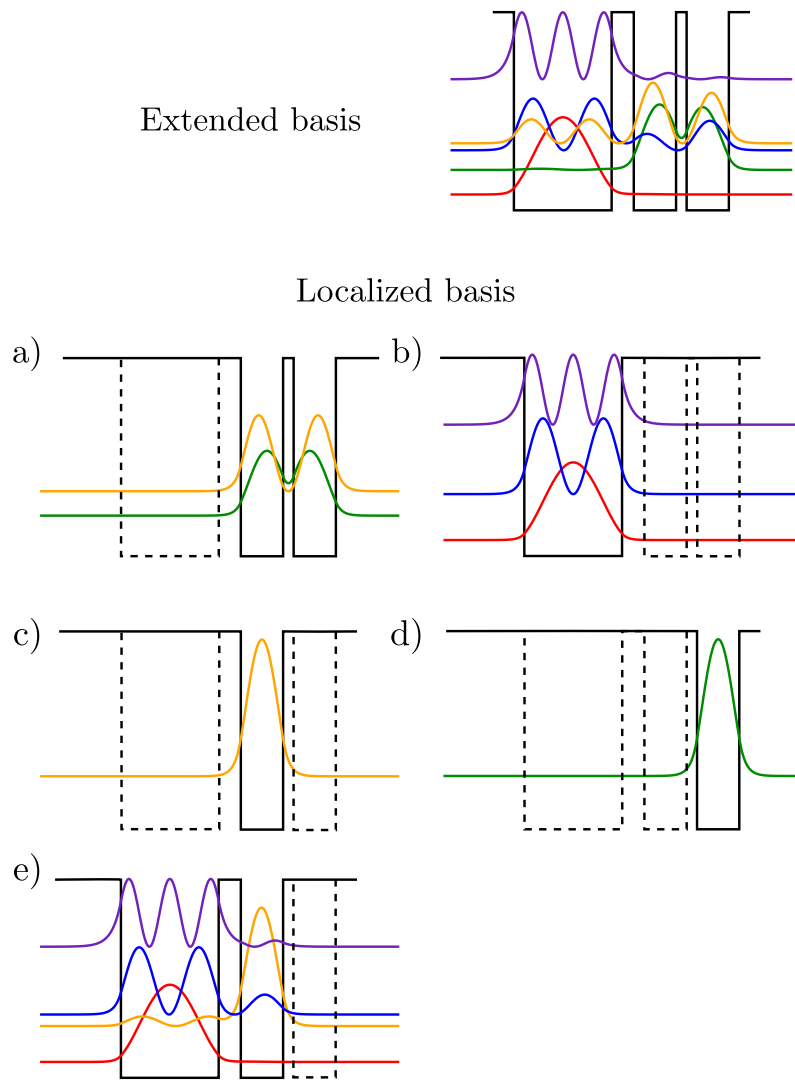


Figure 1.7: Band structure and squared moduli of wavefunctions in a GaAs/Al_{0.15}Ga_{0.85}As structure, measures (in Å) 185/42/80/20/80. Upper panel: Extended basis calculation. Lower panel: Choices of localized regions: the full structure can be decomposed as (a)+(b), or (b)+(c)+(d), or (d)+(e).

1.2.1. Tight-binding approximation

It is possible to estimate the tunnel coupling between localized wavefunctions through an analytical procedure called tight-binding approximation. We sketch here the basic details of this approximation, as it will be used in the following (§3.2). A full discussion can be found for example in [21, 25].

We start by considering a simple system of two coupled quantum wells, like the one schematized in Fig. 1.8.

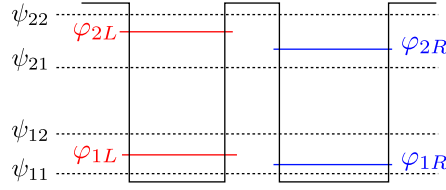


Figure 1.8: Coupled quantum wells: extended and tight-binding basis

If the ground and first excited state of the individual quantum wells are sufficiently separated in energy, the extended basis wavefunctions can be written on left- and right-basis:

$$\begin{aligned}
 \psi_1(z) &= \psi_{11}(z) = L_{11}\varphi_{1L}(z) + R_{11}\varphi_{1R}(z) \\
 \psi_2(z) &= \psi_{12}(z) = L_{12}\varphi_{1L}(z) + R_{12}\varphi_{1R}(z) \\
 \psi_3(z) &= \psi_{21}(z) = L_{21}\varphi_{2L}(z) + R_{21}\varphi_{2R}(z) \\
 \psi_4(z) &= \psi_{22}(z) = L_{22}\varphi_{2L}(z) + R_{22}\varphi_{2R}(z)
 \end{aligned} \tag{1.10}$$

In order to find the coefficients L and R , we define the quantities

$$\begin{aligned}
 s_{LR} &= \int \varphi_L(z)\varphi_R(z) dz && \text{overlap integral} \\
 t_{LR} &= \int \varphi_L(z)V_L(z)\varphi_R(z) dz && \text{tunneling (or transfer) integral} \\
 c_{LR} &= \int \varphi_L(z)V_R(z)\varphi_L(z) dz && \text{shift integral}
 \end{aligned}$$

where V_L and V_R are the conduction band profiles of individual quantum wells.

For each couple of states of energy ε_L and ε_R associated with the ground ($i = 1$) and excited ($i = 2$) state, the Hamiltonian on the tight-binding basis is

$$H_i = \begin{pmatrix} \varepsilon_L + c_{LR} & \varepsilon_R s_{LR} + t_{LR} \\ \varepsilon_L s_{RL} + t_{RL} & \varepsilon_R + c_{RL} \end{pmatrix}$$

Coefficients L and R can be obtained via the solution of the generalized eigenproblem

$$H_i \mathbf{a} = E S \mathbf{a} \tag{1.11}$$

with the overlap matrix

$$S = \begin{pmatrix} 1 & s_{LR} \\ s_{RL} & 1 \end{pmatrix} \quad (1.12)$$

reflecting the fact that φ_R and φ_L are not orthogonal.

The eigenvalues of (1.11) are the new energies E_- and E_+ . The eigenvectors contain the coefficients L and R :

$$\mathbf{a}_1 = \begin{pmatrix} L_{11} & L_{12} \\ R_{11} & R_{12} \end{pmatrix} \quad \mathbf{a}_2 = \begin{pmatrix} L_{21} & L_{22} \\ R_{21} & R_{22} \end{pmatrix} \quad (1.13)$$

In the case of identical quantum wells, $\varepsilon_R = \varepsilon_L = \varepsilon$, the eigenenergies can be found to be

$$E_{\pm} = \varepsilon - \frac{c}{1 \mp s} \pm \frac{t}{1 \mp s} \quad (1.14)$$

If the overlap between wells is weak, the splitting in energy between the two eigenenergies is $\Delta E \approx 2t$. The tunneling integral t is thus responsible for the splitting between the energy levels.

Validity of tight-binding approximation

The founding hypothesis of the presented tight-binding approximation is that the single quantum well wavefunctions are a good basis for the coupled structure; it is then clear that this approximation has a strong dependence on the tunneling barrier width, thus on the strength of tunnel coupling.

To show this, we consider two symmetrical GaAs/AlGaAs quantum wells of width 70 Å separated by a barrier of variable width. Figure 1.9 presents the four wavefunctions calculated in the localized basis.

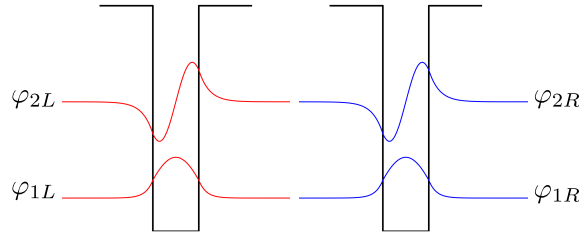


Figure 1.9: 70 Å GaAs/Al_{0.45}Ga_{0.55}As quantum well, localized basis.

We implement numerically the procedure described in the previous section, and report in Fig. 1.10 the wavefunctions of the coupled wells structure calculated by the tight-binding expansion (solid lines), along with the 'exact' wavefunctions calculated in the extended basis (dashed lines). Note that in this simple case we clearly see the appearance of two doublets composed of a bonding (symmetrical) and an antibonding (antisymmetrical) state, in analogy with a diatomic molecule. As it can be seen from Fig. 1.10, the tight-binding expansion is more accurate for thicker barriers. Figure 1.11 shows the calculated

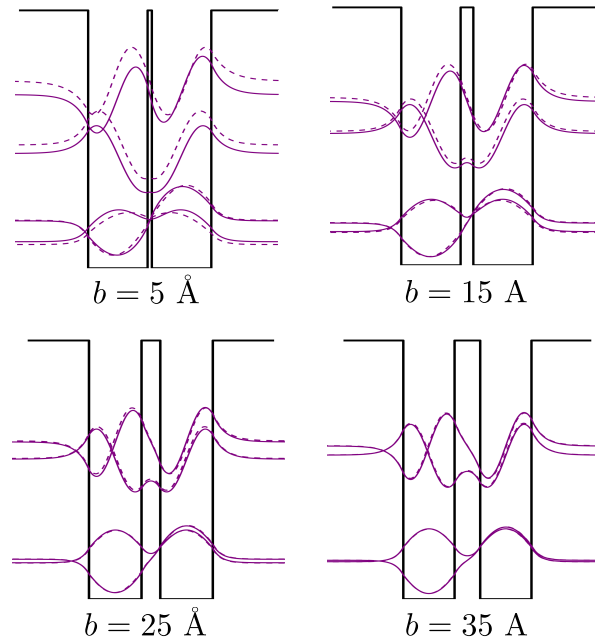


Figure 1.10: GaAs/Al_{0.45}Ga_{0.55}As structure, $70/b/70$ Å. Comparison between wavefunctions calculated in the extended basis (dashed lines) and tight-binding basis (solid lines).

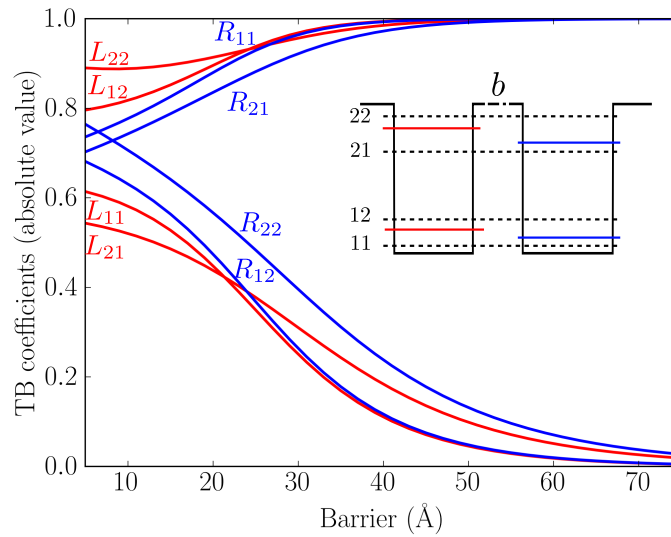


Figure 1.11: GaAs/Al_{0.45}Ga_{0.55}As structure, $70/b/75$ Å. Absolute values of L and R coefficients calculated for the expansion (1.10) for different values of barrier b . Inset: scheme of the coupled wells. Solid lines represent the localized basis states, dashed lines the extended basis states.

coefficients of the tight-binding expansion for two tunnel-coupled quantum wells.

By exploiting the results shown in Figs. 1.10 and 1.11, we can identify three barrier ranges:

- For very small barriers b (smaller than $\approx 10 \text{ \AA}$), the tight-binding expansion is not valid (see Fig. 1.10), because the localized wavefunctions are not a good basis for the system.
- For finite barriers b , L and R coefficients are different from zero: each extended wavefunction contains both a left and a right component.
- For wide barriers b (greater than $\approx 60 \text{ \AA}$), the system wavefunctions are localized in each well, so the extended basis wavefunctions coincide with the localized basis, and L, R coefficients assume only 0 or 1 values.

In the following, we will calculate the eigenenergies and wavefunctions in the extended basis, except for particular applications where the role of tunnel coupling will be explicitly considered.

1.3. Light-matter interaction: intersubband absorption

We describe in this section two models for the calculation of the intersubband absorption of semiconductor quantum wells: Lorentz model (classical) and Fermi's golden rule (semiclassical). Both these models consider a single-particle picture, in which electrons are seen as independent. However, collective effects can have an important influence on the intersubband optical absorption, as it will be discussed in Chapters 2 and 3.

1.3.1. Lorentz model

The Lorentz oscillator model is a classical description of a medium, where electrons are supposed to be bound to the (fixed) positive ions by a harmonic force [29]. If such a medium is excited by an external electric field, the movement of the microscopic bound charges results in a polarization. In this model, N_V electrons per unit volume are therefore seen as N_V oscillators at frequency ω_0 .

Under the influence of an electric field $\mathbf{E}(\omega)$ associated with an electromagnetic radiation, the movement of an electron is described by the relation

$$m_0 (-\omega^2 - i\gamma\omega + \omega_0^2) \mathbf{r}(\omega) = -e\mathbf{E}(\omega)$$

corresponding to a polarization

$$\mathbf{P}(\omega) = -N_V e \mathbf{r} = \frac{N_V e^2}{m_0} \frac{1}{\omega_0^2 - \omega^2 - i\gamma\omega} \mathbf{E}(\omega)$$

The proportionality between $\mathbf{P}(\omega)$ and $\mathbf{E}(\omega)$ is normally expressed as

$$\mathbf{P}(\omega) = \varepsilon_0 \chi(\omega) \mathbf{E}(\omega)$$

and we recognize that the electrical polarizability $\chi(\omega)$ reads in this framework

$$\chi(\omega) = \frac{N_V e^2}{m_0 \varepsilon_0} \frac{1}{(\omega_0^2 - \omega^2 - i\gamma\omega)} \quad (1.15)$$

The electric displacement \mathbf{D} of the medium is related to the electric field \mathbf{E} and polarization \mathbf{P} through:

$$\mathbf{D} = \varepsilon_0 \mathbf{E} + \mathbf{P} \quad (1.16)$$

where \mathbf{P} is composed of a part due to the non-resonant background plus the resonant part: $\mathbf{P} = \mathbf{P}_{\text{background}} + \mathbf{P}_{\text{resonant}}$, with $\mathbf{P}_{\text{background}} = \varepsilon_0 \chi_{\text{bg}} \mathbf{E}$. If we assume that the material is isotropic, the relative dielectric function ε is defined by:

$$\mathbf{D} = \varepsilon_0 \varepsilon \mathbf{E} \quad (1.17)$$

By combining Eqs. (1.15)-(1.17) we obtain the complex relative dielectric function $\varepsilon(\omega)$:

$$\begin{aligned} \varepsilon(\omega) &= 1 + \chi_{\text{bg}} + \chi(\omega) = \\ &= \varepsilon_\infty - \frac{N_V e^2}{m_0 \varepsilon_0} \frac{1}{\omega^2 - \omega_0^2 + i\gamma\omega} \end{aligned} \quad (1.18)$$

where $\varepsilon_\infty = 1 + \chi_{\text{bg}}$ is the limit for high frequencies of the real part of ε . If the system presents many different resonance frequencies ω_j , Eq. (1.18) is generalized to

$$\varepsilon(\omega) = \varepsilon_\infty - \sum_j \frac{N_j e^2}{m_0 \varepsilon_0} \frac{1}{\omega^2 - \omega_j^2 + i\gamma\omega}$$

where N_j is the volume density of oscillators at frequency ω_j .

In order to apply this model to quantum wells, we need to replace the electron free mass m_0 with the effective mass m^* . It is also necessary to introduce a phenomenological oscillator strength f_j for each transition. For instance, to describe absorption from level 1 to level 2, one can write

$$\varepsilon(\omega) = \varepsilon_\infty \left(1 - \frac{N_S e^2}{m^* \varepsilon_0 \varepsilon_\infty L_{\text{eff}}} \frac{f_{12}}{\omega^2 - \omega_{12}^2 + i\gamma\omega} \right)$$

where the factor N_V has been replaced by N_S/L_{eff} , with N_S surface density and L_{eff} effective length of the quantum well [30]. The oscillator strength can be calculated in the framework of the semiclassical model.

1.3.2. Semiclassical model: Fermi's golden rule

The absorption rate between two bound states $|\psi_{i,\mathbf{k}}\rangle$ and $|\psi_{j,\mathbf{k}'}\rangle$ in a quantum well can be calculated with Fermi's golden rule [24]. This corresponds to a semiclassical approach, in which the quantization of the photon field is ignored, and a classical electromagnetic wave is considered.

Let us suppose a linearly polarized electromagnetic plane wave with an electric field

$$\mathbf{E} = E_0 \hat{\varepsilon} \cos(\mathbf{q} \cdot \mathbf{r} - \omega t)$$

of polarization $\hat{\varepsilon}$, angular frequency ω , and propagation vector \mathbf{q} such that $\omega = cq/n$, with c speed of light and $n = \sqrt{\varepsilon_\infty}$ refractive index of the substrate. The vector potential \mathbf{A} associated with this incident electromagnetic wave is given by the relation $\mathbf{E} = -\frac{\partial \mathbf{A}}{\partial t}$ and can be written

$$\mathbf{A} = \frac{iE_0 \hat{\varepsilon}}{2\omega} \left[e^{i(\mathbf{q} \cdot \mathbf{r} - \omega t)} - e^{-i(\mathbf{q} \cdot \mathbf{r} - \omega t)} \right]$$

The Schrödinger equation for an electron (charge $-e$) in an electromagnetic field is obtained by replacing the \mathbf{p} term in Eq. (1.1) with $(\mathbf{p} + e\mathbf{A})$. We can employ the dipole approximation, valid if the wavelength of the radiation is much larger than any characteristic dimension of electronic origin (in the case of intersubband transitions, the quantum well width). This condition is fulfilled in the mid- and far-infrared frequency range ($\approx 3\text{-}300 \mu\text{m}$), which allows one to neglect the wave vector \mathbf{q} , and the spatial dependence of \mathbf{A} . We also neglect the \mathbf{A}^2 term, which becomes important just for high electronic densities, as we will see in Chapter 2. In the effective mass description, the interaction Hamiltonian finally reads [21]:

$$H_{\text{int}} = \frac{e}{m^*} \mathbf{A} \cdot \mathbf{p} = \frac{ieE_0}{2m^*\omega} \hat{\varepsilon} \cdot \mathbf{p}$$

Fermi's golden rule gives the rate of a transition $i \rightarrow j$ under this perturbation Hamiltonian, describing absorption (W_{ij}^-) or stimulated emission (W_{ij}^+):

$$W_{ij}^\pm(\omega) = \frac{2\pi}{\hbar} \frac{e^2 E_0^2}{4m^{*2}\omega^2} |\langle \psi_{j,\mathbf{k}'} | \hat{\varepsilon} \cdot \mathbf{p} | \psi_{i,\mathbf{k}} \rangle|^2 \delta(E_j - E_i \pm \hbar\omega) \quad (1.19)$$

In the envelope function approximation, the transition rate is then proportional to the square of the matrix element

$$\langle \psi_{j,\mathbf{k}'} | \hat{\varepsilon} \cdot \mathbf{p} | \psi_{i,\mathbf{k}} \rangle = \varepsilon_z \delta_{\mathbf{k},\mathbf{k}'} \langle \psi_j(z) | p_z | \psi_i(z) \rangle \quad (1.20)$$

where $\psi_j(z)$ and $\psi_i(z)$ are the envelope functions of final and initial states. The matrix element (1.20) expresses the intersubband polarization selection rule: optical transitions can only occur when the electric field has a non-zero component in the direction of growth z . In fact, only the ε_z component of the polarization is left in the expression of the transition rate, and no transitions are possible if the light propagates perpendicular to the sample surface. The Kroenecker delta $\delta_{\mathbf{k},\mathbf{k}'}$ expresses the fact that the optical transitions are vertical in \mathbf{k} -space: in the parabolic band approximation, the transition energy $E_{ij} = E_j - E_i$ and the transition rate W_{ij} do not depend on the in-plane wave vector.

It is useful to reexpress the absorption rate (1.19) by introducing the oscillator strength of the transition:

$$f_{ij} = \frac{2}{m^* \hbar \omega_{ij}} |\langle \psi_j | p_z | \psi_i \rangle|^2 = \frac{2m^* \omega_{ij}}{\hbar} |\langle \psi_j | z | \psi_i \rangle|^2$$

f_{ij} is a dimensionless quantity that facilitates the comparison of transition strengths in different physical systems. In the parabolic approximation, this quantity verifies the sum rule

$$\sum_j f_{ij} = 1 \quad (1.21)$$

valid for any initial state i , with the sum extending over all possible final states j . The incorporation of nonparabolicity requires more sophistication [26].

If we include the intensity of the z -component of the incident radiation $I_z = \varepsilon_0 cn E_{0z}^2/2$, the absorption rate of Eq. (1.19) takes the form

$$W_{ij}^-(\omega) = \frac{2\pi e^2 I_z}{\varepsilon_0 cn m^* \omega} f_{ij} \delta(\hbar\omega - E_{ij})$$

and it is thus proportional to the oscillator strength f_{ij} .

In the limit case of an infinite quantum well, only parity-changing (odd \rightarrow even or even \rightarrow odd) transitions are allowed due to the symmetry of the potential. The oscillator strength of the allowed transitions can be shown to be [24]:

$$f_{ij} = \frac{64}{\pi^2} \frac{i^2 j^2}{(j^2 - i^2)^3} \quad (1.22)$$

For the transition from ground state to first excited state, one has $f_{12} = 0.96$, which almost fully saturates the sum rule (1.21). As further examples, $f_{14} = 0.03$, $f_{23} = 1.87$, and so on. We see then that transitions between consecutive states (i.e. $j = i + 1$) are the most relevant [24].

If we consider electronic densities per surface unit N_i and N_j for the two subbands, we have $(N_i - N_j)S$ possible transitions, with S surface of the sample. Neglecting the interaction between electrons, each of them contributes equally to absorption:

$$W_{ij}^-(\omega) = \frac{2(N_i - N_j)\pi e^2 I_z S}{\varepsilon_0 cn m^* \omega} f_{ij} \delta(\hbar\omega - E_{ij}) \quad (1.23)$$

As it will be extensively discussed in the following, this approximation of non-interacting electrons is valid just for low-density electron gases (smaller than $\approx 10^{11} \text{ cm}^{-2}$ for optical transitions in the mid-infrared).

In the case of two-dimensional systems, one usually defines the 2D absorption coefficient $\alpha_{2D}(\omega)$, representing the absorbed electromagnetic energy per unit surface. Let us consider for simplicity a quantum well where just the first subband is occupied, thus just the $1 \rightarrow 2$ transition is possible, and $N_1 - N_2 = N_S$. Using Eq. (1.23) we obtain the expression for the 2D absorption coefficient

$$\alpha_{2D}(\omega) = \frac{\hbar\omega_{12}}{SI_z} W_{12}^- = \frac{2N_S\pi\hbar e^2}{\varepsilon_0 cn m^*} f_{12} \frac{\gamma/\pi}{(E_{12} - \hbar\omega)^2 + \gamma^2}$$

where we accounted for the finite width of the subbands by replacing the delta function in (1.23) with a Lorentzian function of full-width at half maximum γ , centered on the transition energy E_{12} .

1.4. Intersubband scattering processes

An electron moving in a perfect crystal lattice with no defects and with stationary atoms would maintain its state indefinitely, and its path would never be perturbed. This does not happen in real crystals, which implies that the electron will change its state at some stage: this process is called scattering [31]. The latter is usually described in terms of Fermi's golden rule: if an electron in a state $|i\rangle$ experiences a time-dependent perturbation H_{scatt} which could scatter it into any of the final states $|f\rangle$, then the lifetime τ_i of the carrier in the state $|i\rangle$ is given by:

$$\frac{1}{\tau_i} = \frac{\Gamma_i}{\hbar} = \frac{2\pi}{\hbar} \sum_f |\langle f|H_{\text{scatt}}|i\rangle|^2 \delta(E_i - E_f - \delta E)$$

where E_f and E_i are the energies of the final and initial states, δE is the energy exchanged during the scattering process (equal to zero in elastic processes), and Γ_i is the associated energy broadening.

Let us suppose an electron is in an excited subband of a quantum well. It may change subband to a lower one through a variety of processes: spontaneous emission of photons, emission of an optical phonon, elastic scattering through an impurity or interface defect (roughness), or through electron-electron scattering [3].

In a quantum well, radiative emission is by far not the dominant intersubband relaxation mechanism. In particular, if the energy separation between the subbands is larger than the optical phonon energy, the emission of a phonon is always possible and leads to lifetimes of the order of 1 ps, representing the dominant scattering process. If the emission of the optical phonon is not possible, the lifetime of levels is given by a combination of the other mechanisms, usually resulting in lifetimes of the order of a few ps.

In this section, we briefly review the basis of the calculation of scattering rates, introduce the level broadening (dephasing), and conclude by comparing non-radiative processes with spontaneous emission. Stimulated emission will be discussed in section §1.5.2.

1.4.1. Intersubband and intrasubband scattering rates

Fermi's golden rule can be applied to determine in a semiclassical picture the intersubband and intrasubband rates $\frac{1}{\tau_{\text{inter}}}$ and $\frac{1}{\tau_{\text{intra}}}$ [3, 32, 33].

$\frac{1}{\tau_{ij}^{\text{inter}}}$ is the transition rate due to intersubband scattering from state $|i\mathbf{k}\rangle$ to all possible states $|j\mathbf{k}'\rangle$, with $j \neq i$, through an interaction H_{scatt} [Fig. 1.12(a) and (c)]:

$$\frac{1}{\tau_{ij}^{\text{inter}}(\mathbf{k})} = \frac{2\pi}{\hbar} \sum_{\mathbf{k}'} |\langle j\mathbf{k}'|H_{\text{scatt}}|i\mathbf{k}\rangle|^2 \delta(E_i(\mathbf{k}) - E_j(\mathbf{k}') - \delta E) \quad (1.24)$$

Intrasubband scattering corresponds to processes where the electron remains in its subband, but changes its wavevector. $\frac{1}{\tau_{ij}^{\text{intra}}}$ gives thus the pure dephasing rate associated

with a $i \rightarrow j$ optical transition [Fig. 1.12(b) and (d)]. It can be expressed as [34]:

$$\frac{1}{\tau_{ij}^{\text{intra}}(\mathbf{k})} = \frac{2\pi}{\hbar} \sum_{\mathbf{k}'} |\langle i\mathbf{k}' | H_{\text{scatt}} | i\mathbf{k} \rangle - \langle j\mathbf{k}' | H_{\text{scatt}} | j\mathbf{k} \rangle|^2 \delta(E_{ij}(\mathbf{k}) - E_{ij}(\mathbf{k}') - \delta E) \quad (1.25)$$

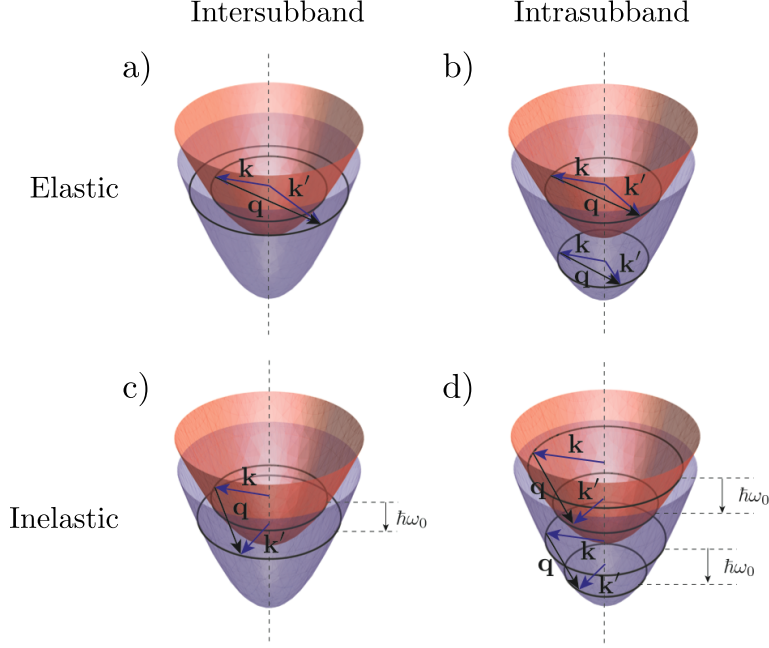


Figure 1.12: Adapted from Ref. [35]: Illustration of Γ^{inter} and Γ^{intra} . \mathbf{k} is the initial vector, \mathbf{k}' the final vector, \mathbf{q} the exchanged momentum. a) Intersubband and b) intrasubband elastic scattering, c) Intersubband and b) intrasubband inelastic scattering, with emission of a photon $\hbar\omega_0$.

We can thus write the broadening of the optical transition γ introduced at the end of §1.3.2 as

$$\gamma = \frac{1}{\tau_{\parallel ij}} = \frac{1}{2} (\Gamma_{ij}^{\text{intra}} + \Gamma_i^{\text{inter}} + \Gamma_j^{\text{inter}}) \quad (1.26)$$

where $\Gamma_{ij}^{\text{intra}}$ is the energy broadening due to dephasing, and $\Gamma_{i,j}^{\text{inter}}$ are the broadenings that originate from the total transition rates out of subbands i and j , respectively³. The total dephasing time associated with γ is usually denoted $\tau_{\parallel ij}$, and describes the loss of coherence due to scattering.

In the following, we will always consider transitions from $\mathbf{k} = 0$, i.e. the initial state is the edge of the initial subband: this corresponds to the approximation

$$\tau_{\text{relax}} \ll \tau \quad (1.27)$$

³Using the terminology of nuclear magnetic resonance, the broadening parameter can also be written as $\gamma = \hbar \left(\frac{1}{2T_1} + \frac{1}{T_2} \right)$, with T_1 upper-state lifetime, and T_2 characteristic time of pure dephasing processes. From comparison with Eq. 1.26, $T_2 = \frac{2\hbar}{\Gamma_{\text{intra}}}$ [3, 35]

with τ_{relax} relaxation time from $\mathbf{k} \neq 0$ to the center of the subband $\mathbf{k} = 0$, and τ any other relaxation time.

In this work, we consider three main scattering mechanisms in the study of electron transport (see Chapter 4):

- interface roughness (elastic);
- alloy disorder (elastic);
- LO-phonon spontaneous emission (inelastic).

We neglect other scattering mechanisms, such as electron-electron scattering and acoustic phonon emission/absorption. We suppose the first to be included in the relaxation mechanisms responsible for the assumption 1.27. It is expected to play a crucial role just for very clean structures at low temperatures [3]. Acoustic phonon scattering, on the other hand, is of significance only for extremely low densities and very clean systems at a high temperatures [3].

We calculate the intersubband term for each of the above mechanisms; we consider instead just the interface roughness intrasubband rate, which contributes to absorption linewidth and to coherence dephasing [36, 37]. Details on the calculation of scattering rates can be found in Appendix B.

1.4.2. Spontaneous emission

If the dipole matrix element between two states i and j is nonzero, spontaneous photon emission between an initial state i and a final state j can occur with a rate [3]:

$$W_{ij}^{\text{sp}} = \frac{e^2 n z_{ij}^2 E_{ij}^3}{3\pi c^3 \varepsilon_0 \hbar^4} = \frac{e^2}{6\pi m_0 c^3 \varepsilon_0 \hbar^2} n f_{ij} E_{ij}^2$$

The spontaneous emission rate is fundamentally proportional to the square of the photon energy. This leads to radiative lifetimes as long as microseconds in the THz range, therefore really long compared to the lifetimes of the order of picoseconds associated with non-radiative mechanisms. It is clear then that a very low radiative efficiency can be expected in mid- and far-infrared spontaneous emission.

To visualize this, we plot in Fig. 1.13 the characteristic times τ_{12}^{sp} and τ_{12}^{LO} for the $2 \rightarrow 1$ transition in a GaAs/AlGaAs quantum well, of variable width (thus variable transition energy). It can be appreciated that there are roughly six orders of magnitude between the two quantities.

From this observation, we understand that we cannot rely on this kind of spontaneous emission to obtain light from semiconductor heterostructures. We will see in the next section how an ingenious design of band structures has been used in quantum cascade lasers [3] to exploit stimulated emission instead.

In Chapters 2 and 3, we will explore a new kind of system which could be promising for obtaining spontaneous light emission from systems of quantum wells, based on superradiant properties of collective electronic excitations [10, 14, 15].

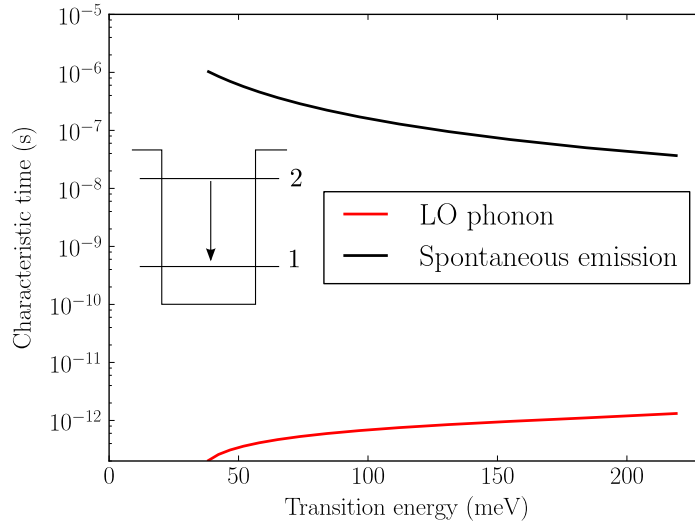


Figure 1.13: Calculated characteristic times of the $2 \rightarrow 1$ transition, for spontaneous emission (black line) and LO-phonon scattering (red line) in a GaAs/ $\text{Al}_{0.45}\text{Ga}_{0.55}\text{As}$ well, for well widths varying between 50 and 180 Å. Times are represented in logscale in function of the transition energy E_{21} .

1.5. Quantum Cascade Lasers

Quantum Cascade Lasers (QCLs) are unipolar semiconductor devices operating in the mid- and far-infrared (or THz) frequency range. The active region of a QCL is composed of several identical periods of a system of tunnel-coupled quantum wells. Its operation relies on electron relaxation between the bound states of these quantum wells.

In the following, we will focus on the electronic transport in the active region, without discussing the other aspects of the operation of a QCL (waveguide properties, fabrication issues). A complete and recent review is Ref. [3].

The theoretical proposal that optical gain could be obtained by using transitions between two-dimensional states in a superlattice biased by an external electrical field dates back to 1971, with the work of Kazarinov and Suris [38]. More than twenty years had to pass before the first experimental QCL demonstration by Faist et al., in 1994 [2].

The first QCLs operated at cryogenic temperatures. After the demonstration of operation at room temperature [39], nowadays QCLs operate at room temperature and continuous wave-operation in the mid-infrared frequency range ($\approx 3 \mu\text{m} - 50 \mu\text{m}$) [40]. Laser operation has also been demonstrated for far-infrared wavelengths ($\approx 50 \mu\text{m} - 200 \mu\text{m}$) [41], but it is up to now still limited to low temperatures ($< 200 \text{ K}$) [42, 43].

Quantum engineering

The high degree of complexity that can be achieved in a QCL is a powerful example of the potential of quantum engineering. This is the possibility of controlling the material properties by defining the size and spatial distribution of the constituents at the nano level, independently of their chemical nature. As a consequence, the principles of operation of the device are not based on the optical properties of the constituent material, but arise from the layer sequence forming the superlattice heterostructure. QCLs have indeed been realized in several material systems: GaAs/AlGaAs, GaInAs/AlInAs, InAs/AlSb, GaInAs/GaAsSb.

Thanks to numerical simulation, it is possible to design the band structure of the system in an ingenious way, in order to obtain the desired transport and emission properties.

Unipolarity and cascading

Two main features are unique to QCLs and distinguish them from conventional semiconductor light emitters (see Fig. 1.14).

The first is unipolarity, i.e. the fact that the device operation relies only on electrons, making transitions between the conduction band subbands arising from size quantization in quantum wells. Their initial and final states have, in a parabolic approximation, the same curvature in the reciprocal space, which makes the joint density of states very sharp, similar to atomic transitions. Besides, the fact that transitions occur within subbands is the reason why the emission wavelength is not directly dependent on the band gap of constituent materials, but can be tuned by changing the layers thickness.

The other fundamental aspect of QCLs is the multistage 'cascaded' geometry of their structure, which gives them their name. Electrons are recycled from period to period, contributing each time to gain and photon emission: every electron injected above threshold generates N_p laser photons, where N_p is the number of periods in the structure.

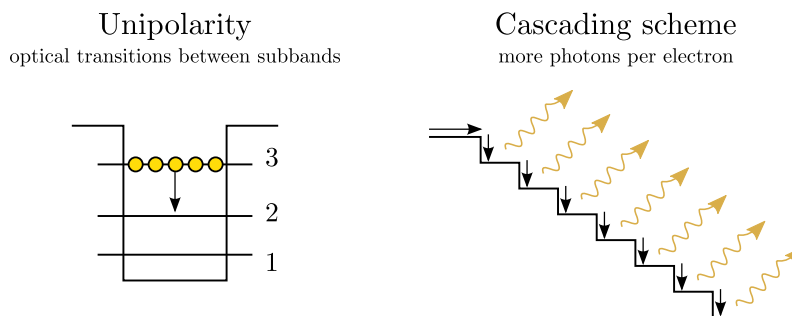


Figure 1.14: Adapted from Ref. [44]: Schematic representation of two features that characterize a quantum cascade laser.

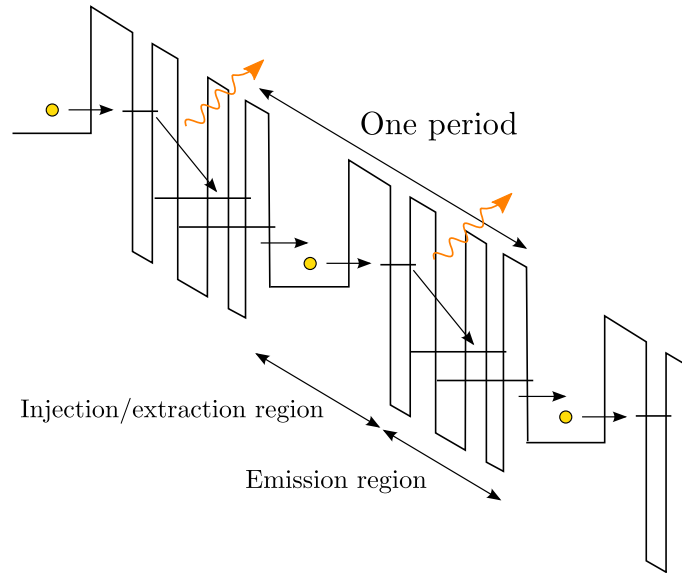


Figure 1.15: Adapted from Ref. [3]: Schematic conduction band diagram of a quantum cascade laser. Each stage of the structure consists of a radiative (active) region and a relaxation/injection region. Electrons can emit up to one photon per stage.

1.5.1. Fundamentals of QCLs active regions

The basis of operation of a QCL is schematically represented in Fig. 1.15. Electric current passes through a biased semiconductor heterostructure, composed of a periodic arrangement of unit cells (periods), each one consisting of a number of wells and barriers. Each QCL period can be divided in two parts:

- An active (emission) region, where the radiative transition takes place. This is the structure enabling a population inversion between the two levels of the laser transition.
- An injection/extraction region, conceived to convey electrons from one active region to the following. A portion of this region is doped, and acts as an electron reservoir, which will feed the carriers to the next period.

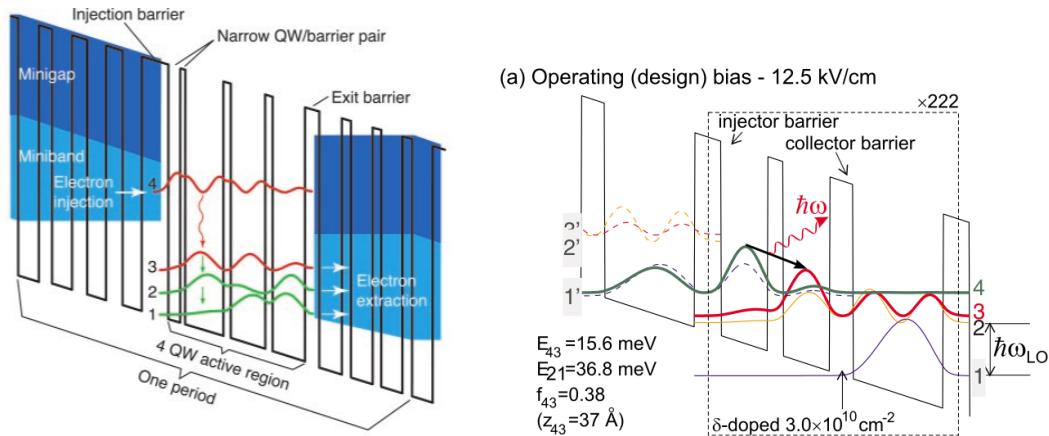
Thanks to the design freedom provided by quantum wells, it is in principle possible to tune the radiative transition in a wide portion of the mid-infrared ($\approx 40\text{-}400$ meV) and far-infrared range ($\approx 4\text{-}40$ meV) of the electromagnetic spectrum by suitably choosing the physical dimensions of the semiconductor layers. However, the design of a successful active region has to comply with a certain number of requirements. In particular, it must be possible to achieve population inversion, and the resulting gain must be able to overcome the optical losses.

Historically, these conditions were first satisfied for lasers emitting in the mid-infrared range (in Ref. [2], $4.2\ \mu\text{m} = 295$ meV). Achievement of lasing in the THz range needed

additional efforts (Ref. [41], $4.4 \text{ THz} = 18 \text{ meV}$). This has very fundamental reasons in the active region design, related to the magnitude of the radiative transition energies. In the THz range, these are close both to the very efficient LO-phonon emission energies and to thermal energies ($k_B T \approx 25 \text{ meV}$ at room temperature). Population inversion is then undermined both by shortened lifetimes of the excited state and backfilling of the ground state from lower levels.

One of the most successful strategies in the active region design is the so-called phonon extraction scheme. This is based on the idea of depopulating the ground state of the radiative transition as efficiently as possible, by exploiting the very short LO-phonon scattering times. The result can be achieved by a careful engineering of the active region, such that levels at the optimal energy separation for LO-phonon emission are available (see discussion at the end of §B.4). The first mid-IR laser operating at room temperature [39] is indeed based on two-phonon extraction [i.e. two levels separated $\hbar\omega_{LO}$ and $2\hbar\omega_{LO}$ from the ground state respectively, see Fig. 1.16(a)]. Three-phonon extraction has also been demonstrated [45].

The photon extraction strategy can be equally applied to THz lasers, see for example the design of Ref. [42], presented in Fig. 1.16(b).



(a) From Ref. [39]: InGaAs/AlInAs mid-IR structure based on two-phonon extraction, emitting at $\approx 140 \text{ meV}$. Levels 3-2 and 2-1 are separated by an energy close to the LO-phonon energy $\hbar\omega_{LO}$.

(b) From Ref. [42]: GaAs/Al_{0.15}Ga_{0.85}As THz structure based on a diagonal design, emitting at $\approx 16 \text{ meV}$. Levels 3 and 1 are separated by an energy close to $\hbar\omega_{LO}$.

Figure 1.16: Examples of QCL designs based on phonon extraction.

1.5.2. Rate equations for electronic transport

The key challenge in the conception of a laser based on intersubband transitions is to obtain a population inversion, which can be achieved through a careful design of the wavefunctions, and hence of the scattering times. In this section, we consider a rate

equation analysis of the steady-state populations in a QCL, and in particular provide the conditions for population inversion and gain. We schematize one period of the active zone with a three-level system, as shown in Fig. 1.17.

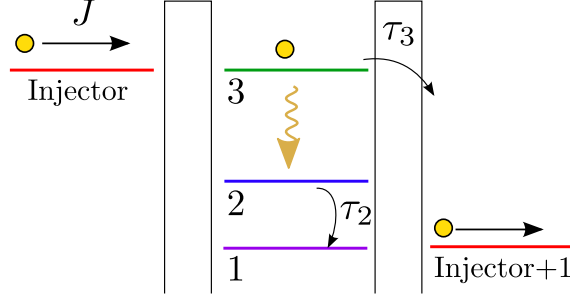


Figure 1.17: Adapted from Ref. [44]: Schematic representation of one active region of a QCL.

We consider the laser action to happen between levels 3 and 2, and the injector is assumed to consist of only one level. Electrons are injected in the $n = 3$ state from the injector of the previous period at a rate equal to J/e , with J current density. They can then scatter from this state to the lower states 2 and 1 with rates τ_{32}^{-1} and τ_{31}^{-1} respectively, resulting in a total relaxation rate of level 3 $\tau_3^{-1} = \tau_{32}^{-1} + \tau_{31}^{-1}$.

We indicate with n_3 the population (in terms of electronic density per unit surface) of the excited state, and with n_2 that of the ground state of the radiative transition. If a population inversion is achieved ($n_3 > n_2$), the structure presents a gain G , defined as the ratio between the photon flux variation (stimulated emission - absorption) and the photon flux (the number of photons of energy $\hbar\omega$ crossing the structure per unit time). If G exceeds the optical losses α , photons are emitted by stimulated emission. We denote their surface density with S .

The rate of change of the populations may be then written as

$$\begin{cases} \frac{dn_3}{dt} = \frac{J}{e} - \frac{n_3}{\tau_3} - \sigma S n_3 + \sigma S n_2 \\ \frac{dn_2}{dt} = -\frac{n_2}{\tau_2} + \frac{n_3}{\tau_{32}} + \sigma S n_3 - \sigma S n_2 \\ \frac{dS}{dt} = \sigma S (n_3 - n_2) - \frac{c}{n} \alpha S = (G - \alpha) \frac{c}{n} S \end{cases}$$

with $G = \sigma(n_3 - n_2) \frac{n}{c}$, where n is the mode effective index and σ is the cross section per unit time for stimulated emission and absorption [44]:

$$\sigma = \frac{4\pi e^2}{\varepsilon_0 n} \frac{|z_{32}|^2}{i} \frac{1}{L_p 2\gamma_{32}} \frac{c}{n} \quad (1.28)$$

L_p is the thickness of one period of the cascade and 2γ FWHM of the laser transition. Note that we are not considering a spontaneous emission term because it would be

negligible with respect to the other mechanisms, as discussed in §1.4.2.

The expression for the current density at threshold J_{th} is found to be:

$$\frac{J_{\text{th}}}{e} = \frac{\alpha c}{\sigma n} \left[\tau_3 \left(1 - \frac{\tau_2}{\tau_{32}} \right) \right]^{-1}$$

The photon density at the equilibrium is

$$S = \frac{1}{\sigma \tilde{\tau}} \left(\frac{J}{J_{\text{th}}} - 1 \right)$$

where

$$\tilde{\tau} = \tau_2 + \tau_3 \left(1 - \frac{\tau_2}{\tau_{32}} \right)$$

In this model, the emitted power is thus linear with the injected current after threshold.

Conclusions

The rate equation approach presented in the last section allows one to link electronic properties (lifetimes) to macroscopic observables, like threshold current density or emitted power. However, this simplified model does not take into account fundamental mechanisms for the electronic transport in QCLs, like resonant tunneling. Furthermore, the optical properties are included in a single-particle approach, even though intersubband transitions are an intrinsically collective phenomenon.

These two latter issues are the main focus of this work. In particular, the collective nature of intersubband transitions from an optical point of view will be studied in Chapters 2 and 3. In Chapter 4, we will introduce a transport model that includes resonant tunneling in a coherent way, and apply it to the modeling of QCLs. Finally, we will present a study of the influence of collective effects in electron transport.

Many-body effects in the optical properties of a bidimensional electron gas

We study the effect of electron density on the optical properties of an electron gas confined in a semiconductor heterostructure, motivated by the intrinsically collective nature of intersubband transitions due to Coulomb interaction [30].

We provide a quantum model describing the coupling between intersubband plasmons in a single quantum well and in systems of tunnel-coupled wells, and its consequences on the infrared absorption spectra [16]. The discussion is divided in two main parts: first, we introduce the concept of collective excitations in intersubband absorption, and review some theoretical and experimental results on single quantum wells on which we base our work. In the second part, we present our quantum model, which generalizes these results to arbitrary confining potentials. We define the relevant quantities for the calculation of the absorption spectra. In particular, we define for each intersubband transition a microscopic current density, which can be related to the oscillator strength of the transition. We demonstrate that the overlap between these currents leads to the definition of a typical length for Coulomb interaction, hence determining the coupling between intersubband plasmons. The diagonalization of the electronic Hamiltonian allows us to define a microscopic current for each collective mode and to calculate the absorption spectrum.

2.1. Intersubband absorption and collective effects

In a single-particle picture, intersubband absorption in low-dimensional structures directly reflects dipole-allowed transitions between subbands. Nevertheless, this process involves a huge number of electrons, with typical densities of the order of 10^{11} cm^{-2} , up to 10^{13} cm^{-2} . It has been shown that intersubband absorption is indeed an intrinsically collective phenomenon [30], and its many-body nature has been the object of a vaste literature.

The study of collective effects in the optical response of a two-dimensional electron gas (2DEG) has been initially applied to inversion layers [46, 47], where many-body contributions are crucial in the interpretation of the experimental optical spectra. Collective effects were then studied also in quantum wells [48–59]. These effects can be divided into

the direct and exchange Coulomb interaction, excitonic correlations (vertex correction), and depolarization field.

Contrary to the case of inversion layers, many-body effects are found to compensate each other in most quantum wells with mid-infrared resonances, with standard electronic density levels and a single occupied subband (typically smaller than 10^{12} cm^{-2}) [57], and specific experiments have to be designed in order to observe their consequences in absorption [58]. On the other hand, the energies involved in the THz range are such that it is easier for collective effects to have a measurable impact [8, 53, 60].

The negligible role of many-body effects in quantum wells for standard doping regimes justifies the widespread use of single-particle approaches in the device modeling, as it is done in several electronic transport models used to simulate intersubband devices characteristics [24, 61–63]. In these models, electron-electron interaction is treated as a scattering process in the Born approximation.

However, it was demonstrated that higher doping levels correspond to an increasing importance of collective effects; in particular, a many-body picture is crucial in the interpretation of the absorption response of systems in which two or more subbands are occupied [55]. It can be indeed shown that the relevance of the depolarization term increases with the electronic density and the width of the well [54, 59].

In this section, we study the optical properties of high-density quantum well systems, for which the depolarization field is the dominant collective effect. In the following, we review some results of the study of depolarization effects in the case of a single squared quantum well. We follow an increasing order of complexity: we start by presenting the case of a single occupied subband in next section, to arrive finally to the case of several occupied subbands in §2.1.3.

2.1.1. One occupied subband

Let us start this discussion by considering a single quantum well of width L_{QW} presenting two confined levels. In the limit of low electron densities, the intersubband absorption of a photon is illustrated as a transition between the two electronic states, and manifests itself in an absorption line centered on the energy difference between the two electronic levels [24].

When the charge density of the bidimensional gas is important (in the mid-infrared, of the order of 10^{12} cm^{-2} and higher), in the presence of an external electromagnetic radiation, each electron feels an effective field induced by the excitation of the other electrons, the *depolarization field*. Exposing the system to an external radiation not only excites electrons into the higher level, but also modulates their charge density: the restoring Coulomb force gives rise to a kind of plasma oscillation [24, 30]. For a single intersubband transition, this results in a blue-shift of the absorption peak with respect to the transition frequency, which is usually denoted as depolarization (or plasma) shift.

The resonance frequency of transition $1 \rightarrow 2$ shifts from ω_{12} to

$$\tilde{\omega}_{12} = \sqrt{\omega_{12}^2 + \omega_{P12}^2} \quad (2.1)$$

with ω_{P12} the plasma frequency associated with the transition, written as [24]

$$\omega_{P12}^2 = \frac{e^2 f_{12} \Delta N_{12}}{m^* \varepsilon_0 \varepsilon_s L_{12}^{\text{eff}}} \quad (2.2)$$

The collective entity corresponding to the resonance frequency $\tilde{\omega}_{12}$ is called *intersubband plasmon* [51]. In Eq. (2.2), f_{12} is the oscillator strength of transition $1 \rightarrow 2$, $\Delta N_{12} = N_1 - N_2$ is the difference in population densities between subbands 1 and 2 (equal to N_1 if we consider just the first subband to be occupied), m^* is the effective mass, and ε_s is the background relative dielectric constant. The quantity L^{eff} represents an effective length of the quantum well, and is defined as [30]:

$$L_{12}^{\text{eff}} = \frac{\hbar}{2m^* \omega_{12}} \frac{f_{12}}{S_{12}} = \frac{z_{12}^2}{S_{12}} \quad (2.3)$$

where S_{12} has the units of length and is given by the expression

$$S_{ij} = \int_{-\infty}^{+\infty} \left[\int_{-\infty}^z \psi_i(z') \psi_j(z') dz' \right]^2 dz \quad (2.4)$$

S_{ij} depends directly on the wavefunctions ψ_i and ψ_j : it is therefore a well-defined quantity not only in the case of square quantum wells, but in any bidimensional structure (parabolic wells, coupled wells...). It was in fact originally introduced in the study of inversion layers of triangular shape [47], where a definition of length based on physical dimensions is ambiguous.

2.1.2. Two occupied subbands

The dependence of the plasma frequency on the population difference as displayed by Eq. (2.2) reflects the dependence of the depolarization shift on the electronic density: the greater the population difference between the two subbands, the greater $\tilde{\omega}_{12}$ will be with respect to ω_{12} . Note, however, that this shift cannot be indeterminately increased, but it has rather an intrinsic upper limit. If the electronic density is such that the Fermi level is higher than the bottom of the second subband, Pauli blocking will cause the difference ΔN_{12} to remain constant and independent from higher values of density. On the other hand, an increasing electronic density is expected to be related to more important Coulomb effects, as the number of electrons interacting with light is increasing. It is then natural to wonder what is the effect of the depolarization field when more than one subband is occupied.

Let us consider the case of a three-subband quantum well, two of which are populated. It has been experimentally observed [55, 64] that Coulomb interaction deeply modifies the optical response of the system. The depolarization field not only shifts the absorption

energies, but also induces a strong renormalization of the resonance amplitudes towards the high-energy peak. This phenomenon is due to the interplay between Coulomb interaction and interaction with light [55], and it can be quantitatively explained in the case of a single quantum well through a semiclassical description of the system with a dielectric function [65], generalization of the Lorentz model presented in §1.3.1.

Semiclassical model: dielectric function description

The interaction between light and a bidimensional gas can be described through a dielectric function. In the case of a quantum well with one occupied subband, like the one schematized in Fig. 2.1, the intersubband contribution to the dielectric function can be written as [24]

$$\varepsilon(\omega) = \varepsilon_s \left(1 - \frac{\omega_{P12}^2}{\omega^2 - \omega_{12}^2 + i\gamma\omega} \right) \quad (2.5)$$

In this expression, ω_{P12} is again defined by Eq. (2.2), and the parameter γ is the absorption linewidth, depending on the electron lifetime on the excited subband. Usually in the mid-infrared range $\gamma/\omega_{12} \approx 5 - 10\%$.

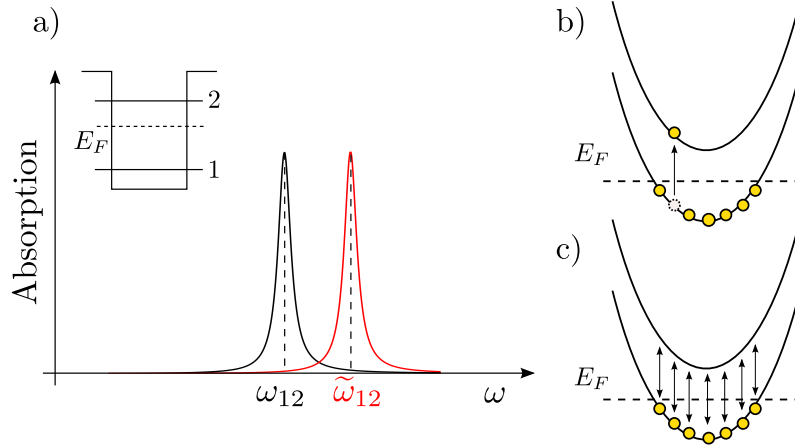


Figure 2.1: a) Schematized absorption spectrum of a quantum well with one occupied subband. Black curve: Coulomb effects not included (low doping limit). Red curve: Coulomb effects included, with the appearance of the depolarization shift. b) Schematic representation of a single-particle excitation between two subbands. c) Schematic representation of a collective excitation between two subbands.

In a single-particle picture, the absorption is directly related to the imaginary part of the dielectric function [29]. In the one-transition case:

$$\text{Abs}^{\text{SP}}(\omega) \propto \text{Im} [\varepsilon(\omega)] = \varepsilon_s \omega_{P12}^2 \mathcal{L}_\gamma(\omega - \omega_{12}) \quad (2.6)$$

where $\mathcal{L}_\gamma(\omega - \omega_{12}) = \frac{\gamma/2}{(\omega - \omega_{12})^2 + (\gamma/2)^2}$ is a Lorentzian function with full width at half maximum γ and centered in ω_{12} . This corresponds to the single-particle absorption spectrum plotted in black in Fig. 2.1.

On the contrary, the optical response accounting for the depolarization field can be calculated as [24, 30]:

$$\text{Abs}(\omega) \propto -\omega \text{Im} \left[\frac{1}{\varepsilon(\omega)} \right] \quad (2.7)$$

The difference between Eq. (2.6) and (2.7) lies in the conceptual distinction between a single-particle spectrum (in which we consider the system to be probed without being perturbed by light) and the absorption in the presence of light-matter interaction. The interaction with light induces oscillating dipoles within the matter, and it is not possible to neglect their contribution to the optical response. The necessity to use Eq. (2.7) derives thus from the fact that the system responds to the total field given by the sum of external radiation and internal polarization, rather than just to the external field [30]. Note that Eq. (2.7) is formally identical to the response function used in Electron Energy Loss Spectroscopy (EELS) [66]. In this case, the oscillating dipoles are induced by a Coulomb field instead than by an optical radiation.

By inverting Eq. (2.5), we obtain

$$\frac{\varepsilon_s}{\varepsilon(\omega)} = 1 + \frac{\omega_{P12}^2}{\omega^2 - \tilde{\omega}_{12}^2 + i\gamma\omega} \quad (2.8)$$

where $\tilde{\omega}_{12} = \sqrt{\omega_{12}^2 + \omega_{P12}^2}$ is the intersubband plasmon frequency defined above. We see then that the shape of the absorption spectrum is given by

$$\text{Abs}(\omega) \propto \varepsilon_s \omega_{P12}^2 \mathcal{L}_\gamma(\omega - \tilde{\omega}_{12})$$

which corresponds to a Lorentzian of full width at half-maximum γ , centered at a frequency $\tilde{\omega}_{12}$ (blue-shifted with respect to the bare intersubband transition ω_{12}), and with an amplitude proportional to ω_{P12}^2 . Eq. (2.8) provides thus a quantitative description of the behaviour illustrated in section §2.1.1.

Let us consider the case of two occupied subbands schematized in Fig. 2.2, considering the two possible transitions between consecutive levels [65] (the $1 \rightarrow 3$ transition being optically forbidden). The two intersubband transitions $1 \rightarrow 2$ and $2 \rightarrow 3$ have energies $\hbar\omega_{12}$ and $\hbar\omega_{13}$, respectively. Each of them contribute to the optical response, and the dielectric function can be written by considering two Lorentz oscillators as:

$$\varepsilon(\omega) = \varepsilon_s \left(1 - \frac{\omega_{P12}^2}{\omega^2 - \omega_{12}^2 + i\gamma\omega} - \frac{\omega_{P23}^2}{\omega^2 - \omega_{23}^2 + i\gamma\omega} \right)$$

It can be shown [65] that the inverse permittivity, directly related to the absorption spectrum, reads

$$\frac{\varepsilon_s}{\varepsilon(\omega)} = 1 + \frac{\Omega_{P+}^2}{\omega^2 - W_+^2 + i\gamma\omega} + \frac{\Omega_{P-}^2}{\omega^2 - W_-^2 + i\gamma\omega} \quad (2.9)$$

where the resonances W_\pm are given by

$$W_\pm^2 = \frac{1}{2} \left(\tilde{\omega}_{12}^2 + \tilde{\omega}_{23}^2 \pm \sqrt{(\tilde{\omega}_{12}^2 - \tilde{\omega}_{23}^2)^2 + 4\omega_{P12}^2\omega_{P23}^2} \right)$$

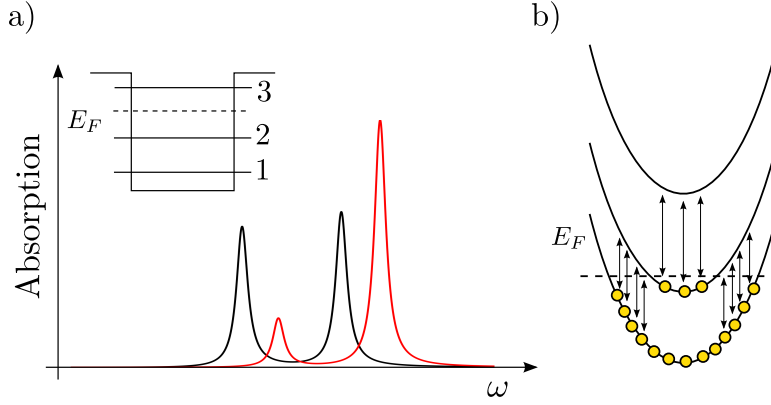


Figure 2.2: a) Absorption spectrum of a quantum well with two occupied subbands. Black curve: Coulomb effects not included (low doping limit). Red curve: Coulomb effects included, with the appearance of oscillator strength transfer. b) Schematic representation of a collective excitation between the three subbands. Note that the number of electrons involved in the excitation is N_1 (population of the first subband).

and the amplitudes $\Omega_{P\pm}$

$$\begin{aligned}\Omega_{P+}^2 &= K_+ (\omega_{P12}^2 + \omega_{P23}^2) \\ \Omega_{P-}^2 &= K_- (\omega_{P12}^2 + \omega_{P23}^2)\end{aligned}\quad (2.10)$$

with

$$K_{\pm} = \frac{1}{2} \pm \frac{(\tilde{\omega}_{12}^2 - \tilde{\omega}_{23}^2) (\omega_{P12}^2 - \omega_{P23}^2) + 4\omega_{P12}^2 \omega_{P23}^2}{2(\omega_{P12}^2 + \omega_{P23}^2) \sqrt{(\tilde{\omega}_{12}^2 - \tilde{\omega}_{23}^2)^2 + 4\omega_{P12}^2 \omega_{P23}^2}}$$

Equation (2.9) corresponds to an absorption spectrum with two resonances of amplitude proportional to Ω_{P+}^2 and Ω_{P-}^2 , at energies $\hbar W_+$ and $\hbar W_-$. We can then identify Ω_{P+} and Ω_{P-} with two effective plasma energies associated with the two absorption peaks. These amplitudes depend on the electronic charge density through the plasma frequencies ω_{P12} and ω_{P23} associated with the intersubband plasmons, as well as on the detuning between the intersubband plasmons energies $\tilde{\omega}_{12}$ and $\tilde{\omega}_{23}$. This is an indication of a coupling between the two transitions, which results in the redistribution of the oscillator strength between the two peaks. This effect was experimentally observed in Refs. [55, 64] in an InAs/AlSb and in a GaAs/AlGaAs quantum well with two occupied subbands. In Ref. [64] the coupling strength was also varied by changing the electronic density through the application of a gate voltage.

2.1.3. Several occupied subbands: cooperative regime

It has been recently demonstrated [14, 65] that Coulomb interaction leads to even more spectacular consequences in highly doped quantum wells, where several subbands are occupied [see Fig. 2.3(a)]. In this case, the measured absorption spectrum

consists of a single resonance, whose energy is completely different from those of the bare intersubband transitions, as illustrated in Fig. 2.3(b), taken from Ref. [14]. The single resonance corresponds to the excitation of a collective mode of the system, the *multisubband plasmon*, resulting from the phase-locking of all the optically active intersubband transitions. Each one of these transitions transfers its oscillator strength to the multisubband plasmon, hence concentrating all the oscillator strength of the system.

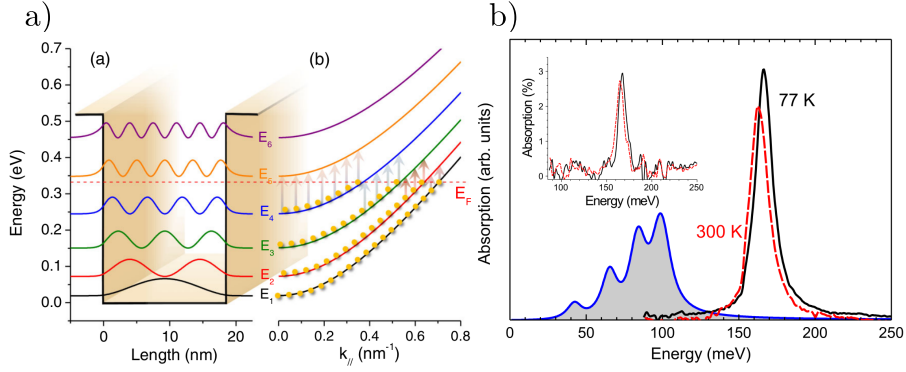


Figure 2.3: From [14]: a) Left: Band structure and energy levels of a 18.5 nm GaInAs/AlInAs quantum well. Right: Electronic dispersion of the subbands. The red dashed line indicates the Fermi energy at 0 K in the sample. The arrows indicate the main optical transitions that can take place in the structure. b) Absorption spectra of the same quantum well measured at 77 K (continuous line) and 300 K (dashed line). The inset presents the 77 K (continuous line) and 300 K (dashed line) spectra measured on the same sample at Brewster angle. The blue line in the main panel represents the simulated absorption spectrum, resulting from a single-particle description and Lorentzian line broadening of the allowed transitions.

The origin of this coherence lies in the charge-induced coupling between intersubband plasmons that was mentioned in the conclusion of the previous section. Indeed, the dielectric function model presented for two transitions can be generalized to the case of a single quantum well with several occupied subbands. It is possible to calculate a dielectric function in the case of N transitions by using the following expression [14, 55]:

$$\varepsilon(\omega) = \varepsilon_s \left(1 - \sum_{i=1}^{n_{\text{occ}}} \frac{\omega_{P,i,i+1}^2}{\omega^2 - \omega_{i,i+1}^2 + i\gamma\omega} \right) \quad (2.11)$$

where n_{occ} denotes the number of occupied subbands, which coincides with the number N of transitions between consecutive levels.

Equation (2.11) is a direct generalization of Eq. (2.9): each intersubband transition involved in the sum contributes to the permittivity through a Drude-Lorentz term, with a weight given by the corresponding squared plasma frequency. It is an useful expression, as it can be easily generalized to the case of non-parabolic subbands; the spectra calculated

in this case is in excellent agreement with the experimental one [14, 67]. Indeed, following a procedure analogous to that outlined in the previous section, numerical inversion of Eq. (2.11) provides N new resonance energies W_j , along with their respective effective plasma frequencies Ω_{Pj} , characterizing their amplitudes. In sufficiently high doping conditions, like in the case of Ref. [14], one of these plasma frequencies will be much higher than all the other $N - 1$, and correspond to the intensity of the bright multisubband plasmon resonance.

It is important to underline, however, that the sum in Eq. (2.11) is restricted to transitions between consecutive levels. An intuitive reason behind this is the fact that these transitions are the most relevant from the optical point of view. However, there is also a more subtle motivation not to include all the possible transitions, which is related to the fact that in a single heavily doped quantum well all the transitions between consecutive levels have an almost constant L^{eff} [appearing in the plasma frequency (2.2)]. As it will be explained in detail in the following of this work, this implies that the definition of dielectric function (2.11) is not general and it does not apply to structures of higher complexity than single quantum wells. In particular, it is not adequate in the case of tunnel-coupled quantum wells, which are at the basis of the engineering of intersubband devices like quantum cascade lasers.

Contributions to the energy of the multisubband plasmon

As observed before, the high-energy mode corresponding to the multisubband plasmon has an effective plasma frequency Ω_{Pn} much greater than the other modes. We denote $\Omega_{P_{\text{MSP}}}$ and W_{MSP} , respectively, the effective plasma frequency and the resonance frequency of this collective mode. We also introduce an index α for the intersubband transitions: $\alpha \equiv i \rightarrow i + 1$. The following sum rule holds [65]:

$$\Omega_{P_{\text{MSP}}}^2 = \sum_{\alpha} \omega_{P\alpha}^2$$

meaning that the squared effective plasma frequency of the multisubband plasmon is equal to the sum of the squared plasma frequencies of the transitions involved in the collective excitations. In other words, the coupling between intersubband plasmons redistributes the absorption amplitudes without changing the total absorption.

It can be shown [65] that the squared frequency of the multisubband plasmon can be expressed as:

$$W_{\text{MSP}}^2 = \frac{\sum_{\alpha} \omega_{P\alpha}^2}{\sum_{\alpha} \frac{\omega_{P\alpha}^2}{\omega_{\alpha}^2}} + \Omega_{P_{\text{MSP}}}^2$$

The first term is the harmonic mean of the different intersubband transition frequencies, weighted by the corresponding plasma frequencies: it represents the intersubband contri-

bution to the total energy of the multisubband plasmon, which we denote as ω_{ISB}^2 .

$$\omega_{\text{ISB}}^2 = \frac{\sum_{\alpha} \omega_{P\alpha}^2}{\sum_{\alpha} \frac{\omega_{P\alpha}^2}{\omega_{\alpha}^2}} \quad (2.12)$$

The second term is the squared effective plasma frequency of the mode, which expresses the plasma contribution to the total frequency. Thus one can write:

$$W_{\text{MSP}} = \sqrt{\omega_{\text{ISB}}^2 + \Omega_{P_{\text{MSP}}}^2} \quad (2.13)$$

which is the multisubband analogous of the plasma-shifted intersubband transition frequency of Eq. (2.1): $\tilde{\omega}_{\alpha} = \sqrt{\omega_{\alpha}^2 + \omega_P^2}$

From semiclassical to quantum model

We see from this introduction that Coulomb interaction has a deep influence on the coupling between infrared light and the electronic excitations of a bidimensional electron gas, and has macroscopic and measurable consequences on the optical response.

The following will be then devoted to a quantitative study of these effects through a fully quantum model. In particular, we will be interested in calculating the optical response of single quantum wells or systems of quantum wells. We will show that the proposed quantum model can be applied to an arbitrary confining potential in the cases where the depolarization effect is the dominant many-body contribution. This will allow the study of the interplay between Coulomb interaction and quantum effects such as confinement and tunneling.

2.1.4. Intersubband transitions as polarizations: coupled oscillators model

Before moving to the description of the model, let us look at the problem from a slightly different angle and try to get a physical grasp of the subject.

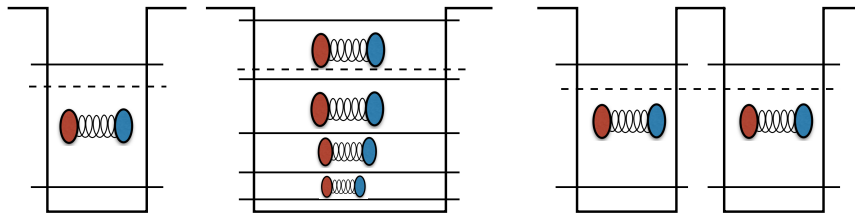


Figure 2.4: Schematic representation of intersubband transitions seen as oscillators.

When light is shone on a bidimensional gas, interaction between light and electrons creates an intersubband polarization in the growth direction z . The origin of this

polarization are the oscillating dipoles associated with intersubband transitions, as schematically represented in Fig. 2.4. In this picture, we can think of dipole-dipole Coulomb interaction as a constraint that connects all the intersubband oscillators, both within the same transition and between different transitions. The higher the electronic density, the stronger the constraint, the more the system responds as a whole 'network' of oscillators rather than as the incoherent sum of all the single oscillators.

In a single quantum well with N occupied subbands, the inverse of the dielectric function (2.11) has N poles W_j , corresponding to the N new eigenmodes of the system, as already mentioned. This is equivalent to a system of N coupled mechanical oscillators, which has N eigenmodes. In the case of two occupied subbands, these new eigenmodes correspond to a $1 \rightarrow 2$ -like mode where the two charge oscillations are predominantly out of phase, and a $2 \rightarrow 3$ -like mode where the oscillations are predominantly in phase. The in-phase mode couples strongly to the oscillating external field, and takes oscillator strength from the out-of-phase mode which couples weakly [55]. Analogously, the bright multisubband plasmon peak is the result of a phase synchronization of intersubband transitions, and is strongly coupled with light. All the other eigenmodes of the system are optically not active, or dark.

With this vision in mind, we decide to describe the intersubband light-matter interaction problem in terms of polarizations.

2.2. Quantum model of multisubband plasmons

We develop in this section a quantum model to describe the optical properties of a dense bidimensional electron gas when the depolarization field is the dominant many-body contribution. Our model is based on the formalism of Refs. [68, 69], which takes advantage of the fact that a treatment of the light-matter coupling in the dipole representation naturally accounts for the depolarization effect introduced in §2.1.1. As we will see in the following, this representation provides a general Hamiltonian to describe the collective electronic excitations and their interaction with light. The matter degrees of freedom are described by the polarization field \mathbf{P} , interacting with the electric field displacement \mathbf{D} . The depolarization effect in the bidimensional electron gas is naturally contained in the self interaction term \mathbf{P}^2 of such Hamiltonian [68, 70].

This part is structured as follows: we start by presenting the Hamiltonian of the light-matter system in the dipole representation in §2.2.1 and write the second quantized form of the free light and matter parts in §2.2.2. As schematized in Fig. 2.5, we then express the matter-matter interaction Hamiltonian in terms of intersubband excitation operators b, b^\dagger , introduce the concept of microscopic current densities and show their relation with the absorption spectrum (§2.2.3). We introduce the intersubband plasmon operators p, p^\dagger in §2.2.4. Section 2.2.5 presents the diagonalization procedure to obtain the new normal modes of the system, the multisubband plasmons, issued from the coupling between intersubband plasmons. We obtain the collective microcurrent densities and the absorption spectrum accounting for collective effects in §2.2.6. Section 2.2.7 outlines the

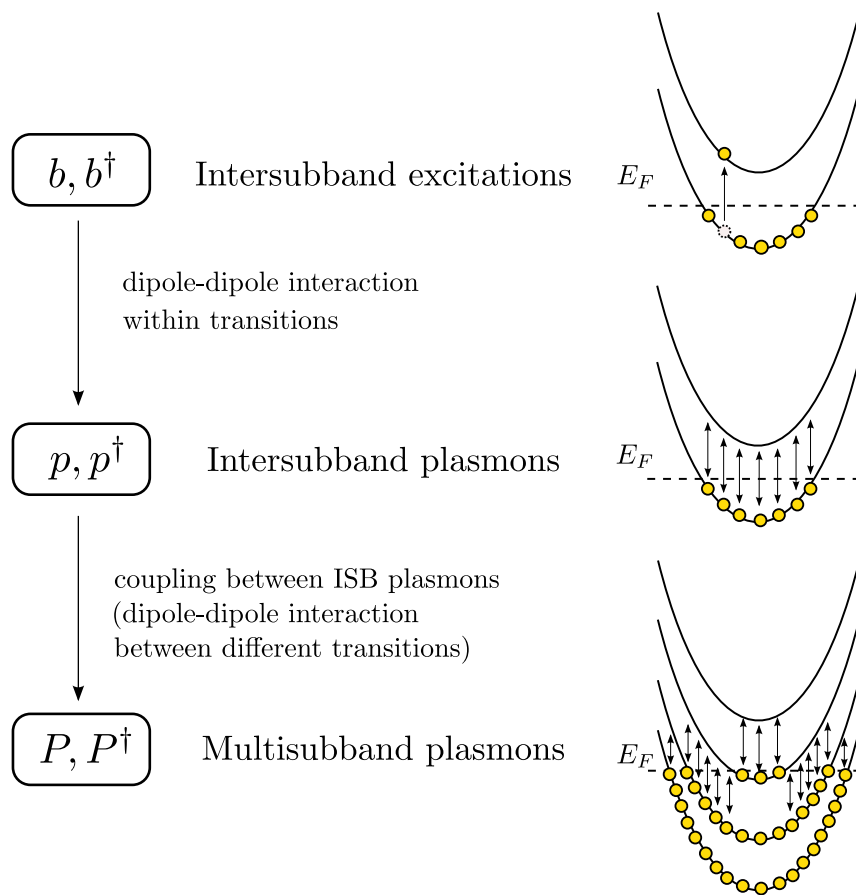


Figure 2.5: Schematization of the diagonalization procedure followed in the model.

generalization of the model to a piecewise constant effective mass m^* . Finally, the last part of the chapter presents the full light-matter Hamiltonian in second quantization (§2.3) and introduces an expression for the dielectric function of the system (§2.4).

2.2.1. Light-matter interaction Hamiltonian in dipole representation

In order to introduce the dipole representation of the light-matter interaction, we start by considering the Hamiltonian of a system of free particles of mass m_i and charge e in the Coulomb gauge [70]

$$\begin{aligned}
 H &= \sum_i \frac{(\mathbf{p}_i - e\mathbf{A})^2}{2m_i} + \int \frac{\varepsilon_0\varepsilon_s\mathbf{E}^2}{2} d^3\mathbf{r} + \int \frac{\mu_0\mathbf{H}^2}{2} d^3\mathbf{r} + V_{\text{Coulomb}} \\
 &= \underbrace{\sum_i \frac{\mathbf{p}_i^2}{2m_i}}_{\text{particles}} + \underbrace{\int \frac{\varepsilon_0\varepsilon_s\mathbf{E}^2}{2} d^3\mathbf{r} + \int \frac{\mu_0\mathbf{H}^2}{2} d^3\mathbf{r}}_{\text{photons}} - \underbrace{\sum_i \frac{e\mathbf{p}_i \cdot \mathbf{A}}{m_i} + \sum_i \frac{e^2\mathbf{A}^2}{2m_i}}_{\text{interactions}} + V_{\text{Coulomb}}
 \end{aligned} \tag{2.14}$$

where ε_0 is the vacuum permittivity, ε_s the material permittivity, μ_0 the vacuum magnetic permeability, \mathbf{p}_i the momentum vector, \mathbf{E} the electric field vector, \mathbf{H} the magnetic field, \mathbf{A} the vector potential, and

$$V_{\text{Coulomb}} = \sum_{i \neq j} \frac{e^2}{4\pi\varepsilon_0|\mathbf{r}_i - \mathbf{r}_j|}$$

The linear term in \mathbf{A} of Eq. (2.14) is what is usually taken as light-matter interaction term:

$$H_{\text{light-matter}} = - \sum_i \frac{\mathbf{p}_i \cdot \mathbf{A}}{m_i} = - \sum_i e\mathbf{v}_i \cdot \mathbf{A}$$

Instead of following this path, we adopt the Power-Zinau-Wooley (or dipole) representation [70, 71]. In this representation, neglecting magnetic interactions:

$$\begin{aligned}
 H &= \underbrace{\sum_i \frac{\mathbf{p}_i^2}{2m_i}}_{\text{particles}} + \underbrace{\int \frac{\mathbf{D}^2}{2\varepsilon_0\varepsilon_s} d^3\mathbf{r} + \int \frac{\mu_0\mathbf{H}^2}{2} d^3\mathbf{r}}_{\text{photons}} - \underbrace{\int \frac{\mathbf{D} \cdot \mathbf{P}}{\varepsilon_0\varepsilon_s} d^3\mathbf{r} + \int \frac{\mathbf{P}^2}{2\varepsilon_0\varepsilon_s} d^3\mathbf{r}}_{\text{interactions}}
 \end{aligned} \tag{2.15}$$

where \mathbf{P} is the polarization density operator and \mathbf{D} is the displacement field operator.

The interaction Hamiltonian in the dipole representation is then:

$$H_{\text{int}} = \int \frac{1}{\varepsilon_0\varepsilon_s} \left(-\mathbf{D} \cdot \mathbf{P} + \frac{1}{2}\mathbf{P}^2 \right) d^3\mathbf{r} = H_{\text{l-pol}} + H_{\text{pol-pol}} \tag{2.16}$$

with

$$H_{\text{l-pol}} = - \int \frac{\mathbf{D} \cdot \mathbf{P}}{\varepsilon_0\varepsilon_s} d^3\mathbf{r} \tag{2.17}$$

$$H_{\text{pol-pol}} = \int \frac{\mathbf{P}^2}{2\varepsilon_0\varepsilon_s} d^3\mathbf{r} \tag{2.18}$$

The Hamiltonian (2.16) is composed of two terms: $H_{1-\text{pol}}$ describes the interaction between the matter polarization and the electromagnetic field, while $H_{\text{pol}-\text{pol}}$ describes the polarization self-interaction.

We note that Coulomb interaction is contained in this Hamiltonian through the relation [70]

$$V_{\text{Coulomb}} = \int d^3\mathbf{r} \frac{\mathbf{P}_{\parallel}^2}{2\varepsilon_0\varepsilon_s}$$

with \mathbf{P}_{\parallel} the longitudinal part of $\mathbf{P} = \mathbf{P}_{\perp} + \mathbf{P}_{\parallel}$ ¹. The full Hamiltonian can then be rewritten as

$$H = \underbrace{\sum_i \frac{\mathbf{p}_i^2}{2m_i} + \int \frac{\mathbf{P}^2}{2\varepsilon_0\varepsilon_s} d^3\mathbf{r}}_{\text{particles and particle-particle interactions}} + \underbrace{\int \frac{\mathbf{D}^2}{2\varepsilon_0\varepsilon_s} d^3\mathbf{r} + \int \frac{\mu_0\mathbf{H}^2}{2} d^3\mathbf{r}}_{\text{photons}} - \underbrace{\int \frac{\mathbf{D} \cdot \mathbf{P}}{\varepsilon_0\varepsilon_s}}_{\text{light-matter interaction}}$$

2.2.2. Second quantization: bosonized Hamiltonian

The full Hamiltonian describing the interaction between light and an electron gas in a quantum heterostructure is

$$H = H_e + H_p + H_{\text{int}} \quad (2.19)$$

where H_e is the Hamiltonian of the electron gas, H_p is the photon Hamiltonian, and H_{int} is interaction Hamiltonian. We can express these terms as in the Hamiltonian in the dipole representation (2.15) by making use of the effective mass of the electron m^* , which includes the effect of the crystal potential.

For a quantum description of the system, we want to write the full Hamiltonian (2.19) in the second quantization formalism. We will then have for the free photon part [70]:

$$H_p = \sum_{\mathbf{q}} \hbar\omega_{\mathbf{q}} \left(a_{\mathbf{q}}^{\dagger} a_{\mathbf{q}} + \frac{1}{2} \right) \quad (2.20)$$

where $\hbar\omega_{\mathbf{q}}$ is the energy of the photonic mode and $a_{\mathbf{q}}^{\dagger}, a_{\mathbf{q}}$ are the bosonic creation and annihilation operators of the modes.

The single electron Hamiltonian is [62]

$$H_e = \sum_{i\mathbf{k}} \hbar\omega_{i\mathbf{k}} c_{i\mathbf{k}}^{\dagger} c_{i\mathbf{k}} \quad (2.21)$$

where i runs over the electronic subbands, $\hbar\omega_{i\mathbf{k}} = \hbar\omega_i + \frac{\hbar^2\mathbf{k}^2}{2m^*}$ is the total energy of an electron in the subband i with in plane momentum \mathbf{k} , and $c_{i\mathbf{k}}^{\dagger}, c_{i\mathbf{k}}$ are the fermionic creation and destruction operators.

¹In vector calculus, a regular vector field \mathbf{F} can always be decomposed in longitudinal (curl-free, $\nabla \times \mathbf{F}_{\parallel} = 0$) and transverse (divergence-free, $\nabla \cdot \mathbf{F}_{\perp} = 0$) components (see for example [70]).

Let us now label each electronic transition $i \rightarrow j$ (approximated as vertical in the reciprocal space, neglecting the photon wavevector) with a greek index α , i.e. $\alpha \equiv i \rightarrow j$. In order to study the interaction between light and the electronic subbands, we replace the fermionic Hamiltonian H_e with an effective bosonic Hamiltonian, which contains only the polarization degrees of freedom [68, 72]:

$$H_e = \sum_{\alpha\mathbf{q}} \hbar\omega_\alpha b_{\alpha\mathbf{q}}^\dagger b_{\alpha\mathbf{q}} \quad (2.22)$$

with

$$b_{\alpha\mathbf{q}}^\dagger = \frac{1}{\sqrt{\Delta N_\alpha}} \sum_{\mathbf{k}} c_{j\mathbf{k}+\mathbf{q}}^\dagger c_{i\mathbf{k}}$$

where $\Delta N_\alpha = \langle N_i \rangle - \langle N_j \rangle$ is the difference in the subband populations². $b_{\alpha\mathbf{q}}^\dagger$ is a bosonic operator in the limit of weakly excited systems:

$$[b_{\alpha\mathbf{q}}, b_{\alpha'\mathbf{q}'}^\dagger] = \delta_{\mathbf{q},\mathbf{q}'}$$

Equations (2.20)-(2.22) represent the non-interacting state of the system. To write the remaining interaction term, H_{int} , in second quantization, we have to define the microscopic polarization density of the electron gas \mathbf{P} . The latter will be associated with the excitation of an ensemble of intersubband oscillators along the growth direction, in the spirit of the picture described in §2.1.4. The dipole-dipole interaction between intersubband oscillators, hence the depolarization field, will be described by the $H_{\text{pol-pol}}$ term introduced in Eq. (2.16).

2.2.3. Microscopic expression of the polarization and microscopic current densities

In order to use the electrical dipole representation and the Hamiltonian (2.15), we need an expression for the local polarization operator $\hat{\mathbf{P}}(\mathbf{r})$ ³. The classical definition of the polarization $\mathbf{P}(\mathbf{r})$ is that of an average dipole moment of the charge distribution over some microscopic volume [29]. The definition of this microscopic volume, though, presents in general some subtleties [73], and this is particularly the case for heterostructures. For example, in the case of a simple quantum well of width L_{QW} , the volume could be defined as the volume of the quantum well, but it is difficult to generalize this to an arbitrary system of quantum wells, or to confinement potentials with an arbitrary shape. Since the microscopic intersubband dipole z_{ij} is defined starting from the electronic wavefunctions $\psi_i(z)$, a good microscopic expression for $\hat{\mathbf{P}}(\mathbf{r})$ should involve the wavefunctions [68].

We define a microscopic polarization $\hat{\mathbf{P}}(\mathbf{r})$ as generating a microscopic current $\hat{\mathbf{j}}$ under the action of the full Hamiltonian \hat{H} :

$$\frac{d\hat{\mathbf{P}}(\mathbf{r})}{dt} = \frac{1}{i\hbar} [\hat{\mathbf{P}}(\mathbf{r}), \hat{H}(t)] = \hat{\mathbf{j}}(\mathbf{r}) \quad (2.23)$$

²In the following, we will consider the dipole approximation ($\mathbf{q} \ll \mathbf{k}$) and omit the sum over the in-plane wavevector \mathbf{q} of Eq. (2.22).

³In this section, we will denote with a hat symbol $\hat{}$ some of the operators, to distinguish the operator \hat{A} from the scalar quantity A .

As the polarization operator commutes with \mathbf{D} , the evolution of \mathbf{P} is driven just by the electronic Hamiltonian (2.22).

We write the microscopic current operator in the dipole representation as

$$\hat{\mathbf{j}}(\mathbf{r}) = i \frac{e\hbar}{2m^*} \left[\Psi^\dagger(\mathbf{r})(\nabla_{\mathbf{r}}\Psi(\mathbf{r})) - (\nabla_{\mathbf{r}}\Psi^\dagger(\mathbf{r}))\Psi(\mathbf{r}) \right] \quad (2.24)$$

Here, we consider m^* constant for notation simplicity; the model can be extended to a piecewise constant effective mass, as further explained in §2.2.7.

The field operator is written on the one-particle wavefunction basis:

$$\Psi(z, \mathbf{r}_{\parallel}) = \sum_{\lambda\mathbf{k}} c_{\lambda\mathbf{k}} \psi_{\lambda}(z) \frac{e^{i\mathbf{k}\cdot\mathbf{r}_{\parallel}}}{\sqrt{S}} \quad (2.25)$$

with S surface of the sample. As we are interested in intersubband transitions, we shall from now on restrict ourselves to the z -component of the microscopic current, because of the intersubband absorption selection rule (see §1.3.2).

Inserting Eq. (2.25) in Eq. (2.24), the z -component of the current operator can be written as:

$$\begin{aligned} \hat{j}_z &= i \frac{e\hbar}{2m^*\sqrt{S}} \sum_{\alpha} \xi_{\alpha}(z) \sqrt{\Delta N_{\alpha}} (b_{\alpha} - b_{\alpha}^{\dagger}) = \\ &= i \sum_{\alpha} j_{\alpha}(z) (b_{\alpha} - b_{\alpha}^{\dagger}) \end{aligned} \quad (2.26)$$

where $\xi_{\alpha}(z)$ is given by

$$\xi_{\alpha}(z) \equiv \xi_{ij}(z) = \psi_i(z) \frac{\partial \psi_j(z)}{\partial z} - \psi_j(z) \frac{\partial \psi_i(z)}{\partial z} \quad (2.27)$$

The quantity

$$j_{\alpha}(z) = \frac{e\hbar}{2m^*\sqrt{S}} \xi_{\alpha}(z) \sqrt{\Delta N_{\alpha}} \quad (2.28)$$

is a current per unit surface associated with each intersubband transition α . Its spatial variation is determined by $\xi_{\alpha}(z)$, which can thus be considered as a current distribution⁴.

By using the expression of the current operator (2.26), we now define an intersubband polarization operator \hat{P}_z through Eq. (2.23), which contains contributions from all the intersubband transitions and can be written as:

$$\begin{aligned} \hat{P}_z &= \frac{e\hbar}{2m^*\sqrt{S}} \sum_{\alpha} \frac{\xi_{\alpha}(z)}{\omega_{\alpha}} \sqrt{\Delta N_{\alpha}} (b_{\alpha}^{\dagger} + b_{\alpha}) = \\ &= \sum_{\alpha} \frac{j_{\alpha}(z)}{\omega_{\alpha}} (b_{\alpha}^{\dagger} + b_{\alpha}) \end{aligned} \quad (2.29)$$

⁴In the following, we shall refer to the objects $\xi_{\alpha}(z)$ as 'microcurrents' for simplicity.

Note that the spatial variation of the polarization operator is also described by the current distribution $\xi_\alpha(z)$. Interestingly, this quantity can be easily related to the dipole matrix element z_α of the transition α . In fact, by making use of the relations $p_z = -i\hbar \frac{\partial}{\partial z}$ and $p_z = \frac{im^*}{\hbar} [H, z]$ one finds:

$$\int_{-\infty}^{+\infty} \xi_\alpha(z) dz = \frac{2m^* \omega_\alpha}{\hbar} z_\alpha \quad (2.30)$$

Equation (2.30) is very relevant for the following part of the work, as it establishes a link between the optical properties of the electron gas and the intersubband current densities through the dipole matrix element z_α .

Figure 2.6(a) shows the calculated microcurrent spatial distributions $\xi_{ij}(z)$ in a three-subband quantum well. Panel (b) presents an alternative representation of the same spatial distributions (in color scale), plotted between the electronic levels of the corresponding transitions. For the purpose of illustration, each microcurrent is also multiplied by a Gaussian function along the energy axis. The figure provides a visual interpretation of Eq. (2.30). It can be indeed appreciated that optically allowed transitions, such as $1 \rightarrow 2$ and $2 \rightarrow 3$, correspond to distributions $\xi_{12}(z)$ and $\xi_{23}(z)$, *even* with respect to the center of the well; on the contrary, the forbidden transition $1 \rightarrow 3$ is associated with an *odd* $\xi_{13}(z)$. It is then apparent that the integral of $\xi_{12}(z)$ and $\xi_{23}(z)$ will lead to a finite dipole, and the integral of $\xi_{13}(z)$ to a dipole equal to zero.

Oscillating charge distributions

We can also introduce a function $\rho_\alpha(z)$ describing the spatial distribution of the charge oscillating at the frequency of the transition α :

$$\rho_\alpha(z) = \frac{\partial \xi_\alpha(z)}{\partial z} \quad (2.31)$$

To see a justification of this, from the definition of the spatial variation of the current (2.27) we can write

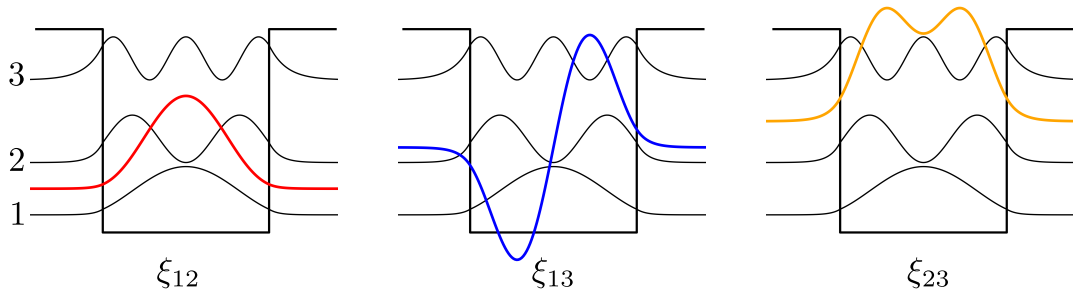
$$\begin{aligned} \frac{\partial \xi_{ij}}{\partial z} &= \frac{\partial}{\partial z} \left(\psi_i \frac{\partial}{\partial z} \psi_j \right) - \frac{\partial}{\partial z} \left(\psi_j \frac{\partial}{\partial z} \psi_i \right) = \\ &= \psi_i \frac{\partial^2 \psi_j}{\partial z^2} - \psi_j \frac{\partial^2 \psi_i}{\partial z^2} \end{aligned}$$

Then, recalling Schrödinger equation for the envelope functions

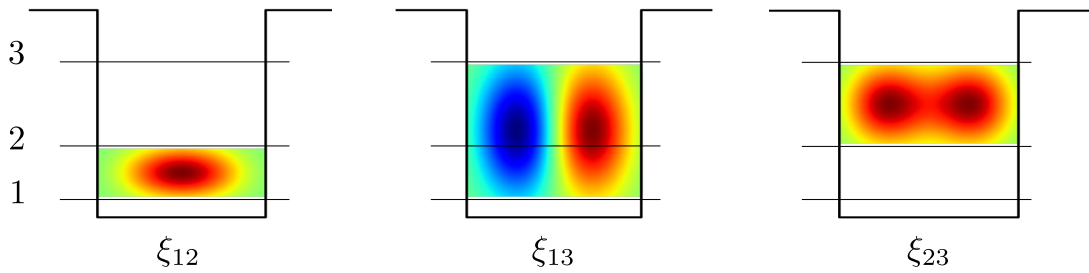
$$-\frac{\hbar^2}{2m^*} \frac{\partial^2 \psi_i}{\partial z^2} + V(z) \psi_i = \hbar \omega_i \psi_i$$

we can write:

$$\frac{\partial \xi_{ij}}{\partial z}(z) = \frac{2m^*(\omega_i - \omega_j)}{\hbar} \psi_i(z) \psi_j(z) = \rho_{ij}(z)$$



(a) In black: Calculated square moduli of wavefunctions in a 100 Å GaAs/Al_{0.45}Ga_{0.55}As quantum well. In color: calculated microcurrent spatial distributions $\xi_{ij}(z)$ for the possible intersubband transitions, plotted mid-way between the electronic levels of the corresponding transition.



(b) Alternative representation of the microcurrents in (a), in color scale and normalized to their maximum value, plotted between the electronic levels of the corresponding transition, and multiplied by a Gaussian function along the energy axis for visualization purposes. In the colorscale, red corresponds to +1 and blue to -1.

Figure 2.6: Representation of microcurrent spatial distributions $\xi_{\alpha}(z)$.

where we recognize a density-like term $\psi_i\psi_j$. The definition of the charge distribution suggests another physical interpretation of Eq. (2.30):

$$-\int_{-\infty}^{+\infty} z\rho_\alpha(z) dz = \frac{2m^*\omega_\alpha}{\hbar} z_\alpha \quad (2.32)$$

The above relation suggests an interpretation for the optical dipole z_α as the average displacement of the charge oscillation, obtained as the first moment of the distribution $\rho_\alpha(z)$.

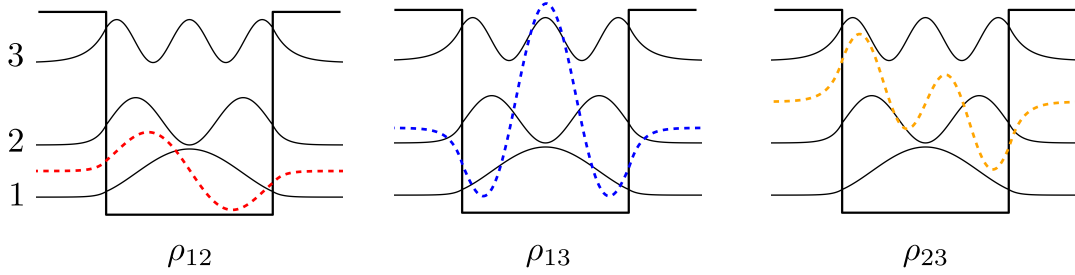


Figure 2.7: In black: calculated square moduli of wavefunctions in a 100 Å GaAs/Al_{0.45}Ga_{0.55}As quantum well. In color: calculated charge spatial distributions $\rho_{ij}(z)$ for the possible intersubband transitions, plotted mid-way between the electronic levels of the corresponding transition.

The calculated charge distributions ρ_α for a 100 Å GaAs/Al_{0.45}Ga_{0.55}As quantum well are presented in Fig. 2.7. Note that their parity properties are opposite with respect to the microcurrents $\xi_\alpha(z)$ (cf. Fig. 2.6): optically allowed transitions correspond to odd charge distributions, and optically forbidden to even charge distributions.

Microscopic current densities and single-particle absorption spectrum

Combining Eqs. (2.28) and (2.30), the integral of the current density can be related to the dipole matrix element through:

$$\frac{S}{e^2\omega_\alpha} \left| \int_{-\infty}^{+\infty} j_\alpha(z) dz \right|^2 = \omega_\alpha |z_\alpha|^2 \Delta N_\alpha \quad (2.33)$$

As the dipole matrix element also determines the strength of the interaction with light, Eq. (2.33) allows us to establish a relation between the current density integral and the absorption spectrum.

In a single-particle picture, the absorption coefficient is calculated as [24]:

$$\alpha_{2D}(\omega) = \frac{e^2\hbar}{2\varepsilon_0 c m^* \sqrt{\varepsilon_s}} \sum_{\alpha} f_{\alpha} \Delta N_{\alpha} \mathcal{L}_{\hbar\gamma}(\hbar\omega - \hbar\omega_{\alpha}) = \frac{e^2}{\varepsilon_0 c \sqrt{\varepsilon_s}} \sum_{\alpha} \omega_{\alpha} |z_{\alpha}|^2 \Delta N_{\alpha} \mathcal{L}_{\hbar\gamma}(\hbar\omega - \hbar\omega_{\alpha})$$

where $f_\alpha = \frac{2m^*\omega_\alpha}{\hbar} z_\alpha^2$ is the oscillator strength of the transition, ε_s is the background dielectric constant, c is the speed of light, and $\mathcal{L}_{\hbar\gamma}(\hbar\omega - \hbar\omega_\alpha) = \frac{\hbar\gamma/2}{(\hbar\omega_\alpha - \hbar\omega)^2 + (\hbar\gamma/2)^2}$ is a Lorentzian function of full width at half maximum $\hbar\gamma$, centered at the intersubband transition energy $\hbar\omega_\alpha$. By using Eq. (2.33), the absorption coefficient can be related to the current densities through:

$$\alpha_{2D} = \frac{S}{\varepsilon_0 c \sqrt{\varepsilon_s}} A(\omega) \quad (2.34)$$

$$A(\omega) = \sum_\alpha \frac{1}{\omega_\alpha} \left| \int_{-\infty}^{+\infty} j_\alpha(z) dz \right|^2 \mathcal{L}_{\hbar\gamma}(\hbar\omega - \hbar\omega_\alpha) \quad (2.35)$$

The term $\frac{1}{\omega_\alpha} \left| \int_{-\infty}^{+\infty} j_\alpha(z) dz \right|^2$ can thus be considered as a measure of the absorption amplitude, being proportional to both the oscillator strength and to the density of electrons involved in the transition.

Absorption in Fermi's golden rule

Note that the above result for the absorption rate (2.35) can be obtained through Fermi's golden rule by calculating the matrix element of the light-plasmon Hamiltonian $H_{1\text{-pol}}$ (2.17) between an initial state $a_{\mathbf{q}}^\dagger|F\rangle$ (the system is in the ground state, there is one photon) and a final state $b_{\alpha\mathbf{q}}^\dagger|F\rangle$ (there is no photon and an intersubband excitation). To this end, we write the polarization P_z and displacement field D_z as

$$P_z = \sum_{\alpha, \mathbf{q}} \frac{j_\alpha(z)}{\omega_\alpha} e^{i\mathbf{q}\cdot\mathbf{r}} (b_{\mathbf{q}\alpha} + b_{-\mathbf{q}\alpha}^\dagger) \quad (2.36)$$

$$D_z = i \sum_{\mathbf{q}} A_{\mathbf{q}} f_{\mathbf{q}}(z) \frac{|\mathbf{q}|}{\omega_{c\mathbf{q}}} e^{i\mathbf{q}\cdot\mathbf{r}} (a_{\mathbf{q}} - a_{-\mathbf{q}}^\dagger) \quad (2.37)$$

with

$$A_{\mathbf{q}} = \sqrt{\frac{\hbar\omega_{c\mathbf{q}}}{2\mu_0 S L_{\mathbf{q}}}} \int f_{\mathbf{q}}^2(z) dz = L_{\mathbf{q}}$$

where $f_{\mathbf{q}}(z)$ is an arbitrary guided mode with wavevector \mathbf{q} , S is the area of the system and $L_{\mathbf{q}}$ the light-matter interaction length.

Let us consider a perturbative regime where the external field is weak. The absorption rate can then be evaluated as:

$$\begin{aligned} A_\alpha(\omega) &= |\langle F | a_{\mathbf{q}}^\dagger H_{1\text{-pol}} b_{\alpha\mathbf{q}}^\dagger | F \rangle|^2 \delta(\omega - \omega_\alpha) = \\ &= |C_{\mathbf{q}}|^2 \sin^2 \theta_{\mathbf{q}} \frac{1}{\omega_\alpha} \left| \int_{-\infty}^{+\infty} j_\alpha(z) dz \right|^2 \delta(\omega - \omega_\alpha) \end{aligned}$$

Here $\omega = \omega_{c\mathbf{q}}$ is the frequency of the incident photon, and the factor $\sin^2 \theta_{\mathbf{q}}$ expresses the selection rule for intersubband transitions. Equation (2.35) can be recovered by summing on all the possible transitions α , replacing the Dirac δ with broadened Lorentzians, and discarding the \mathbf{q} dependence.

2.2.4. From intersubband transitions to intersubband plasmons

In order to consider the effect of the polarization self-interaction term, we diagonalize the Hamiltonian

$$H_{\text{plasmon}} = H_e + H_{\text{pol-pol}}$$

which physically describes the ensemble of interacting intersubband dipolar oscillators. We use the microscopic expression of the polarization (2.29) to write $H_{\text{pol-pol}}$ [Eq. (2.18)] in terms of the intersubband excitation operators as:

$$H_{\text{pol-pol}} = \frac{e^2}{2\varepsilon_0\varepsilon_s} \sum_{\alpha,\beta} S_{\alpha\beta} \sqrt{\Delta N_\alpha \Delta N_\beta} (b_\alpha^\dagger + b_\alpha) (b_\beta^\dagger + b_\beta)$$

where $S_{\alpha\beta}$ is given by:

$$S_{\alpha\beta} = \frac{1}{\hbar\omega_\alpha} \frac{1}{\hbar\omega_\beta} \left(\frac{\hbar^2}{2m^*} \right)^2 \int_{-\infty}^{+\infty} \xi_\alpha(z) \xi_\beta(z) dz \quad (2.38)$$

$S_{\alpha\beta}$ defines a characteristic length, depending on the overlap between microcurrents. Diagonal terms $S_{\alpha\alpha}$ refer to the interaction between dipoles associated with the same transition, while off-diagonal terms $S_{\alpha\beta}$ refer to dipoles belonging to different transitions. Note that this expression is equivalent to the Coulomb tensor [30, 47, 74]:

$$S_{\alpha\beta} \equiv S_{ij,kl} = \int_{-\infty}^{+\infty} \left[\int_{-\infty}^z \psi_i(z') \psi_j(z') dz' \right] \left[\int_{-\infty}^z \psi_k(z'') \psi_l(z'') dz'' \right] dz \quad (2.39)$$

The diagonalization of H_{plasmon} is done in two steps. We first consider the interaction between oscillators corresponding to the same intersubband transition ($\alpha = \beta$), resulting in the usual intersubband plasmons [8, 68]. We combine the $\alpha = \beta$ terms with the electronic Hamiltonian (2.22) to obtain

$$H_e + H_{\text{pol-pol}}(\alpha = \beta) = \sum_{\alpha} \left[\hbar\omega_\alpha b_\alpha^\dagger b_\alpha + \frac{e^2}{2\varepsilon_0\varepsilon_s} S_{\alpha,\alpha} \Delta N_\alpha (b_\alpha^\dagger + b_\alpha) (b_\alpha^\dagger + b_\alpha) \right] \quad (2.40)$$

This quadratic Hamiltonian can be diagonalized by introducing new bosonic operators p_α satisfying

$$[p_\alpha, H_e + H_{\text{pol}}(\alpha = \beta)] = \hbar\tilde{\omega}_\alpha p_\alpha$$

where $\tilde{\omega}_\alpha$ denotes the new eigenvalues. This diagonalization procedure yields

$$p_\alpha = \frac{\tilde{\omega}_\alpha + \omega_\alpha}{2\sqrt{\tilde{\omega}_\alpha \omega_\alpha}} b_\alpha + \frac{\tilde{\omega}_\alpha - \omega_\alpha}{2\sqrt{\tilde{\omega}_\alpha \omega_\alpha}} b_\alpha^\dagger$$

with $\tilde{\omega}_\alpha = \sqrt{\omega_\alpha^2 + \omega_{P\alpha}^2}$ the plasma-shifted transition frequency of the intersubband plasmon, already introduced in §2.1.1.

Coulomb lengths in an infinite quantum well

For illustrative purposes, let us calculate the values of $S_{ij,kl}$ in the case of an infinite quantum well of width L_{QW} . As mentioned in §1.1.2, the system eigenfunctions are given by:

$$\psi_n^{\text{infinite}}(z) = \sqrt{\frac{2}{L_{\text{QW}}}} \sin\left(\frac{n\pi z}{L_{\text{QW}}}\right)$$

Equation 2.39 becomes

$$\begin{aligned} S_{ij,kl} &= \int_0^{L_{\text{QW}}} \left[\frac{2}{L_{\text{QW}}} \int_0^z \sin\left(\frac{i\pi z'}{L_{\text{QW}}}\right) \sin\left(\frac{j\pi z'}{L_{\text{QW}}}\right) dz' \right] \times \\ &\quad \times \left[\frac{2}{L_{\text{QW}}} \int_0^z \sin\left(\frac{k\pi z''}{L_{\text{QW}}}\right) \sin\left(\frac{l\pi z''}{L_{\text{QW}}}\right) dz'' \right] dz = \\ &= \frac{1}{\pi^2} \int_0^{L_{\text{QW}}} \left[\frac{\sin\left(\frac{\pi z(i-j)}{L_{\text{QW}}}\right)}{i-j} - \frac{\sin\left(\frac{\pi z(i+j)}{L_{\text{QW}}}\right)}{i+j} \right] \left[\frac{\sin\left(\frac{\pi z(k-l)}{L_{\text{QW}}}\right)}{k-l} - \frac{\sin\left(\frac{\pi z(k+l)}{L_{\text{QW}}}\right)}{k+l} \right] dz \end{aligned} \quad (2.41)$$

The highest values for $S_{ij,kl}$ obtained through Eq. (2.41) are those that involve transitions between consecutive levels:

$$\begin{aligned} S_{n,n+1,n,n+1} &= \frac{2n^2 + 2n + 1}{(2n + 1)^2} \frac{L_{\text{QW}}}{\pi^2} && \text{diagonal terms} \\ S_{n,n+1,m,m+1} &= \frac{L_{\text{QW}}}{2\pi^2} && \text{off-diagonal terms, } n \neq m \end{aligned}$$

Note that the succession of $S_{n,n+1,n,n+1}$ is $\left\{ \frac{5}{9}, \frac{13}{25}, \frac{25}{49}, \frac{41}{81}, \dots \right\} \frac{L_{\text{QW}}}{\pi^2}$, and

$$\lim_{n \rightarrow +\infty} S_{n,n+1,n,n+1} = \frac{L_{\text{QW}}}{2\pi^2} \quad (2.42)$$

These considerations suggest that transitions between consecutive levels and their couplings will play an important role in the optical response of a single quantum well. This is reasonable, since they are the most optically active transitions. This information is thus concisely included in $S_{ij,kl}$.

It is also interesting to note that all of these transitions are characterized by a similar value of S , as the succession rapidly converges to the value $\frac{L_{\text{QW}}}{2\pi^2}$.

$S_{ij,kl}$ and effective lengths in plasma definitions

The quantity $S_{ij,kl}$ is the four-index generalization of the quantity S_{ij} appearing in the definition of effective length of a quantum well with a single optically active intersubband transition $L_{ij}^{\text{eff}} = z_{ij}^2/S_{ij}$ [see Eqs. (2.2)-(2.4)].

The diagonal elements of $S_{ij,kl}$ and the effective length L_{ij}^{eff} of the transition $i \rightarrow j$ are related, and indeed it is possible to write an alternative expression for the plasma

frequency in terms of S :

$$\omega_{Pij}^2 = \frac{e^2 f_{ij} \Delta N_{ij}}{m^* \varepsilon_0 \varepsilon_s L_{ij}^{\text{eff}}} = \frac{2e^2 \Delta N_{ij} \omega_{ij}}{\hbar \varepsilon_0 \varepsilon_s} S_{ij,ij} \quad (2.43)$$

Note that in this expression the oscillator strength f_{ij} cancels in the expression of the plasma frequency, meaning that it has no influence on the value of the depolarization shift [24].

The effective length L_{ij}^{eff} is the expression of the quantum-mechanical effects due to confinement, as suggested from the fact that it is derived directly from the wavefunctions. For confined states in a single quantum well of width L_{QW} , it holds

$$L_{ij}^{\text{eff}} < L_{\text{QW}}$$

which implies that the plasma frequency (2.2) is determined by a length smaller than the physical dimensions of the well. For an infinite quantum well, it is indeed possible to use the relations presented above to calculate

$$S_{12} = \frac{5}{9} \frac{L_{\text{QW}}}{\pi^2} = 0.0056 L_{\text{QW}}$$

$$L_{12}^{\text{eff}} = f_{12} \frac{3}{5} L_{\text{QW}} = 0.576 L_{\text{QW}}$$

If we consider a generic transition between consecutive levels $n \rightarrow n+1$ we have, recalling Eq. (1.6) and Eq. (1.22):

$$E_{n,n+1} = \frac{(2n+1)\pi^2 \hbar^2}{2m^* L_{\text{QW}}} \quad f_{n,n+1} = \frac{64 n^2 (n+1)^2}{\pi^2 (2n+1)^3}$$

which, combined with the above limit for $S_{n,n+1,n,n+1}$ (2.42), give us the following limit for L^{eff} :

$$\lim_{n \rightarrow +\infty} L_{n,n+1}^{\text{eff}} = \frac{8}{\pi^2} L_{\text{QW}} = 0.81 L_{\text{QW}}$$

As an example, Fig. 2.8(a) shows the calculated effective lengths L^{eff} for transitions between consecutive levels [see Fig. 2.8(b)] in a wide GaAs/Al_{0.45}Ga_{0.55}As quantum well (1000 Å). It can be appreciated that the L^{eff} 's tend to a common value, indeed approximately $0.8L_{\text{QW}}$. This is equivalent to the observation that the values of S between consecutive transitions are almost constant.

Effective lengths and extension of microcurrents

Remarkably, the effective length L_{α}^{eff} can also be expressed in terms of the microcurrent $j_{\alpha}(z)$. Indeed, by using the microcurrent definition (2.28), along with Eqs. (2.33) and (2.38), one can obtain:

$$\left| \int_{-\infty}^{+\infty} j_{\alpha}(z) dz \right|^2 = \frac{e^2}{S} \omega_{\alpha}^2 |z_{\alpha}|^2 \Delta N_{\alpha}$$

$$\int_{-\infty}^{+\infty} j_{\alpha}^2(z) dz = \frac{1}{S} \left(\frac{e\hbar}{2m^*} \right)^2 \Delta N_{\alpha} \int_{-\infty}^{+\infty} \xi_{\alpha}^2(z) dz = \frac{e^2}{S} \omega_{\alpha}^2 S_{\alpha\alpha} \Delta N_{\alpha}$$

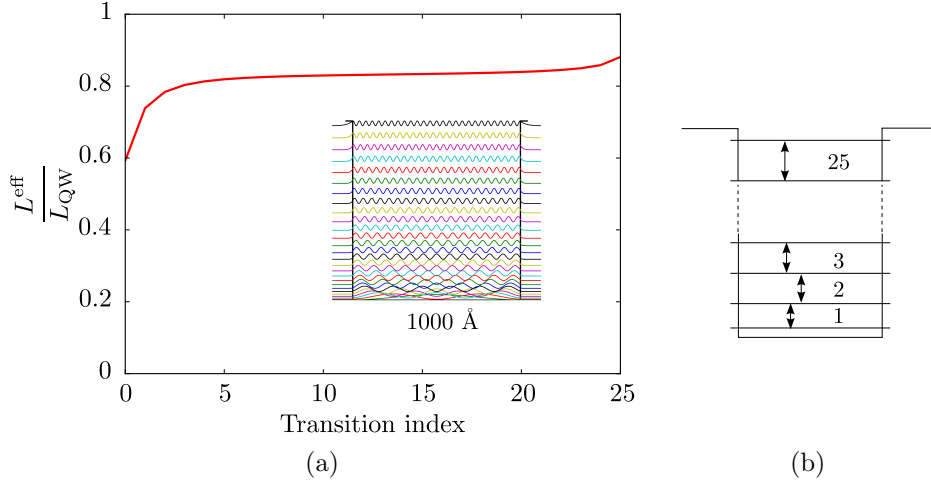


Figure 2.8: a) Calculated L_α^{eff} for a 1000 Å GaAs/Al_{0.45}Ga_{0.55}As quantum well (shown in inset). Transitions between consecutive levels are considered. b) Scheme of transition numbering.

The combination of the relations above makes it possible to write an alternative definition for the effective length L_α^{eff} :

$$L_\alpha^{\text{eff}} = \frac{|z_\alpha|^2}{S_{\alpha\alpha}} = \frac{\left| \int_{-\infty}^{+\infty} j_\alpha(z) dz \right|^2}{\int_{-\infty}^{+\infty} j_\alpha^2(z) dz} \quad (2.44)$$

Equation (2.44) shows that the extension of the polarization associated with a transition α can be derived directly from the microcurrent $j_\alpha(z)$.

2.2.5. From intersubband to multisubband plasmons

In this section, we consider the coupling between intersubband plasmons, to finally obtain the new eigenmodes of the system, the multisubband plasmons.

The Hamiltonian H_{plasmon} can be obtained by adding the terms $\alpha \neq \beta$ to (2.40), and written in terms of intersubband plasmons and their coupling as:

$$\begin{aligned} H_{\text{plasmon}} &= H_e + H_{\text{pol-pol}}(\alpha = \beta) + H_{\text{pol-pol}}(\alpha \neq \beta) = \\ &= \underbrace{\sum_{\alpha} \hbar \tilde{\omega}_{\alpha} p_{\alpha}^{\dagger} p_{\alpha}}_{\text{intersubband plasmons}} + \underbrace{\frac{\hbar}{2} \sum_{\alpha \neq \beta} \Xi_{\alpha\beta} (p_{\alpha} + p_{\alpha}^{\dagger})(p_{\beta} + p_{\beta}^{\dagger})}_{\text{coupling between intersubband plasmons}} \end{aligned} \quad (2.45)$$

The first term of H_{plasmon} is the diagonalized version of Hamiltonian (2.40), and the second term expresses the dipole-dipole interaction between intersubband plasmons associated with different transitions [64], characterized by a coupling strength which can be shown

to be [68]:

$$\begin{aligned}\Xi_{\alpha\beta} &= \frac{\omega_{P\alpha}\omega_{P\beta}}{2\sqrt{\tilde{\omega}_\alpha\tilde{\omega}_\beta}} C_{\alpha\beta} \\ C_{\alpha\beta} &= \frac{S_{\alpha\beta}}{\sqrt{S_{\alpha\alpha}S_{\beta\beta}}}\end{aligned}\quad (2.46)$$

Expression (2.46) shows that the coupling strength depends not only on the characteristics of the individual intersubband plasmons, but also on the quantity $C_{\alpha\beta}$, which is the overlap (defined between -1 and 1) between the corresponding microcurrent distributions.

We now want to rewrite the Hamiltonian (2.45) in terms of new bosonic operators P_n representing N independent normal modes (corresponding to N multisubband plasmons):

$$H_{\text{plasmon}} = \sum_n \hbar W_n P_n^\dagger P_n$$

For simplicity, let us show the diagonalization procedure in the case of two coupled intersubband plasmons. The procedure will be then generalized to the N transition case.

Two intersubband plasmons

Let us refer as an example to transitions $1 \rightarrow 2$ and $2 \rightarrow 3$ in the quantum well represented in Fig. (2.6). Let us call p_1^\dagger and p_2^\dagger the creation operators of the two corresponding intersubband plasmons. The Hamiltonian (2.45) in this case reads:

$$H = \hbar\tilde{\omega}_1 p_1^\dagger p_1 + \hbar\tilde{\omega}_2 p_2^\dagger p_2 + \frac{1}{2}\hbar\Xi_{12}(p_1 + p_1^\dagger)(p_2 + p_2^\dagger) \quad (2.47)$$

where 1 indicates the transition $1 \rightarrow 2$ and 2 the transition $2 \rightarrow 3$. In this simple case, just one coupling frequency between intersubband plasmons is involved:

$$\Xi_{12} = \frac{\omega_{P1}\omega_{P2}}{2\sqrt{\tilde{\omega}_1\tilde{\omega}_2}} C_{12}$$

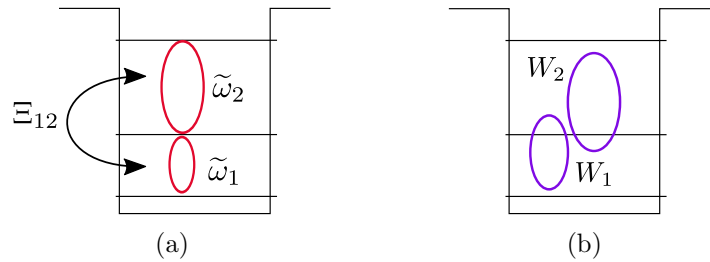


Figure 2.9: a) Representation of intersubband plasmons of two transitions $1 \rightarrow 2$ and $2 \rightarrow 3$ (in red) and the coupling between them Ξ_{12} . b) Representation of the corresponding two uncoupled multisubband plasmons of energy W_1 and W_2 .

Figure 2.9(a) schematically represents the interaction between the two intersubband plasmons. The coupling Ξ_{12} gives rise to the multisubband plasmons, represented in

purple in Fig. 2.9(b).

The Hamiltonian (2.47) is diagonalized in the form:

$$H = \hbar W_1 P_1^\dagger P_1 + \hbar W_2 P_2^\dagger P_2$$

for which it holds

$$[P_n, H] = \hbar W_n P_n \quad n = 1, 2 \quad (2.48)$$

To this end, we calculate the commutators:

$$\begin{aligned} [p_1, H] &= \hbar \tilde{\omega}_1 p_1 + \hbar \Xi_{12} (p_2^\dagger + p_2) \\ [p_2, H] &= \hbar \tilde{\omega}_2 p_2 + \hbar \Xi_{12} (p_1^\dagger + p_1) \\ [p_1^\dagger, H] &= -\hbar \tilde{\omega}_1 p_1^\dagger - \hbar \Xi_{12} (p_2^\dagger + p_2) \\ [p_2^\dagger, H] &= -\hbar \tilde{\omega}_2 p_2^\dagger - \hbar \Xi_{12} (p_1^\dagger + p_1) \end{aligned} \quad (2.49)$$

The new operators P_n are written as linear combinations of the intersubband plasmon operators p_1, p_2 :

$$\begin{aligned} P_1 &= a_{11} p_1 + b_{11} p_1^\dagger + a_{12} p_2 + b_{12} p_2^\dagger \\ P_2 &= a_{21} p_1 + b_{21} p_1^\dagger + a_{22} p_2 + b_{22} p_2^\dagger \end{aligned}$$

which we use to rewrite Eq. (2.48) for $n = 1, 2$:

$$[P_n, H] = \hbar W_n (a_{n1} p_1 + b_{n1} p_1^\dagger + a_{n2} p_2 + b_{n2} p_2^\dagger) \quad (2.50)$$

Eq. (2.50) can also be written by using Eqs. (2.49):

$$\begin{aligned} [P_n, H] &= a_{n1} [p_1, H] + b_{n1} [p_1^\dagger, H] + a_{n2} [p_2, H] + b_{n2} [p_2^\dagger, H] = \\ &= a_{n1} [\hbar \tilde{\omega}_1 p_1 + \hbar \Xi_{12} (p_2^\dagger + p_2)] + b_{n1} [-\hbar \tilde{\omega}_1 p_1^\dagger - \hbar \Xi_{12} (p_2^\dagger + p_2)] + \\ &\quad + a_{n2} [\hbar \tilde{\omega}_2 p_2 + \hbar \Xi_{12} (p_1^\dagger + p_1)] + b_{n2} [-\hbar \tilde{\omega}_2 p_2^\dagger - \hbar \Xi_{12} (p_1^\dagger + p_1)] \end{aligned} \quad (2.51)$$

By comparing Eq. (2.50) and (2.51) we obtain the system of linear equations

$$\begin{cases} W_n a_{n1} = \tilde{\omega}_1 a_{n1} + \Xi a_{n2} - \Xi b_{n2} \\ W_n b_{n1} = -\tilde{\omega}_1 b_{n1} + \Xi a_{n2} - \Xi b_{n2} \\ W_n a_{n2} = \Xi a_{n1} - \Xi b_{n1} + \tilde{\omega}_2 a_{n2} \\ W_n b_{n2} = \Xi a_{n1} - \Xi b_{n1} - \tilde{\omega}_2 b_{n2} \end{cases}$$

which translates into the eigenproblem

$$W_n \begin{pmatrix} a_{n1} \\ b_{n1} \\ a_{n2} \\ b_{n2} \end{pmatrix} = \begin{pmatrix} \tilde{\omega}_1 & 0 & \Xi & -\Xi \\ 0 & -\tilde{\omega}_1 & \Xi & -\Xi \\ \Xi & -\Xi & \tilde{\omega}_2 & 0 \\ \Xi & -\Xi & 0 & -\tilde{\omega}_2 \end{pmatrix} \begin{pmatrix} a_{n1} \\ b_{n1} \\ a_{n2} \\ b_{n2} \end{pmatrix}$$

The eigenvalues W_1 and W_2 of this matrix give the energies renormalized by plasmon-plasmon coupling.

N intersubband plasmons

Having solved the problem for the two-transition case, we can easily generalize to N transitions. The new operators P_n are linear combinations of the operators describing intersubband plasmons:

$$P_n = \sum_{\alpha} \left(a_{n\alpha} p_{\alpha} + b_{n\alpha} p_{\alpha}^{\dagger} \right) \quad (2.52)$$

As these are eigenmodes of H_{plasmon} with eigenfrequencies W_n , it holds:

$$[P_n, H_{\text{plasmon}}] = \hbar W_n P_n \quad (2.53)$$

Relation (2.53), along with the symmetry property $\Xi_{\alpha\beta} = \Xi_{\beta\alpha}$, and the commutator

$$[p_{\alpha}, H_{\text{plasmon}}] = \hbar \tilde{\omega}_{\alpha} p_{\alpha} + \sum_{\alpha \neq \beta} \hbar \Xi_{\alpha\beta} (p_{\beta}^{\dagger} + p_{\beta})$$

lead to the eigenvalue problem

$$\mathbf{M} \mathbf{V}_n = W_n \mathbf{V}_n$$

where

$$\mathbf{M} = \begin{pmatrix} \tilde{\omega}_1 & 0 & \Xi_{12} & -\Xi_{12} & & \Xi_{1N} & -\Xi_{1N} \\ 0 & -\tilde{\omega}_1 & \Xi_{12} & -\Xi_{12} & \cdots & \Xi_{1N} & -\Xi_{1N} \\ \Xi_{12} & -\Xi_{12} & \tilde{\omega}_2 & 0 & & \Xi_{2N} & -\Xi_{2N} \\ \Xi_{12} & -\Xi_{12} & 0 & -\tilde{\omega}_2 & & \Xi_{2N} & -\Xi_{2N} \\ & & \vdots & & \ddots & & \\ \Xi_{1N} & -\Xi_{1N} & \Xi_{2N} & -\Xi_{2N} & & \tilde{\omega}_N & 0 \\ \Xi_{1N} & -\Xi_{1N} & \Xi_{2N} & -\Xi_{2N} & \cdots & 0 & -\tilde{\omega}_N \end{pmatrix}_{2N \times 2N} \quad (2.54)$$

In the following, we will refer to \mathbf{M} as a Hopfield matrix, as it is issued from a Bogoliubov diagonalization procedure similar to that used by Hopfield [75] to treat light-matter strong interaction. The matrix \mathbf{M} admits $2N$ eigenvalues, and if W_n is an eigenvalue, then $-W_n$ is as well. The N distinct frequencies W_n are the normal plasmon modes. The coefficients $a_{n\alpha}$ and $b_{n\alpha}$ appearing in Eq. (2.52) are the components of the eigenvectors \mathbf{V}_n of the matrix \mathbf{M} , written in the form:

$$\mathbf{V}_n = \begin{pmatrix} a_{n1} \\ b_{n1} \\ \vdots \\ a_{nN} \\ b_{nN} \end{pmatrix}_{2N \times 1}$$

with the normalization condition $\sum_i (|a_{ni}|^2 - |b_{ni}|^2) = 1$, which ensures the bosonicity of the operators.

2.2.6. Multisubband plasmon current densities and absorption spectrum

In order to calculate the effect of the polarization self-interaction term on the absorption spectrum, we use the same approach as in §2.2.3. We write the intersubband polarization in terms of the multisubband plasmons. The corresponding current densities are then calculated and related to the absorption spectrum of the electron gas in the presence of dipole-dipole interaction.

Let us define the $N \times N$ matrix inverse

$$X_{\alpha n} = (a_{n\alpha} + b_{n\alpha})^{-1}$$

By using Eq. (2.52), the intersubband polarization operator reads:

$$\hat{P}_z = \frac{e\hbar}{2m^*\sqrt{S}} \sum_n \sum_\alpha \frac{\xi_\alpha(z)\sqrt{\Delta N_\alpha}}{\sqrt{\omega_\alpha\tilde{\omega}_\alpha}} X_{\alpha n} (P_n + P_n^\dagger)$$

The multisubband current density can now be calculated as the time evolution of the polarization under the Hamiltonian H_{plasmon} :

$$\hat{J}_z = \frac{i}{\hbar} [\hat{P}_z, H_{\text{plasmon}}] = i \sum_n J_n(z) (P_n - P_n^\dagger)$$

with the spatial distribution of the multisubband plasmon current density given by

$$J_n(z) = \frac{e\hbar}{2m^*\sqrt{S}} W_n \sum_\alpha \frac{\xi_\alpha(z)\sqrt{\Delta N_\alpha}}{\sqrt{\omega_\alpha\tilde{\omega}_\alpha}} X_{\alpha n} \quad (2.55)$$

As an example, Fig. 2.10 shows the three collective microcurrents calculated in a three-subband structure, with two subbands occupied⁵.

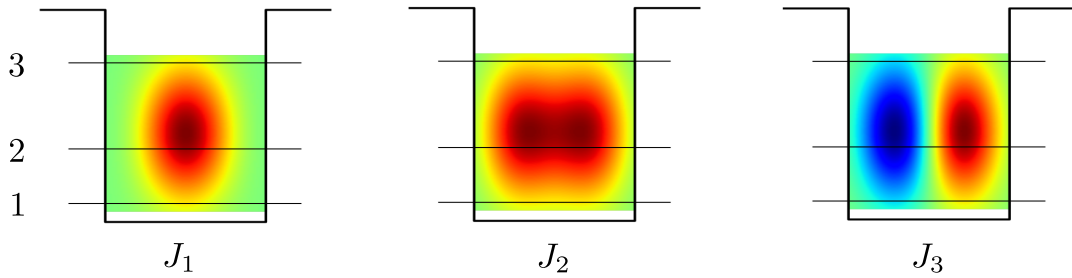


Figure 2.10: Calculated spatial distributions $J_n(z)$ for the collective microcurrents in a 100 Å GaAs/Al_{0.45}Ga_{0.55}As quantum well, with two occupied subbands.

⁵As they are not associated with a particular electronic transition, they are plotted in Fig. 2.10 in the same energy interval. Only their distribution along z is meaningful in this plot.

In analogy to Eq. (2.31), we can also define the distribution of charge oscillating at the frequency W_n of the multisubband plasmon n :

$$\rho_{\text{MSP}_n}(z) = \frac{\partial J_n(z)}{\partial z} \quad (2.56)$$

Note, however, that this relation is not exactly equivalent to (2.31), because there is no direct counterpart of $\xi_\alpha(z)$ in the collective picture. Indeed, the spatial variation of $J_n(z)$ is given by the full term $\sum_\alpha \frac{\xi_\alpha(z)\sqrt{\Delta N_\alpha}}{\sqrt{\omega_\alpha\tilde{\omega}_\alpha}} X_{\alpha n}$, which is clearly not dimensionally homogeneous to $\xi_\alpha(z)$. It is thus not possible to write for ρ_{MSP_n} an expression corresponding to Eq. (2.32).

On the other hand, we can define a multisubband effective length L_n^{eff} as a function of the collective microcurrents $J_n(z)$, in analogy to Eq. (2.44):

$$L_n^{\text{eff}} = \frac{\left| \int_{-\infty}^{+\infty} J_n(z) dz \right|^2}{\int_{-\infty}^{+\infty} J_n^2(z) dz} \quad (2.57)$$

This normalized length quantifies the extension of the polarization associated with the collective mode n .

The absorption coefficient is obtained by integrating the contributions of the different multisubband plasmon current densities. Indeed, the absorption is related to the polarization of the medium, induced by the various intersubband transitions and in the presence of the depolarization field. The absorption coefficient is hence written as:

$$\alpha_{2D}(\omega) = \frac{S}{\varepsilon_0 c \sqrt{\varepsilon_s}} A(\omega) \quad (2.58)$$

$$A(\omega) = \sum_n \frac{1}{W_n} \left| \int_{-\infty}^{+\infty} J_n(z) dz \right|^2 \mathcal{L}_{\hbar\gamma}(\hbar\omega - \hbar W_n) \quad (2.59)$$

The above expression is the multisubband equivalent of Eq. (2.35). The quantity $A(\omega)$ can also be expressed in terms of the eigenvalues and eigenvectors of the matrix \mathbf{M} , together with the characteristics of the individual intersubband transitions:

$$A(\omega) = \frac{e^2}{S} \sum_n W_n F_n \mathcal{L}_{\hbar\gamma}(\hbar\omega - \hbar W_n) \quad (2.60)$$

$$F_n = \left| \sum_\alpha \sqrt{\Delta N_\alpha} \sqrt{\frac{\omega_\alpha}{\tilde{\omega}_\alpha}} z_\alpha X_{\alpha n} \right|^2 \quad (2.61)$$

The quantity $W_n F_n$ can be considered as an effective oscillator strength of the multisubband plasmon modes (the multisubband equivalent of $f_\alpha \Delta N_\alpha$). It is important to underline that each effective oscillator strength results from the contribution of all the optically active intersubband plasmons. They are weighted by the different quantities associated with individual transitions (dipole matrix element, transition frequencies) but

also depend on the coupling between intersubband plasmons, which enters through the eigenvectors of the matrix \mathbf{M} ($a_{J\alpha}$ and $b_{J\alpha}$).

The total absorption satisfies the following sum rule:

$$\boxed{\sum_{\alpha} \omega_{\alpha} |z_{\alpha}|^2 \Delta N_{\alpha} = \sum_n W_n F_n} \quad (2.62)$$

which expresses the conservation of the total transition probability, hence the total probability of light-matter interaction. We have found that this sum rule is numerically satisfied in all the systems we have studied.

We see then that the coupling between intersubband plasmons results in a redistribution of the absorption amplitude from the intersubband transitions to the multisubband plasmon modes.

2.2.7. Extension to piecewise constant mass

The definition of the microcurrents distribution $\xi(z)$ can be extended to the case of a piecewise constant effective mass. Indeed, one can define:

$$\begin{aligned} \xi_{ij}^m(z) &= \psi_i(z) \frac{\partial}{\partial z} \left[\frac{1}{\bar{m}^*(z)} \psi_j(z) \right] - \psi_j(z) \frac{\partial}{\partial z} \left[\frac{1}{\bar{m}^*(z)} \psi_i(z) \right] = \\ &= \frac{1}{\bar{m}^*(z)} \left[\psi_i(z) \frac{\partial}{\partial z} \psi_j(z) - \psi_j(z) \frac{\partial}{\partial z} \psi_i(z) \right] = \\ &= \frac{1}{\bar{m}^*(z)} \xi_{ij} \end{aligned} \quad (2.63)$$

where $\bar{m}^*(z) = \frac{m^*(z)}{m_0}$. Note that we can factor out the mass from the derivative term because of our hypothesis of \bar{m}^* being piecewise constant. This expression of the microcurrent distribution is more appropriate for systems of tunnel-coupled quantum wells, where it is important to properly treat the wavefunctions in the barriers. All the relevant quantities that can be expressed in terms of $\xi_{\alpha}(z)$ can also be expressed in terms of $\xi_{\alpha}^m(z)$. In fact, we can rewrite the Coulomb length (2.38) as:

$$S_{\alpha\beta}^m = \frac{\hbar}{2m_0\omega_{\alpha}} \frac{\hbar}{2m_0\omega_{\beta}} \int_{-\infty}^{+\infty} \xi_{\alpha}^m(z) \xi_{\beta}^m(z) dz$$

Then Eqs. (2.43) and (2.46) become

$$\begin{aligned} [\omega_{P\alpha}^m]^2 &= \frac{2e^2 \Delta N_{\alpha} \omega_{\alpha}}{\hbar \varepsilon_0 \varepsilon_s} S_{\alpha\alpha}^m \\ C_{\alpha\beta}^m &= \frac{S_{\alpha\beta}^m}{\sqrt{S_{\alpha\alpha}^m S_{\beta\beta}^m}} \end{aligned}$$

If \bar{m}^* is constant, all the definitions of the previous paragraphs are recovered.

2.3. Coupling between multisubband plasmons and a cavity mode

Let us consider now the full Hamiltonian (2.19), which includes also light terms. We can write it in terms of intersubband plasmon operators $p_\alpha, p_\alpha^\dagger$ as [68]:

$$\begin{aligned}
H = & \underbrace{\sum_{\alpha} \hbar \tilde{\omega}_{\alpha} p_{\alpha}^{\dagger} p_{\alpha}}_{\text{intersubband plasmons}} + \underbrace{\hbar \omega_c \left(a^{\dagger} a + \frac{1}{2} \right)}_{\text{photons}} + \\
& + \underbrace{\frac{1}{2} \sum_{\alpha \neq \beta} \hbar \Xi_{\alpha \beta} \left(p_{\alpha} + p_{\alpha}^{\dagger} \right) \left(p_{\beta} + p_{\beta}^{\dagger} \right)}_{\text{plasmon-plasmon interactions}} + \\
& + \underbrace{i \sum_{\alpha} \hbar \Omega_{\alpha} \left(a^{\dagger} - a \right) \left(p_{\alpha}^{\dagger} + p_{\alpha} \right)}_{\text{light-plasmon interactions}}
\end{aligned}$$

where the light-matter coupling constant is

$$\begin{aligned}
\Omega_{\alpha} &= \sqrt{\frac{e^2}{2\hbar \varepsilon_0 \varepsilon_s L_{\text{cav}}}} \sqrt{\omega_{\text{cav}}} \sqrt{\Delta N_{\alpha}} \sqrt{\frac{\omega_{\alpha}}{\tilde{\omega}_{\alpha}}} z_{\alpha} = \\
&= \frac{\omega_{P\alpha}}{2} \sqrt{\frac{\omega_{\text{cav}}}{\tilde{\omega}_{\alpha}}} \sqrt{\frac{L_{\alpha}^{\text{eff}}}{L_{\text{cav}}}}
\end{aligned}$$

with L_{cav} length of the cavity associated with the photonic mode of frequency ω_{cav} . We use the relation

$$(p_{\alpha} + p_{\alpha}^{\dagger}) = \sum_n X_{\alpha n} (P_n + P_n^{\dagger})$$

to rewrite the plasmon-light interaction term in the form

$$\begin{aligned}
H_{\text{light-plasmons}} &= i \sum_{\alpha} \hbar \Omega_{\alpha} \left(a^{\dagger} - a \right) \left(p_{\alpha}^{\dagger} + p_{\alpha} \right) = \\
&= i \hbar \sqrt{\frac{e^2}{2\hbar \varepsilon_0 \varepsilon_s L_{\text{cav}}}} \sum_{\alpha, n} \sqrt{\omega_{\text{cav}}} \sqrt{\Delta N_{\alpha}} \sqrt{\frac{\omega_{\alpha}}{\tilde{\omega}_{\alpha}}} z_{\alpha} X_{\alpha n} \left(a^{\dagger} - a \right) \left(P_n^{\dagger} + P_n \right) \\
&= i \hbar \sum_n \frac{R_n}{2} \sqrt{\frac{\omega_{\text{cav}}}{W_n}} \left(a^{\dagger} - a \right) \left(P_n^{\dagger} + P_n \right)
\end{aligned}$$

where we have defined R_n as

$$\begin{aligned}
R_n &= \sqrt{\frac{2e^2}{\hbar \varepsilon_0 \varepsilon_s L_{\text{cav}}}} \sum_{\alpha} \sqrt{W_n} \sqrt{\Delta N_{\alpha}} \sqrt{\frac{\omega_{\alpha}}{\tilde{\omega}_{\alpha}}} z_{\alpha} X_{\alpha n} = \\
&= \sum_{\alpha} \omega_{P\alpha} X_{\alpha n} \sqrt{\frac{W_n}{\tilde{\omega}_{\alpha}}} \sqrt{\frac{L_{\alpha}^{\text{eff}}}{L_{\text{cav}}}}
\end{aligned} \tag{2.64}$$

This quantity can be considered as an effective plasma frequency, as it is the coefficient weighting the light-matter interaction in the Hamiltonian $H_{\text{light-plasmons}}$. The full Hamiltonian is then expressed in terms of multisubband plasmons as

$$\begin{aligned}
 H = & \underbrace{\sum_n \hbar W_n P_n^\dagger P_n}_{\text{multisubband plasmons}} + \underbrace{\hbar \omega_c \left(a^\dagger a + \frac{1}{2} \right)}_{\text{photons}} + \\
 & + \underbrace{i \sum_n \hbar \frac{R_n}{2} \sqrt{\frac{\omega_{\text{cav}}}{W_n}} (a^\dagger - a) (P_n^\dagger + P_n)}_{\text{interaction between multisubband plasmons and cavity mode}}
 \end{aligned} \tag{2.65}$$

If the broadening of the cavity mode is larger than the light-matter coupling strength, the system is in a weak coupling regime. It is therefore possible to apply a perturbative method (Fermi's golden rule) equivalent to that described at the end of §2.2.3 to calculate the absorption rate. By considering instead of Eq. (2.36) the expression of the polarization field for multisubband plasmons

$$P_z = \sum_{n, \mathbf{q}} \frac{J_n(z)}{W_n} e^{i\mathbf{q}\cdot\mathbf{r}} (P_{\mathbf{q}n} + P_{-\mathbf{q}n}^\dagger)$$

we would obtain a result equivalent to Eq. (2.59).

On the contrary, if the cavity mode broadening is smaller or comparable to the light-matter coupling, we need to solve the problem exactly, with a diagonalization procedure similar to that followed to diagonalize the matter part. This procedure is described in the next section.

2.3.1. One multisubband plasmon coupled with light

Let us solve the problem (2.65) in the simple case of just one multisubband plasmon of frequency W_{MSP} interacting with one cavity mode. This situation is particularly interesting, as in a single quantum well with several occupied subbands only one multisubband plasmon mode is bright, and hence can couple with a cavity mode. This situation corresponds to that experimentally studied in Refs. [14, 67], where it has been demonstrated that such a coupling gives rise to new eigenmodes, called intersubband polaritons.

We consider the Hamiltonian

$$H = \hbar W_{\text{MSP}} P^\dagger P + \hbar \omega_{\text{cav}} \left(a^\dagger a + \frac{1}{2} \right) + i \hbar \Omega_R (a^\dagger - a) (P^\dagger + P) \tag{2.66}$$

where we have defined the Rabi frequency, expressing the coupling between the cavity mode and the matter excitation (in our case, the multisubband plasmon):

$$\Omega_R = \frac{R_{\text{MSP}}}{2} \sqrt{\frac{\omega_{\text{cav}}}{W_{\text{MSP}}}}$$

with R_{MSP} the effective plasma frequency of the multisubband plasmon. We look for new polariton operators Q_1, Q_2

$$\begin{aligned} Q_1 &= A_{11}a + B_{11}a^\dagger + A_{12}P_1 + B_{12}P_1^\dagger \\ Q_2 &= A_{21}a + B_{21}a^\dagger + A_{22}P_1 + B_{22}P_1^\dagger \end{aligned}$$

such that the Hamiltonian can be diagonalized as

$$H = \hbar M_1 Q_1^\dagger Q_1 + \hbar M_2 Q_2^\dagger Q_2$$

Following a Bogoliubov diagonalization procedure similar to the one used in §2.2.5, it is possible to write the system of equations

$$\begin{cases} M_K A_{K1} = A_{K1}\omega_{\text{cav}} - iA_{K2}\Omega_R + iB_{K2}\Omega_{W_{\text{MSP}}} \\ M_K B_{K1} = -B_{K1}\omega_{\text{cav}} - iB_{K2}\Omega_R + iA_{K2}\Omega_{W_{\text{MSP}}} \\ M_K A_{K2} = iA_{K1}\Omega_R + iB_{K1}\Omega_R + A_{K2}W_{\text{MSP}} \\ M_K B_{K2} = iA_{K1}\Omega_R + iB_{K1}\Omega_R - B_{K2}W_{\text{MSP}} \end{cases}$$

equivalent to

$$M_K \begin{pmatrix} A_{K1} \\ B_{K1} \\ A_{K2} \\ B_{K2} \end{pmatrix} = \begin{pmatrix} \omega_{\text{cav}} & 0 & -i\Omega_R & i\Omega_R \\ 0 & -\omega_{\text{cav}} & i\Omega_R & -i\Omega_R \\ i\Omega_R & i\Omega_R & W_{\text{MSP}} & 0 \\ i\Omega_R & i\Omega_R & 0 & -W_{\text{MSP}} \end{pmatrix} \begin{pmatrix} A_{K1} \\ B_{K1} \\ A_{K2} \\ B_{K2} \end{pmatrix} \quad (2.67)$$

The solutions of this system of equations are the two polariton modes, issued from the coupling between the multisubband plasmon and the cavity mode.

Let us remark that the Hamiltonian (2.66) has a general form, which includes antiresonant terms. These terms are often neglected in the study of light-matter interaction in the so-called strong coupling regime, where $\Omega_R/\omega_{\text{matter}} \ll 1$. On the contrary, the inclusion of the antiresonant contribution is necessary to the description of the ultra-strong coupling regime, in which the coupling frequency is comparable to the matter excitation frequency [72]. This situation is therefore automatically described by our model, thanks to the use of the dipole representation of the Hamiltonian [68].

The characteristic polynomial of the eigenproblem (2.67) can be written as

$$(\omega^2 - \omega_{\text{cav}}^2)(\omega^2 - W_{\text{MSP}}^2) = \Omega_R^2 \omega_{\text{cav}}^2$$

The solutions of the above equation represent the frequencies of the polaritonic modes, the so-called *upper* (higher energy) and *lower* (lower energy) polariton branches:

$$\omega_{\text{UP,LP}}^2 \equiv M_{1,2}^2 = \frac{1}{2} \left[W_{\text{MSP}}^2 + \omega_{\text{cav}}^2 \pm \sqrt{(\Delta\omega^2)^2 + 4\Omega_R^2 \omega_{\text{cav}}^2} \right]$$

where $\Delta\omega^2 = \omega_{\text{cav}}^2 - W_{\text{MSP}}^2$.

The Hopfield coefficients α and β represent the light and matter component of polariton

modes, respectively [68]. In the present case, they can be found equal to

$$\alpha_{\text{UP}} = \beta_{\text{LP}} = \frac{\Delta\omega^2 + \sqrt{(\Delta\omega^2)^2 + 4\Omega_R^2\omega_{\text{cav}}^2}}{2\sqrt{(\Delta\omega^2)^2 + 4\Omega_R^2\omega_{\text{cav}}^2}} = \left| |A_{K1}|^2 - |B_{K1}|^2 \right|$$

$$\alpha_{\text{LP}} = \beta_{\text{UP}} = 1 - \alpha_{\text{UP}}$$

We plot the polariton dispersion in Fig. 2.11, normalized to the matter excitation frequency W_{MSP} , considering a Rabi coupling $\Omega_R = 0.8W_{\text{MSP}}$. The size of the dots is proportional to the photonic weight of the mode, given by the Hopfield coefficient α .

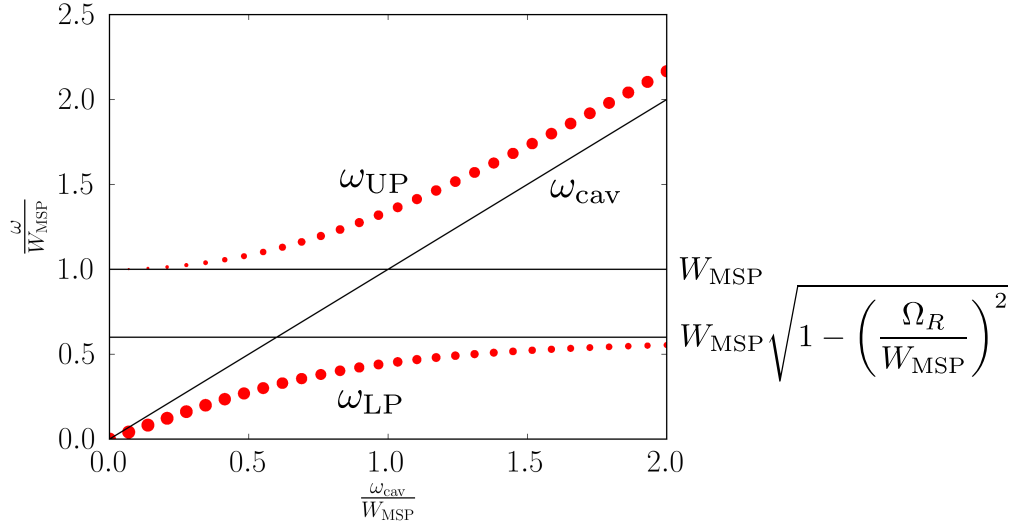


Figure 2.11: Frequency of the polariton branches as a function of the frequency of the cavity mode, normalized to the multisubband plasmon frequency W_{MSP} . We take $\Omega_R/W_{\text{MSP}} = 0.8$.

The horizontal asymptote of the upper polariton branch is W_{MSP} , while that of the lower polariton branch is $W_{\text{MSP}}\sqrt{1 - \left(\frac{\Omega_R}{W_{\text{MSP}}}\right)^2}$. This implies the opening of a gap in the dispersion, whose width is given by

$$\omega_{\text{gap}} = \left(1 - \sqrt{1 - \left(\frac{\Omega_R}{W_{\text{MSP}}}\right)^2}\right) W_{\text{MSP}}$$

and thus depends on the strength of the Rabi coupling Ω_R . This gap is considered an experimental signature of the ultra-strong coupling regime [8]. The possibility of engineering the polariton dispersion through Ω_R has been experimentally studied in Ref. [67].

2.4. Dielectric function and absorption spectrum

The result of the eigenproblem (2.67) can also be applied to derive an expression for the dielectric function and for the absorption spectrum, as it could be measured for example by means of multipass transmission in a waveguide.

Starting from the characteristic polynomial of the eigenproblem (2.67) and using the dispersion relation

$$\varepsilon(\omega)\omega^2 = \varepsilon_s\omega_{\text{cav}}^2$$

it is possible to express the effective dielectric function of the electron gas inserted in a cavity as [69]:

$$\frac{\varepsilon_s}{\varepsilon(\omega)} = 1 + \sum_n \frac{R_n^2}{\omega^2 - W_n^2 + i\gamma\omega} \quad (2.68)$$

The knowledge of this dielectric function permits to calculate an absorption spectrum through the expression $-\text{Im} \left[\frac{1}{\varepsilon(\omega)} \right]$, which will have the same form as the spectrum calculated using Eq. (2.60). However, we must note that the amplitudes of the absorption resonances calculated with this second procedure depend on the ratio $L_{\text{cav}}/L_{\text{eff}}^\alpha$ [Eq. (2.64)]. This represents the necessity to account for the overlap between the cavity mode and the lengths L_α^{eff} over which collective effects occur.

It is worth checking whether the dielectric function defined by using the procedure above obeys the sum rules [76]

$$\begin{aligned} \int_0^\infty d\omega \omega \text{Im} [\varepsilon(\omega)] &= \frac{1}{2} \pi \omega_{P,\text{bulk}}^2 \\ - \int_0^\infty d\omega \omega \text{Im} \left[\frac{1}{\varepsilon(\omega)} \right] &= \frac{1}{2} \pi \omega_{P,\text{bulk}}^2 \end{aligned}$$

where $\omega_{P,\text{bulk}}^2$ is the bulk plasma frequency

$$\omega_{P,\text{bulk}}^2 = \frac{N_V e^2}{\varepsilon_0 \varepsilon_s m^*}$$

These sum rules represent only a three dimensional upper limit for our dielectric function (2.68), due to its dependence on L_{cav} . The reason for this is that the charge density involved in the plasma oscillation is not the total N_V : the dimension along the growth direction z is indeed determined in a non-trivial way by the effective lengths of the transitions L_{eff} , thus by the quantum nature of the system.

We will show in the next chapter how the plasma frequency R_{MSP} tends to $\omega_{P,\text{bulk}}$ in the limit of large quantum wells and high doping levels (see §3.1.3).

By comparing Eq. (2.61) and (2.64), we get

$$R_n^2 = \frac{2e^2}{\hbar \varepsilon_0 \varepsilon_s L_{\text{cav}}} W_n F_n \quad (2.69)$$

We see then that the relation between the effective oscillator strengths $W_n F_n$ and the effective plasma frequencies R_n is exactly equivalent to the definition of plasma frequency (2.2):

$$\omega_{P\alpha}^2 = \frac{e^2}{m^* \varepsilon_0 \varepsilon_s L_\alpha^{\text{eff}}} f_\alpha \Delta N_\alpha = \frac{2e^2}{\hbar \varepsilon_0 \varepsilon_s L_\alpha^{\text{eff}}} \omega_\alpha z_\alpha^2 \Delta N_\alpha$$

As already mentioned in the first part of this chapter, the role of L_α^{eff} in the plasma frequency definition is that of accounting for the quantum effects due to confinement. In the expression (2.69) this same role is included within the effective oscillator strengths $W_n F_n$.

Conclusions

We have presented a quantum model, based on microscopic polarizations and microcurrents, which makes it possible to calculate the optical response of a bidimensional electron gas confined in an arbitrary potential. We have shown that the optical response of a highly doped system of quantum wells can be understood in terms of coupling between the intersubband plasmons, collective entities due to Coulomb interactions corresponding to the intersubband transitions and depending on the electron density involved in the transitions.

In the following chapter, we will study the interplay between collective excitations and tunnel coupling by applying the model to a set of relevant examples.

For convenience, we summarize here some results that will be referred to in the following chapter:

- We associate with every intersubband transition $\alpha \equiv i \rightarrow j$ a microscopic current density, whose spatial dependence is given by:

$$\xi_\alpha(z) \equiv \xi_{ij}(z) = \psi_i(z) \frac{\partial \psi_j(z)}{\partial z} - \frac{\partial \psi_i(z)}{\partial z} \psi_j(z) \quad (2.70)$$

- A central quantity for the intersubband plasmon coupling is the Coulomb tensor $S_{\alpha\beta}$, which can be defined in terms of microcurrents as:

$$S_{\alpha\beta} = \frac{1}{\hbar \omega_\alpha} \frac{1}{\hbar \omega_\beta} \left(\frac{\hbar^2}{2m^*} \right)^2 \int_{-\infty}^{+\infty} \xi_\alpha(z) \xi_\beta(z) dz \quad (2.71)$$

- The diagonal $S_{\alpha\alpha}$ is related to the plasma frequency $\omega_{P\alpha}$ through:

$$\omega_{P\alpha}^2 = \frac{e^2 f_\alpha \Delta N_\alpha}{m^* \varepsilon_0 \varepsilon_s L_\alpha^{\text{eff}}} = \frac{2e^2 \Delta N_\alpha \omega_\alpha}{\hbar \varepsilon_0 \varepsilon_s} S_{\alpha\alpha} \quad (2.72)$$

- It is possible to write the following relation between microcurrent spatial distributions $\xi_\alpha(z)$ and the optical dipole matrix element z_α :

$$\int_{-\infty}^{+\infty} \xi_\alpha(z) dz = \frac{2m^* \omega_\alpha}{\hbar} z_\alpha$$

- The intersubband plasmon coupling frequency reads

$$\Xi_{\alpha\beta} = \frac{\omega_{P\alpha}\omega_{P\beta}}{2\sqrt{\tilde{\omega}_\alpha\tilde{\omega}_\beta}} \frac{S_{\alpha\beta}}{\sqrt{S_{\alpha\alpha}S_{\beta\beta}}} \quad (2.73)$$

- In a single quantum well, the S elements defined by Eq. (2.71) associated with transitions between consecutive levels are the most important. Their values are similar, and tend to $\frac{L_{\text{QW}}}{2\pi^2}$ in the case of an infinite quantum well. This is not the case for an arbitrary confining potential.
- The absorption spectrum can be expressed in terms of microcurrents as:

$$A(\omega) = \sum_{\alpha} \frac{1}{\omega_{\alpha}} \left| \int_{-\infty}^{+\infty} j_{\alpha}(z) dz \right|^2 \mathcal{L}_{\hbar\gamma}(\hbar\omega - \hbar\omega_{\alpha}) \quad \text{single-particle} \quad (2.74)$$

$$A(\omega) = \sum_n \frac{1}{W_n} \left| \int_{-\infty}^{+\infty} J_n(z) dz \right|^2 \mathcal{L}_{\hbar\gamma}(\hbar\omega - \hbar W_n) \quad \text{collective} \quad (2.75)$$

- The absorption coefficient α_{2D} can be written as:

$$\alpha_{2D}(\omega) = \frac{e^2}{\varepsilon_0 c \sqrt{\varepsilon_s}} \sum_{\alpha} \omega_{\alpha} |z_{\alpha}|^2 \Delta N_{\alpha} \mathcal{L}_{\hbar\gamma}(\hbar\omega - \hbar\omega_{\alpha}) \quad \text{single-particle}$$

$$\alpha_{2D}(\omega) = \frac{e^2}{\varepsilon_0 c \sqrt{\varepsilon_s}} \sum_n W_n F_n \mathcal{L}_{\hbar\gamma}(\hbar\omega - \hbar W_n) \quad \text{collective}$$

- The total absorption satisfies the sum rule:

$$\sum_{\alpha} \omega_{\alpha} |z_{\alpha}|^2 \Delta N_{\alpha} = \sum_n W_n F_n$$

with W_n energies of the collective modes, and

$$F_n = \left| \sum_{\alpha} \sqrt{\Delta N_{\alpha}} \sqrt{\frac{\omega_{\alpha}}{\tilde{\omega}_{\alpha}}} z_{\alpha} X_{\alpha n} \right|^2$$

Absorption spectra of single and tunnel-coupled quantum wells

The quantum model presented in the previous chapter allows us to reproduce the experimental absorption spectrum of a dense electron gas confined in a quantum well. Furthermore, it makes it possible to investigate the possibility of engineering new quantum structures based on collective excitations. In this chapter, we explore the interplay between charge-induced coherence and tunnel coupling, in order to understand how to control these two different coherences to give rise to new collective states.

In §3.1, the theory is applied to the case of a single quantum well with several occupied subbands. We demonstrate that the semiclassical model describing the intersubband absorption in terms of Drude-Lorentz oscillators is recovered as a special case of our formalism, when all the overlap integrals between intersubband currents are comparable. Section 3.2 presents an analytical tight-binding analysis of the coupling between transitions, introducing the interplay between Coulomb effects and tunnel coupling. Then, in §3.3, the absorption spectrum of a dense electron gas in a system of asymmetric wells is investigated. In this case, we demonstrate that the coupling between a bright and an almost dark transition results in an optical spectrum composed of two peaks of equal amplitude. Here the coherence induced by Coulomb interaction gives rise to a phenomenon similar to the Autler-Townes effect [77, 78]. We explore in §3.4 a system of two tunnel-coupled quantum wells with several occupied subbands. The resulting absorption spectrum is interpreted in terms of the collective currents of the multisubband plasmons of the system. Section 3.5 proposes a structure to investigate the coexistence of different characteristic lengths for plasmons in the same system, and §3.6 a design featuring the coupling between a multisubband plasmons and a single-particle transition. Finally, we show how our model can be used to describe the ultra-strong coupling regime between a bright multisubband plasmon and a cavity mode in §3.7.

3.1. Single quantum well with several occupied subbands

As a first application, we consider a single quantum well with several occupied subbands. This is the same kind of system that has been experimentally studied in Ref. [14], where it has been demonstrated that even though several intersubband transitions are optically excited, the absorption spectrum displays a single peak, concentrating the whole interaction with light, as discussed in §2.1.3. We will show that our model recovers this result.

Let us consider a 15 nm GaAs/Al_{0.45}Ga_{0.55}As quantum well, n-doped with a density $1.05 \times 10^{13} \text{ cm}^{-2}$ (corresponding to $N_V = 7 \times 10^{18} \text{ cm}^{-3}$), such that three subbands are occupied¹. Fig. 3.1 presents the corresponding band structure, where the Fermi level is indicated by a dashed line.

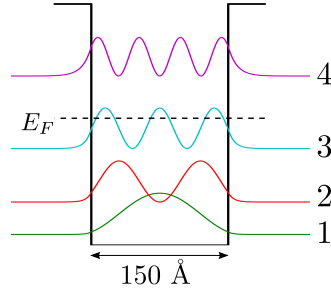


Figure 3.1: Calculated band structure and squared moduli of wavefunctions in a 150 Å GaAs/Al_{0.45}Ga_{0.55}As quantum well, $N_S = 1.05 \times 10^{13} \text{ cm}^{-2}$ ($N_V = 7 \times 10^{18} \text{ cm}^{-3}$). The dashed line indicates the Fermi energy at 0 K.

3.1.1. Single-particle properties

Table 3.1 presents some relevant parameters relative to all the possible intersubband transitions in the quantum well. The single-particle absorption spectrum of this quantum well is shown in Fig. 3.2, calculated as

$$\text{Abs}(\omega) \propto \sum_{\alpha} \omega_{\alpha} |z_{\alpha}|^2 \Delta N_{\alpha} \mathcal{L}_{\hbar\gamma}(\hbar\omega - \hbar\omega_{\alpha}) \quad (3.1)$$

where, as in the previous chapter, the sum runs over the transitions $\alpha \equiv i \rightarrow j$, ω_{α} is the frequency of the intersubband transition α , z_{α} is the optical dipole, ΔN_{α} is the difference between electronic densities of subbands i and j , and $\mathcal{L}_{\hbar\gamma}(\hbar\omega - \hbar\omega_{\alpha})$ is a Lorentzian of width $\hbar\gamma$ centered on the transition energy $\hbar\omega_{\alpha}$.

¹We consider here a case with just three occupied subbands in order to present the main concepts while keeping the discussion as clear as possible. Similar results are valid, and indeed even more remarkable, for higher numbers of occupied subbands; for example the experimental results of Ref. [14] refer to a quantum well with four occupied subbands.

α	(i,j)	z_α (Å)	ΔN_α (cm ⁻²)	f_α	$\hbar\omega_\alpha$ (meV)	$\hbar\tilde{\omega}_\alpha$ (meV)	$\hbar\omega_{P\alpha}$ (meV)	$S_{\alpha\alpha}$ (Å)	L_α^{eff} (Å)
1	(1, 2)	32.2	1.5e+12	0.97	52.8	73.5	51.1	10.04	103.3
2	(2, 3)	35.1	2.4e+12	1.89	87.1	119.5	81.8	9.45	130.1
3	(3, 4)	36.6	1.4e+12	2.79	118.1	138.0	71.4	9.43	142.3
4	(1, 4)	2.6	5.3e+12	0.03	258.0	269.4	77.5	1.32	5.1
5	(1, 3)	0	3.9e+12	0	140.0	157.2	71.6	2.81	0
6	(2, 4)	0	3.8e+12	0	205.2	220.4	80.4	2.48	0

Table 3.1: Calculated characteristics for the different intersubband transitions in the structure in Fig. 3.1.

The spectrum features three clearly visible peaks, corresponding to transitions between consecutive levels $1 \rightarrow 2$, $2 \rightarrow 3$, and $3 \rightarrow 4$, in agreement with the higher dipole values reported in Table 3.1. The fourth high-energy peak corresponds to the weak optically active transition $1 \rightarrow 4$ (z_{14} is less than 10% of $z_{i,i+1}$, $i = 1, 2, 3$). These four resonances represent the excitations of the system when Coulomb interactions are not taken into account.

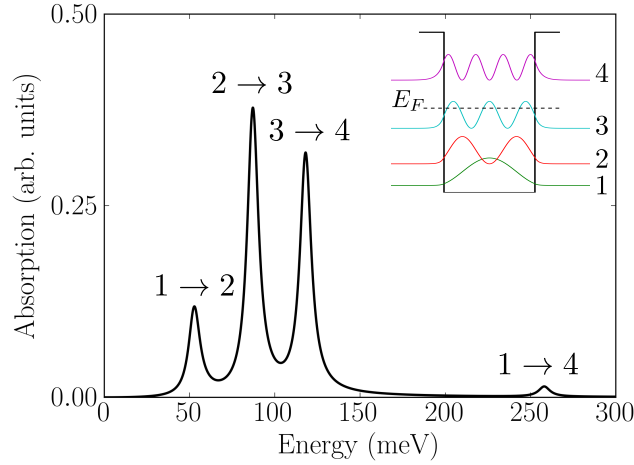


Figure 3.2: Absorption in single-particle picture, 150 Å GaAs/Al_{0.45}Ga_{0.55}As quantum well shown in inset. $\hbar\gamma = 8$ meV, $N_S = 1.05 \times 10^{13}$ cm⁻².

An alternative visualization of these excitations is shown in Fig. 3.3, which presents the spatial extension of the calculated single-particle microscopic current densities, as defined by Eq. (2.28):

$$j_\alpha(z) = \frac{e\hbar}{2m^*\sqrt{S}} \xi_\alpha(z) \sqrt{\Delta N_\alpha}$$

$$\xi_\alpha(z) \equiv \xi_{ij}(z) = \psi_i(z) \frac{\partial \psi_j(z)}{\partial z} - \psi_j(z) \frac{\partial \psi_i(z)}{\partial z}$$

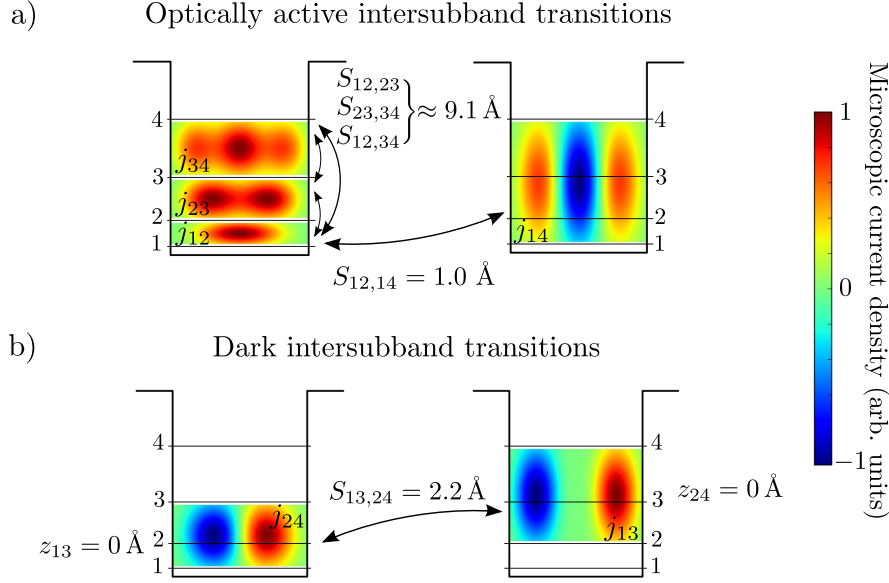


Figure 3.3: Calculated spatial distributions of the microscopic current densities j_{ij} for optically active (a) and dark (b) transitions in the 15 nm GaAs/Al_{0.45}Ga_{0.55}As quantum well of Fig. 3.1, plotted between the level energies and multiplied by a Gaussian function along the energy axis for visualization purposes. Coulomb lengths $S_{ij,kl}$ are also shown.

Each microcurrent, normalized to its maximum amplitude, is reported in color scale as a function of z , plotted in the energy interval between the confined levels involved in the corresponding transition, and multiplied by a Gaussian function along the energy axis for visualization purposes. As already noted, microcurrents associated with dipole-allowed transitions are symmetric with respect to the center of the quantum well, as shown in panel (a), while microcurrents whose dipole is zero for parity are odd [panel (b)].

Table 3.2 reports the calculated values for the Coulomb lengths $S_{\alpha\beta}$, some of which are also indicated in Fig. 3.3. As in the case of the infinite quantum well reported in §2.2.5, the highest values ($\approx 10 \text{ \AA}$) appear on the diagonal $S_{\alpha\alpha}$, and correspond to the interaction between dipoles belonging to the same intersubband transition. These terms are responsible for the depolarization shift, and indeed determine the plasma frequency of the transition α [see Eq. (2.43)].

We calculate values of $S_{\alpha\beta}$ comparable to the diagonal ones ($\approx 9 \text{ \AA}$) for pairs of transitions between consecutive subbands, regardless of the quantum number of the subbands involved [Fig. 3.3(a)]. All these values are exactly equal in the case of an infinite quantum well, where $S_{n,n+1;m,m+1} = L_{\text{QW}}/(2\pi^2)$ for all n, m , as previously shown. Smaller values of $S_{\alpha\beta}$ are instead obtained when the transition 1-4 is involved, indicating the existence of different scales of Coulomb lengths in the same quantum well. As an example, in Fig. 3.3 we report the value of $S_{12,14}$, the highest one. Note that $S_{\alpha\beta}$ is also non negligible when the microcurrents involved present the same parity, even when they

(i,j)	(1,2)	(2,3)	(3,4)	(1,3)	(1,4)	(2,4)
(1,2)	10.0	9.1	9.1	0.0	-1.0	0.0
(2,3)	9.1	9.5	9.2	0.0	0.3	0.0
(3,4)	9.1	9.2	9.4	0.0	0.0	0.0
(1,3)	0.0	0.0	0.0	2.8	0.0	2.2
(1,4)	-1.0	0.3	0.0	0.0	1.3	0.0
(2,4)	0.0	0.0	0.0	2.2	0.0	2.5

Table 3.2: Calculated values of $S_{\alpha,\beta}$ in Angstrom.

(i,j)	(1,2)	(2,3)	(3,4)	(1,3)	(1,4)	(2,4)
(1,2)	1	0.93	0.93	0	-0.28	0
(2,3)	0.93	1	0.97	0	0.09	0
(3,4)	0.93	0.97	1	0	0	0
(1,3)	0	0	0	1	0	0.84
(1,4)	-0.28	0.09	0	0	1	0
(2,4)	0	0	0	0.84	0	1

Table 3.3: Calculated values of the normalized overlap $C_{\alpha\beta}$ between microscopic currents.

correspond to optically forbidden intersubband transitions, like 1-3 and 2-4 [Fig. 3.3(b)].

Table 3.3 presents the calculated values of the normalized overlap between intersubband currents $C_{\alpha\beta}$ for all the possible pairs of transitions. $C_{\alpha\beta}$ is very close to 1 whenever transitions between consecutive subbands are involved, and it is in general non negligible for microcurrents presenting the same parity. This reflects the behavior already mentioned for $S_{\alpha\beta}$.

3.1.2. Collective renormalization: bright multisubband plasmon and absorption spectrum

The mutual coupling between the six possible intersubband transitions in this system leads to six multisubband plasmons. Table 3.4 shows their energies W_n [calculated as eigenvalues of the Hopfield-like matrix \mathbf{M} , Eq. (2.54)] and factors F_n [Eq. (2.61)]. The table also reports the values of the effective oscillator strengths $W_n F_n$, along with their normalized values $\overline{W_n F_n} = W_n F_n / \max_n \{W_n F_n\}$, and the effective lengths L_n^{eff} [Eq. (2.57)].

The current densities (2.55)

$$J_n(z) = \frac{e\hbar}{2m^* \sqrt{S}} W_n \sum_{\alpha} \frac{\xi_{\alpha}(z) \sqrt{\Delta N_{\alpha}}}{\sqrt{\omega_{\alpha} \tilde{\omega}_{\alpha}}} X_{\alpha n} \quad (3.2)$$

corresponding to these six eigenmodes are plotted in Fig. 3.4. It is evident from Table 3.4 and Fig. 3.4 that two of the multisubband plasmons ($n = 4, 5$) are dark, and indeed the corresponding current densities are odd with respect to the center of the quantum well.

n	$\hbar W_n$ (meV)	F_n (number)	$\hbar W_n F_n$ (meV)	$\overline{W_n F_n}$ (number)	L_n^{eff} (Å)
1	61.63	0.0085	0.52	0.0099	39.0
2	103.73	0.026	2.70	0.052	90.6
3	155.38	0.34	52.83	1	136.2
4	154.17	0	0	0	0
5	222.54	0	0	0	0
6	269.45	0.0035	0.94	0.018	5.1

Table 3.4: Calculated parameters of collective modes after diagonalization. The line in bold corresponds to the bright multisubband plasmon.

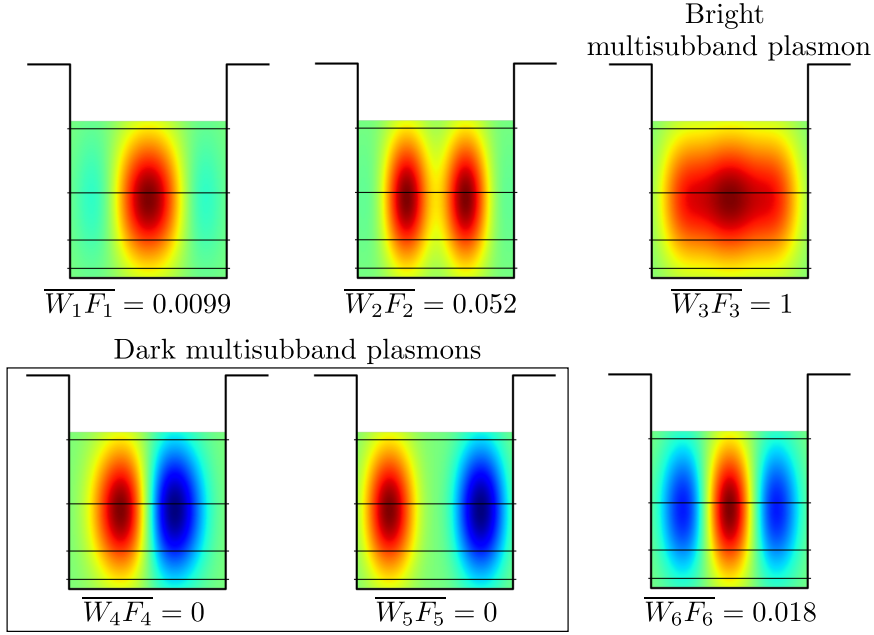


Figure 3.4: Calculated spatial distributions of the microscopic collective current densities J_n [Eq. (2.55)] in the 150 Å GaAs/Al_{0.45}Ga_{0.55}As quantum well of Fig. 3.1, multiplied by a Gaussian function along the energy axis for visualization purposes.

Values of effective oscillator strengths $\overline{W_n F_n} = W_n F_n / \max_n \{W_n F_n\}$ are also shown, with $W_n F_n$ defined by Eq. (2.60).

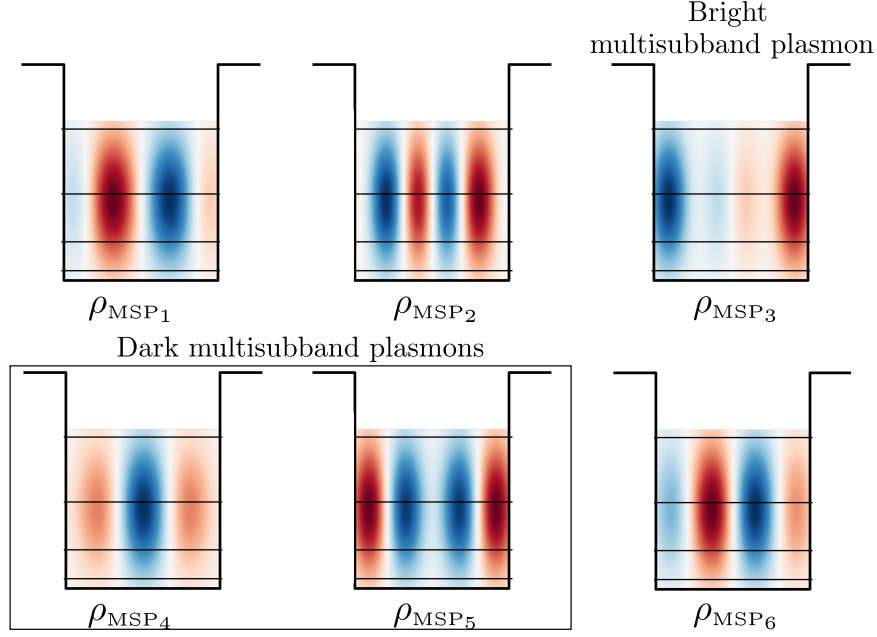


Figure 3.5: Calculated spatial distributions of the charge oscillation ρ_{MSP_n} [Eq. (2.56)] corresponding to the multisubband plasmons in the 150 Å GaAs/Al_{0.45}Ga_{0.55}As quantum well of Fig. 3.1.

Figure 3.5 presents the corresponding distributions of charge oscillations ρ_{MSP_n} , as defined by Eq. (2.56). As expected from their definition, the parity properties of these charge oscillations are opposite to those of the microcurrents distributions.

Even though there are four modes with a non-zero effective oscillator strength, we can consider that just one is *bright* ($n = 3$), as its effective oscillator strength, $W_B F_B$, is at least 20 times greater than the others. It is then possible to approximate Eq. (2.62) as

$$\sum_{\alpha} \omega_{\alpha} |z_{\alpha}|^2 \Delta N_{\alpha} = W_B F_B$$

Thanks to this observation, we can estimate an effective dipole of the bright multisubband plasmon, Z_B . For this, we first observe that, due to Pauli blocking, in a quantum well with several occupied subbands not all the electrons in the system are involved in the interaction with light, but only a fraction corresponding to the occupation of the first subband: $N_{\text{eff}} = N_1$, as schematized in Fig. 3.6. As a consequence, $W_B F_B = N_1 W_B |Z_B|^2$. In the present example we obtain $Z_B = 25.3$ Å, corresponding to an oscillator strength of $f_{\text{MSP}} = \frac{2m^* W_B}{\hbar} Z_B^2 = 1.75$.

Note that it may be tempting to use the calculated ρ_{MSP_n} to obtain an expression for the collective dipole, in analogy to expression (2.32). As already discussed in §2.2.6, this is not possible, since $\rho_{\text{MSP}_n}(z)$ is not perfectly equivalent to the single-particle charge

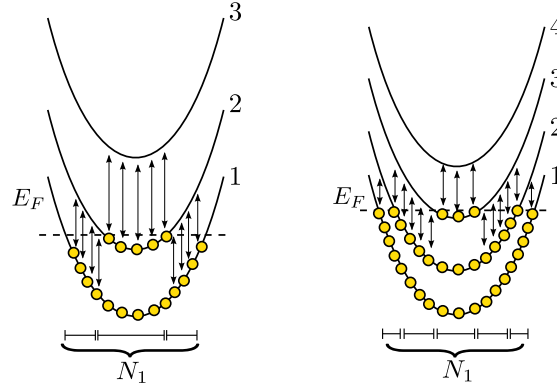


Figure 3.6: Illustration of the fraction of electrons involved in intersubband plasma oscillations. Independently of the number of occupied subbands, the number of electrons involved in the interaction with light is N_1 .

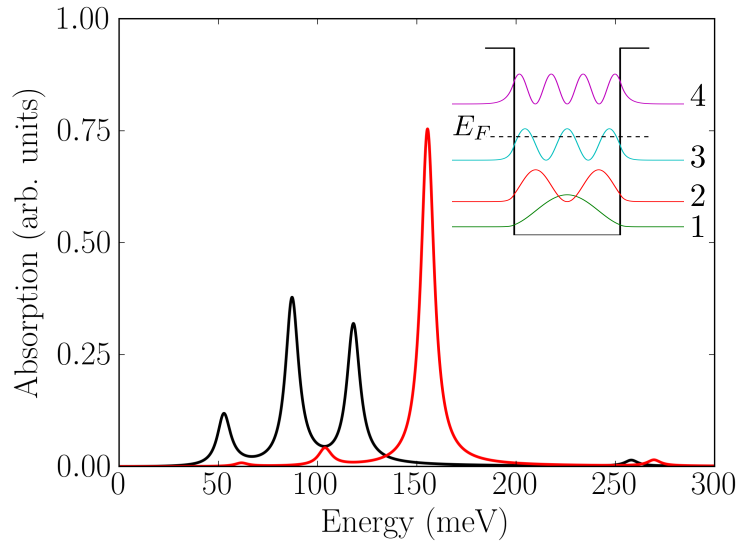


Figure 3.7: Inset: GaAs/Al_{0.45}Ga_{0.55}As structure, 150 Å, $N_V = 7 \times 10^{18} \text{cm}^{-3}$. Black line: Absorption in single-particle picture. Red: absorption accounting for collective effects calculated with our model. We set a phenomenological broadening $\hbar\gamma = 8 \text{ meV}$.

oscillation distribution $\rho_\alpha(z)$. Nevertheless, the graphical representation of $\rho_{\text{MSP}_n}(z)$ in Fig. 3.5 gives a qualitative idea of the extension of the charge oscillations, intended as the distance between the two main amplitude peaks of the optically active plasmons. It can be appreciated that for the bright multisubband plasmon ($n = 3$) this distance is almost equal to the entire quantum well width.

A more quantitative description of the spatial extension of the collective oscillations can be provided by the effective length L_n^{eff} defined by Eq. (2.57):

$$L_n^{\text{eff}} = \frac{\left| \int_{-\infty}^{+\infty} J_n(z) dz \right|^2}{\int_{-\infty}^{+\infty} J_n^2(z) dz} \quad (3.3)$$

The last column of Table 3.4 presents the six calculated values of L_n^{eff} , representing the extension of the polarization associated with the collective modes. As expected, the spatial extension associated with the bright multisubband plasmon ($n = 3$) is a significant fraction of the quantum well width, more than 90%.

The absorption spectrum calculated with our model is shown in Fig. 3.7 (red line) and compared with the single-particle one (black line). As anticipated, the optical response of the electron gas is almost completely concentrated into a single peak, which has an amplitude more than one order of magnitude greater than the other resonances, in agreement with the experimental results obtained in Ref. [14]. However, a resonance is visible for each of the four optically active multisubband plasmons of Table 3.4, with an amplitude proportional to their effective oscillator strength $W_n F_n$ [see also the logarithmic representation of the spectrum reported in Fig. (3.12)].

3.1.3. Electronic density and well width dependence

In this section, we investigate the single quantum well problem in a more systematic way. As already observed in Chapter 2, the multisubband plasmon has a plasma and an intersubband contribution:

$$E_{\text{MSP}}^2 = E_{\text{P}}^2 + E_{\text{ISB}}^2 \quad (3.4)$$

It is hence interesting to study its evolution with varying values of electronic density $N_V = N_S/L_{\text{QW}}$, affecting the plasma contribution, and of the quantum well width L_{QW} , affecting the intersubband contribution.

Variable N_V

Figure 3.8 shows a logarithmic scale color plot of the calculated absorption spectra for increasing doping N_V , i.e. for increasing Fermi level; in this doping range, E_F moves from above the first subband to above the third (vertical dashed lines). The horizontal dashed lines indicate the energy position of the single-particle excitations, which are independent of the electronic density.

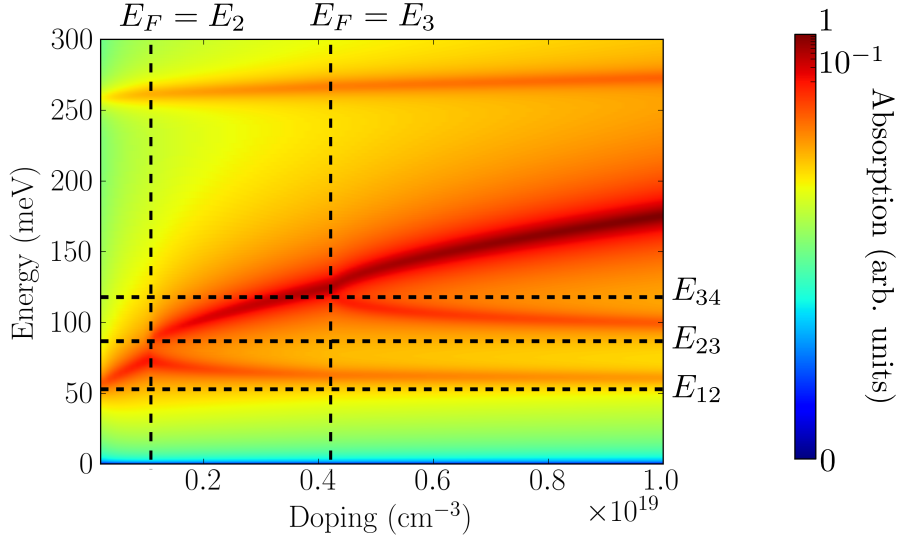


Figure 3.8: Calculated spectra for a GaAs/Al_{0.45}Ga_{0.55}As 150 Å quantum well for variable doping N_V , plotted in logarithmic scale. Horizontal dashed lines: single-particle transition energies. Vertical dashed lines: doping levels for which the Fermi energy corresponds to levels 2 and 3.

Some of the spectra composing Fig. 3.8 are reported in Fig. 3.9 for clarity (in red), along with the corresponding single-particle spectra (in black). When just one subband is occupied we observe a blue shift of the $1 \rightarrow 2$ resonance, the depolarization shift [Fig. 3.9(a)]. When the Fermi level is between the second and the third subband, an oscillator strength transfer is visible, from the low energy mode to the high energy one [Fig. 3.9(b)]. If the Fermi level is higher than the third subband [Fig. 3.9(c)-(d)], essentially just one peak is observed, concentrating almost the whole absorption amplitude. Its energy is blueshifted and its amplitude increases if the electronic density is further increased.

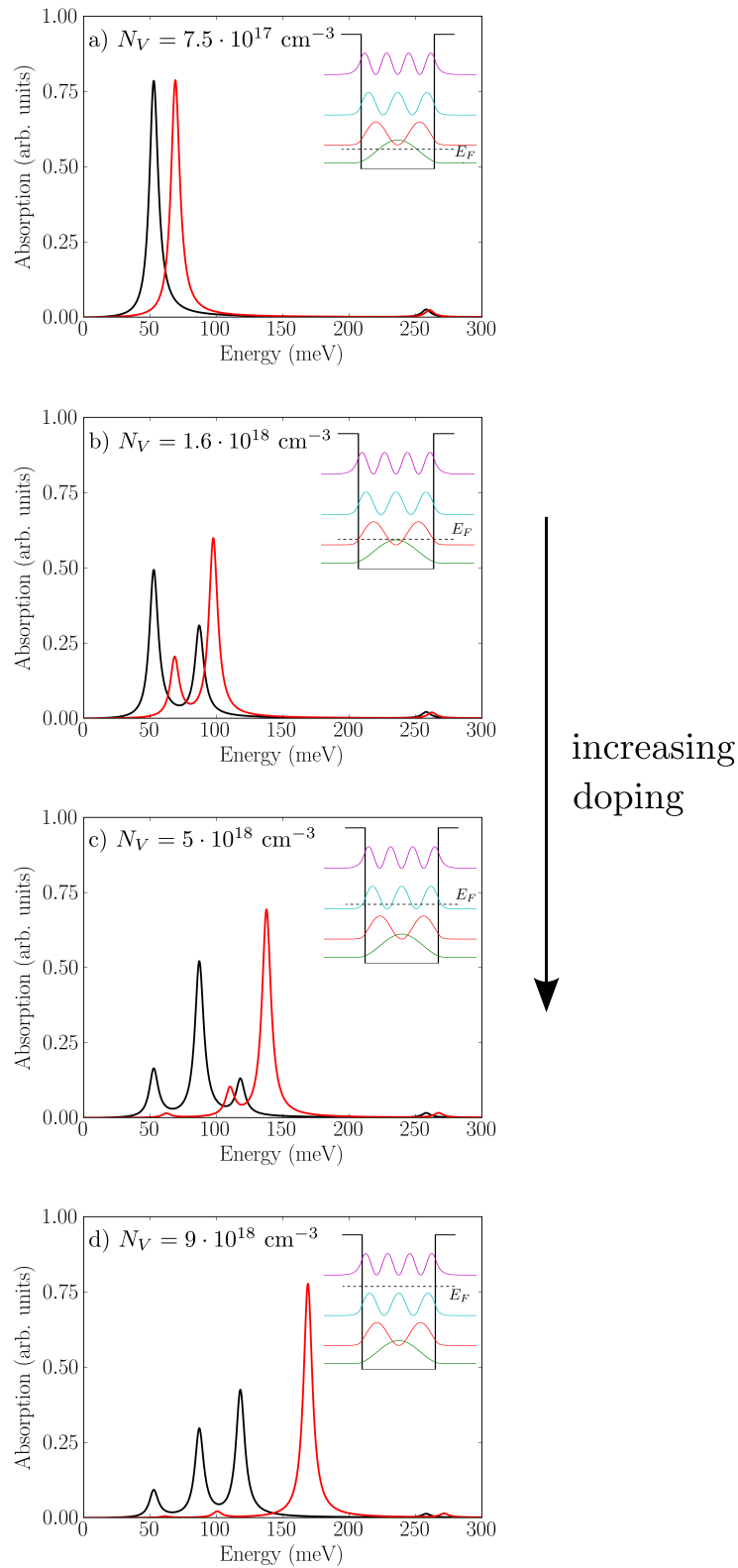


Figure 3.9: Selected spectra from those composing Fig. 3.8 (red lines) for increasing doping. The black curves represent the corresponding single-particle spectra. All the curves share the same normalization for visualization purposes, and $\hbar\gamma = 8 \text{ meV}$.

Variable L_{QW}

We set again the doping level to $N_V = 7 \times 10^{18} \text{ cm}^{-3}$, and consider the absorption response of a single quantum well of varying width L_{QW} .

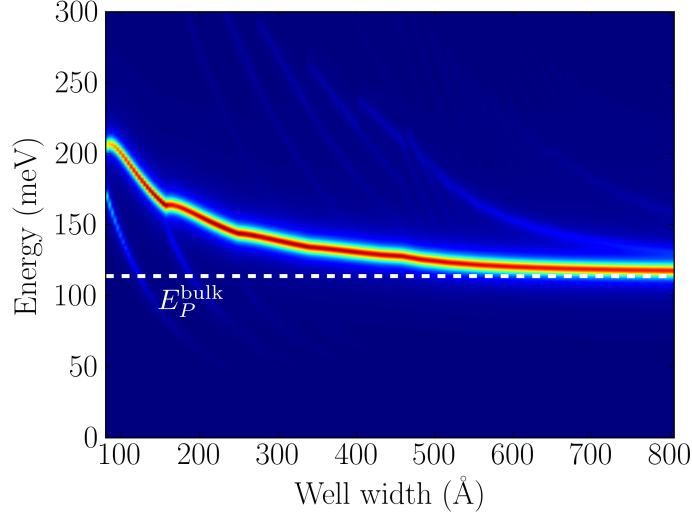


Figure 3.10: Calculated spectra for a GaAs/Al_{0.45}Ga_{0.55}As Å quantum well, $N_V = 7 \times 10^{18} \text{ cm}^{-3}$, with variable L_{QW} . All the absorption spectra have been normalized to 1.

The result is shown in Fig. 3.10: a single peak is observed for mostly all width values. Remarkably, the position of this peak tends for wide quantum wells to the value of the plasma energy E_P^{bulk} :

$$E_P^{\text{bulk}} = \hbar \sqrt{\frac{e^2 N_V}{m^* \epsilon_0 \epsilon_s}}$$

This limit value can be understood by recalling that the multisubband plasmon has two contributions, one related to the confinement, the other one to the collective excitation of electrons. We recall that E_{ISB} in Eq. (3.4) represents the intersubband contribution to the total energy of the multisubband plasmon, and is given by the harmonic mean of the different intersubband transition energies [see Eq. (2.12)]. As it can be seen from Fig. 3.11, for wider quantum wells the separation between subbands tends to zero; the quantum confinement becomes less and less important, as it can be reasonably expected. Consequently, the intersubband contribution to E_{MSP} tends to zero as well: the total energy is reduced to the sole plasma contribution, which we can write as

$$\Omega_{P_{\text{MSP}}}^2 = \frac{e^2 N_1 f_{\text{MSP}}}{m^* \epsilon_0 \epsilon_s L_{\text{MSP}}^{\text{eff}}}$$

From comparison of the above expression with the bulk plasma frequency, we deduce that

the following limit holds:

$$\frac{N_1 f_{\text{MSP}}}{L_{\text{MSP}}^{\text{eff}}} \xrightarrow{L_{\text{QW}} \rightarrow \infty} N_V$$

In the case of a 800 Å quantum well, we calculate $f_{\text{MSP}} = 8.52$, $N_1 = 5.62 \times 10^{12} \text{ cm}^{-2}$. This corresponds thus to $L_{\text{MSP}}^{\text{eff}} = 684 \text{ Å}$, 85% of the quantum well width. A similar value ($L^{\text{eff}} = 671 \text{ Å}$) is obtained by calculating the effective length with Eq. (3.3). Note that this really wide quantum well is a limit situation for the electron confinement. Nevertheless, the unique peak expected by our calculation at the plasma frequency is experimentally observed [67] and recovers the Berreman mode that can be observed in highly doped thin films [79].

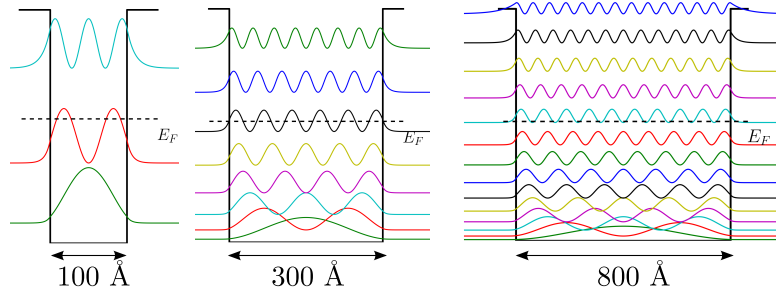


Figure 3.11: Calculated band structure and squared moduli of wavefunctions for some of the structures considered in Fig. 3.10, $N_V = 7 \times 10^{18} \text{ cm}^{-3}$.

3.1.4. Relation to the semiclassical model

In the case of a single quantum well with several occupied subbands, the coupling with light is mainly determined by intersubband transitions between consecutive levels, mutually interacting on the same length scale, as determined by the value of $S_{\alpha\beta}$ (see Table 3.2 and Fig. 3.3). The normalized overlap $C_{\alpha\beta}$ between the corresponding microcurrents is very close to one, as it can be seen in Table 3.3. This means that the electron gas behaves as a set of oscillators interacting with each other and with the light on the same length scale. This is precisely the case in which it is possible to calculate the intersubband contribution to the dielectric function by using the Drude-Lorentz expression presented in the previous chapter (§2.1.3):

$$\varepsilon(\omega) = \varepsilon_s \left(1 - \sum_{n=1}^{n_{\text{occ}}} \frac{\omega_{P_{n,n+1}}^2}{\omega^2 - \omega_{n,n+1}^2 + i\gamma\omega} \right) \quad (3.5)$$

Figure 3.12 presents in black in panel (a) the spectrum calculated with our model in logarithmic scale, and in blue in panel (b) the absorption spectrum corresponding to Eq. (3.5) for a 150 Å GaAs quantum well. It can be appreciated that the two are very similar, except for the absence of the peak at $\approx 270 \text{ meV}$, very close to energy $\hbar\tilde{\omega}_{14}$, which is not included in Eq. (3.5).

The red line in Fig. 3.12(b) presents the absorption spectrum obtained by extending the sum in Eq. (3.5) to all the optically active transitions, in this case all those between

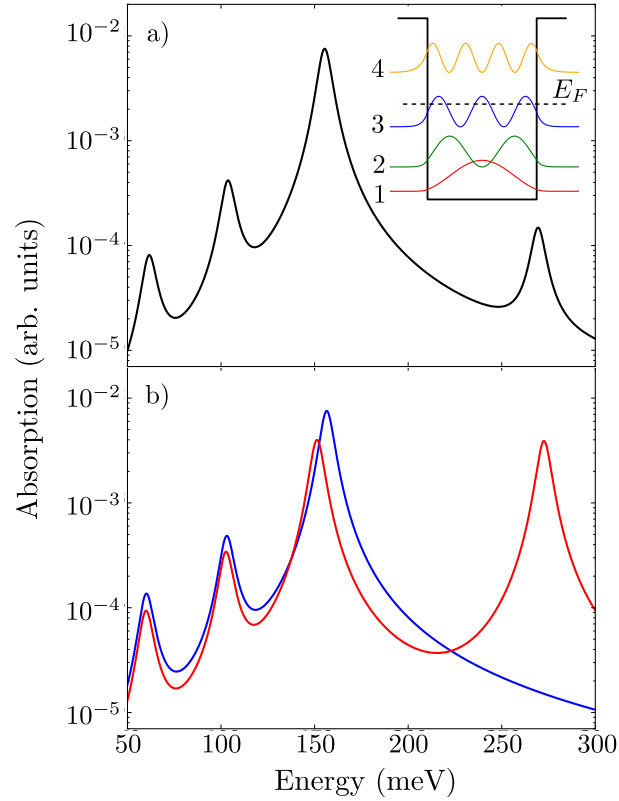


Figure 3.12: a) Inset: Calculated band structure, energy levels and square moduli of the wave functions of a GaAs/Al_{0.45}Ga_{0.55}As quantum well, 150 Å wide, doped $N_V = 7 \times 10^{18} \text{ cm}^{-3}$. The corresponding Fermi energy at 0K is indicated with a black dashed line. Black line: Absorption spectrum in logarithmic scale calculated by using our quantum model. b) Blue line: absorption spectrum calculated by using Eq. (3.5). Red line: absorption spectrum calculated by extending the sum in Eq. (3.5) to all optically active transitions.

consecutive subbands plus the $1 \rightarrow 4$ transition. In this curve, the amplitude of the peak at 270 meV is almost equal to that of the peak at 155 meV. The different amplitude assigned to the 270 meV peaks in the two models is due to the fact that in Eq. (3.5) all the dipoles interact with the same Coulomb length, while our model does take into account the different Coulomb lengths between dipoles.

The above observation implies that Eq. (3.5) does not provide a general expression of the dielectric function. Indeed, it can only be used when all the Coulomb lengths involved are equal.

The $C_{\alpha\beta}$ coefficients

It is interesting to devote a brief discussion to the role in our quantum model of the coefficients $C_{\alpha\beta}$, which have no equivalent in the semiclassical expression of the dielectric function. As we have seen in Table 3.3, the C coefficients of the couplings between consecutive transitions are almost equal to 1. Indeed, if we set $C_{\alpha\beta} = 1$ everywhere in our model, and take into account just the transitions between consecutive levels, we obtain the same absorption spectrum as in the semiclassical model of Eq. (3.5).

On the other hand, if we calculate the absorption with $C_{\alpha\beta} = 1$, but including all the possible transitions, the result is plainly wrong. As it can be seen in Fig. 3.13, neglecting the role of the microcurrents overlap brings to wrong absorption amplitudes for the six multisubband plasmons resonances. In particular, all the multisubband plasmons are bright. This proves the crucial role of the signed values of coefficients $C_{\alpha\beta}$ in weighting correctly the contribution of each transition.

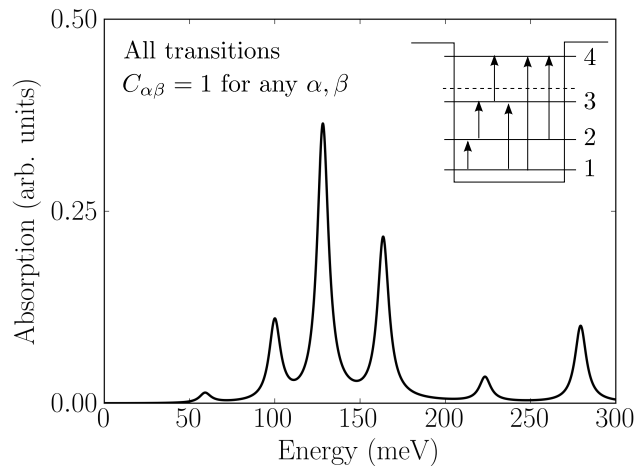


Figure 3.13: Calculated absorption spectrum of the 150 Å quantum well, considering all possible transitions and manually setting the normalized overlap $C_{\alpha\beta}$ to 1, $\hbar\gamma = 8$ meV.

An equivalently incorrect result would be obtained by including all the transitions in

the expression of the dielectric function (3.5), precisely because of the lack of the weighting that we obtain with the coefficients $C_{\alpha\beta}$.

We see therefore that the perfect equivalence between the absorption spectrum calculated by using the semiclassical expression of the dielectric function and the quantum model is achieved only if just consecutive transitions are included and all C coefficients are set to 1.

The applicability of Eq. (3.5) to the single quantum well case is somewhat fortunate, as the transitions that are naturally included in the dielectric function, because they are the most optically relevant, are also the ones that can be mixed with no need of a correct weighting. In the case of more complicated structures, notably for tunnel-coupled quantum wells, it can be more difficult (if not impossible) to identify transitions with these properties and apply Eq. (3.5). We see then the strength of our model, which has no such restrictions, as every contribution is correctly weighted by $C_{\alpha\beta}$. We conclude then that our model can be used to calculate the dielectric response of electron gases confined in arbitrary one-dimensional potentials, unlike Eq. (3.5).

Despite this, Eq. (3.5) is not without interest, as it allows an easy inclusion of non-parabolicity of subbands in the cases in which it can be applied [67].

3.2. Tunnel-coupled quantum wells: tight-binding analysis

In the remaining part of the chapter, we investigate systems of tunnel-coupled quantum wells. Figure 3.14 summarizes the main point made at the end of the previous section. In a single quantum well, the microcurrents overlap coefficients $C_{\alpha\beta}$ between the relevant transitions are almost equal to unity, which establishes the equivalence between the generalized Drude-Lorentz model and the quantum model [panel (a)].

However, the overlap between microcurrents is normally not perfect in the generalized case of systems composed of tunnel-coupled quantum wells, as the one sketched in panel (b), in which intersubband plasmons couplings Ξ are modulated by $C_{\alpha\beta} \neq 1$. As already mentioned, our quantum model is suited for taking into account this aspect of the intersubband plasmon coupling, and can thus be applied to these systems.

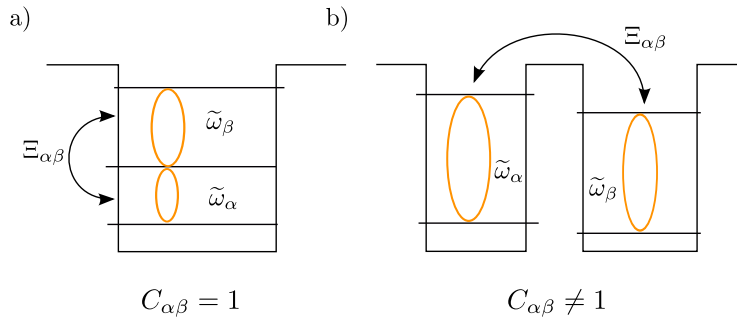


Figure 3.14: Coupling between intersubband plasmons in single (a) and coupled quantum wells (b).

Before presenting the results that can be obtained by means of a numerical procedure, we discuss the coupling through an analytical tight-binding study, in order to get some insight on the role of tunneling in the coefficients $C_{\alpha\beta}$. We consider the same system presented in §1.2, two coupled quantum wells presenting two subbands each, as schematized in Fig. 3.15.

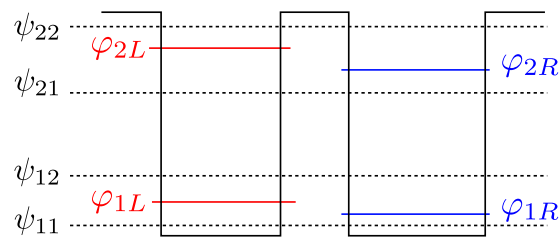


Figure 3.15: Coupled quantum wells: schematization of extended and tight-binding basis.

For sufficiently thick barriers (at least greater than 15 Å), we can approximate the system wavefunctions with

$$\psi_{nm}(z) = L_{nm}\varphi_{nL}(z) + R_{nm}\varphi_{nR}(z)$$

where $n = 1, 2$ indicate the doublet associated with the ground (1) or the excited (2) state, and $m = 1, 2$ indicate respectively the bonding and antibonding state of the doublet (see Fig. 3.15).

We can define a tight-binding version of the microcurrents ξ_{ij} , as schematized in Fig. 3.16.

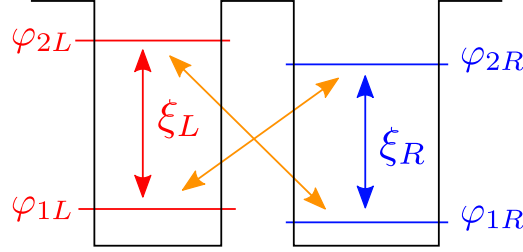


Figure 3.16: Scheme of tight-binding microcurrents in coupled quantum wells.

ξ_L and ξ_R are the microcurrents associated with the $1 \rightarrow 2$ transition in the left and right well, respectively:

$$\begin{aligned}\xi_L(z) &\equiv \xi_{1L,2L}(z) = \varphi_{1L} \frac{\partial \varphi_{2L}}{\partial z} - \varphi_{2L} \frac{\partial \varphi_{1L}}{\partial z} \\ \xi_R(z) &\equiv \xi_{1R,2R}(z) = \varphi_{1R} \frac{\partial \varphi_{2R}}{\partial z} - \varphi_{2R} \frac{\partial \varphi_{1R}}{\partial z}\end{aligned}$$

Besides these, we consider two other possible microcurrents, associated with diagonal transitions $\xi_{1L,2R}$ and $\xi_{1R,2L}$, represented in orange in Fig. 3.16. We neglect intra-doublet microcurrents ξ_{1L1R} and ξ_{2L2R} , corresponding to very low energy transitions not expected to contribute to absorption.

The wavefunctions and microcurrents written on the single well basis can be used to express the microcurrents between levels:

$$\begin{aligned}\xi_{nm,n'm'}(z) &= \psi_{nm} \frac{\partial \psi_{n'm'}}{\partial z} - \psi_{n'm'} \frac{\partial \psi_{nm}}{\partial z} = \\ &= R_{nm} R_{n'm'} \xi_{nR,n'R} + R_{nm} L_{n'm'} \xi_{nR,n'L} + R_{n'm'} L_{nm} \xi_{n'R,nL} + L_{nm} L_{n'm'} \xi_{nL,n'L}\end{aligned}\quad (3.6)$$

Let us consider some examples of formula (3.6). We have for instance:

$$\begin{aligned}\xi_{13} &\equiv \xi_{11,21} = R_{11} R_{21} \xi_R + R_{11} L_{21} \xi_{1R,2L} + L_{11} R_{21} \xi_{2R,1L} + L_{11} R_{21} \xi_L \\ \xi_{14} &\equiv \xi_{11,22} = R_{11} R_{22} \xi_R + R_{11} L_{22} \xi_{1R,2L} + L_{11} R_{22} \xi_{2R,1L} + L_{11} R_{22} \xi_L\end{aligned}$$

Before writing the expression of the plasmon-plasmon coupling in the tight-binding ap-

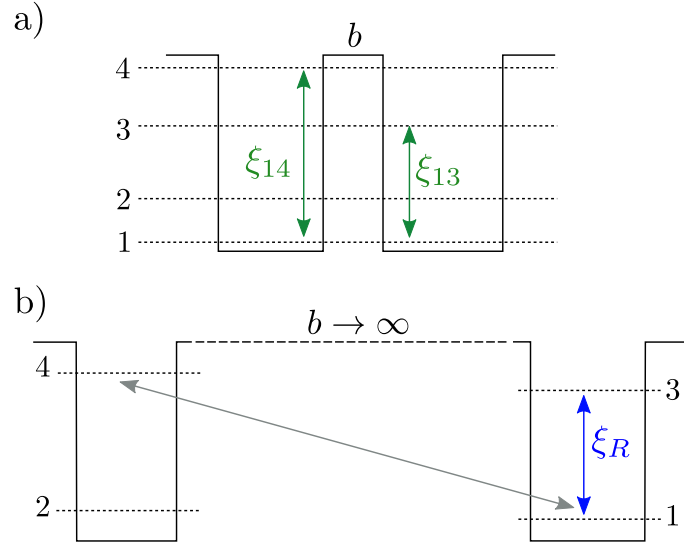


Figure 3.17: a) Microcurrents corresponding to transitions $1 \rightarrow 3$ and $1 \rightarrow 4$, for a finite value of the barrier b . b) Same microcurrents in the limit of very large barrier.

proximation, let us check its validity in the limit of large barriers (uncoupled quantum wells). In this limit, the diagonal microcurrents $\xi_{1L,2R}$ and $\xi_{1R,2L}$ are zero:

$$\begin{aligned}\xi_{13} &= R_{11}R_{21}\xi_R + L_{11}R_{21}\xi_L \\ \xi_{14} &= R_{11}R_{22}\xi_R + L_{11}R_{22}\xi_L\end{aligned}$$

Furthermore, we recall that for $b \rightarrow \infty$

$$\begin{aligned}R_{11} &= 1 & L_{11} &= 0 \\ R_{21} &= 1 & L_{21} &= 0 \\ R_{22} &= 0 & L_{22} &= 1\end{aligned}$$

as shown in Fig. 1.11. All considered, we have

$$\begin{aligned}\xi_{13} &= \xi_R \\ \xi_{14} &= 0\end{aligned}$$

as it would be expected from physical considerations (see Fig. 3.17).

We see from this example that the tight-binding coefficients ensure the correct behaviour of the microcurrents in the limit of large barriers.

3.2.1. Tunnel contribution to plasmon-plasmon coupling

The formalism introduced above can be used to investigate the tunnel contribution to the plasmon-plasmon coupling frequency Ξ , which was introduced in §2.2.5 as

$$\Xi_{ij,kl} = \underbrace{\frac{\omega_{Pij} \omega_{Pkl}}{2\sqrt{\omega_{ij}\omega_{kl}}}}_{\text{plasma effects}} \cdot \underbrace{C_{ij,kl}}_{\text{microcurrents overlap}} \quad (3.7)$$

The coupling $\Xi_{ij,kl}$ is composed of two factors, reflecting its double origin, due the interplay between Coulomb interaction and tunneling. Indeed, the term $\frac{\omega_{Pij}\omega_{Pkl}}{2\sqrt{\omega_{ij}\omega_{kl}}}$ depends on the electronic density through the plasma frequencies $\omega_{Pij}, \omega_{Pkl}$: it is thus mainly the expression of Coulomb interaction. In this term, tunnel interaction enters just through the energies of the levels, while it strongly affects the overlap factor between microcurrents $C_{ij,kl}$.

Recalling Eq. (2.38), the overlap factor can be easily expressed as

$$C_{ij,kl} = \frac{\int_{-\infty}^{+\infty} \xi_{ij}(z) \xi_{kl}(z) dz}{\sqrt{\int_{-\infty}^{+\infty} \xi_{ij}^2(z) dz \int_{-\infty}^{+\infty} \xi_{kl}^2(z) dz}} = \frac{I_{ij,kl}}{\sqrt{I_{ij,ij} I_{kl,kl}}}$$

where we have defined the microcurrent-microcurrent overlap integral² [68]:

$$I_{ij,kl} = \int_{-\infty}^{+\infty} \xi_{ij}(z) \xi_{kl}(z) dz \quad (3.8)$$

By using Eq. (3.6), we obtain

$$\begin{aligned} I_{ij,kl} = & R_i R_j R_k R_l \int_{-\infty}^{+\infty} \xi_{\bar{i}R, \bar{j}R} \xi_{\bar{k}R, \bar{l}R}(z) dz + \\ & + R_i R_j R_k L_l \int_{-\infty}^{+\infty} \xi_{\bar{i}R, \bar{j}R} \xi_{\bar{k}R, \bar{l}L}(z) dz + \\ & \dots \\ & + L_i L_j L_k L_l \int_{-\infty}^{+\infty} \xi_{\bar{i}L, \bar{j}L} \xi_{\bar{k}L, \bar{l}L}(z) dz \end{aligned} \quad (3.9)$$

where we denote with \bar{i} the index of the tunnel doublet to which ψ_i belongs to³. In other words, any current-current overlap $I_{ij,kl}$ can be expressed as a linear combination of the overlap integrals $I_{ij,kl}$ of the localized microcurrents

$$\int_{-\infty}^{+\infty} \xi_L^2(z) dz, \int_{-\infty}^{+\infty} \xi_R^2(z) dz, \int_{-\infty}^{+\infty} \xi_L(z) \xi_R(z) dz, \int_{-\infty}^{+\infty} \xi_{1R,2L}(z) \xi_{1L,2R}(z) dz \dots \quad (3.10)$$

We can study the importance of these components numerically. Let us consider a slightly asymmetric system: two tunnel-coupled GaAs/Al_{0.45}Ga_{0.55}As quantum wells of width 70 and 75 Å. We plot in Fig. 3.18 the values of the components (3.10) for varying values of the coupling barrier.

²Note that $I_{ij,kl}$ is closely related to $S_{ij,kl}$: $S_{ij,kl} = \frac{1}{\hbar\omega_\alpha} \frac{1}{\hbar\omega_\beta} \left(\frac{\hbar^2}{2m^*}\right)^2 I_{ij,kl}$

³We abandon the matricial notation for clarity reasons: to be fully consistent, we should write $\xi_{nm, n'/m'}, R_{nm}, \xi_{nR}$, etc.

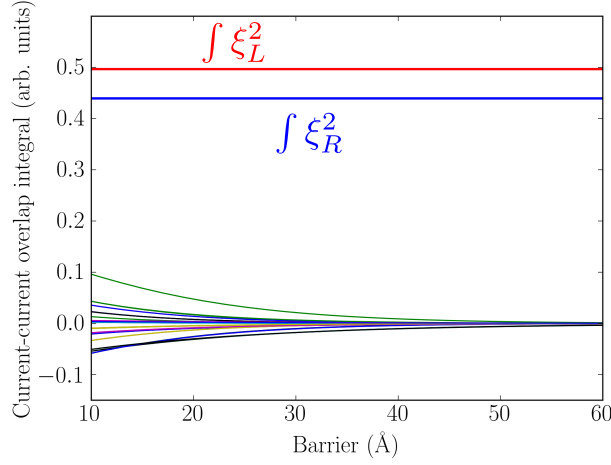


Figure 3.18: Components of the current-current overlap integral on the localized basis for variable barrier b in a $70/b/75$ GaAs/ $\text{Al}_{0.45}\text{Ga}_{0.55}\text{As}$ structure.

From Fig. 3.18 we deduce that the most relevant terms in the decomposition of the extended current-current overlap integral are the terms $\int \xi_L^2$ and $\int \xi_R^2$, i.e. those corresponding to the currents in each well (and thus independent of the barrier thickness). This implies that $I_{ij,kl}$ involving transitions within the same doublet will be small, as their expansion (3.9) does not include these two terms. For transitions between levels of different doublets [in a four-subband well [(14, 23) and (13, 24)] we can approximate

$$\int_{-\infty}^{+\infty} \xi_{ij}(z) \xi_{kl}(z) dz \approx R_i R_j R_k R_l \int_{-\infty}^{+\infty} \xi_R^2(z) dz + L_i L_j L_k L_l \int_{-\infty}^{+\infty} \xi_L^2(z) dz \quad (3.11)$$

Therefore we can write a tight-binding version of the coefficient $C_{ij,kl}$ in terms of left and right current integrals as

$$C_{ij,kl} \approx [C_{ij,kl}]^{\text{TB}} = \frac{\prod_p R_p \int \xi_R^2 dz + \prod_p L_p \int \xi_L^2 dz}{\sqrt{\left(\prod_p R_p \int \xi_R^2 dz\right)^2 + \left(\prod_p L_p \int \xi_L^2 dz\right)^2 + B_{ij,kl} \int \xi_R^2 dz \int \xi_L^2 dz}} \quad (3.12)$$

where $p = i, j, k, l$ and the term B is

$$B_{ij,kl} = (R_i R_j L_k L_l)^2 + (L_i L_j R_k R_l)^2$$

Note that in Eq. (3.12) the barrier dependence is entirely expressed by the tight-binding coefficients L and R , and the only microcurrents included are the ones localized in the left and right well.

Figure 3.19 shows the calculated C coefficients for the couple of transitions (14, 23) and (13, 24) in a $70/b/75$ Å GaAs/Al_{0.45}Ga_{0.55}As structure, both in the extended basis (dashed lines) and with Eq. (3.12) (solid lines). We can appreciate that the tight-binding expansion is a good approximation for barriers thicker than 30 Å. This condition is more restrictive than the validity of tight-binding approximation for wavefunction calculation (see §1.2), for which barriers thicker than ≈ 15 Å are sufficient. This is because each C coefficient depends on four wavefunctions, and consequently deviations from the extended basis are more important than in the single wavefunction case.

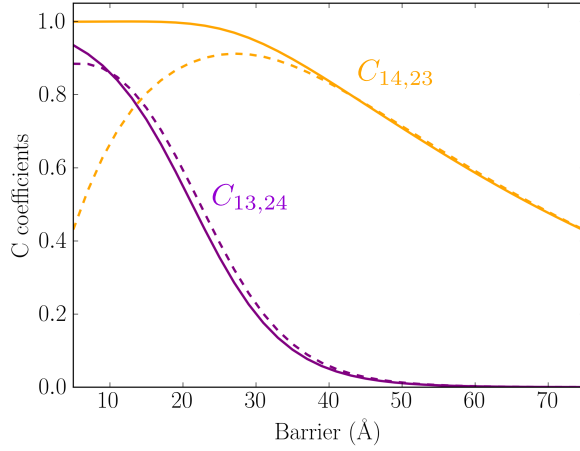


Figure 3.19: Comparison between C coefficients calculated with the tight-binding approximation of Eq. (3.12) (solid lines) and those calculated in the extended basis (dashed lines).

As an example, let us fix the barrier value to 30 Å and consider a $70/30/75$ Å GaAs/Al_{0.45}Ga_{0.55}As structure. We can use the tight-binding expression for C in Eq. (3.12) to calculate the coupling Ξ between intersubband plasmons and consequently obtain the absorption spectra. Figure 3.20 confirms that for this structure the result in tight-binding approximation (orange line) is very close to the one obtained through the full model (black line).

In the situation above, the tight-binding expansion makes it possible to describe tunneling through the coefficients R_i and L_i appearing in Eq. (3.12). However, the conditions for this approximation to be valid are the thickness of the barrier (see Fig. 3.19) and the fact that just two subbands are occupied. We will see in the following that interesting phenomena occur out of these restrictions, and especially for thin barriers. A full numerical implementation of our quantum model will allow us to study these cases.

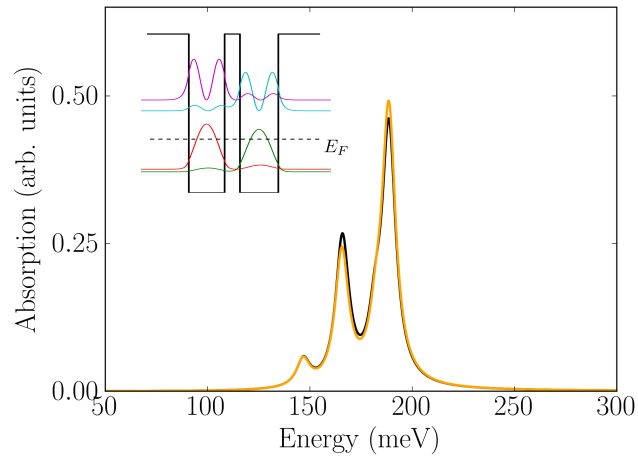


Figure 3.20: Calculated absorption spectrum for a GaAs/Al_{0.45}Ga_{0.55}As 70/30/75 Å structure (shown in inset), $N_V = 3 \times 10^{18} \text{ cm}^{-3}$, full model (black line) and in tight-binding approximation (orange line), $\hbar\gamma = 8 \text{ meV}$.

3.3. Two tunnel-coupled asymmetric quantum wells

We consider as a second application of our model the calculation of the absorption spectrum for a system of two tunnel-coupled GaAs/Al_{0.45}Ga_{0.55}As quantum wells (81/30/23 Å). Figure 3.21(a) presents the band diagram and the square moduli of the wavefunctions

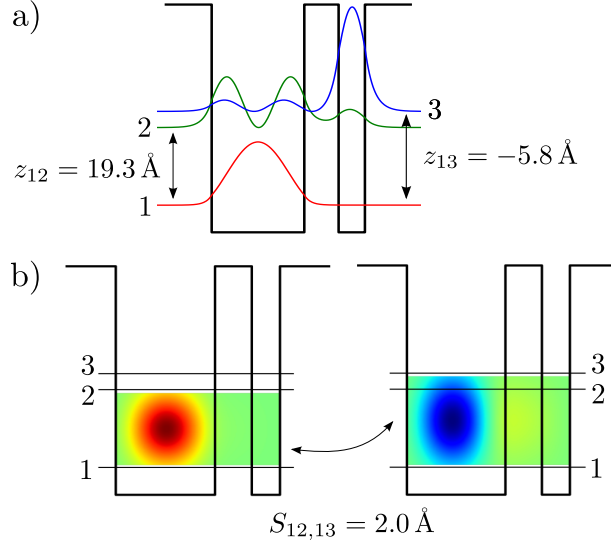


Figure 3.21: a) Calculated band structure for coupled GaAs/Al_{0.45}Ga_{0.55}As quantum wells, with dimensions (in Å) 81/30/23. b) Calculated microscopic current densities $\xi_{i,j}$ for the two possible transitions 1→2 and 1→3.

in this system. The values of the dipole matrix elements are also reported: as the 1-3 transition is diagonal in the real space, its dipole is 70% lower than the one of the 1-2 vertical transition. Panel (b) presents the microscopic current densities (normalized to their maximum amplitude) of the 1-2 and 1-3 transitions. They are mostly localized in the largest quantum well. As a consequence, their Coulomb length is non negligible, resulting in an overlap factor close to one in modulus ($C_{12,13} = -0.95$).

3.3.1. Tight-binding analysis

Before presenting the numerical results obtained by using our model, let us apply to this system the tight-binding approach presented in the previous section. In this framework, we schematize the structure as shown in Fig. 3.22.

The extended wavefunctions can be written as

$$\begin{aligned}\psi_1 &= L_1\varphi_{1L} + R_1\varphi_{1R} = \varphi_{1L} & (L_1 = 1, R_1 = 0) \\ \psi_2 &= L_2\varphi_{1L} + R_2\varphi_{1R} \\ \psi_3 &= L_3\varphi_{2L} + R_3\varphi_{2R}\end{aligned}$$

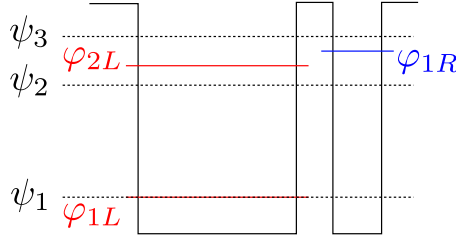


Figure 3.22: Coupled asymmetric quantum wells: schematization of extended and tight-binding basis.

Consequently microcurrents are:

$$\begin{aligned}\xi_{12} &= L_2 \xi_{1L2L} + R_2 \xi_{1L2R} \\ \xi_{13} &= L_3 \xi_{1L2L} + R_3 \xi_{1L2R}\end{aligned}$$

Let us suppose that just the first subband is occupied. As before, we use the expressions above to write the current-current overlap integrals for the two relevant transitions, $1 \rightarrow 2, 1 \rightarrow 3$:

$$\begin{aligned}I_{12,13} &= L_2 L_3 \int \xi_{1L2L}^2(z) dz + (L_2 R_3 + R_2 L_3) \int \xi_{1L2L}(z) \xi_{1L2R}(z) dz + \\ &\quad + R_2 R_3 \int \xi_{1L2R}^2(z) dz\end{aligned}$$

$$I_{12,12} = \int \xi_{12}^2(z) dz = L_2^2 \int \xi_{1L2L}^2(z) dz + R_2^2 \int \xi_{1L2R}^2(z) dz + 2L_2 R_2 \int \xi_{1L2L}(z) \xi_{1L2R}(z) dz$$

$$I_{13,13} = \int \xi_{13}^2(z) dz = L_3^2 \int \xi_{1L2L}^2(z) dz + R_3^2 \int \xi_{1L2R}^2(z) dz + 2L_3 R_3 \int \xi_{1L2L}(z) \xi_{1L2R}(z) dz$$

Figure 3.23, analogous to Fig. 3.18, shows that in the validity range of the tight-binding approximation (barriers thicker than 30 Å), the left current integral $\int \xi_{1L2L}^2$ is the most relevant component of the expansion over the tight-binding current integrals. Then the tight-binding expansion of the $C_{12,13}$ coefficient $C_{12,13} = \frac{I_{12,13}}{\sqrt{I_{12,12} I_{13,13}}}$ reduces to

$$C_{12,13}^{\text{TB}} = \frac{L_2 L_3 \int \xi_{1L2L}^2(z) dz}{\sqrt{\left[L_2^2 \int \xi_{1L2L}^2(z) dz \right] \left[L_3^2 \int \xi_{1L2L}^2(z) dz \right]}} = \frac{L_2 L_3}{|L_2 L_3|} = -1 \quad (3.13)$$

Figure 3.24 presents the calculated $C_{12,13}$ coefficient and $\Xi_{12,13}$ coupling in the extended basis, in the case of the structure presented in Fig. 3.21(a). It can be observed that for wide barriers the coefficient $C_{12,13}$ tends indeed to -1. Note, however, that the overall coupling $\Xi_{12,13}$ goes to zero for increasing values of the barrier, because of the plasma term [see Eq. (3.7)]. As it could be expected, the two transitions interaction is negligible when the spatial separation becomes too large.

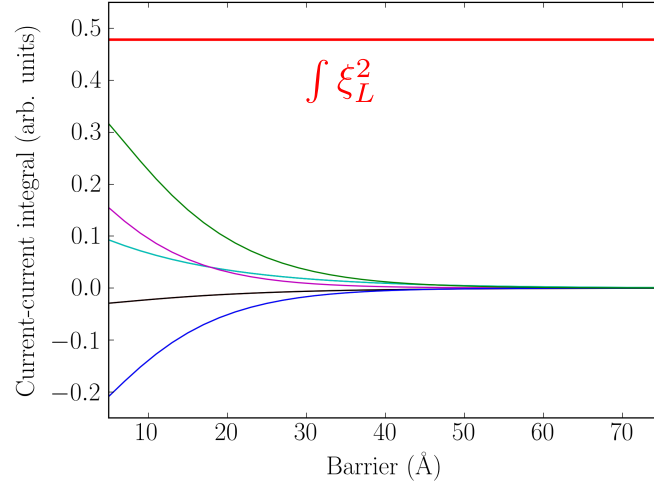


Figure 3.23: Current-current overlap integral components for variable barrier b in an asymmetric coupled quantum wells structure.

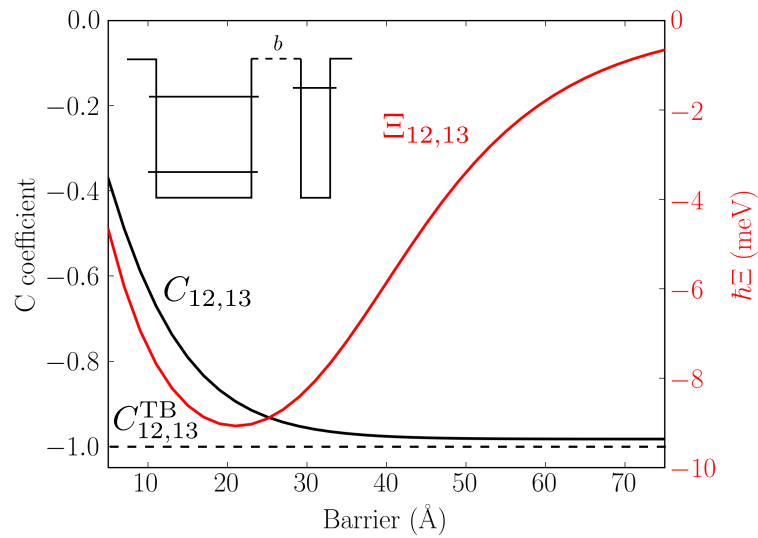


Figure 3.24: Calculated $C_{12,13}$ and $\Xi_{12,13}$ in extended basis in a GaAs/Al_{0.45}Ga_{0.55}As structure $81/b/23$ (Å), with doping $N_S = 2.4 \cdot 10^{12} \text{ cm}^{-2}$, for variable values of the barrier b . The tight-binding result of Eq. 3.13 is represented with the black dashed line.

The above tight-binding analysis, along with that of the previous section, allows understanding the emergence of tunnel coupling between plasmons starting from the wavefunctions of the individual quantum wells. However, it is not a good approximation for thin barriers, and its generalization to quantum wells with several occupied subbands is complicated. In the following, we will thus focus on the application of the exact quantum model to describe the tunnel coupling between plasmons.

3.3.2. Numerical results

The single-particle absorption spectrum corresponding to the 81/30/23 Å structure with only one occupied subband is presented in Fig. 3.25(a). It shows that, in this picture, the interaction with light is almost completely concentrated in the 1-2 transition peak, due to the difference in the dipole matrix elements between the vertical and the diagonal transition.

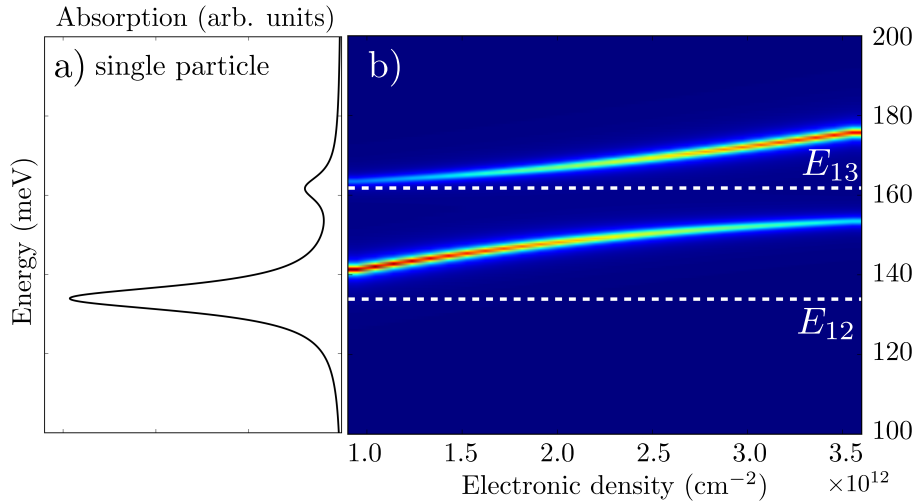


Figure 3.25: a) Calculated absorption spectrum for the coupled well structure presented in Fig. 3.21(a) in the single-particle picture, $\hbar\gamma = 8$ meV. b) Calculated absorption spectrum with our model for different values of electronic densities on the first subband.

The absorption spectrum calculated by using our model is shown in Fig. 3.25(b), in color scale, as a function of the electronic density in the first subband. The single-particle transition energies are indicated by dashed lines. It is apparent that, with the increasing electronic density, dipole-dipole Coulomb interaction redistributes the absorption amplitude between two peaks, at different energies with respect to the single-particle ones. In particular, for a density 2.4×10^{12} cm $^{-2}$ the two peaks have the same amplitude. The absorption spectrum calculated for this electronic density is presented in Fig. 3.26(a) (red line) and compared to the single-particle one (black line).

The activation of the 1-3 transition, almost dark in single-particle picture, can be seen as the result of its coupling with the higher dipole 1-2 transition.

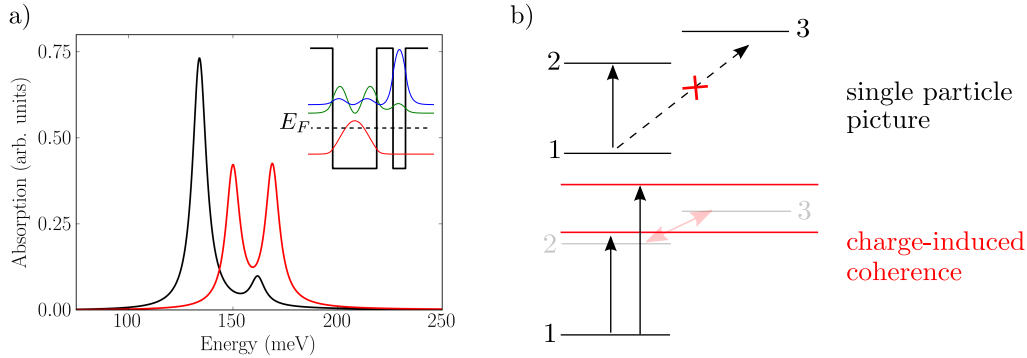


Figure 3.26: a) Absorption spectrum calculated by using our model with $N_S = 2.4 \times 10^{12} \text{ cm}^{-2}$ (red line), compared with the single-particle absorption spectrum (black line), $\hbar\gamma = 8 \text{ meV}$. Inset: calculated band structure for coupled GaAs/Al_{0.45}Ga_{0.55}As quantum wells, with dimensions (in AA) 81/30/23. b) Level energies schematization of the charge-induced coherence between level 2 and 3, reminiscent of the Autler-Townes effect.

3.3.3. Laser-free Autler-Townes effect

The activation of the weak 1-3 transition is reminiscent of the Autler-Townes effect. The latter is a general quantum-mechanical effect observed in three-level quantum systems (cascade, lambda, or vee configurations) presenting an allowed 1-2 and a forbidden 1-3 transition [77, 78, 80].

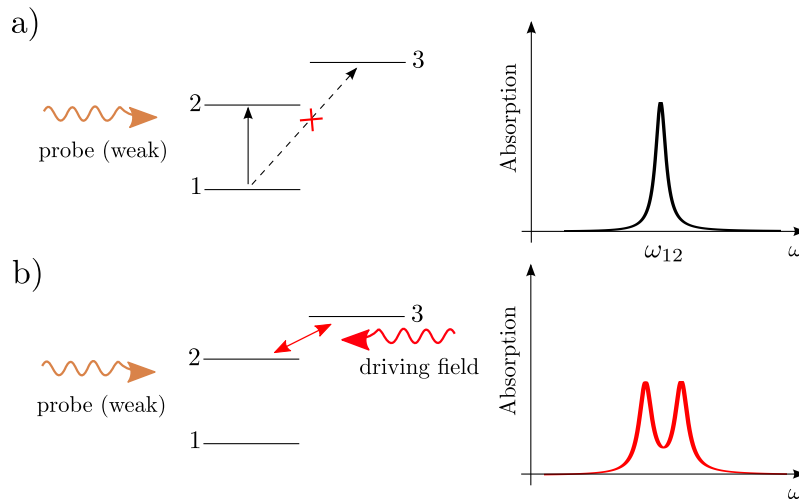


Figure 3.27: Schematization of the Autler-Townes effect, a) absorption b) absorption when an external driving field close to frequency ω_{23} is applied, and a doublet appears.

Figure 3.27 sketches the basics of the formation of the so-called Autler-Townes doublet (also known as dynamic Stark splitting) in a vee three-level system. When an intense and coherent coupling field at a frequency close to that of the 2-3 transition is shone on the

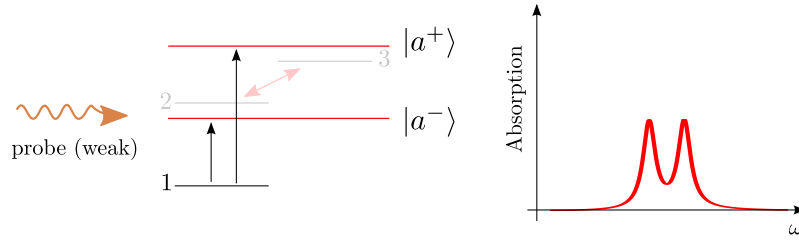


Figure 3.28: Schematization of the dressed-states description of the Autler-Townes doublet.

system, the absorption of a second probe field (weak) presents a splitting, as schematized in Fig. 3.27(b). This phenomenon was first observed in 1955 by Autler and Townes in the particular case of a microwave transition of an OCS molecule [77]. However, features of the Autler-Townes effect emerge in many different systems, among which quantum wells [78, 81, 82].

The appearance of a doublet can be understood in a quantum treatment that deals with the total coupled system 'atom + external field', called dressed-atom approach [83]. In this picture, the external coupling field induces an interaction between levels 2 and 3. The field coherence confers a bright component to the originally dark transition $1 \rightarrow 3$, so that a doublet can be observed, due to the excitation to the states $|a^+\rangle$ and $|a^-\rangle$, dressed by the coherent field (Fig. 3.28).

The splitting observed in the absorption spectrum in Fig. 3.26(a) can thus be seen as the signature of a laser-free Autler-Townes effect, in which the external coupling field is replaced by the charge-induced coherence [see Fig. 3.26(b)].

3.3.4. Variable external electric field

Another way to modify the coupling between intersubband plasmons in this system is to apply a uniform electric field along the growth direction. Figure 3.29 presents in color plot the calculated absorption spectra for an external field ranging from -40 kV/cm to 30 kV/cm. The electronic density is kept fixed at $N_S = 2.4 \times 10^{12} \text{ cm}^{-2}$.

Some of these spectra are shown explicitly in Fig. 3.30. The application of an electric field moves the two intersubband plasmons in and out of coupling: the two are resonant at $F = 0 \text{ kV/cm}$. We note that the tunnel coupling between the wavefunctions (corresponding to a peak doublet in the single-particle absorption spectrum) occurs at a completely different field value, $F = -26 \text{ kV/cm}$. This is yet another proof that collective effects create in the system new entities that are completely unrelated to the single-particle vision.

In Fig. 3.31, the values of $C_{12,13}$ and $\Xi_{12,13}$ are plotted for varying electric field. The value that maximises the coupling frequency $\Xi_{12,13}$ ($\approx -20 \text{ kV/cm}$) does not coincide with the value for which the plasmons are maximally coupled, 0 kV/cm . To study this point,

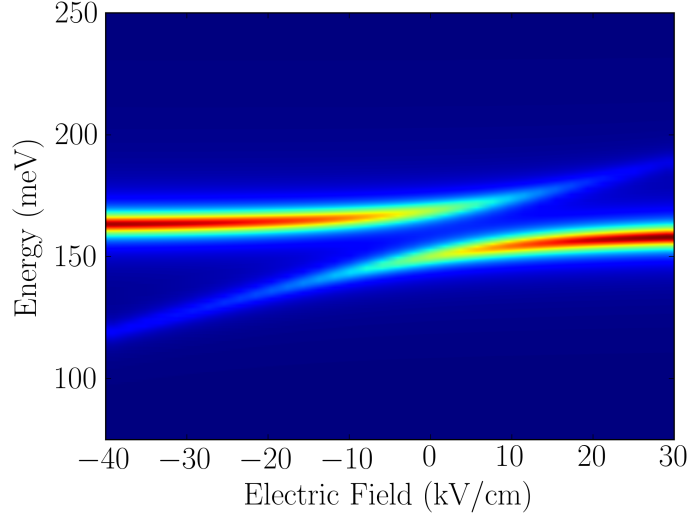


Figure 3.29: Calculated absorption spectra for the 81/30/23 Å GaAs/Al_{0.45}Ga_{0.55}As structure, for variable applied electric field, $N_S = 2.4 \times 10^{12} \text{ cm}^{-2}$.

we recall the tight-binding analysis, and express our problem through the Hopfield matrix

$$\mathbf{M} = \begin{pmatrix} \tilde{\omega}_{12} & [\Xi_{12,13}]^{\text{TB}} \\ [\Xi_{12,13}]^{\text{TB}} & \tilde{\omega}_{13} \end{pmatrix} \quad (3.14)$$

with $[\Xi_{12,13}]^{\text{TB}}$ only depending on the plasma and transition energies, as the overlap factor C is ≈ -1 . From the form of (3.14), it is clear that another element contributing to the final absorption response, apart from the coupling strength, is the detuning between the energies of the intersubband plasmons $\tilde{\omega}_{12}$ and $\tilde{\omega}_{13}$. Finally, the amplitudes $W_n F_n$ of the absorption peaks depend not only on the eigenvectors of \mathbf{M} (through $X_{\alpha n}$) but also on single-particle quantities (see §2.2.6):

$$W_n F_n = W_n \left| \sum_{\alpha} \sqrt{\Delta N_{\alpha}} \sqrt{\frac{\omega_{\alpha}}{\tilde{\omega}_{\alpha}}} z_{\alpha} X_{\alpha n} \right|^2$$

These observations suggests that, even in this simple system, the coupling between plasmons is the result of the interplay of many components and it cannot be simply accounted for by the quantity Ξ .

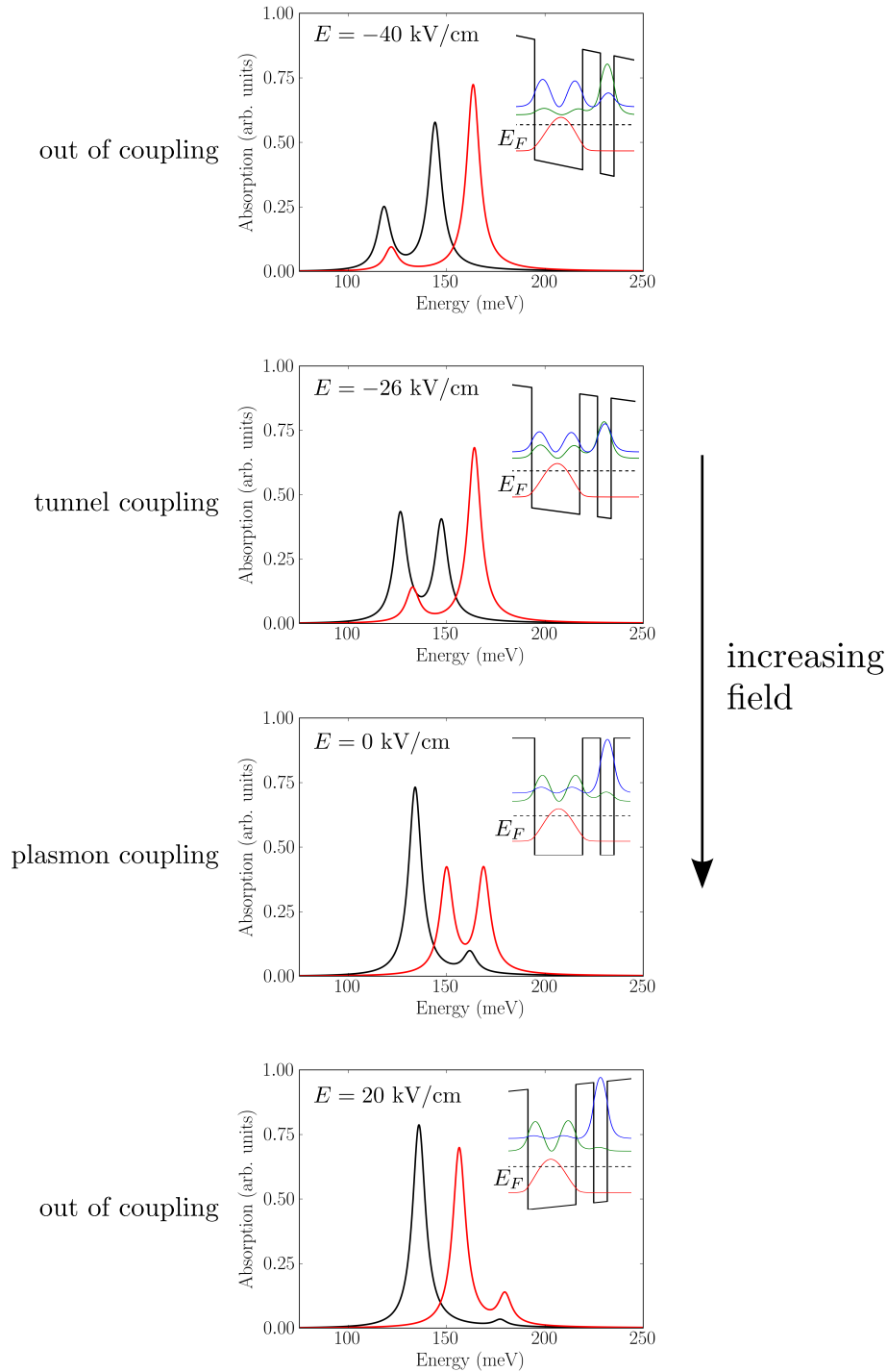


Figure 3.30: Selected spectra from those composing Fig. 3.29 (red lines) for varying applied electric field. The black curves represent the corresponding single-particle spectra.

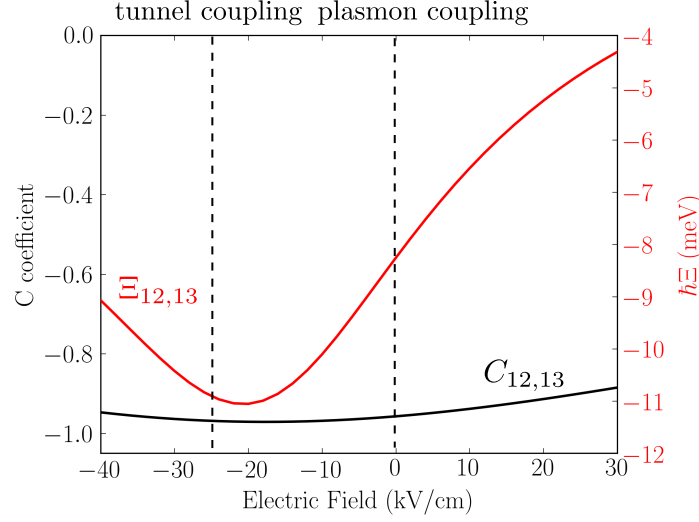


Figure 3.31: Calculated $C_{12,13}$ and $\Xi_{12,13}$ in a GaAs/Al_{0.45}Ga_{0.55}As structure 81/30/23 (Å), with doping $N_S = 2.4 \cdot 10^{12} \text{ cm}^{-2}$, for variable applied external electric field.

3.3.5. Comparison with the absorption spectrum in time-dependent perturbation theory

Only two transitions are involved in the asymmetric structure under consideration. This allows the application of the approach derived by Allen et al. by using time-dependent perturbation theory for the case of one occupied subband and two possible final states in an inversion layer [47]. Therefore, we are able to compare the absorption spectrum predicted by our model with the one calculated by using the expression [47]:

$$\begin{aligned}
 \text{Abs}(\omega) &= \frac{N_s e^2}{\epsilon_0 \epsilon \hbar} \omega^2 \times \\
 &\times \left[\frac{\omega_{12} \gamma_{12}}{\hbar} \frac{(z_{12} H_3 - z_{13} \bar{\omega}_{32}^2)^2 + |z_{12}|^2 \left(\frac{\omega_{13} \gamma_{13}}{\hbar} \right)^2}{\left(H_2 H_3 - \frac{\omega_{12} \gamma_{12} \omega_{13} \gamma_{13}}{\hbar^2} - \bar{\omega}_{23}^2 \bar{\omega}_{32}^2 \right)^2 + \left(H_2 \frac{\omega_{13} \gamma_{13}}{\hbar} + H_3 \frac{\omega_{12} \gamma_{12}}{\hbar} \right)^2} + \right. \\
 &\left. + \frac{\omega_{23} \gamma_{23}}{\hbar} \frac{(z_{13} H_2 - z_{12} \bar{\omega}_{23}^2)^2 + |z_{13}|^2 \left(\frac{\omega_{12} \gamma_{12}}{\hbar} \right)^2}{\left(H_2 H_3 - \frac{\omega_{12} \gamma_{12} \omega_{13} \gamma_{13}}{\hbar^2} - \bar{\omega}_{23}^2 \bar{\omega}_{32}^2 \right)^2 + \left(H_2 \frac{\omega_{13} \gamma_{13}}{\hbar} + H_3 \frac{\omega_{12} \gamma_{12}}{\hbar} \right)^2} \right] \quad (3.15)
 \end{aligned}$$

where

$$\begin{aligned}
 H_i(\omega) &= \omega_{1i}^2 + \bar{\omega}_{ii}^2 - \omega^2 \\
 \bar{\omega}_{ij}^2 &= \frac{2N_s e^2}{\epsilon_0 \epsilon \hbar} \omega_{1i} S_{1i,1j}
 \end{aligned}$$

With these definitions, $\bar{\omega}_{22} = \omega_{P12}$ and $\bar{\omega}_{33} = \omega_{P13}$. The mixed terms $\bar{\omega}_{23}$ and $\bar{\omega}_{32}$, instead, couple transitions $1 \rightarrow 2$ and $1 \rightarrow 3$.

The normalized spectrum resulting from Eq. (3.15) is shown in blue in Fig. 3.32.

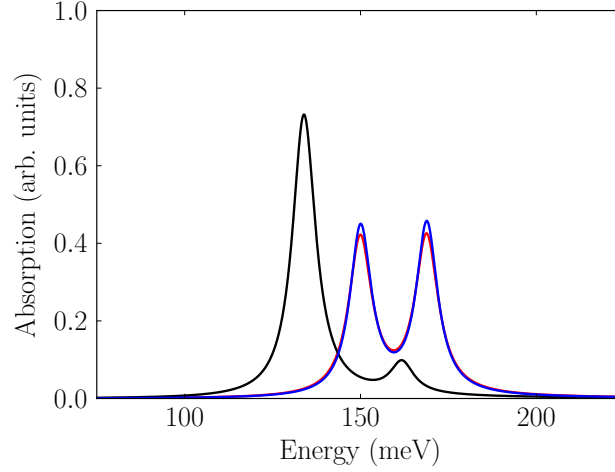


Figure 3.32: Calculated absorption spectra for structure of Fig. 3.21, normalized. Black line: single-particle picture. Red line: our model, $\hbar\gamma = 8$ meV. Blue line: Eq. (3.15), result from time-dependent perturbation theory.

We observe an excellent agreement between the two independent approaches, and are thus motivated to apply our method to more complicated systems, for which Eq. (3.15) would be difficult to generalize.

3.4. Tunnel coupling between multisubband plasmons

In order to further investigate the role of tunneling in the presence of Coulomb interaction, we study the optical response of highly doped quantum wells with several occupied subbands coupled through a barrier.

3.4.1. Two identical highly doped quantum wells

Let us consider two tunnel-coupled GaAs quantum wells, each of thickness $L = 150 \text{ \AA}$, identical to that presented in §3.1, separated by a $\text{Al}_{0.45}\text{Ga}_{0.55}\text{As}$ barrier, as shown in Fig. 3.33. The quantum wells are uniformly doped with an electronic density $N_S = 2.1 \times 10^{13} \text{ cm}^{-2}$ ($N_V = 7 \times 10^{18} \text{ cm}^{-3}$).

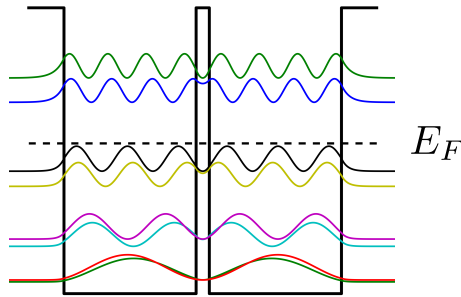


Figure 3.33: Calculated band structure for two 150 \AA GaAs/ $\text{Al}_{0.45}\text{Ga}_{0.55}\text{As}$ quantum wells separated by a 15 \AA barrier, $N_S = 2.1 \times 10^{13} \text{ cm}^{-2}$ ($N_V = 7 \times 10^{18} \text{ cm}^{-3}$).

Two different lengths determine the properties of the system: the wavefunction extension in the barrier and the length of dipole-dipole interaction between intersubband plasmons. Our model allows the calculation of the optical properties of the electron gas by including these two characteristic lengths. Tunnel coupling is taken into account by considering the single-particle eigenstates of the coupled well system, while charge-induced coherence is included by calculating the coupling between all the intersubband plasmons associated with the transitions between extended states.

The main panel of Fig. 3.34 presents the calculated absorption (in color scale) as a function of the energy and of the barrier thickness, for a constant doping $N_V = 7 \times 10^{18} \text{ cm}^{-3}$. In the limit of a large barrier, the absorption spectrum of a single well of thickness L (presented in the right panel) is recovered. This is characterized by a main bright mode at energy E_L , indicated by a dashed white line. In the opposite limit, for a barrier thickness approaching zero, the spectrum shown in the left panel is obtained, which presents a single resonance at energy E_{2L} . Note that $E_{2L} < E_L$, as expected from the study of §3.1.3, because the intersubband contribution to the total multisubband plasmon energy is lower in the wider well.

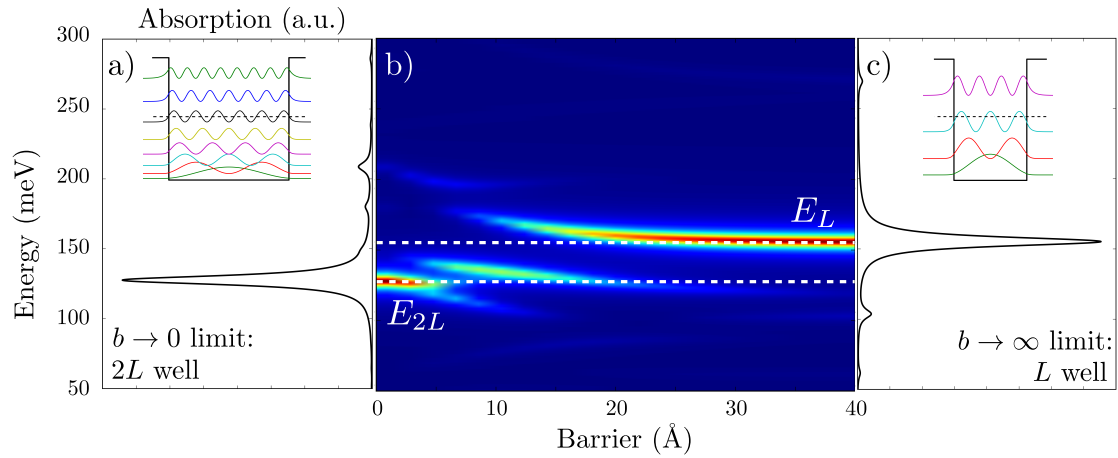


Figure 3.34: Calculated absorption spectra for a 300 Å [panel (a)] and 150 Å [panel (c)] GaAs/Al_{0.45}Ga_{0.55}As quantum well, $\hbar\gamma = 8$ meV. Inset: Band diagram and square moduli of the wavefunctions in the structure. b) Calculated absorption spectrum for a GaAs/Al_{0.45}Ga_{0.55}As structure 15/b/15 (in nm) for different values of the coupling barrier.

In Fig. 3.34(b) one can notice that for barrier thicknesses between 10 Å and 20 Å two absorption resonances with comparable amplitudes are observed. Interestingly, their energies present only a slight variation with the barrier thickness and stay close to E_L and E_{2L} .

In order to understand the microscopic origin of these resonances and the role of tunneling, let us fix the barrier thickness at 15 Å. The calculated band diagram and the square moduli of the wavefunctions are presented in Fig. 3.35(d), showing the electronic doublets resulting from tunnel coupling. The absorption spectrum is presented in Fig. 3.35(c), reporting two bright multisubband modes of comparable absorption amplitude. Their closeness to the energies E_L and E_{2L} (indicated by dashed lines) suggests that tunneling affects multisubband plasmons of adjacent quantum wells in an unconventional way. Instead of giving rise to a doublet around the uncoupled energy (E_L), it produces the coexistence of two single-well multisubband plasmons, one due to a $L = 150$ Å well and the other to a $2L = 300$ Å well.

This observation is reinforced by the spatial distribution of the collective currents $J_n(z)$, shown in Fig. 3.36. The current associated with the peak at E_L is composed of two lobes, localized in the individual quantum well. The multisubband current relative to the E_{2L} peak still has two lobes, but in this case it is non zero also in the barrier.

The figure also indicates the effective lengths calculated for the two multisubband plasmons, representing the extension of the corresponding polarization. For the lower energy peak $L_1^{\text{eff}} = 279.2$ Å, $\approx 93\%$ of the width $2L$. For the higher energy peak we find $L_2^{\text{eff}} = 250.8$ Å; if we consider the presence of a zero in the spatial extension of the collective microcurrent, we can divide this number by two and find $\bar{L}_2^{\text{eff}} = 125.4$ Å, corresponding to $\approx 84\%$ of the width L .

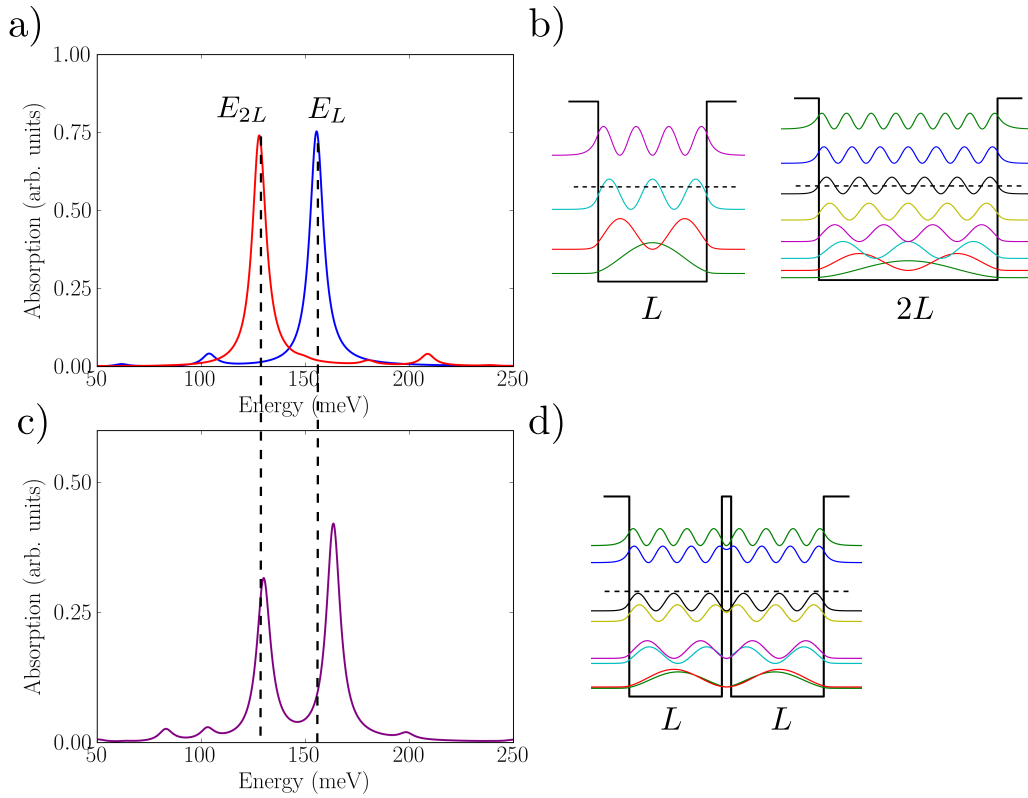


Figure 3.35: a) Calculated absorption spectra of a 150 Å (blue line) and 300 Å (red line) GaAs/Al_{0.45}Ga_{0.55}As quantum well, $N_V = 7 \times 10^{18} \text{ cm}^{-3}$, $\hbar\gamma = 8 \text{ meV}$. b) Calculated band structures and squared moduli of the wavefunctions for the two wells c) Calculated absorption spectra of GaAs/Al_{0.45}Ga_{0.55}As quantum wells of structure 150/15/150 Å, $N_V = 7 \times 10^{18} \text{ cm}^{-3}$, $\hbar\gamma = 8 \text{ meV}$. d) Calculated band structures and squared moduli of the wavefunctions.

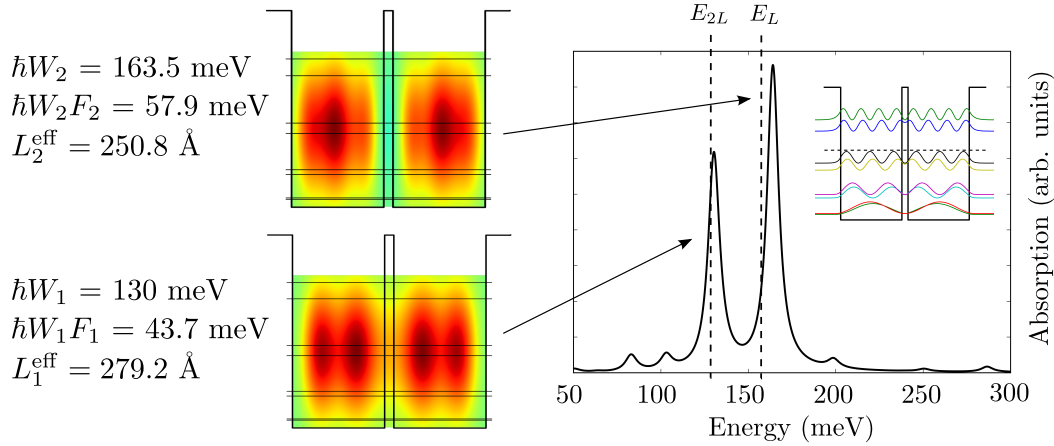


Figure 3.36: On the right, calculated absorption spectrum for coupled GaAs/Al_{0.45}Ga_{0.55}As quantum wells of structure 150/15/150 Å, $N_V = 7 \times 10^{18} \text{ cm}^{-3}$, $\hbar\gamma = 8 \text{ meV}$. The vertical dashed lines indicate the resonances of quantum wells of width L (150 Å) and $2L$ (300 Å). Inset: band diagram and squared moduli of the wavefunctions in the structure. On the left, spatial distribution of microscopic collective currents corresponding to the two resonances (arbitrary units for the color scale). Also shown are the resonance energies $\hbar W_n$, the effective oscillator strengths $\hbar W_n F_n$, and the effective lengths L_n^{eff} .

The coexistence of the two absorption peaks is limited to a very short range of barrier thicknesses, between ≈ 10 and 20 Å . In fact, when the barrier is thin (below $\approx 5 \text{ Å}$) the wavefunctions of the quantum well of thickness $2L$ are only perturbatively modified. In the opposite limit, for barriers thicker than 20 Å , the influence of tunneling, still present on the shape of the wavefunctions, cannot be seen in the absorption spectrum. This is the result of two different contributions. Firstly, it is a manifestation of the oscillator strength transfer in favour of the high energy mode E_L , as already discussed in previous sections. Secondly, the coupling between microscopic current densities involves four wavefunctions [see the expression of $C_{\alpha\beta}$, Eq. (2.46)], while the tunnel coupling results from the overlap between two wavefunctions, so it is reasonable to expect the coupling C to be more sensitive to a change in the barrier width.

3.4.2. Coupling between active transitions

The results of the previous paragraphs are obtained by including all the possible transitions in the diagonalization procedure. As a matter of fact, the dimension of the problem can be reduced by restricting the calculation to the optically active transitions, i.e. those between levels with different symmetry. Considering that each tunnel doublet contains a symmetric and an antisymmetric component, in our structure there are six of these transitions, namely (numbering levels from bottom to top) (1, 4), (2, 3), (3, 6), (4, 5), (5, 8) and (6, 7) (see also the tight-binding discussion of §3.2).

The red line in Fig. 3.37(a) is the result of a reduced calculation based on the six transitions, whose oscillator strengths and intersubband plasmon frequencies $\tilde{\omega}_\alpha$ are reported in Table 3.5. It can be appreciated that this reduced problem gives a solution which perfectly reproduces the main features of the full calculation [black line in Fig. 3.37(a)].

α	(i,j)	f_α	$\hbar\tilde{\omega}_\alpha$ (meV)
1	(1, 4)	0.6609	68.97
2	(2, 3)	1.275	58.85
3	(3, 6)	1.04	117.3
4	(4, 5)	2.752	94.85
5	(5, 8)	1.233	156.3
6	(6, 7)	4.372	109.5

Table 3.5: Calculated parameters for the six effective transitions of the tunnel-coupled symmetric structure.

The couplings $\hbar\Xi$ between the six intersubband plasmons are all different from zero, and comprised between 7 and 19 meV. Note that despite this uniformity of couplings, the system does not have a unique collective resonance like in the case of a single quantum well. The reason for this lies in the values of the intersubband plasmon energies $\hbar\tilde{\omega}_\alpha$. As it can be seen from Table 3.5, one of the active transitions ($5 \rightarrow 8$) has a much higher energy than the other five. Indeed, a calculation including just these five yields a spectrum with a unique peak [orange line in Fig. 3.37(b)], close to the lower energy peak of the full calculation (black line). The peak associated to $5 \rightarrow 8$ is instead closer to the high energy peak. In this picture, the full spectrum can be seen as the result of the coupling between an higher energy intersubband plasmon and a multisubband plasmon.

3.4.3. Increasing quantum well width

To conclude this study, let us consider two larger quantum wells, 500Å wide. It is visible in Fig. 3.38 that for these values of well thickness the absorption spectrum of the coupled wells (purple line) is not remarkably different from those of a 500 (blue line) and 1000 Å (red line) quantum wells. Once again, the reason for this lies in the composition of the energy of the multisubband plasmon (2.13):

$$E_{\text{MSP}} = \sqrt{E_{\text{ISB}}^2 + E_P^2}$$

For wide quantum wells, the energy separation between the electronic levels becomes so small [see Fig. 3.38(b)] that the intersubband part E_{ISB} gives no contribution. With no intersubband component, the effect of tunneling is also negligible.

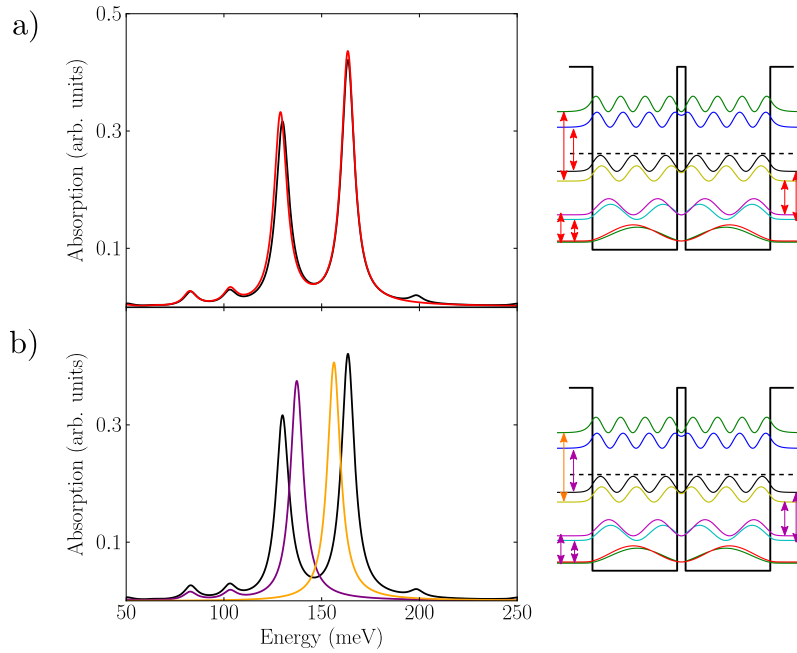


Figure 3.37: a) Left: Absorption spectra for coupled GaAs/ $\text{Al}_{0.45}\text{Ga}_{0.55}\text{As}$ quantum wells of structure $150/15/150 \text{ \AA}$, $N_V = 7 \times 10^{18} \text{ cm}^{-3}$, $\hbar\gamma = 8 \text{ meV}$. Black line: full calculation, as in Fig. 3.35(b). Red line: calculation considering just the six optically active transitions. Right: Band structure and squared moduli of wavefunctions, with red arrows indicating the transitions under consideration. b) Left: Same as above, with purple line: calculation considering transitions (1, 4), (2, 3), (3, 6), (4, 5) and (6, 7); orange line: calculation considering just transition (5, 8).

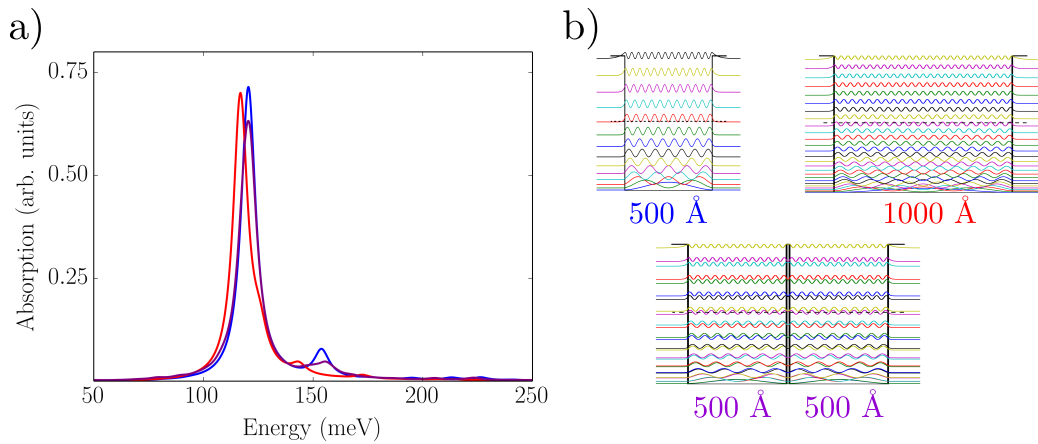


Figure 3.38: a) Calculated absorption spectra of a 500 \AA (blue line), 1000 \AA (red line) and $500/15/500 \text{ \AA}$ (purple line) GaAs/ $\text{Al}_{0.45}\text{Ga}_{0.55}\text{As}$ structure, with $\hbar\gamma = 8 \text{ meV}$ b) Calculated band structures and squared moduli of the wavefunctions for the three structures.

3.4.4. Comparison with the experimental spectrum

In order to experimentally confirm the tunnel coupling between multisubband plasmons, we designed a InGaAs/InAlAs structure, with thicknesses (in Å) 155/15/155, shown in Fig. 3.39.

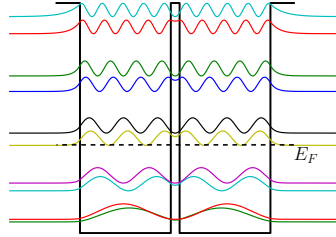


Figure 3.39: Calculated band structure and squared moduli of wavefunctions of a InGaAs/InAlAs structure, 155/15/155 Å, $N_V = 3.3 \times 10^{18} \text{cm}^{-3}$ ($N_S = 1.0 \times 10^{13} \text{cm}^{-2}$).

The sample has been grown by Isabelle Sagnes et Grégoire Beaudoin at the Laboratoire de Photonique et de Nanostructures (Marcoussis) by MOCVD. The absorption spectrum has been measured by Baptiste Dailly in our team, through a transmission experiment at the Brewster angle at room temperature.

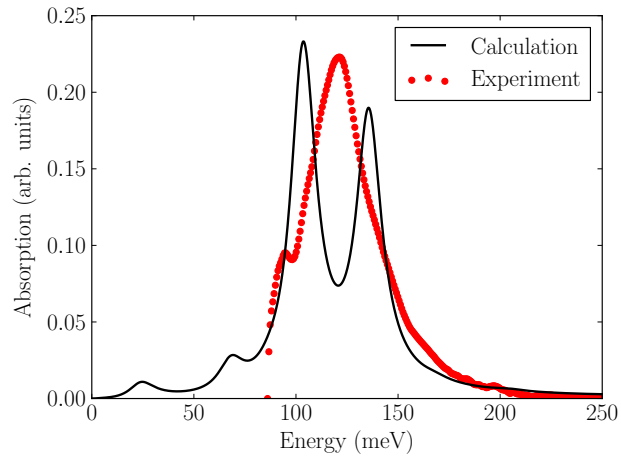


Figure 3.40: Experimental absorption spectrum obtained from a transmission experiment at Brewster angle (red dots) for the coupled wells structure presented in Fig. 3.39. The calculated spectrum (black line) is shown for comparison, in which a phenomenological broadening $\hbar\gamma = 15 \text{ meV}$ was considered. The experimental measurement was performed by Baptiste Dailly.

Figure 3.40 presents the experimental spectrum (red dots) along with the theoretical

calculation (black line). A single broad peak instead of the two expected peaks is observed. This is an indication of the fact that a disorder in the structure could have strongly affected the tunnel and charge induced coherence.

Indeed, by studying the band diagram, we can notice that the lowest-energy doublet presents an energy separation of ≈ 5 meV. This value is smaller than the typical linewidth of intersubband transitions induced by disorder, which can originate from interface roughness, non uniform distribution of charge, etc. The disorder in the structure can be at the origin of the localization of wavefunctions.

An easy way to simulate this localization is to apply an electric field. We can then calculate the absorption spectra under different values of applied external field, to try to reproduce the experimentally observed spectrum. Figure 3.41 shows that a variation of the electric field applied to the structure produces changes in the absorption shape. We represent in Fig. 3.42 the result of averaging on absorption spectra calculated between 0 and 25 kV/cm, showing that the general shape of the measured spectrum is well reproduced. The electric field can be associated with a charge fluctuation in the system. By using the expression of the electric field between two infinite parallel plates $E = \frac{\sigma}{2\epsilon_0\epsilon_R}$, we estimate the electron density difference needed to obtain such an electric field to 3×10^{11} cm⁻², corresponding to $\approx 3\%$ of the charge in our system.

With this simple estimation of the role of disorder, we find a reasonable explanation for the difference between expected and observed optical response.

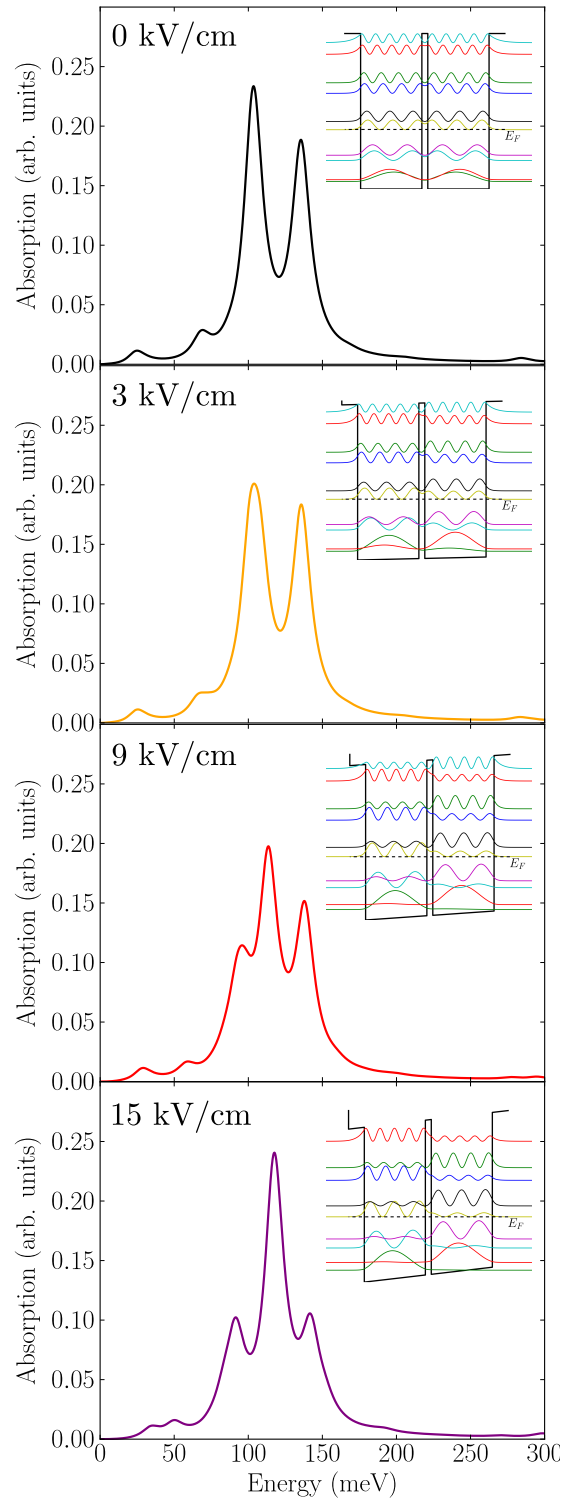


Figure 3.41: Calculated absorption spectra for the structure presented in Fig. 3.39 for different values of applied electric field.

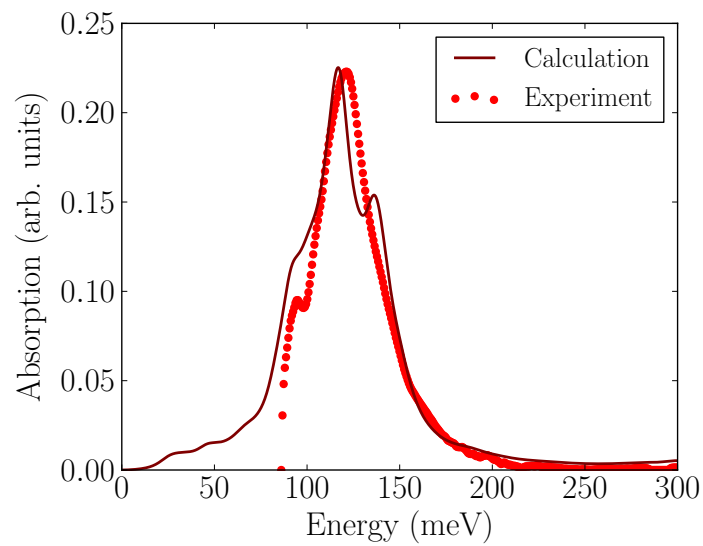


Figure 3.42: Absorption spectra calculated by averaging on the responses at electric fields ranging from 0 to 25 kV/cm (brown curve), compared to the experimental results (red dots). The measurement was performed by Baptiste Dailly.

3.5. Symmetric step well

The observation of two different bright plasmons in the structure of §3.4.4 was hindered by the small energy separation between tunnel-coupled states. In order to overcome this issue, we need a structure with a separation between levels that is greater than the typical broadening (10-15 meV).

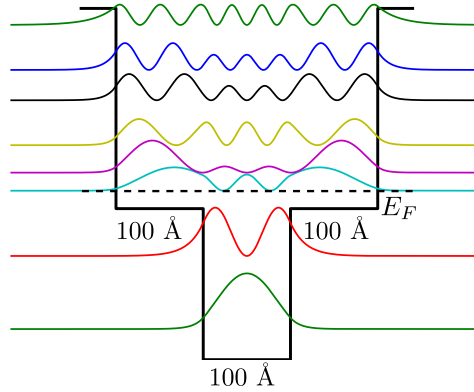


Figure 3.43: Calculated band structure and squared moduli of wavefunctions of a In-GaAs/InAlAs structure. The three layers measure 100 Å, as indicated. The two side barriers (steps) are composed of a compound with 43% of the Al composition of the barriers. $N_V = 1 \times 10^{19} \text{ cm}^{-3}$, just in the central well ($N_S = 1 \times 10^{13} \text{ cm}^{-2}$).

To this end, we design the structure represented in Fig. 3.43. It is a symmetric step well consisting of two $\text{Al}_{0.48}\text{In}_{0.52}\text{As}$ barriers, two inner barriers of a quaternary compound $(\text{Al}_{0.48}\text{In}_{0.52}\text{As})_{0.43}(\text{In}_{0.53}\text{Ga}_{0.47}\text{As})_{0.57}$ that sandwich the central GaInAs well.

The resulting system presents two characteristic lengths: the size of the central small quantum well (100 Å) and the total size of well and side steps (300 Å).

The corresponding calculated absorption spectrum is displayed in Fig. 3.44, together with the collective microcurrents associated with the two peaks. The two peaks in the absorption spectrum can be related to two multisubband plasmons. The higher energy resonance corresponds to an oscillation of charge localized in the small part of the structure: indeed, the corresponding microcurrent visible in Fig. 3.44 is clearly confined in the central section, and has an associated effective length equal to $L_2^{\text{eff}} = 87 \text{ Å}$. On the other hand, the second peak is due to an oscillation that leaks also out of the central section ($L_1^{\text{eff}} = 156.5 \text{ Å}$), and is thus less energetic. As a consequence, its absorption spectrum presents two resonances associated with different length scales.

A single-particle description of the structure would predict substantially different resonances, as it can be observed from the lower panel of Fig. 3.44.

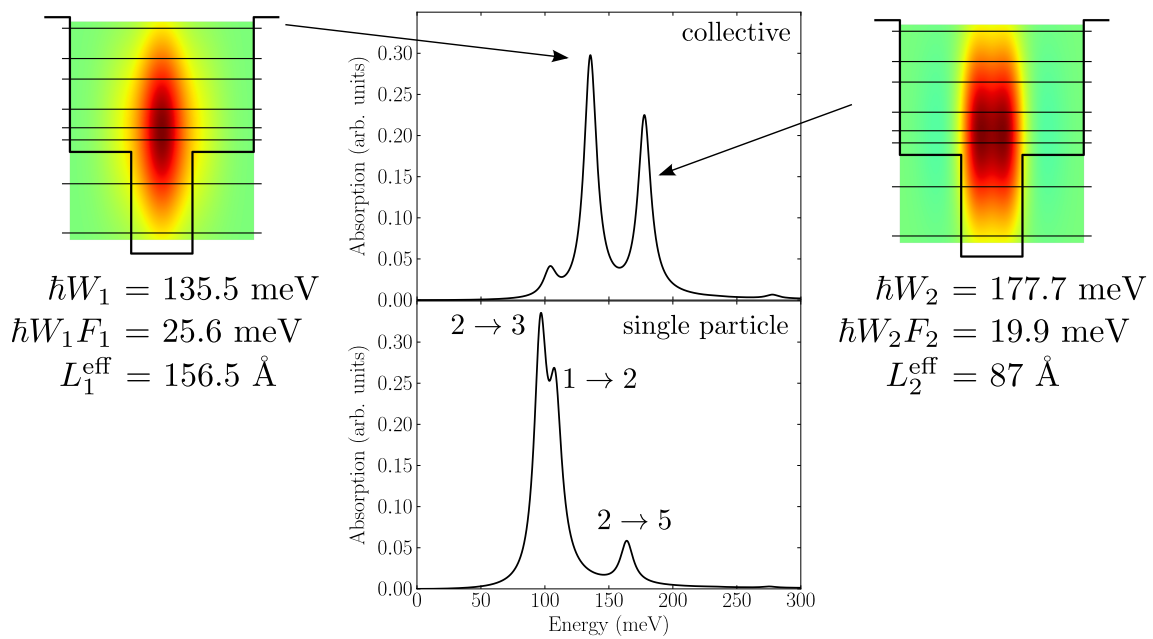


Figure 3.44: Upper panel: calculated absorption of the structure presented in Fig. 3.43, with phenomenological broadening set to $\hbar\gamma = 12$ meV. Also shown are the collective microcurrents corresponding to the two multisubband peaks, along with the values of the resonance energies $\hbar W_n$, effective oscillator strengths $\hbar W_n F_n$, and effective lengths L_n^{eff} . Lower panel: absorption spectrum in single-particle picture.

3.5.1. Comparison with the experimental spectrum

A sample based on this structure has been grown by Isabelle Sagnes and Grégoire Beaudoin (LPN). The absorption spectrum has been measured by Benjamin Askenazi and Baptiste Dailly, through a transmission experiment at Brewster angle at room temperature. A preliminary experimental result is presented in Fig. 3.45, showing a very good agreement between experiment and calculation.

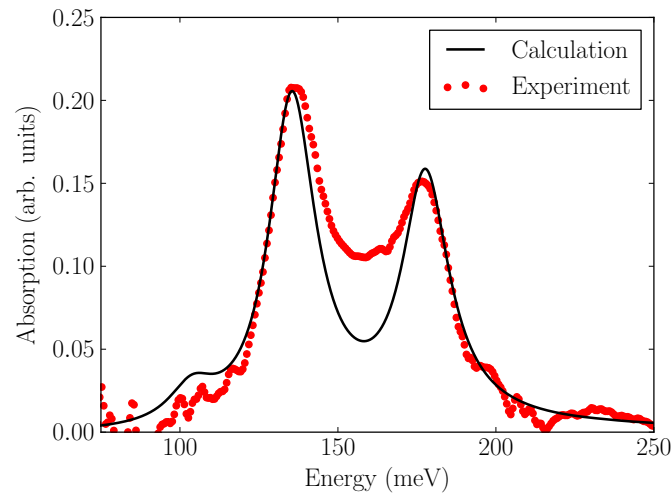


Figure 3.45: Experimental absorption spectrum obtained from a transmission experiment at Brewster angle (red dots) for the coupled wells structure presented in Fig. 3.43. The calculated spectrum (black line) is shown for comparison, in which a phenomenological broadening $\hbar\gamma = 18$ meV was considered. The measurement was performed by Benjamin Askenazi and Baptiste Dailly.

3.6. Coupling between a multisubband plasmon and a single-particle transition

An interesting problem for device application is the electrical excitation of the bright multisubband plasmon. This has already been experimentally achieved by applying an in-plane current, in order to thermally excite the collective mode [15].

It would also be appealing to excite the collective mode under vertical transport, in a quantum-cascade-like device. For this, one can design a quantum cascade structure in which a single-particle transition is excited thanks to an injection miniband. This transition can then be coupled to a multisubband plasmon.

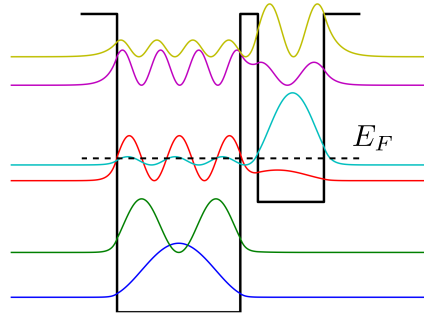


Figure 3.46: Calculated band structure and squared moduli of wavefunctions of a GaAs/AlGaAs structure, 140/20/75 Å. The Al concentration in barriers is 45%, and in the 75 Å well is 17%. The Fermi level shown corresponds to $N_V = 4.4 \times 10^{18} \text{ cm}^{-3}$.

Pursuing this idea, we consider the structure shown in Fig. 3.46, composed of two coupled wells, one 140 Å wide and the other 75 Å wide. The smaller well is composed of AlGaAs such that its potential V is 37% of the band offset. For suitable values of doping, we expect a multisubband plasmon (originated from the left well) and a single-particle transition (right well) to interact.

The optical absorption of this structure for variable values of the doping is presented in the color plot of Fig. 3.47(a). The threshold density for the ground level of the right well to be occupied is $\approx 4 \times 10^{18} \text{ cm}^{-3}$.

In the doping range $4 - 5 \times 10^{18} \text{ cm}^{-3}$, two main resonances are present. As it can be deduced from the collective microcurrents displayed in Fig 3.47(b), these derive from the hybridization of a multisubband plasmon created by a polarization in the left well, and a weakly renormalized single-particle transition localized in the right well.

In order to investigate the role of tunneling in this structure, we fix the doping at $N_V = 4.6 \times 10^{18} \text{ cm}^{-3}$ and calculate the absorption spectra for variable width of the barrier. The result is presented in Fig. 3.48. For thick barriers ($> 45 \text{ Å}$), the two wells are

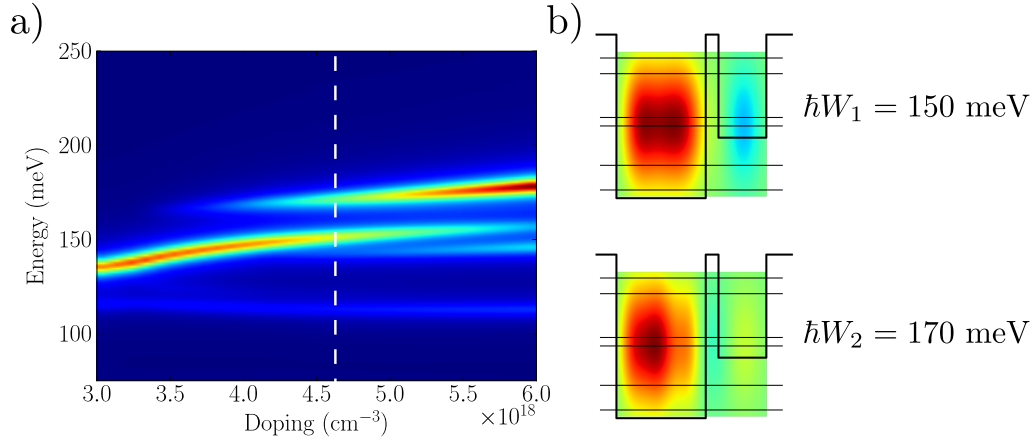


Figure 3.47: a) Calculated absorption spectra of the structure in Fig. 3.46 for variable values of doping N_V b) Calculated collective microcurrents for the two most relevant resonances for $N_V = 4.6 \times 10^{18} \text{ cm}^{-3}$ [dashed line in panel (a)].

completely decoupled, and the absorption spectrum consists of the multisubband plasmon resonance originating from the left well (E_{MSP}) and the very weak transition E_{sp} due to the right well, almost single-particle (low electronic density). For thinner barriers, however, tunneling does play a role, and two resonances are visible, as a result of the interplay between tunnel and Coulomb coupling.

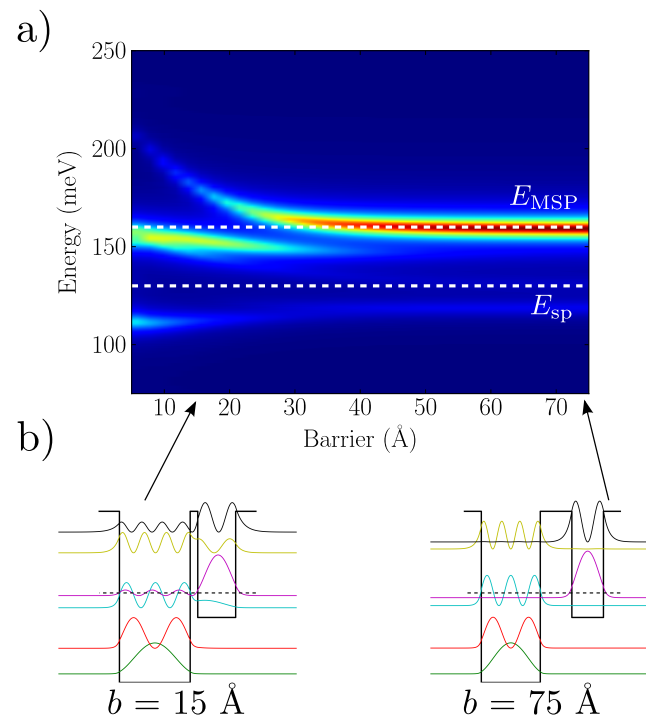


Figure 3.48: a) Calculated absorption spectra of the structure in Fig. 3.46 for variable values of the barrier, $N_V = 4.6 \times 10^{18} \text{ cm}^{-3}$. b) Band structure and square moduli of wavefunctions for barrier = 15 Å and 75 Å.

3.7. Ultra-strong coupling between a multisubband plasmon and a cavity mode

To conclude the chapter, let us suppose that the highly doped 150 Å quantum well studied in §3.1 is inserted in a cavity: the whole system will be then described by the full light-matter Hamiltonian (2.65) discussed in §2.3. Analogous systems have been experimentally investigated in Refs. [14, 65, 67]. The photonic mode is supposed to be uniform in the entire cavity thickness, as it can be achieved by using a metal-dielectric-metal cavity.

Similarly to the analysis of §2.3.1, let us start by considering only the coupling $\Omega_{W_{\text{MSP}}}$ between the bright multisubband plasmon and the cavity mode, and neglecting the other collective modes. The polariton dispersion obtained for this case is presented in Fig. 3.49(a).

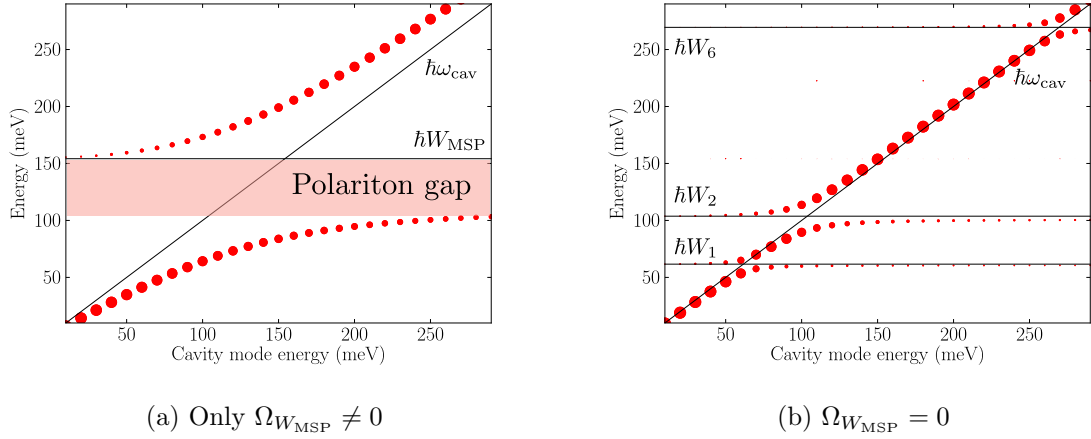


Figure 3.49: Polariton dispersion for a 150 Å GaAs/Al_{0.45}Ga_{0.55}As quantum well, $N_V = 7 \times 10^{18} \text{ cm}^{-3}$, inserted in a cavity of length $L_{\text{cav}} = 160 \text{ Å}$, with selective activation of light-matter couplings Ω_{W_n} . Solid black lines represent bare energies, and red dots are the renormalized modes, the dot size being proportional to the photonic Hopfield coefficient. In a) just the coupling between the bright multisubband plasmon and the cavity $\Omega_{W_{\text{MSP}}}$ is considered, while in b) all the couplings are considered with the exception of $\Omega_{W_{\text{MSP}}}$.

We recognize the same form of the dispersion obtained in the general case of §2.3.1, in particular the opening of a polariton gap. The size of the dots represents their photonic Hopfield coefficient (see §2.3). The minimum separation between the branches is 109 meV; this value corresponds to twice the Rabi energy.

However, we know that a quantum well with three occupied subbands features four optically active multisubband plasmons, all of which are expected to interact with the cavity mode. To investigate this interaction further, we take into account the couplings Ω_{W_n} between the cavity and all the multisubband plasmons, with the exception of the bright multisubband plasmon coupling ($\Omega_{W_{\text{MSP}}} = 0$). The result in this case is

presented in Fig. 3.49(b). We can appreciate that also the other optically active plasmons couple with the cavity mode, though more weakly, the intensity of the coupling being proportional to the effective oscillator strength $W_n F_n$ (or equivalently, to the effective plasma frequencies R_n). Their photonic Hopfield coefficient is not negligible only for energies close to that of the cavity mode, and the anticrossings reveal coupling energies smaller than ≈ 15 meV

Finally, we consider the diagonalization of the full light-matter Hamiltonian, taking into account all the possible light-multisubband plasmon couplings Ω_{W_n} . The resulting dispersion⁴ is shown in Fig. 3.50.

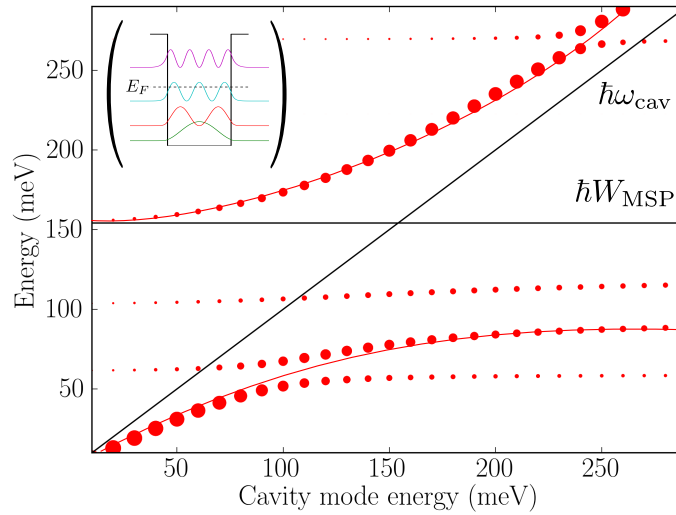


Figure 3.50: Polariton dispersion for a 150 Å GaAs/Al_{0.45}Ga_{0.55}As quantum well, $N_V = 7 \times 10^{18} \text{ cm}^{-3}$, inserted in a cavity of length $L_{\text{cav}} = 160$ Å. Solid black lines represent bare energies, and red dots are the renormalized modes, the dot size being proportional to the photonic Hopfield coefficient. The solid red lines indicate the polariton modes. Inset: calculated band structure and squared moduli of wavefunctions for a 150 Å GaAs/Al_{0.45}Ga_{0.55}As quantum well, $N_v = 7 \times 10^{18} \text{ cm}^{-3}$, represented within an ideal cavity.

The five dotted lines represent the eigenmodes of the coupled system, renormalization of the four optically active multisubband plasmons and the cavity mode. The two polariton modes issued from the coupling between the bright multisubband plasmon ($\hbar W_3 = 155.4$ meV) and the cavity mode are visible and marked by the red solid lines. Note that the polaritonic dispersion issued from W_{MSP} is slightly modified by the presence of the other multisubband plasmon modes. This can also be seen by plotting the absorption spectrum.

⁴The dispersion obtained here only accounts for the interaction between the cavity mode and collective intersubband excitations. In order to correctly reproduce experimental data, one would have to include also the interaction with optical phonons, relevant for energies below ≈ 50 meV [67].

To see this, we set the cavity mode energy at 100 meV and calculate the optical response accounting for the interaction between the cavity mode and the plasmons. The absorption spectrum of the quantum well is reported in the upper panel of Fig. 3.51 for comparison. In the lower panel, we compare the optical response when just the bright multisubband plasmon is considered (blue curve) and when all couplings are taken into account (red curve). It can be appreciated that the shape of the spectrum changes due to the additional couplings inserted in the system. In particular, the peak associated with the lower polariton splits into a doublet, thus spreading the absorption strength over a wider energy range.

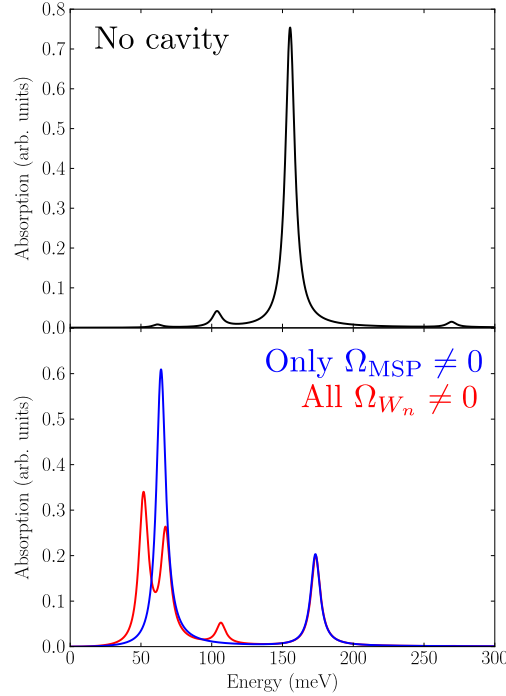


Figure 3.51: Absorption spectra of a 150 Å GaAs/AlGaAs quantum well, $N_V = 7 \times 10^{18} \text{ cm}^{-3}$, $\gamma = 8 \text{ meV}$. Upper panel: no cavity. Lower panel: absorption in the presence of interaction with a cavity mode, $\omega_{\text{cav}} = 100 \text{ meV}$. Blue curve: only the interaction between the bright multisubband plasmon and the cavity mode taken into account. Red curve: inclusion of couplings between the cavity mode and all the optically active multisubband plasmons. In the simulation, the linewidth has been taken equal to 8 meV.

The addition of a cavity might be exploited as a mechanism to engineer the oscillator strength transfer, in a similar way tunneling is exploited in the case of the asymmetrical quantum wells discussed in §3.3. It might therefore represent a further degree of freedom in the multisubband plasmon engineering, in addition to tunnel coupling.

Conclusions

We have applied the model presented in the previous chapter to describe the optical properties of a dense electron gas in a single or in tunnel-coupled quantum wells. The examples presented in this chapter may provide an interesting framework for an engineering of multisubband plasmons. We presented an extensive study of the origin of the multisubband plasmon observed in a single heavily doped quantum well (§3.1), and investigated the role of tunnel coupling in §3.2, §3.3 and §3.4. This latter example and the one presented in §3.5 suggest the possibility of designing structures in which different characteristic lengths co-exist, where scattering mechanisms between multisubband plasmon resonances may be of interest in device design. The coupling between a multisubband plasmon and an almost single-particle transition presented §3.6 may prove promising in the study of electrical resonant excitation of the collective states.

Finally, we showed that our model can describe the ultra-strong coupling regime between a multisubband plasmon and a cavity mode in §3.7. This phenomenon has been already experimentally observed [14, 65, 67] and may provide an additional degree of freedom in multisubband plasmon engineering.

Electron transport in multiple quantum wells: role of tunneling and Coulomb interaction

In the previous two chapters, we have studied the interplay between tunneling and Coulomb interaction in the optical response of multiple quantum wells (MQWs). As summarized in Fig. 4.1, tunnel coupling creates a coherence between electronic levels, and dipole-dipole Coulomb interaction between intersubband transitions.

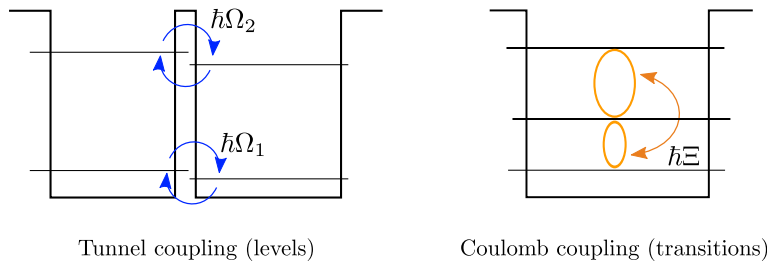


Figure 4.1: Schematization of tunnel coupling between levels and Coulomb coupling between transitions.

In this chapter, we want to investigate the effect of these two coherences on the electron transport, i.e. the study of the current flowing in a system of quantum wells given certain external conditions. Our starting point will be the Hamiltonian

$$H = H_0 + H_{\text{tunnel}} + H_C$$

where H_0 contains the kinetic energy and the confinement potential, H_{tunnel} the resonant tunneling term and H_C the Coulomb interaction. We have already considered these terms in the study of the optical response in §2.2, with tunneling included in the heterostructure potential (in the wavefunctions' extended basis calculation), and Coulomb interaction contained in the \mathbf{P}^2 term. However, we have to make some formal changes in order to study transport, in particular we need to abandon the bosonization procedure described

by definition.

Under resonant bias conditions, the ground state 1' in one well is aligned with the excited state 2 of the second one. These two states are then tunnel-coupled, and form a spatially extended doublet composed of a lower-energy symmetric wavefunction $|S\rangle$ and a higher-energy antisymmetric wavefunction $|A\rangle$, separated by an energy $2\hbar\Omega_{1'2}$. The fact that the two wavefunctions are spatially extended across the barrier has an important consequence: in the extended basis picture, the transport through the barrier is effectively instantaneous.

On the other hand, Fig. 4.2(b) presents a localized basis representation of the same system, as in §1.2. In this picture, electron transport through the barrier occurs via a coherent time evolution of the states. Electrons take a finite time to get from one well to the next. The electron wave packet oscillates across the middle barrier at the oscillation frequency $\Omega_{1'2}$, which will be damped with a characteristic dephasing time τ_{\parallel} . This approach is particularly interesting when the coupling frequency is a significant fraction of the transition frequencies.

In order to properly describe both incoherent population relaxation and coherent resonant tunneling, we adopt a density matrix formalism. Some details on this framework are provided in Appendix C, and a more complete discussion may be found for example in Ref. [87]. The density matrix ρ is the representation of the density operator $\hat{\rho} = |\psi\rangle\langle\psi|$. We will write it on the basis of the electronic wavefunctions ψ_i .

Some of the density matrix properties will be relevant for our work:

- The diagonal element ρ_{ii} represents the population of level i .
- The off-diagonal element ρ_{ij} represents the coherence (polarization) between levels i and j .
- The expectation value of an operator A may be obtained through the density matrix as:

$$\langle A \rangle = \text{Tr} [A\rho] \tag{4.1}$$

- The time evolution of the density matrix is given by Liouville equation:

$$\frac{d\rho}{dt} = \frac{1}{i\hbar} [H, \rho] \tag{4.2}$$

4.1.1. One-dimensional transport in a weakly coupled superlattice

We review in this section a model of one-dimensional electron transport in a superlattice, following the seminal paper [38]. Our aim is to calculate the current density passing through the system as a function of the applied external field, expressed in terms of the tunnel coupling frequency between the electronic states involved.

We know that classically the current density is given by $\mathbf{j} = -nev$, with n electron density per unit volume. Let us introduce a velocity operator

$$\mathbf{v} = \frac{\mathbf{P}}{m}$$

This operator is directly related to the Hamiltonian of the system

$$H_0 = \frac{p_z^2}{2m} + V(z)$$

through the relation

$$v_z = \frac{p_z}{m} = \frac{i}{\hbar} [H_0, z]$$

from which, by making use of the property (4.1), we can rewrite the expression for the average current density as

$$\boxed{j_z = -ne \operatorname{Tr} [\rho v_z] = -ne \frac{i}{\hbar} \operatorname{Tr} [\rho [H_0, z]]} \quad (4.3)$$

As a first application of the general expression (4.3), let us consider the case schematized in Fig. 4.2, in which each period of the superlattice consists only of a quantum well with two confined levels, as in [38], and discussed also in [88, 89].

We call 1' the ground state resonant with level 2 of the following period. We choose as basis for our calculation the localized basis (see §1.2), in which each quantum well is seen as isolated. The resulting levels are schematized in Fig. 4.2(b). In this approximation, the quantum wells are weakly coupled: we consider the resonant tunneling to be the only interaction between periods and neglect other relaxation mechanisms.

The unperturbed single-particle Hamiltonian will then read

$$H_{\text{sp}} = H_0 + H_{\text{tunnel}} = \begin{pmatrix} E_{1'} & \hbar\Omega_{1'2} & 0 \\ \hbar\Omega_{1'2} & E_2 & 0 \\ 0 & 0 & E_1 \end{pmatrix}$$

where the off-diagonal elements $\hbar\Omega_{1'2}$ represent the resonant tunnel coupling between the two periods. After finding the expression of the matrix elements of the commutator $[H_{\text{sp}}, z]$, one can write:

$$\operatorname{Tr} [[H_{\text{sp}}, z] \rho] = [\hbar\Omega_{1'2}(z_{1'1'} - z_{22}) + z_{21'}(E_2 - E_{1'})] (\rho_{1'2} - \rho_{21'})$$

As the overlap between functions 2 and 1' is very small, we consider $z_{21'} = 0$ and we obtain for the current, using Eq. (4.3)

$$j_z = -nei\Omega_{1'2}(z_{1'1'} - z_{22})(\rho_{1'2} - \rho_{21'}) = 2ne\Omega_{1'2}(z_{1'1'} - z_{22}) \operatorname{Im} \rho_{1'2} \quad (4.4)$$

from which we see that in this approximation the current depends on $\operatorname{Im} \rho_{1'2}$ [or equivalently, on the difference between coherences $(\rho_{1'2} - \rho_{21'}) = 2i \operatorname{Im} \rho_{1'2}$] and on the

tunnel coupling frequency $\Omega_{1'2}$.

We now want to solve Liouville equation (4.2) for the steady state condition, in order to get an explicit expression for the term $\text{Im } \rho_{1'2}$.

The Hamiltonian of the system can be written in the form $H_{\text{tot}} = H_{\text{sp}} + H_{\text{diff}}$, where H_{diff} contains the perturbations due to incoherent scattering (with phonons, impurities, interface roughness...). We can express the H_{diff} contribution to the $\frac{d\rho}{dt}$ derivative as [37]

$$\frac{1}{i\hbar}[H_{\text{diff}}, \rho] = \begin{pmatrix} \frac{\rho_{22}}{\tau_{21}} & -\frac{\rho_{1'2}}{\tau_{\parallel 1'2}} \\ -\frac{\rho_{21'}}{\tau_{\parallel 1'2}} & -\frac{\rho_{22}}{\tau_{21}} \end{pmatrix}$$

In this expression, the diagonal part contains the population relaxation terms, where the times τ are obtained with Fermi's golden rule, as explained in §1.4. The off-diagonal part expresses the dephasing terms, i.e. the loss of coherence due to $\tau_{\parallel 1'2}$, the characteristic dephasing time of tunneling 1'-2.

From the full expression of Liouville equation it is possible to obtain the following system of equations, whose unknowns are the density matrix elements:

$$\begin{cases} \frac{d\rho_{22}}{dt} = 2\Omega_{1'2} \text{Im } \rho_{1'2} - \frac{\rho_{22}}{\tau_{21}} \\ \frac{d\rho_{1'2}}{dt} = -i\frac{\Delta_{1'2}}{\hbar}\rho_{1'2} + i\Omega_{1'2}(\rho_{1'1'} - \rho_{22}) - \frac{\rho_{1'2}}{\tau_{\parallel 1'2}} \\ \frac{d\rho_{21'}}{dt} = i\frac{\Delta_{1'2}}{\hbar}\rho_{21'} - i\Omega_{1'2}(\rho_{1'1'} - \rho_{22}) - \frac{\rho_{21'}}{\tau_{\parallel 1'2}} \\ \frac{d\rho_{1'1'}}{dt} = -2\Omega_{1'2} \text{Im } \rho_{1'2} + \frac{\rho_{22}}{\tau_{21}} \end{cases} \quad (4.5)$$

with $\Delta_{1'2} = E_{1'} - E_2$. From Eqs. (4.5) at the steady state condition, along with the conservation law $\rho_{1'1'} + \rho_{22} = 1$, it is possible to obtain

$$\text{Im } \rho_{1'2} = \frac{\Omega_{1'2}}{\tau_{\parallel 1'2} \left(\frac{1}{\tau_{\parallel 1'2}^2} + \frac{\Delta_{1'2}^2}{\hbar^2} \right) + 4\Omega_{1'2}^2 \tau_{21}} \quad (4.6)$$

Expression (4.6) can be finally inserted into Eq. (4.4) to get [88]:

$$j_z = \frac{2ne\Omega_{1'2}^2 \tau_{\parallel 1'2} (z_{1'1'} - z_{22})}{1 + \frac{\Delta_{1'2}^2}{\hbar^2} \tau_{\parallel 1'2}^2 + 4\Omega_{1'2}^2 \tau_{21} \tau_{\parallel 1'2}} \quad (4.7)$$

Application to a GaAs/AlGaAs superlattice

Let us consider the example of a GaAs/Al_{0.3}Ga_{0.7}As structure, composed of 120 Å quantum wells coupled through 40 Å barriers. The wavefunctions calculated in extended

basis are presented in Fig. 4.3(a), and those calculated in the localized basis in Fig. 4.3(b).

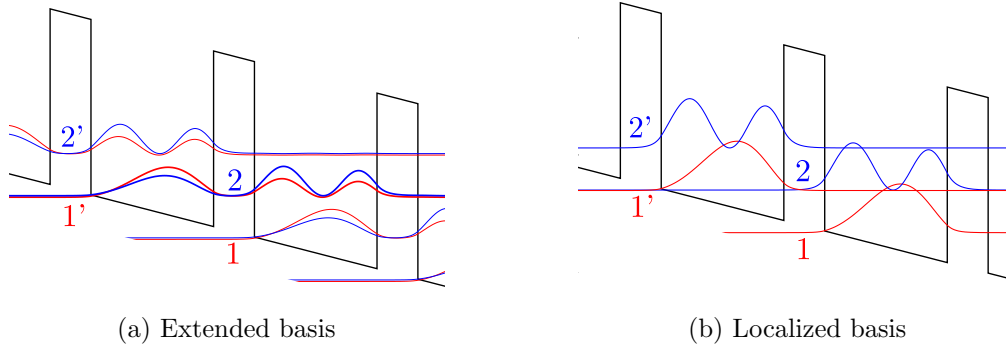


Figure 4.3: Band structure and square moduli of wavefunctions in a GaAs/Al_{0.3}Ga_{0.7}As superlattice composed of 120 Å quantum wells coupled through 40 Å barriers. The applied field is 45 kV/cm.

Figure 4.5 presents the current-voltage (I-V) curve for different values of the coherence time $\tau_{\parallel 1'2}$, calculated by using Eq. (4.7).

The scattering time τ_{21} accounts for interface roughness, alloy and LO-phonon emission scattering times (see Appendix B). The tunnel coupling $\Omega_{1'2}$ is obtained by tracing the energies of the levels in the extended and localized basis (Fig. 4.4) and identifying the anticrossing energy, which is equal to $2\hbar\Omega_{1'2}$.

The I-V curves present the negative differential resistance typical of resonant tunneling devices. The current density has a maximum for the electric field at which $E_{1'} = E_2$. This maximum has a Lorentzian shape, whose width is determined by the coherence time. We see how tunnel coherences have macroscopic consequences, and profoundly affect the current-voltage characteristics. In next section we will show how his property can be verified in a quantum cascade laser.

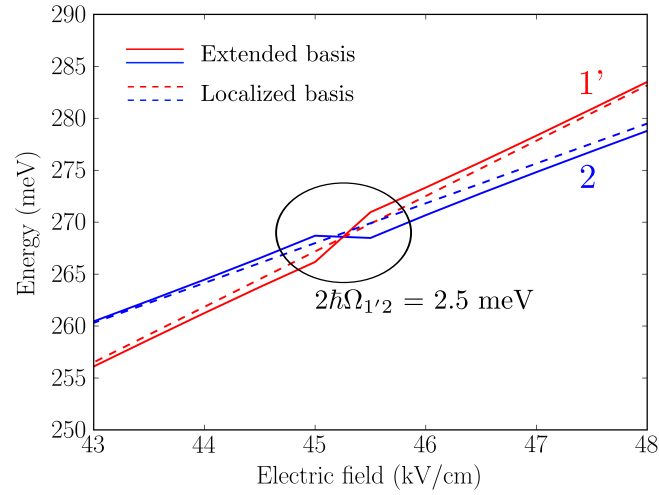


Figure 4.4: Energies of levels 1' and 2 versus applied bias, in extended (solid lines) and localized (dashed lines) basis. The anticrossing in correspondence of alignment is shown.

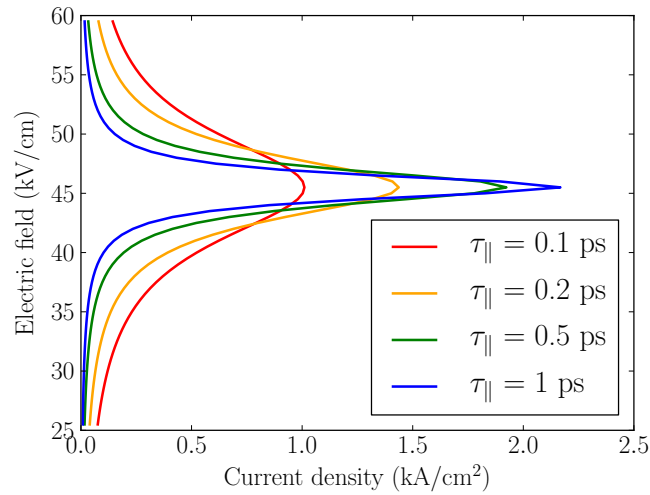


Figure 4.5: Calculated VI for the two-level structure shown in Fig. 4.3, for various values of the coherence time $\tau_{||1'2}$. $N_V = 10^{16} \text{ cm}^{-3}$.

4.1.2. Application to a THz quantum cascade laser

The density matrix approach is applied here to a THz QCL [35, 37, 89–96].

In this case, anticrossing gaps of the order of few meV represent a significant fraction of photon energies, $\hbar\omega \approx 10\text{-}20$ meV, and the inclusion of coherent tunneling is critical to the transport description.

As an example, we consider the design presented in Ref. [42], whose band structure is shown in Fig. 4.6¹. This active region was used to demonstrate the first THz laser operating above 180 K. Four electronic levels per period contribute to electron transport: injector (level 1), excited and ground state of the laser transition (2, 3) and extractor (4). The radiative transition $2 \rightarrow 3$ ($E_{23} \approx 15$ meV) is designed to be diagonal in order to increase the excited level lifetime. The structure features also a phonon extraction scheme, the energy difference between level 4 and 1' being close to the optical phonon energy $\hbar\omega_{\text{LO}}$, to the end of decreasing the ground level lifetime.

In the band diagram of Fig. 4.6(a) we highlight the emission region, where the radiative transition takes place, and the extraction region, ensuring the population inversion. The two regions are tunnel-coupled, and this coupling is crucial for the electron transport. Therefore, a partially localized basis will be used, with the two modules sketched in Fig. 4.6(b)-(c).

Figure 4.7 shows a schematization of the four levels involved in the calculation, along with the relevant couplings and scattering times.

We solve for the steady state the evolution equation of the density matrix:

$$\frac{d\rho}{dt} = \frac{1}{i\hbar} [H_{\text{sp}}, \rho] + \frac{1}{i\hbar} [H_{\text{diff}}, \rho]$$

In the four-level case, we have

$$[H_{\text{sp}}, \rho] = \left[\begin{pmatrix} E_1 & \hbar\Omega_{12} & \hbar\Omega_{13} & \hbar\Omega_{14} \\ \hbar\Omega_{12} & E_2 & \hbar\Omega_{23} & \hbar\Omega_{24} \\ \hbar\Omega_{13} & \hbar\Omega_{23} & E_3 & \hbar\Omega_{34} \\ \hbar\Omega_{14} & \hbar\Omega_{24} & \hbar\Omega_{34} & E_4 \end{pmatrix}, \begin{pmatrix} \rho_{11} & \rho_{12} & \rho_{13} & \rho_{14} \\ \rho_{21} & \rho_{22} & \rho_{23} & \rho_{24} \\ \rho_{31} & \rho_{32} & \rho_{33} & \rho_{34} \\ \rho_{41} & \rho_{42} & \rho_{43} & \rho_{44} \end{pmatrix} \right]$$

$$\begin{aligned} & \frac{1}{i\hbar} [H_{\text{diff}}, \rho] = \\ & = \begin{pmatrix} -\frac{\rho_{11}}{\tau_1} + \frac{\rho_{44}}{\tau_4} & -\frac{\rho_{12}}{\tau_{\parallel 12}} & -\frac{\rho_{13}}{\tau_{\parallel 13}} & -\frac{\rho_{14}}{\tau_{\parallel 14}} \\ -\frac{\rho_{21}}{\tau_{\parallel 12}} & -\frac{\rho_{22}}{\tau_2} + \frac{\rho_{33}}{\tau_3} - \frac{\rho_{22} - \rho_{33}}{\tau_{\text{st}}} & -\frac{\rho_{23}}{\tau_{\parallel 23}} & -\frac{\rho_{24}}{\tau_{\parallel 24}} \\ -\frac{\rho_{31}}{\tau_{\parallel 13}} & -\frac{\rho_{32}}{\tau_{\parallel 23}} & \frac{\rho_{22}}{\tau_2} - \frac{\rho_{33}}{\tau_3} + \frac{\rho_{22} - \rho_{33}}{\tau_{\text{st}}} & -\frac{\rho_{34}}{\tau_{\parallel 34}} \\ -\frac{\rho_{41}}{\tau_{\parallel 14}} & -\frac{\rho_{42}}{\tau_{\parallel 24}} & -\frac{\rho_{43}}{\tau_{\parallel 34}} & -\frac{\rho_{44}}{\tau_4} + \frac{\rho_{11}}{\tau_1} \end{pmatrix} \end{aligned}$$

¹The same structure was mentioned in §1.5.1 as an example of THz active region.

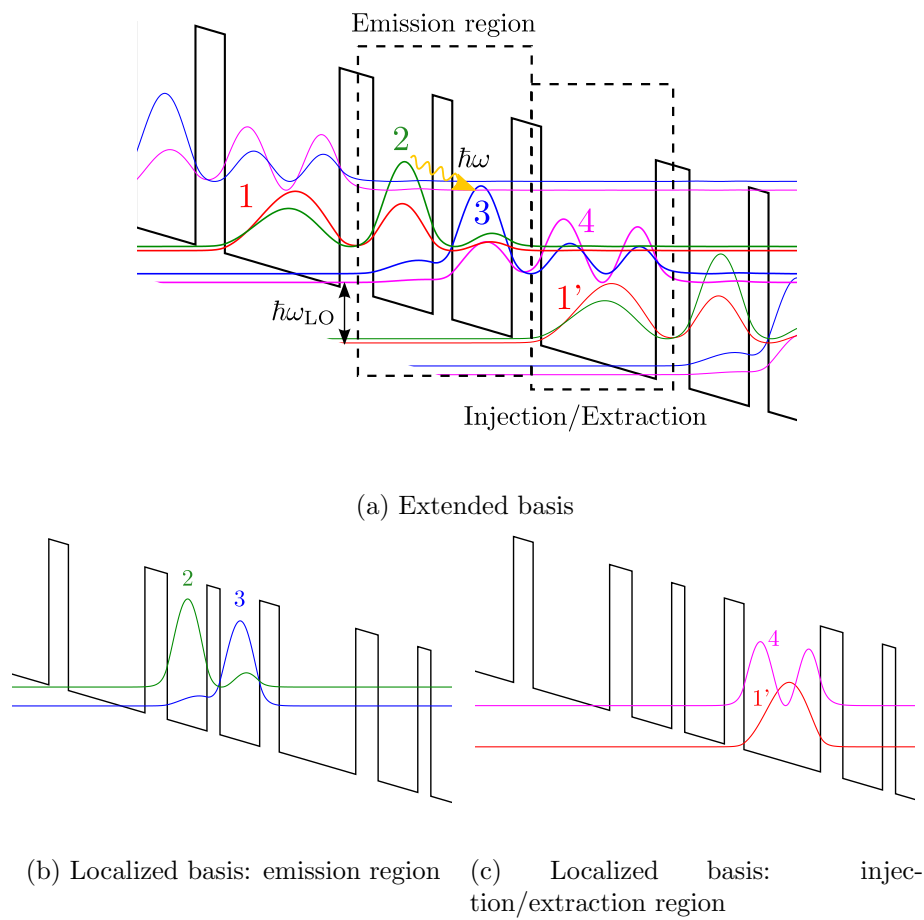


Figure 4.6: Band structure and square moduli of wavefunctions in the THz structure of Ref. [42]. Starting from the injector barrier, the layer thicknesses in Å are: 48/85/28/85/42/164. The external electric field is 12.5 kV/cm.

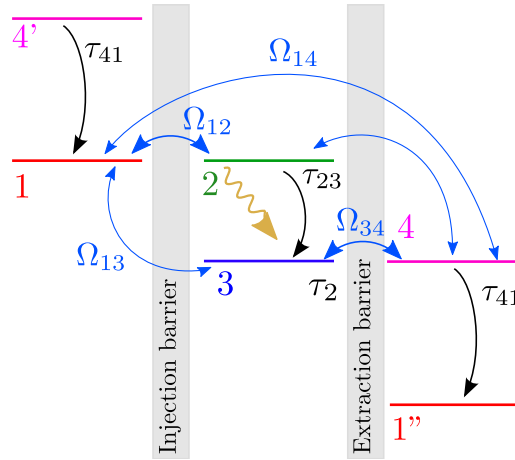


Figure 4.7: Scheme of the levels included in the calculations, and their interactions.

where relaxation times τ_i indicate the total lifetime of level i , and τ_{st} is the time of stimulated emission/absorption ($\tau_{st} \rightarrow \infty$ in the cold cavity limit).

Like in the two-level case introduced in §4.1.1, we need to calculate the scattering times τ among levels in the same module (Fermi's golden rule), and the tunnel couplings Ω among levels in different modules. The latter are directly obtained from the splitting of electronic levels calculated in the extended basis², as shown in Fig. 4.8. The main couplings for the laser operation are Ω_{12} , between the injector and the excited state of the laser transition, and Ω_{34} , ensuring extraction out of the ground laser state.

However, more couplings are visible in Fig. 4.8, which can be considered as associated with 'parasitic' alignments, as it was observed in Ref. [42]. These couplings are indeed responsible for a current flowing in the device out of the ideal operation conditions. In particular, levels (1,3) and levels (2,4) anticross around an electric field value of ≈ 6 kV/cm, and levels (1,4) for an electric field of ≈ 8.5 kV/cm, as illustrated in Fig. 4.9.

Figure 4.10 presents the populations of the different electronic states, calculated following the procedure detailed in §C.2.2. The population inversion between excited and ground state of the laser transition is correctly observed for an electric field of 7 kV/cm, when both injector and extractor are tunnel-coupled to excited and ground state, respectively.

²The extraction of the coupling energy is done automatically in our program, thanks to an algorithm that identifies the extended wavefunctions and follows them while the electric field varies. The identification is based on the comparison with the energies and spatial distributions obtained in the localized basis.

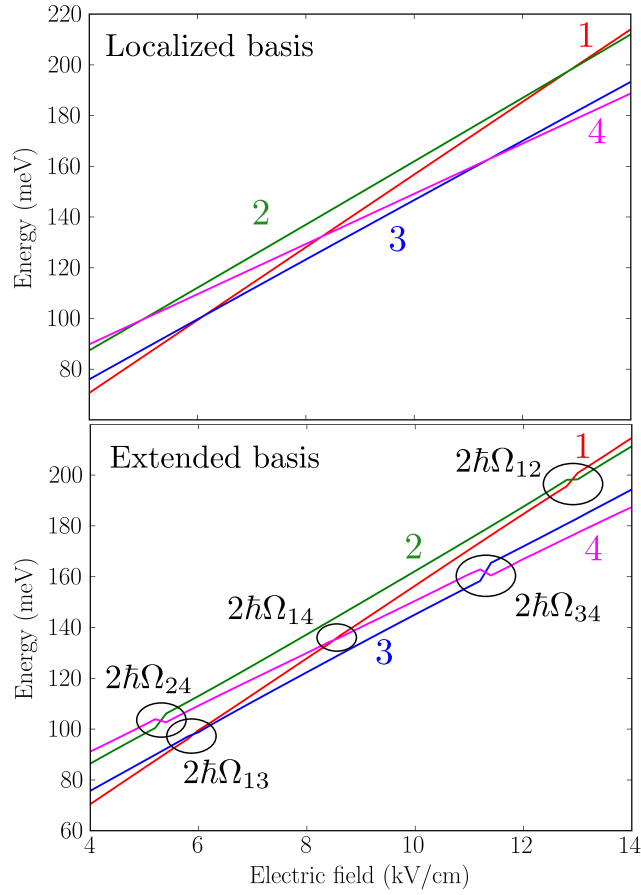


Figure 4.8: Energies of levels versus applied bias, in localized (upper panel) and extended (lower panel) basis. The anticrossings in correspondence of level alignments are shown. We find $2\hbar\Omega_{12} = 2.5$ meV, $2\hbar\Omega_{34} = 4.6$ meV, $2\hbar\Omega_{24} = 3.4$ meV, $2\hbar\Omega_{13} = 0.8$ meV, and $2\hbar\Omega_{14} = 0.7$ meV.

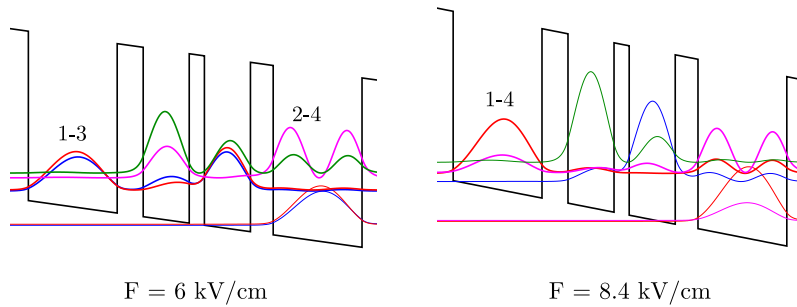


Figure 4.9: Parasitic bias for the structure. Left: ≈ 6 kV/cm, coupling between levels 1-3 and 2-4. Right: ≈ 8.5 kV/cm, coupling between levels 1-4.

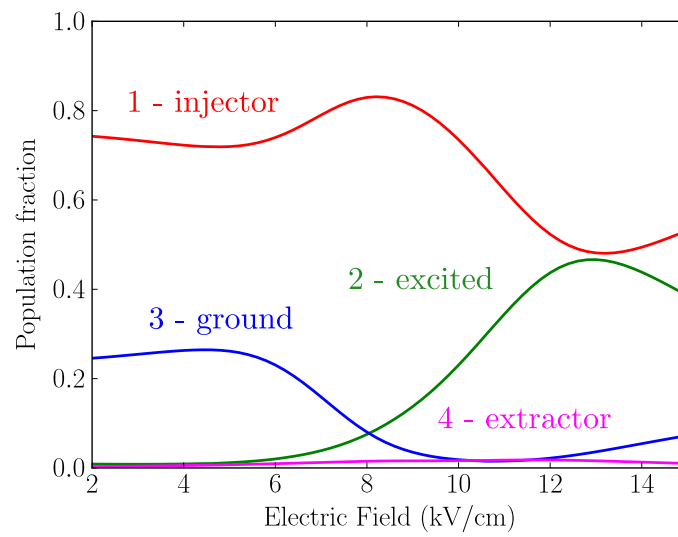


Figure 4.10: Calculated populations versus applied external field for the THz QCL introduced in Ref. [42].

In order to observe the signature of tunneling coherences in the current-voltage characteristics, we define the matrix

$$U = \frac{1}{\hbar} [H_{\text{sp}}, z]$$

whose elements can be shown to be

$$U_{ij} = \frac{\Delta_{ij}}{\hbar} z_{ij} + \Omega_{ij} (z_{jj} - z_{ii}) + \sum_{k \neq i,j}^4 (\Omega_{ik} z_{jk} - \Omega_{jk} z_{ik})$$

The current density is expressed in terms of matrices U and ρ as:

$$J = -nei \sum_{i < j}^4 U_{ij} (\rho_{ij} - \rho_{ji})$$

To account for stimulated emission, we introduce the gain for each transition in the active region:

$$G_{ij} = \Gamma \sigma_{ij} N_V L_p (\rho_{ii} - \rho_{jj}) \frac{n}{c}$$

where σ_{ij} is the cross section per unit time for stimulated emission [44]:

$$\sigma_{ij} = \frac{4\pi e^2 |z_{ij}|^2 c}{\varepsilon_0 n \lambda} \frac{1}{n L_p 2\gamma}$$

with N_V the electronic density per unit volume, L_p the length of the period, n the mode effective index and Γ the overlap between the active region and the cavity mode.

The total gain is then computed as the sum of all these contributions, multiplied by a Lorentzian function centered on the energy of the radiative transition E_{rad} :

$$G = \sum_{i < j} G_{ij} \frac{\gamma^2/4}{(E_{ij} - E_{\text{rad}})^2 + \gamma^2/4}$$

If the total gain equals the losses α , there is stimulated emission in the structure. We can thus calculate a τ_{stim} with a self-consistent procedure, imposing $\frac{dS}{dt} = 0$, as in the discussion of §1.5.2.

The last parameter needed for the calculation of the I-V characteristics is the lifetime of the coherences (see §1.4). Following Kumar [92], we set a phenomenological broadening $\tau_{\parallel} = 0.8$ ps for the injection (Ω_{12}) and extraction (Ω_{34}) couplings. The parasitic couplings Ω_{13} , Ω_{24} and Ω_{14} are also taken into account, with a shorter coherence time with respect to injection and extraction ($\tau_{\parallel} = 0.1$ ps).

The resulting LIV characteristic is displayed in Fig. 4.11(a). The figure shows the calculated I-V curve taking into account all the possible couplings (black solid line) and the 'idealized' I-V curve with no parasitic coupling (black dashed line), as in the model in Ref. [92]. The inclusion of parasitic couplings significantly changes the shape of the curve,

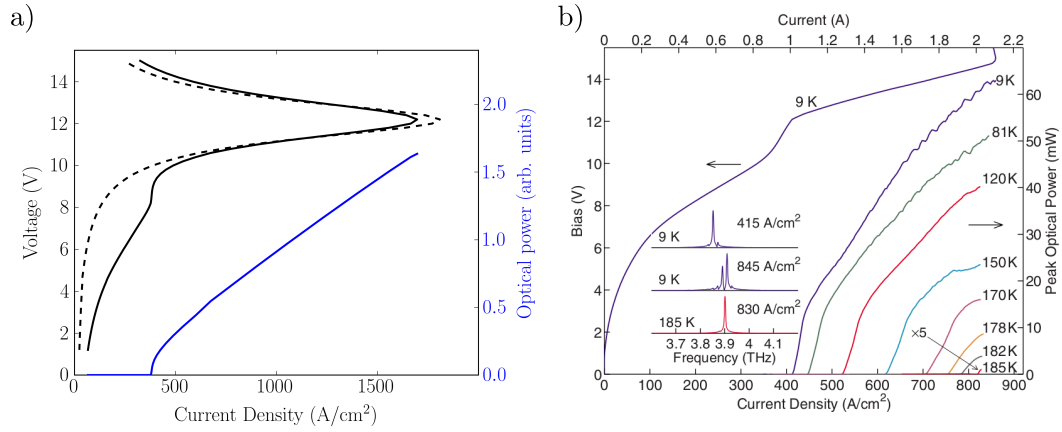


Figure 4.11: a) Calculated L-V-I for the four-level structure of Fig. 4.6. The solid curve is the calculation accounting for all the possible couplings and the dashed curve the calculation with just the injection and extraction couplings. We considered $\alpha = 20 \text{ cm}^{-1}$ for the loss coefficient, $N_V = 6.6 \times 10^{15}$, $\Gamma = 1$, $N_p = 222$. b) From [42]: measured L-I-V characteristic.

and determines a current leakage for voltages lower than the alignment ($\approx 12 \text{ kV/cm}$). This feature was indeed experimentally observed [see Fig. 4.11(b)].

A possible way to improve the agreement between simulation and experimental data could be the inclusion in the heterostructure potential of the Hartree correction, due to the static charges contribution. This could be implemented with a self-consistent resolution of Poisson-Schrödinger equation [30]. Other effects to account for would be the electronic subbands dispersion and the effects due to backfilling of the lower laser level [3].

The presented density matrix method for electron transport in QCL can be generalized to N levels. Details of this procedure are discussed in §C.2.3, and an application to the modeling of a mid-IR laser is presented in Appendix D.

4.2. Transport in the presence of Coulomb interaction

We now turn to the inclusion of Coulomb interaction in the study of transport. This interaction creates a coherence between two transitions involving several electrons, i.e. four electronic levels, as opposed to tunneling, which couples two levels (see Fig. 4.1 in the chapter introduction).

In this section, we will adopt an equation of motion method, similar to the density matrix model of the previous section. An alternative approach to include many-body effects in transport in a theoretically rigorous way are Green's functions methods [62, 63, 97, 98].

The passage from coupling between levels to coupling between transitions involving large densities of electrons requires a change in the formalism. Therefore, we work in the second quantization framework, which allows us to describe an electronic excitation from level i to level j with the creation operator c_{ij}^\dagger . Rather than the evolution of states, like in the density matrix model of the previous section, we consider then the evolution of quantum operators.

In the Heisenberg picture, the dynamics of an operator A is given by [63, 87]

$$\frac{d}{dt}A = \frac{1}{i\hbar}[A, H] \quad (4.8)$$

where H is the Hamiltonian, which can be written in terms of single-particle and higher order contributions (two-particle terms)

$$H = H_{\text{single-particle}} + H_{\text{two particles}} \quad (4.9)$$

In second quantization, the single-particle part reads

$$H_{\text{single-particle}} = H_0 = \sum_{j,\mathbf{k}} \epsilon_{j,\mathbf{k}} c_{j,\mathbf{k}}^\dagger c_{j,\mathbf{k}}$$

where $\epsilon_{j,\mathbf{k}}$ is the single-particle energy of an electron in the j -th subband and wave vector \mathbf{k} . Two-particle contributions arise from coupling terms with external fields, phonons, etc, but most importantly for this work, from Coulomb interaction:

$$H_{\text{two particles}} = H_C = \frac{1}{2} \sum_{i,j,m,n} \sum_{\mathbf{k}\mathbf{k}'\mathbf{q}} V_{\mathbf{q}}^{imnj} c_{i,\mathbf{k}+\mathbf{q}}^\dagger c_{m,\mathbf{k}'-\mathbf{q}}^\dagger c_{n,\mathbf{k}'} c_{j,\mathbf{k}} \quad (4.10)$$

where

$$V_{\mathbf{q}}^{imnj} = \frac{e^2}{2\epsilon_0\epsilon_s q} \int_{-\infty}^{+\infty} dz \int_{-\infty}^{+\infty} dz' \psi_i(z)\psi_j(z)e^{-q|z-z'|}\psi_m(z')\psi_n(z') \quad (4.11)$$

is the two-dimensional Coulomb matrix element [62, 99].

Equation (4.10) describes elementary processes where two electrons from subbands n and j with wave vectors \mathbf{k} and \mathbf{k}' are scattered into subbands i and m with wave vectors $\mathbf{k} + \mathbf{q}$ and $\mathbf{k}' - \mathbf{q}$, respectively, as schematized in Fig. 4.12.

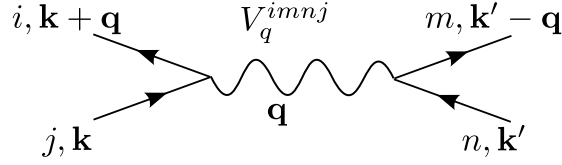


Figure 4.12: Index convention of the matrix element V_q^{imnj} . Two electrons in subbands j and n , with momenta \mathbf{k} and \mathbf{k}' , are scattered into subbands i and m , with momenta $\mathbf{k} + \mathbf{q}$ and $\mathbf{k} - \mathbf{q}$, respectively.

Coulomb matrix elements in a two-subband quantum well

Let us consider a two-subband quantum well, like the one depicted in Fig. 4.13. In the density matrix model for coherent tunneling described in §4.1, we used a description based on energy levels, as in panel (a). This approximation can be justified for low temperatures, assuming that intrasubband relaxation is much faster than the intersubband one. However, for the purpose of treating Coulomb interaction in the terms of Eq. (4.9), we need to account also for k -space dispersion [panel (b)].

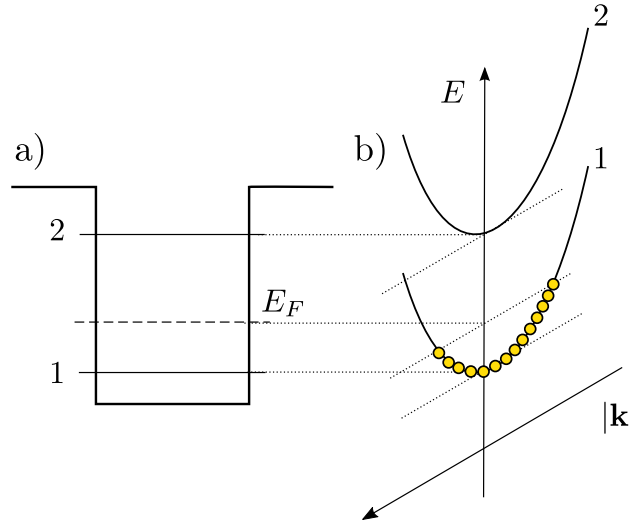


Figure 4.13: a) Energy level representation of a two-subband quantum well. b) Corresponding parabolic dispersion in k -space.

The Hamiltonian (4.9) for this system reads:

$$H = \sum_{\mathbf{k}} \left(\hbar\omega_{2\mathbf{k}} c_{2\mathbf{k}}^\dagger c_{2\mathbf{k}} + \hbar\omega_{1\mathbf{k}} c_{1\mathbf{k}}^\dagger c_{1\mathbf{k}} \right) + \frac{1}{2} \sum_{i,j,m,n=1,2, \mathbf{k}\mathbf{k}'\mathbf{q}} V_{\mathbf{q}}^{imnj} c_{i,\mathbf{k}+\mathbf{q}}^\dagger c_{m,\mathbf{k}'-\mathbf{q}}^\dagger c_{n,\mathbf{k}'} c_{j,\mathbf{k}}$$

Figure 4.14 represents the different interaction coefficients in such a system.

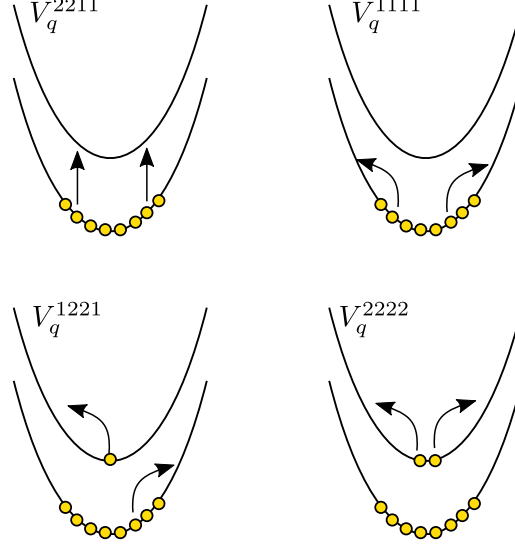


Figure 4.14: Graphical representation of the four qualitatively different kinds of scattering processes.

Some of the $V_{\mathbf{q}}^{imnj}$ are zero for symmetry reasons [99]. This is the case for all the matrix elements with an odd number of 1 or 2 indices:

$$\begin{aligned} V_{\mathbf{q}}^{1112} = V_{\mathbf{q}}^{1121} = V_{\mathbf{q}}^{1211} = V_{\mathbf{q}}^{2111} &= 0 \\ V_{\mathbf{q}}^{2111} = V_{\mathbf{q}}^{2212} = V_{\mathbf{q}}^{2122} = V_{\mathbf{q}}^{1222} &= 0 \end{aligned}$$

The other elements are:

$$\begin{aligned} V_{\mathbf{q}}^{1222} = V_{\mathbf{q}}^{1212} = V_{\mathbf{q}}^{2121} = V_{\mathbf{q}}^{2211} = V_{\mathbf{q}}^{\text{dep}} &= \\ = \frac{e^2}{2\varepsilon_0\varepsilon_s q} \iint dz dz' \psi_1(z)\psi_2(z)e^{-q|z-z'|}\psi_2(z')\psi_1(z') &\quad \text{depolarization term} \end{aligned} \quad (4.12)$$

$$\begin{aligned} V_{\mathbf{q}}^{1221} = V_{\mathbf{q}}^{2112} &= \frac{e^2}{2\varepsilon_0\varepsilon_s q} \iint dz dz' \psi_1^2(z)e^{-q|z-z'|}\psi_2^2(z') \\ V_{\mathbf{q}}^{1111} &= \frac{e^2}{2\varepsilon_0\varepsilon_s q} \iint dz dz' \psi_1^2(z)e^{-q|z-z'|}\psi_1^2(z') \quad \text{direct and exchange terms} \\ V_{\mathbf{q}}^{2222} &= \frac{e^2}{2\varepsilon_0\varepsilon_s q} \iint dz dz' \psi_2^2(z)e^{-q|z-z'|}\psi_2^2(z') \end{aligned} \quad (4.13)$$

Equations (4.12)-(4.13) correspond to different scattering processes.

In particular, the Coulomb term (4.12) represents intersubband excitations, where each electron is scattered from one subband to another. These processes are responsible for the depolarization shift [54], and are the only ones relevant for superradiant collective processes: for small values of \mathbf{q} , a great number of electrons can undergo the same transition,

approximately at the same energy. Indeed, the most relevant component of the depolarization term is $\mathbf{q} \rightarrow 0$ [54]. In this limit, V_0^{dep} is linked to the Coulomb length S_{ijij} we already defined in the study of the optical response:

$$S_{ijkl} = \int_{-\infty}^{+\infty} dz \left[\int_{-\infty}^z dz' \psi_i(z') \psi_j(z') \right] \left[\int_{-\infty}^z dz'' \psi_k(z'') \psi_l(z'') \right]$$

In fact it holds [74]:

$$V_0^{1212} = \frac{e^2}{\varepsilon_0 \varepsilon_s} S_{1212}$$

We recall the relation between the diagonal part of the matrix S and the plasma frequency (2.43):

$$\omega_{P12}^2 = \frac{2e^2 \Delta N_{12} \omega_{12}}{\hbar \varepsilon_0 \varepsilon_s} S_{1212}$$

Finally we can express the depolarization term V_0^{1212} as

$$V_0^{1212} = \frac{\hbar}{2\Delta N_{12}} \frac{\omega_{P12}^2}{\omega_{12}}$$

The terms (4.13) describe instead intrasubband processes, which do not involve great numbers of electrons, due to Pauli blocking and nonflat energy dispersion [99].

4.2.1. Observables and equations of motion

Physical observables (population distributions) are given by the ensemble average $\langle \rangle$ of the operators $c_{j,\mathbf{k}}^\dagger, c_{i,\mathbf{k}}$. A common way to represent this is through the density matrix in second quantization:

$$\rho_{j\mathbf{i}\mathbf{k}} = \langle c_{j,\mathbf{k}}^\dagger c_{i,\mathbf{k}} \rangle$$

As in the first-quantization formalism adopted in the first part of this chapter, this is a concise way to represent two different quantities:

- Distribution functions $\rho_{ii\mathbf{k}}$, on the diagonal, represent the expected number of electrons on subband i and wave vector \mathbf{k} .
- The intersubband polarizations are the off-diagonal elements of ρ : $\rho_{j\mathbf{i}\mathbf{k}} = \rho_{i\mathbf{j}\mathbf{k}}^*$.

The evolution of the density matrices can be obtained with Eq. (4.8) for the single-particle operator $A = c_{j,\mathbf{k}}^\dagger c_{i,\mathbf{k}}$ and then taking the ensemble average.

$$\frac{d}{dt} A = \frac{i}{\hbar} [H_0 + H_C, A] \quad (4.14)$$

Equation (4.14) shows that the temporal change of the expectation values is composed of two contributions, corresponding to the commutator with H_0 and H_C respectively.

The first term gives

$$\frac{d\rho_{j\mathbf{i}\mathbf{k}}}{dt} = \frac{i}{\hbar} (\epsilon_{j,\mathbf{k}} - \epsilon_{i,\mathbf{k}}) \rho_{j\mathbf{i}\mathbf{k}}$$

i.e., a rotation of the polarizations ($j \neq i$) in the complex plane, with a frequency corresponding to the energy difference between subband j and i , at wave vector \mathbf{k} . Note that this term due to H_0 can be observed also in the equations that we wrote for a two-level system with tunnel coupling, Eqs. (4.5).

Contrary to tunnel coupling, Coulomb interaction H_C leads to a coupling of the single-particle density matrices to two-particle density matrices $\langle c_{j',\mathbf{k}_2}^\dagger c_{i',\mathbf{k}_1}^\dagger c_{i,\mathbf{k}_1} c_{j,\mathbf{k}_2} \rangle$. The evolution of these two-particle density matrices can be obtained in the same way through Eq. (4.8): this would lead though to equations of motion containing three-particle density matrices, and so on. This is a manifestation of the Bogoliubov hierarchy [17]: the equation of an n -particle distribution function contains the $(n+1)$ - distribution function, generating thus a coupled chain of equations.

In order to obtain a closed set of equations, this infinite hierarchy of many-particle correlations must be truncated. One common approach is that of replacing the expectation value of a product of field operator pairs with the product of their expectation values, i.e. by introducing a mean-field (Hartree-Fock) approximation at some stage [62]. We will thus start from this single-particle approach in §4.2.2, and postpone a more detailed discussion of the hierarchy problem to section §4.2.3.

4.2.2. Single-particle density matrix

If we stick to the mean field (Hartree-Fock) approximation, we do not consider electron correlations beyond exchange interaction, and the relevant quantities are the density matrix elements $\langle c_{ik}^\dagger c_{jk} \rangle$:

$$\begin{aligned} n_{1\mathbf{k}} = \rho_{11\mathbf{k}} &= \langle c_{1\mathbf{k}}^\dagger c_{1\mathbf{k}} \rangle && \text{population subband 1} \\ n_{2\mathbf{k}} = \rho_{22\mathbf{k}} &= \langle c_{2\mathbf{k}}^\dagger c_{2\mathbf{k}} \rangle && \text{population subband 2} \\ \rho_{21\mathbf{k}} &= \langle c_{1\mathbf{k}}^\dagger c_{2\mathbf{k}} \rangle && \text{coherence 1-2} \end{aligned}$$

The equations of motion in the screened Hartree-Fock approximation can be written as [54, 100]:

$$\begin{aligned} \frac{dn_{2\mathbf{k}}}{dt} &= -\frac{i}{\hbar} \sum_{\mathbf{q} \neq 0} V_{\mathbf{q}}^{2112} (\rho_{21\mathbf{k}} \rho_{21\mathbf{k}+\mathbf{q}}^* - \rho_{21\mathbf{k}}^* \rho_{21\mathbf{k}+\mathbf{q}}) + \\ &\quad -\frac{i}{\hbar} V_0^{2121} \sum_{\mathbf{k}' \neq \mathbf{k}} (\rho_{21\mathbf{k}'} \rho_{21\mathbf{k}}^* - \rho_{21\mathbf{k}'}^* \rho_{21\mathbf{k}}) + \\ &\quad + \left. \frac{dn_{2\mathbf{k}}}{dt} \right|_{\text{incoherent}} \end{aligned} \quad (4.15)$$

$$\begin{aligned}
\frac{dn_{1\mathbf{k}}}{dt} = & + \frac{i}{\hbar} \sum_{\mathbf{q} \neq 0} V_{\mathbf{q}}^{1221} (\rho_{21\mathbf{k}} \rho_{21\mathbf{k}+\mathbf{q}}^* - \rho_{21\mathbf{k}}^* \rho_{21\mathbf{k}+\mathbf{q}}) + \\
& + \frac{i}{\hbar} V_0^{1212} \sum_{\mathbf{k}' \neq \mathbf{k}} (\rho_{21\mathbf{k}'} \rho_{21\mathbf{k}}^* - \rho_{21\mathbf{k}'}^* \rho_{21\mathbf{k}}) + \\
& + \left. \frac{dn_{1\mathbf{k}}}{dt} \right|_{\text{incoherent}}
\end{aligned} \tag{4.16}$$

$$\begin{aligned}
\frac{d\rho_{21\mathbf{k}}}{dt} = & -i\omega_{12}\rho_{21\mathbf{k}} + \\
& + \frac{i}{\hbar} \rho_{21\mathbf{k}} \sum_{\mathbf{q} \neq 0} (V_{\mathbf{q}}^{2222} n_{2\mathbf{k}+\mathbf{q}} - V_{\mathbf{q}}^{1111} n_{1\mathbf{k}+\mathbf{q}}) + \\
& + \frac{i}{\hbar} (n_{1\mathbf{k}} - n_{2\mathbf{k}}) \sum_{\mathbf{q} \neq 0} V_{\mathbf{q}}^{2112} \rho_{21\mathbf{k}+\mathbf{q}} + \\
& - \frac{i}{\hbar} (n_{1\mathbf{k}} - n_{2\mathbf{k}}) V_0^{2121} \sum_{\mathbf{k}' \neq \mathbf{k}} \rho_{21\mathbf{k}'} + \\
& + \left. \frac{d\rho_{21\mathbf{k}}}{dt} \right|_{\text{incoherent}}
\end{aligned} \tag{4.17}$$

In these equations of motion, the last term of the form $\left. \frac{d\rho_{ijk}}{dt} \right|_{\text{incoherent}}$ takes into account all the incoherent mechanisms, i.e. the non radiative relaxation ($\Gamma_{i\mathbf{k}}$), and the polarization decay rate (Γ_{ρ}). Also tunneling is not considered here as a coherent mechanism, but we include in our equations incoherent injection and extraction rates such that [101]:

$$\begin{aligned}
\left. \frac{dn_{1\mathbf{k}}}{dt} \right|_{\text{incoherent}} &= -\Gamma_{1\mathbf{k}}(n_{1\mathbf{k}} - n_{1\mathbf{k}}^0) - \Gamma_{\mathbf{k}}^{1,\text{out}} n_{1\mathbf{k}} + \Gamma_{\mathbf{k}}^{1,\text{in}}(1 - n_{1\mathbf{k}}) \\
\left. \frac{dn_{2\mathbf{k}}}{dt} \right|_{\text{incoherent}} &= -\Gamma_{2\mathbf{k}}(n_{2\mathbf{k}} - n_{2\mathbf{k}}^0) + \Gamma_{\mathbf{k}}^{2,\text{in}}(1 - n_{2\mathbf{k}}) - \Gamma_{\mathbf{k}}^{2,\text{out}} n_{2\mathbf{k}} \\
\left. \frac{d\rho_{21\mathbf{k}}}{dt} \right|_{\text{incoherent}} &= -\Gamma_{\rho} \rho_{21\mathbf{k}}
\end{aligned}$$

where $n_{1\mathbf{k}}^0$ and $n_{2\mathbf{k}}^0$ are the equilibrium occupation numbers. Figure 4.15 schematizes these incoherent processes.

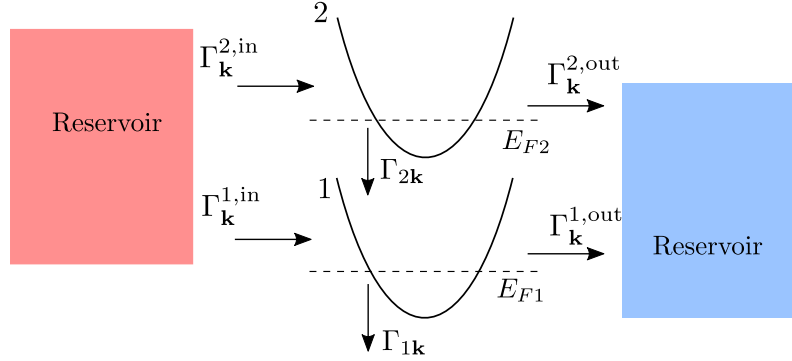


Figure 4.15: Schematic representation of the incoherent mechanisms included in Eqs. (4.15)-(4.17).

Following [99], let us consider negligible all Coulomb matrix elements except the depolarization terms at $\mathbf{q} = 0$ ($V_0^{2121} = V_0^{1212} = v$), which at high electronic densities are the only ones relevant for collective effects. With these assumptions, Eqs. (4.15)-(4.17) are simplified to:

$$\frac{dn_{2\mathbf{k}}}{dt} = -\frac{i}{\hbar}v \sum_{\mathbf{k}' \neq \mathbf{k}} (\rho_{21\mathbf{k}'} \rho_{21\mathbf{k}}^* - \rho_{21\mathbf{k}'}^* \rho_{21\mathbf{k}}) + \left. \frac{dn_{2\mathbf{k}}}{dt} \right|_{\text{incoherent}} \quad (4.18)$$

$$\frac{dn_{1\mathbf{k}}}{dt} = \frac{i}{\hbar}v \sum_{\mathbf{k}' \neq \mathbf{k}} (\rho_{21\mathbf{k}'} \rho_{21\mathbf{k}}^* - \rho_{21\mathbf{k}'}^* \rho_{21\mathbf{k}}) + \left. \frac{dn_{1\mathbf{k}}}{dt} \right|_{\text{incoherent}} \quad (4.19)$$

$$\frac{d\rho_{21\mathbf{k}}}{dt} = -i\omega_{12}\rho_{21\mathbf{k}} - \frac{i}{\hbar}v(n_{1\mathbf{k}} - n_{2\mathbf{k}}) \sum_{\mathbf{k}' \neq \mathbf{k}'} \rho_{21\mathbf{k}'} - \Gamma_{\rho} \rho_{21\mathbf{k}} \quad (4.20)$$

In the present model, differently from the Kazarinov-Suris model of Eqs. (4.5), the electron injection is an incoherent process. As a consequence, there is no source term for the coherences in the last of the equations above. Therefore, the system of equations (4.18)-(4.20) simply reduces to the incoherent rate equations described in §1.5.2. This means that in these equations the Coulomb term v cannot have any effect on the electron transport. For the terms $\rho_{21\mathbf{k}}$ to be relevant at this level of approximation, it would be necessary to introduce an additional coherence in the system, such as tunneling or an external electromagnetic field [54].

Generalized intersubband semiconductor Bloch Equations

If an electromagnetic field couples subbands 1 and 2, a source term is added to the equation describing the evolution of coherences. In this case, the modification of the equations of motion (4.15)-(4.17) leads to the intersubband semiconductor Bloch equations (ISBE). The latter are a generalization of the interband semiconductor Bloch equations [62, 102], which describe the optical response of a semiconductor system in the

presence of an applied coherent electromagnetic field.

Let us consider an applied field $E(z, t)$ of amplitude \mathcal{E} , with a detuning Δ with respect to the intersubband transition frequency ω_{12} . We recall the definition of the Rabi frequency $\Omega = z_{12}\mathcal{E}/\hbar$ (with z_{12} optical dipole), which expresses the coupling between the transition and the external field. If we consider just the depolarization terms as above, Eqs. (4.18)-(4.20) read [48, 49, 54, 59]:

$$\begin{aligned} \frac{dn_{2\mathbf{k}}}{dt} &= + 2 \operatorname{Im} [\Omega \rho_{21\mathbf{k}}] + \\ &\quad - \frac{i}{\hbar} v \sum_{\mathbf{k}' \neq \mathbf{k}} (\rho_{21\mathbf{k}'} \rho_{21\mathbf{k}}^* - \rho_{21\mathbf{k}'}^* \rho_{21\mathbf{k}}) + \left. \frac{dn_{2\mathbf{k}}}{dt} \right|_{\text{incoherent}} \\ \frac{dn_{1\mathbf{k}}}{dt} &= - 2 \operatorname{Im} [\Omega \rho_{21\mathbf{k}}] + \\ &\quad + \frac{i}{\hbar} v \sum_{\mathbf{k}' \neq \mathbf{k}} (\rho_{21\mathbf{k}'} \rho_{21\mathbf{k}}^* - \rho_{21\mathbf{k}'}^* \rho_{21\mathbf{k}}) + \left. \frac{dn_{1\mathbf{k}}}{dt} \right|_{\text{incoherent}} \\ \frac{d\rho_{21\mathbf{k}}}{dt} &= + i\Delta \rho_{21\mathbf{k}} + i\Omega(n_{1\mathbf{k}} - n_{2\mathbf{k}}) + \\ &\quad - \frac{i}{\hbar} v (n_{1\mathbf{k}} - n_{2\mathbf{k}}) \sum_{\mathbf{k}' \neq \mathbf{k}} \rho_{21\mathbf{k}'} - \Gamma_\rho \rho_{21\mathbf{k}} \end{aligned}$$

A common notation that simplifies the expression of the above equations is the definition of the generalized Rabi frequency modified by Coulomb interaction [62, 103], in this case

$$\tilde{\Omega}_{\mathbf{k}} = \frac{1}{\hbar} \left[z_{12}\mathcal{E} - v \sum_{\mathbf{k}' \neq \mathbf{k}} \rho_{21\mathbf{k}'} \right] = \Omega - \frac{1}{\hbar} v \sum_{\mathbf{k}' \neq \mathbf{k}} \rho_{21\mathbf{k}'}$$

As expected, for a non vanishing external field \mathcal{E} , Coulomb interaction has an impact on the electron dynamics, as the polarizations $\rho_{21\mathbf{k}}$ do not go to zero.

A further generalization of ISBE to include coherent tunneling can also be made [103, 104]. This approach thus seems to be promising in order to treat electronic transport in the presence of tunnel coupling and light-matter interaction, including the effect of the depolarization field. As an example, they are suitable to describe an intersubband system under optical pumping [54].

4.2.3. Cluster-expansion approach

In this section, we analyze the form of the equations of motion for the populations and the coherences beyond the Hartree-Fock approximation [17].

In general, we can write the expectation value of an observable as

$$\langle \hat{O} \rangle = \langle a_1^\dagger \cdots a_K^\dagger a_J \cdots a_1 c_1^\dagger \cdots c_{N_F}^\dagger c_{N_F} \cdots c_1 \rangle$$

where \hat{O} consists of N_F fermionic operators and $N_B = J + K$ bosonic operators³. We can then define an order $N = N_B + N_F$ for each operator, corresponding to the number of bosonic operators and couples of fermionic operators composing it. Operators with the same order are considered formally equivalent.

It can be shown [17] that Coulomb interaction and coupling to photons lead to hierarchy problems in the dynamical evolution of observables in the form

$$i\hbar \frac{d}{dt} \langle N \rangle = T[\langle N \rangle] + Hi[\langle N + 1 \rangle] \tag{4.21}$$

Equation (4.21) shows that the evolution of an operator of order N can be split in two contributions: a functional T of N -particle operators expectation values and a functional Hi representing coupling to higher order operators.

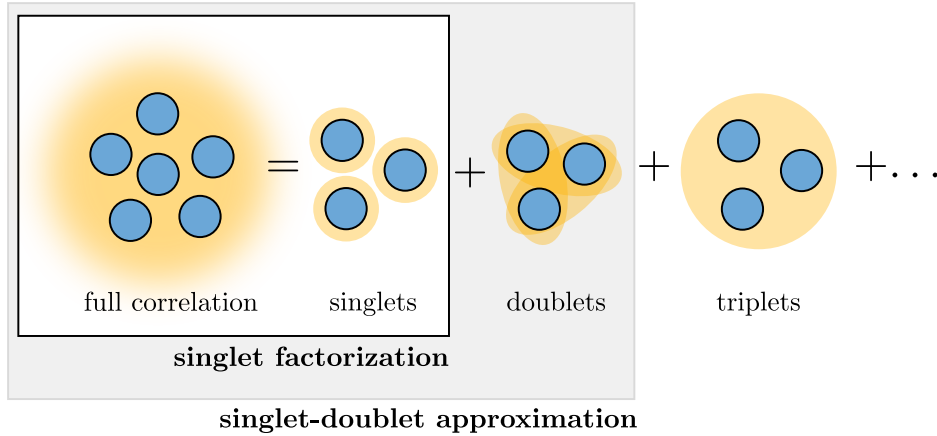


Figure 4.16: Schematic representation of the cluster-expansion-based classification. The full correlation is composed of singlets, doublets, triplets, and higher-order correlations, all uniquely defined by the cluster-expansion approach. Each blue sphere corresponds to one particle operator and yellow circles/ellipses to correlations. The number of spheres within a correlation identifies the cluster number.

The hierarchy problem is then encountered when using the equation of motion method to study the dynamics of a light-matter coupled system. A way to deal with this is the so-called cluster expansion method, in which many-body quantities are systematically grouped into clusters based on their importance for the overall quantum dynamics. These clusters contain (in order of complexity):

1. independent single particles (singlets);
2. interacting pairs (doublets);
3. interacting groups of three particles (triplets);

³The number of fermionic creation and annihilation operators must be equal for the expectation value to be different from zero.

4. and so on with higher orders.

In order to truncate the hierarchy at a set level, $\langle N \rangle$ is approximated through a functional containing clusters up to the desired order. In most cases, the method converges quickly, and the first two orders suffice [17]. In this approximation, one has to study not only the time evolution of the single-particle expectation values $\langle 1 \rangle$, as in Hartree-Fock approximation, but also the evolution of two-particle correlations, usually indicated as $\Delta \langle 2 \rangle$.

Correlations up to second order

Following Ref. [101, 105], we write the equations of motion for a fermionic system in the presence of Coulomb interaction, retaining correlations up to order 2. We consider just vertical transitions ($\mathbf{q} = 0$). We introduce the two-particle correlation

$$X_{imnj}(\mathbf{k}, \mathbf{k}') = \Delta \langle c_{j\mathbf{k}} c_{n\mathbf{k}'} c_{m\mathbf{k}}^\dagger c_{i\mathbf{k}}^\dagger \rangle$$

with the symmetry property $X_{imnj} = X_{jnmi}^*$. In the case of a two-subband system, retaining as previously just depolarization terms, $V_0^{1122} = V_0^{2211} = V_0^{1212} = V_0^{2121} = v$, we find⁴:

$$\frac{dn_{1\mathbf{k}}}{dt} = -\frac{i}{2\hbar}v \sum_{\mathbf{k}'} [X_{1212}(\mathbf{k}, \mathbf{k}') - X_{1212}^*(\mathbf{k}, \mathbf{k}') + X_{1122}(\mathbf{k}, \mathbf{k}') - X_{1122}^*(\mathbf{k}, \mathbf{k}')] + \left. \frac{dn_{1\mathbf{k}}}{dt} \right|_{\text{incoherent}} \quad (4.22)$$

$$\frac{dn_{2\mathbf{k}}}{dt} = \frac{i}{2\hbar}v \sum_{\mathbf{k}'} [X_{1212}(\mathbf{k}, \mathbf{k}') - X_{1212}^*(\mathbf{k}, \mathbf{k}') + X_{1122}(\mathbf{k}, \mathbf{k}') - X_{1122}^*(\mathbf{k}, \mathbf{k}')] + \left. \frac{dn_{2\mathbf{k}}}{dt} \right|_{\text{incoherent}} \quad (4.23)$$

$$\begin{aligned} \frac{dX_{1212}(\mathbf{k}, \mathbf{k}')}{dt} = & -\frac{i}{\hbar}v \left\{ + [X_{1212}(\mathbf{k}, \mathbf{k}') + X_{1122}^*(\mathbf{k}, \mathbf{k}')] (n_{1\mathbf{k}} - n_{2\mathbf{k}}) + \right. \\ & - [X_{1212}(\mathbf{k}, \mathbf{k}') + X_{1122}(\mathbf{k}, \mathbf{k}')] (n_{1\mathbf{k}'} - n_{2\mathbf{k}'}) + \\ & \left. + G_{1212}(\mathbf{k}, \mathbf{k}') \right\} + \left. \frac{dX_{1212}(\mathbf{k}, \mathbf{k}')}{dt} \right|_{\text{incoherent}} \quad (4.24) \end{aligned}$$

$$\begin{aligned} \frac{dX_{1122}(\mathbf{k}, \mathbf{k}')}{dt} = & -2iE_{12}X_{1122}(\mathbf{k}, \mathbf{k}') - \frac{i}{\hbar}v \left\{ + [X_{1212}^*(\mathbf{k}, \mathbf{k}') + X_{1122}(\mathbf{k}, \mathbf{k}')] (n_{1\mathbf{k}} - n_{2\mathbf{k}}) + \right. \\ & + [X_{1212}(\mathbf{k}, \mathbf{k}') + X_{1122}(\mathbf{k}, \mathbf{k}')] (n_{1\mathbf{k}'} - n_{2\mathbf{k}'}) + \\ & \left. + G_{1122}(\mathbf{k}, \mathbf{k}') \right\} + \left. \frac{dX_{1122}(\mathbf{k}, \mathbf{k}')}{dt} \right|_{\text{incoherent}} \quad (4.25) \end{aligned}$$

where

$$G_{imnj}(\mathbf{k}, \mathbf{k}') = [(1 - n_{j\mathbf{k}})(1 - n_{n\mathbf{k}'})n_{m\mathbf{k}}n_{i\mathbf{k}} - n_{j\mathbf{k}}n_{n\mathbf{k}'}(1 - n_{m\mathbf{k}})(1 - n_{i\mathbf{k}})]$$

⁴To obtain this system of equations, we neglect the polarizations corresponding to exchange (X_{1221} , X_{2112}).

is a collision term, as in Boltzmann transport equation [63, 97, 105]. Neglecting the other corrections on the left-hand side of the equation, this term would lead to an electron-electron scattering rate equivalent to what would be obtained applying Fermi's golden rule (see Eq. §B.5) [63].

We can appreciate the fact that while the polarization terms in Eqs. (4.15)-(4.17) are expressed in the form

$$\rho_{21\mathbf{k}}^* \rho_{21\mathbf{k}'} = \langle c_{2,\mathbf{k}}^\dagger c_{1,\mathbf{k}} \rangle \langle c_{1,\mathbf{k}}^\dagger c_{2,\mathbf{k}} \rangle$$

the presence of the correlations $X(\mathbf{k}, \mathbf{k}')$ in Eqs. (4.22)-(4.25) is the manifestation of a higher-order approximation.

Differently from the single-particle picture, in this case the collision terms G_{1212} and G_{1122} are source terms for the correlations X . Nevertheless, a numerical analysis of this problem needs to be performed to evaluate the extent of the impact of these second-order correlations on transport.

The numerical implementation of the system of equations (4.22)-(4.25), describing transport in a two-subband system, is already quite complex. Its generalization to an arbitrary number of occupied subbands would be even more challenging. For this reason, it could be interesting to explore other possible theoretical tools to tackle this interesting but difficult physical problem (see for example Refs. [98]).

Conclusions

In the first part of this chapter, we have presented a simplified density matrix model accounting for coherent tunneling between quantum wells. As an application, we showed in §4.1.2 that this formalism can be used to study electron transport in QCLs. Its general matrix form allows for the inclusion of an arbitrary number of electronic levels, making possible the application both to mid-IR and THz lasers. The low computational complexity of the method makes it particularly suitable for establishing a quick and direct link with experimental characterization and design, of which we show an application in a systematic study of MOCVD-grown QCLs in Appendix D.

The second part of the chapter has presented a preliminary study on the effect of the inclusion of Coulomb interaction in an electron transport model. We have shown how a single-particle density matrix model with the sole inclusion of depolarization terms reduces to a semiclassical rate equations approach, like the one presented in §1.5.2. On the other hand, a formulation of the problem in the presence of an external electromagnetic field is described by the intersubband semiconductor Bloch equations, and could be used to characterize systems featuring an optical pump.

An analysis of the equations of motion with depolarization terms written including second-order correlations (§4.2.3) shows instead a deviation from the rate equations, thanks to the presence of a collision term. As a perspective, its influence on coherences and thus on the electron transport may be numerically investigated.

A final perspective of this subject is the possibility of including in the same description coherent tunneling and second-order correlations.

Conclusions and perspectives

This work has focused on the investigation of the interplay between two couplings in systems of semiconductor quantum wells: resonant tunneling and dipole-dipole interaction. The main impulse for this theoretical analysis has been the recent experimental demonstration [14] of the possibility of creating collective bright states in highly doped semiconductor quantum wells, the multisubband plasmons.

A relevant part of the work has been devoted to the development of a fully quantum model for the optical response of highly doped semiconductor quantum well potentials, where both tunneling and collective effects have a role. This formalism, based on the diagonalization of a bosonized Hamiltonian, has been the object of Chapter 2. We have shown how the macroscopic optical response can be understood in terms of microscopic polarizations and their mutual couplings. The absorption spectra have been derived in terms of microcurrents, describing the collective charge oscillations. A sum rule for the conservation of oscillator strength in the system has been obtained, stating that the collective modes concentrate the whole absorption strength of all individual intersubband transitions. These results have been recently published in *Phys. Rev. B* (Ref. [16]).

We have presented in Chapter 3 an extensive investigation of significant cases of application of our model. Firstly, we have shown that our method correctly recovers the experimental results [14] in the case of a single heavily doped quantum well. Successively, we have examined the role of tunneling in coupled wells. We have observed structures featuring more than one characteristic length, suggesting the coexistence of multiple multisubband plasmons associated with each of these lengths. This study can be considered as a first step towards multisubband plasmon engineering.

In this perspective, we have also investigated the coupling between a multisubband plasmon and a single-particle transition, as this system may prove promising for electrical resonant excitation of collective states. Finally, in Chapter 3 we have also theoretically demonstrated that multisubband plasmons can be ultra-strongly coupled with a cavity mode (an experimental proof of this can be found in Refs. [14, 67]).

Chapter 4 has been dedicated to the investigation of a method to account for coherent

tunneling and collective effects in the description of electron transport. In the absence of depolarization effects, a density matrix model [93] is suitable to describe both the effect of coherent tunneling and incoherent relaxation. This formalism has been applied to the case of both THz and mid-IR quantum cascade lasers. A complete transport model also including collective effects constitutes a much more complex problem. A preliminary study has been presented in the second part of the chapter, but needs to be completed by further investigation. The definition and implementation of a complete transport model fully accounting for coherent tunneling and collective effects would indeed represent a relevant result for design and modeling of devices based on collective effects.

One major accomplishment of this thesis is the implementation of a model that allows one to use collective effects as a new degree of freedom in the design of electronic devices. The developed numerical tools may prove useful in this sense, in the same way as the numerical calculation of wavefunctions is essential to the design of QCLs. Furthermore, the bosonic character of multisubband plasmons suggests the possibility of investigating mechanisms of stimulated emission, for example in a system where two or more multisubband plasmons are present. In this perspective, the scattering between collective states, assisted for example by phonons or impurities, has to be investigated.

An experimental investigation of electrical excitation of the multisubband plasmon mode has been recently carried out by our team [15, 65]. In the experiment, a structure based on heavily doped quantum wells is inserted in a transistor-like device. When a source-drain voltage is applied to the device, an electrical current flows in the quantum well plane and the electron gas is thermally excited. The observed electroluminescence signal features a peak at the same energy as the corresponding multisubband plasmon absorption resonance, suggesting its origin to be the spontaneous emission from the collective mode. The experimental results suggest that the associated lifetime is ≈ 100 fs [15], thus several orders of magnitude shorter than the typical intersubband spontaneous emission lifetime (≈ 100 ns). Theoretical calculations based on non-local electrodynamics also predict a similar result [106]. The formalism of the bosonized Hamiltonian discussed in Chapter 2 could be also used to calculate this spontaneous emission rate within Fermi's golden rule, and even beyond in a non-perturbative approach.

Finally, a fascinating perspective is that of a spatial mapping of the plasmons through Electron Energy Loss Spectroscopy (EELS). The feasibility of this kind of technique has been recently demonstrated in the case of metallic nanoparticles [107]. It could in principle be possible to map plasmons in quantum wells, and establish a direct link between the microscopic collective charge densities discussed in Chapters 2 and 3 and the outcomes of an EELS experiment. This would equally be an opportunity to study dark multisubband modes, otherwise undetectable to standard absorption measurements. A direct experimental study of the effects of tunneling on the spatial distribution of polarization would represent an appealing complement to the theoretical investigations realized in the course of this work. In this context, a collaboration between the Laboratoire de Physique des Solides (Orsay) and our group has been recently established. The project will take advan-

tage of the new generation of microscope that will be soon available at LPS, featuring an energy resolution of 10 meV and a spatial resolution of 1 nm.

A

Implementation details

We present here a scheme of the programs used for the numerical calculations needed in this work, along with some implementation details specified here to simplify the main text. Two C++ codes have been written for two different goals:

- The calculation of the absorption spectra in systems of highly doped quantum wells. The corresponding model is detailed in Chapter 2, and examples of applications are provided in Chapter 3.
- The calculation of current-voltage characteristics in multiple quantum wells, accounting for coherent tunneling, presented in the first part of Chapter 4. A more detailed description of the implemented algorithm can be found in §C.2.

These two programs share a common part for the band structure calculation, based on the Kane model presented in §1.1.2.

A.1. Absorption spectrum calculation

Figure A.1 summarizes the procedure followed to obtain the absorption spectra of systems of highly doped quantum wells, as those presented in Chapter 3.

The first step required is the band structure calculation. Given the doping of the structure, the program determines next the population density N_i of each level through the procedure detailed in §A.1.1.

Microscopic current distributions $\xi_\alpha(z)$ [Eq. (2.70)] for each transition $\alpha \equiv i \rightarrow j$ can then be obtained from wavefunctions $\psi_i(z)$, along with the single particle absorption spectrum [Eq. (2.74)]. Wavefunctions, along with level populations, are sufficient to calculate for each transition the plasma frequency $\omega_{P\alpha}$ [Eq. (2.72)], and the couplings $\Xi_{\alpha\beta}$ [Eq. (2.73)] for each couple of transitions.

The core of the calculation is the diagonalization of the matrix \mathbf{M} [Eq. (2.54)], from which the new resonances W_n and their amplitudes $W_n F_n$ are determined. The eigenvalues and eigenvectors of \mathbf{M} are also used in the determination of the collective currents J . The graphical representation of these quantities, as the one shown also in Fig. A.1, is obtained through a Python/Matplotlib script.

The absorption spectrum is finally calculated by considering a Lorentzian shape with phenomenological broadening γ for each of these collective resonances, using Eq. (2.75).

A.1.1. Electron population distribution

One of the first steps of the program schematized in Fig. A.1 is the calculation of the electronic levels' populations.

We call the confining energies $E_i(0)$. The dispersion curves of the subbands are given by the self-consistent formula [52]:

$$E_i(k) = E_i(0) + \frac{\hbar^2 k^2}{2m^*(k)} = E_i(0) + \frac{\hbar^2 k^2}{2m_0} \frac{E_p}{3} \left[\frac{2}{E_i(k) + E_g} + \frac{1}{E_i(k) + E_{SO} + E_g} \right]$$

where E_p is the Kane energy, E_g the gap, and E_{SO} the split-off band energy.

We fix the electronic density of the system, and numerically deduce the Fermi level from the expression:

$$N = \sum_i N_i = \sum_i \int dE \rho_i(E) f_{\text{FD}}(E) \quad (\text{A.1})$$

with $f_{\text{FD}}(E)$ Fermi-Dirac distribution

$$f_{\text{FD}}(E) = \frac{1}{e^{\frac{E-E_F(T)}{k_B T}} + 1}$$

and $\rho_i(E)$ density of states per unit of surface:

$$\rho_i(E) = \rho_i(k) \frac{dk}{dE} = \frac{1}{\pi} k \frac{dk}{dE} = \frac{1}{\pi \hbar^2} \left[m^*(E) + E \frac{dm^*}{dE} \right] \quad (\text{A.2})$$

The successive steps in the calculation of the subband populations are:

1. Definition of the Kane effective mass $m(E)$ [Eq. (1.9)] (in parabolic approximation, this is constant and equal to m_w).
2. Numerical calculation of the derivative $\frac{dm^*}{dE}$ (in parabolic approximation, equal to 0).
3. Construction of the density of states $\rho(E)$ with Eq. (A.2), (in parabolic approximation, equal to $\frac{m_w}{\pi \hbar^2}$).
4. Construction of the density $\rho_{2D}(E) = \sum_i \rho(E)$ (in parabolic approximation, step density over the levels).
5. Calculation of the Fermi energy $E_F = E_F(0)$ by filling the levels up to N_s : $n_s = e \sum_i \Delta E \rho_{2D}(E_i)$ [corresponding to Eq. (A.1) at $T = 0$, with $f_{\text{FD}} = \Theta(E_F)$].
6. Calculation of the Fermi level $E_F(T)$ through the convergence of the expression

$$n_s = e \sum_i \Delta E \rho_{2D}(E_i) \frac{1}{e^{\frac{E-E_F(T)}{k_B T}} + 1}$$

with initial guess $E_F(T) = E_F$.

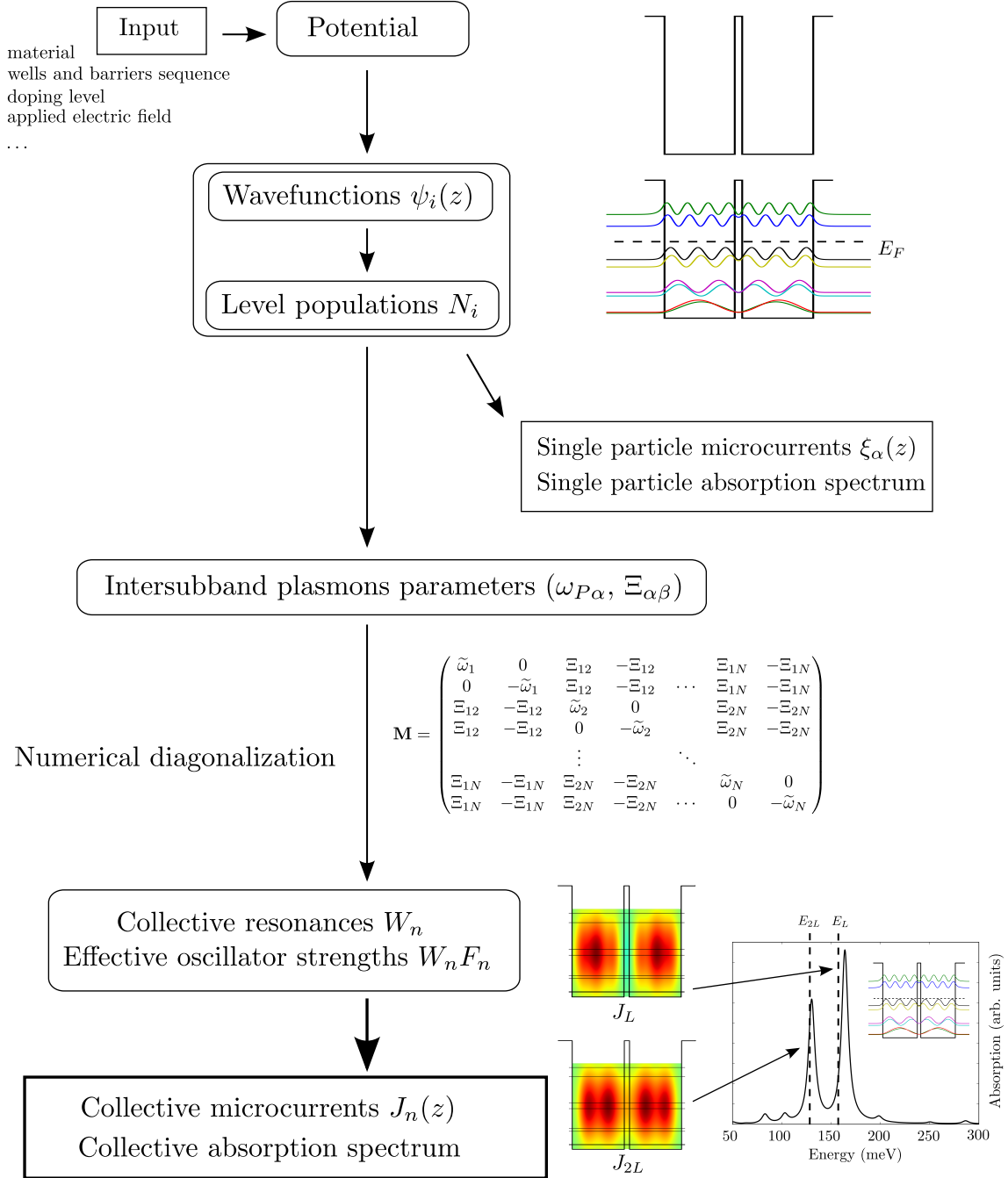


Figure A.1: Scheme of the code for the calculation of the optical response of highly doped MQWs, based on the model discussed in Chapter 2.

7. Calculation of the subband populations N_j with Eq. (A.1).
In parabolic approximation,

$$N_j = e \sum_{E_i=E_j}^{E_{\max}} \Delta E \frac{m_w}{\pi \hbar^2} f_{\text{FD}}(E_i)$$

If nonparabolicity is accounted for, the infinitesimal population element is

$$dn_j(k) = \rho(E_j(k)) \frac{dE_i(k)}{dk} f_{\text{FD}}(E(k)) dk$$

which we numerically implement as

$$N_j = \frac{1}{\pi \hbar^2} \sum_k \left(m_{j,k} + E_{j,k} \frac{m_{j,k+1} - m_{j,k}}{E_{j,k+1} - E_{j,k}} \right) (E_{j,k+1} - E_{j,k}) f_{\text{FD}}(E_{j,k})$$

A.2. Density matrix model for electron transport

Figure A.2 schematizes the code for the calculation of electron transport in MQWs with the inclusion of coherent tunneling, as presented in §4.1.

The program consists of two independent parts:

- First, intersubband scattering times and coherences are calculated over a range of applied electric field values.
The starting point for this step is the band structure calculation. The latter is performed twice, considering two bases: extended and localized (see §1.2), as schematized in the upper part of Fig. A.2. Intersubband scattering times τ_{ij} due to interface roughness, alloy scattering and LO-phonon emission (see Appendix B) are calculated over a range of external applied electric fields. At the end of the loop on the external applied fields, tunnel couplings Ω_{ij} are obtained from the comparison between energies in extended and localized basis, as schematized in Fig. A.2 (see also Fig. 4.8 and related discussion).
- Once the quantities τ_{ij} and Ω_{ij} have been calculated, it is possible to follow the procedure based on density matrix formalism, detailed in §C.2, to obtain the level populations ρ_{ii} and the coherences differences ($\rho_{ij} - \rho_{ji}$) at the steady state. Given the laser specifications (number of periods, ridge length, ridge width, doping), these allow the calculation of I-V characteristics. It is possible to account also for stimulated emission and obtain L-I curves, as described in §4.1.2.

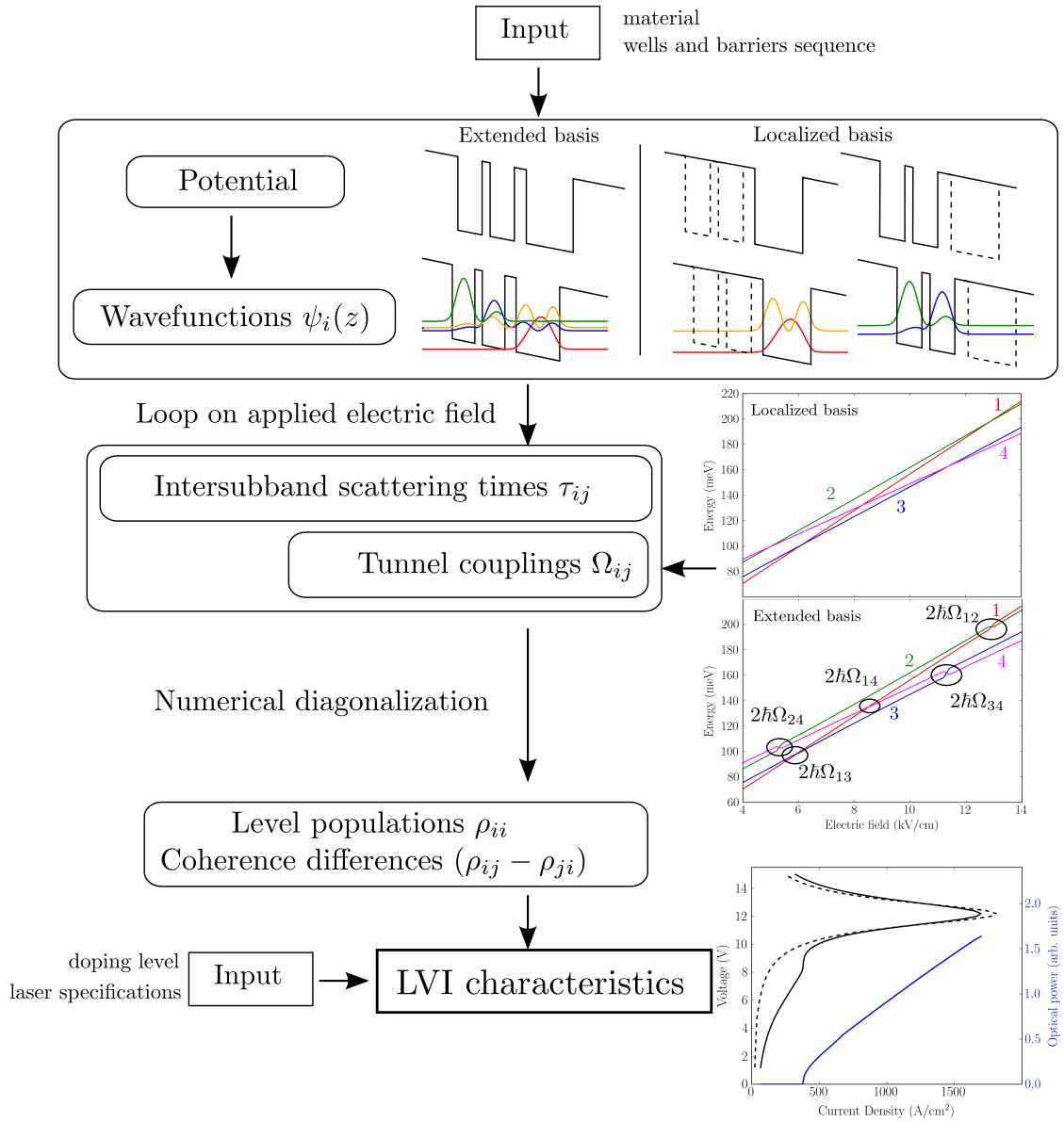


Figure A.2: Scheme of the code for the calculation of electron transport with a density matrix formalism, discussed in §4.1 and §C.2.

B

Intersubband and intrasubband scattering times

We give here some details for the calculation of intersubband and intersubband scattering times introduced in §1.4. Throughout the discussion, we follow Ref. [33] for the main definitions, which is in turn based on Ando's work [30, 32, 108].

B.1. Interface roughness

Interface roughness is caused by growth imperfections at the junction between two semiconductors. Fluctuations of interface concentration occur over one monolayer, creating static scatterers that diffuse electrons. The distribution of these defects is not precisely known, and can be assumed to be Gaussian [30, 33, 109].

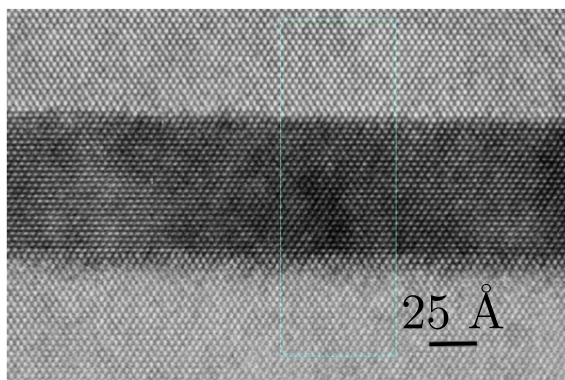


Figure B.1: Electronic microscope image of two interfaces in an InAs/AlSb structure (Université de Montpellier).

Let us consider a single interface, which we label m . We model the mean height of the

roughness $\Delta(\mathbf{r})$ through the auto-correlation function

$$\langle \Delta(\mathbf{r})\Delta(\mathbf{r}') \rangle = \Delta^2 \exp\left(-\frac{|\mathbf{r} - \mathbf{r}'|^2}{\Lambda^2}\right)$$

where Δ is the mean height of the roughness and Λ is the in-plane correlation length. This relation means that the distance between similar composition fluctuations follows a Gaussian law, the mean distance being given by Λ . The interaction Hamiltonian can be written as

$$H_{\text{rough}} = V_0 \delta(z - z_m) \Delta(\mathbf{r})$$

with V_0 band discontinuity between well and barrier semiconductors, and z_m position of the interface.

The scattering matrix element is given by

$$\langle j\mathbf{k}' | H_{\text{rough}} | i\mathbf{k} \rangle = \int F_{ji}^m \Delta(\mathbf{r}) e^{i\mathbf{q}\cdot\mathbf{r}} d^2\mathbf{r}$$

where $\mathbf{q} = \mathbf{k} - \mathbf{k}'$ is the exchanged momentum and

$$F_{ij}^m = F_{ji}^m = -\delta V(z_m) \psi_i(z_m) \psi_j(z_m) \quad \delta V(z_m) = V(z_m^+) - V(z_m^-)$$

strength of the interaction, where $V(z)$ is the conduction band-edge profile. Interface roughness is equivalent to fluctuations of the well width, and it can be shown that in the case of an infinite quantum well

$$F \propto L^{-3}$$

As the typical well width for structures operating in the mid-infrared is smaller than that of far-infrared structures, we expect the interface roughness to play a more important role in the mid-infrared frequency range [35].

Intersubband interface roughness scattering

For the intersubband scattering time due to interface roughness, Eq. (1.24) gives for a transition $i \rightarrow j$ [35, 110]:

$$\frac{1}{\tau_{ij}^{\text{inter,IR}}} = \frac{m^*}{\hbar^3} \Lambda^2 \Delta^2 \sum_{m,n} F_{ij}^m F_{ij}^n \int_0^\pi \exp\left(-\frac{q^2(\theta)\Lambda^2}{4}\right) d\theta$$

with q exchanged momentum and θ angle between \mathbf{k} and \mathbf{k}' . In the case $\mathbf{k} = 0$, this exchanged momentum is equal to

$$\tilde{q} = \sqrt{\frac{2m^* E_{ij}}{\hbar^2}} \quad E_{ij} = E_i - E_j$$

and therefore

$$\frac{1}{\tau_{ij}^{\text{inter,IR}}} = \frac{\pi m^*}{\hbar^3} \Lambda^2 \Delta^2 \sum_{m,n} F_{ij}^m F_{ij}^n \exp\left(-\frac{\tilde{q}^2 \Lambda^2}{4}\right) \quad (\text{B.1})$$

which is valid if $E_{ij} > 0$, that is for transitions to lower energy subbands.

Equation (B.1) can be easily extended in order to take into account the vertical correlation of the roughness between interfaces [111].

Intrasubband interface roughness scattering

The calculations to obtain the contribution of interface roughness to intrasubband scattering are similar to the ones for the intersubband term. The strength of the interaction is given by

$$F_{jj}^m = V_0 \psi_j^2(z_m) \quad F_{ii}^m = V_0 \psi_i^2(z_m)$$

The intrasubband scattering rate of Eq. (1.25) in the case of interface roughness is

$$\frac{1}{\tau_{ij}^{\text{intra,IR}}} = \frac{\pi m^*}{\hbar^3} \Lambda^2 \Delta^2 \sum_{m,n} (F_{jj}^m - F_{ii}^m) (F_{jj}^n - F_{ii}^n) \quad (\text{B.2})$$

B.2. Alloy disorder

In the presence of ternary semiconductor layers of the type $A_x B_{1-x} C$, electrons are scattered by the alloy disorder [33, 112]. The scattering Hamiltonian is

$$H_{\text{alloy}} = \Delta E_C \delta x(r)$$

where ΔE_C is the difference in conduction band minima of crystals AC and BC (in the case of $\text{Al}_x \text{Ga}_{1-x} \text{As}$, AlAs and GaAs) and $\Delta x(r)$ is the concentration fluctuation that we model once again via the correlation function

$$\langle \Delta x(r) \Delta x(r') \rangle = \frac{a^2}{4} x(1-x) \Delta(r-r')$$

where a is the lattice constant. The corresponding scattering matrix element for alloy disorder is given by [33]

$$|\langle j\mathbf{k}' | H_{\text{alloy}} | i\mathbf{k} \rangle|^2 = \frac{a^3 (\Delta E_C)^2 x(1-x)}{4} \int_{\text{alloy}} \psi_i^2(z) \psi_j^2(z) dz$$

and the integral is performed over all the region containing an alloy. Note that there is no energy dependence, so that two wavefunctions distant in energy but with an important overlap may be characterized by a short alloy scattering time. The expression is also independent of the scattering vector owing to the short-range nature of the scatterers. Therefore, we have [35, 112]

$$\frac{1}{\tau_{ij}^{\text{inter,AD}}} = \frac{1}{8} \frac{m_i^* a^3 (\Delta E_C)^2 x(1-x)}{\pi \hbar^3} \int_{\text{alloy}} \psi_i^2(z) \psi_j^2(z) dz$$

Following [113], the previous formula in case of quaternary compounds $A_{1-x} B_x C_{1-y} D_y$ holds if the factor $x(1-x)(\Delta E_C)^2$ is replaced by

$$x(1-x)(1-y)^2 |\Delta U_{ABC}|^2 + x(1-x)y^2 |\Delta U_{ABD}|^2 + y(1-y)x^2 |\Delta U_{BCD}|^2 + y(1-y)(1-x)^2 |\Delta U_{ACD}|^2 \quad (\text{B.3})$$

where ΔU_{ABC} denotes the difference in conduction band minima in the ternary ABC. As expected, Eq. (B.3) recovers the result for ternary alloys in the case $y = 1$.

B.3. Electron-electron scattering

In intersubband electron-electron scattering, two electrons exchange energy and momentum. Provided that the total energy and momentum are conserved, electrons may also change subband, therefore the process is usually labeled with four indexes. We adopt the convention of process $imnj$ being an interaction with an electron scattering from subband j to i and a second electron scattering from n to m (see also Figs. 4.12 and 4.14 in the main text).

The calculation of the electron-electron scattering rate depends on the Coulomb matrix element introduced in §4.2:

$$V_{\mathbf{q}}^{imnj} = \frac{e^2}{2\varepsilon_0\varepsilon_s q} \int_{-\infty}^{+\infty} dz \int_{-\infty}^{+\infty} dz' \psi_i(z)\psi_j(z)e^{-q|z-z'|}\psi_m(z')\psi_n(z') = \quad (\text{B.4})$$

where q is the wavevector exchanged during the process. The transition rate for electron-electron scattering can be evaluated using Fermi's golden rule. The total scattering out an initial electron state (j, \mathbf{k}_j) reads [3, 114, 115]

$$\begin{aligned} \Gamma^{imnj}(\mathbf{k}_j) = & \frac{2\pi}{\hbar} \int d^2\mathbf{k}_m \int d^2\mathbf{k}_n \int d^2\mathbf{k}_i \frac{|V_{\mathbf{q}}^{imnj}|^2}{\varepsilon_{\text{sc}}(q)} n_n(\mathbf{k}_n)(1 - n_i(\mathbf{k}_i))(1 - n_m(\mathbf{k}_m)) \times \\ & \times \delta(E_i(\mathbf{k}_i) + E_m(\mathbf{k}_m) - E_n(\mathbf{k}_j) - E_j(\mathbf{k}_m)) \delta(\mathbf{k}_i + \mathbf{k}_m - \mathbf{k}_n - \mathbf{k}_j) \end{aligned} \quad (\text{B.5})$$

with ε_{sc} correction to permittivity due to screening, and $n_i(\mathbf{k}_i)$ carrier distribution function. We note that the calculation of this rate requires a computationally expensive three-dimensional integral.

B.4. Inelastic scattering: LO phonon

The emission of longitudinal optical phonons is the most efficient relaxation mechanism for intersubband relaxation, and it is widely exploited in the band structure engineering for quantum cascade lasers (see §1.5).

The interaction Hamiltonian corresponding to the relaxation from a subband i to a subband j via emission of a LO phonon is given by the sum over the possible different phonon modes defined by the vector $\mathbf{q} = (\mathbf{q}_{\parallel}, q_z)$ [109, 116]:

$$H_{\text{e-phonon}} = \sum_{\mathbf{q}} \alpha(\mathbf{q}) e^{-i\mathbf{q}\cdot\mathbf{r}} b_{\mathbf{q}}^{\dagger} + \alpha^*(\mathbf{q}) e^{i\mathbf{q}\cdot\mathbf{r}} b_{\mathbf{q}}$$

where $b_{\mathbf{q}}^{\dagger}$ is the creation operator for a phonon in the mode \mathbf{q} and

$$|\alpha(\mathbf{q})|^2 = 2\pi\hbar\omega_{\text{LO}} \frac{e^2}{\varepsilon_p V q}$$

is the strength of the electron-optical phonon interaction (Frölich term), with $\varepsilon_p = \frac{4\pi\varepsilon_0}{\varepsilon_{\infty}^{-1} - \varepsilon_s^{-1}}$ (ε_{∞} high-frequency, ε_s static permittivity), V volume of the system and $\hbar\omega_{\text{LO}}$ energy of

one phonon.

We consider just the bulk phonon modes of the well material. We also approximate the energy dispersion of the phonons to be flat and equal to the energy at $q = 0$. The scattering rate due to LO phonon emission at $T = 0$ K is equal to [109]

$$\frac{1}{\tau_{ij}^{\text{inter,LO}}|_{0\text{K}}} = \frac{m^* e^2 \omega_{\text{LO}}}{2\hbar^2 \epsilon_p} \int_0^{2\pi} \frac{I^{ij}(Q)}{Q} d\theta \quad (\text{B.6})$$

with

$$\begin{aligned} Q &= \sqrt{k_i^2 + k_j^2 - 2k_i k_j \cos \theta} \\ k_j^2 &= k_i^2 + \frac{2m^*}{\hbar} (E_i - E_j - \hbar\omega_{\text{LO}}) \end{aligned} \quad (\text{B.7})$$

The integral $I^{ij}(Q)$ is defined as

$$I^{ij}(Q) = \int dz \int dz' \psi_i(z) \psi_j(z) e^{-Q|z-z'|} \psi_i(z') \psi_j(z')$$

At finite temperature, the emission time of a LO-phonon decreases and the rate is written as

$$\frac{1}{\tau_{ij}^{\text{inter,LO}}(T)} = \frac{1}{\tau_{ij}^{\text{inter,LO}}|_{0\text{K}}} (1 + n_{\text{LO}}) = \frac{1}{\tau_{ij}^{\text{inter,LO}}|_{0\text{K}}} \left[1 + \frac{1}{\exp\left(\frac{\hbar\omega_{\text{LO}}}{k_B T}\right) - 1} \right]$$

where n_{LO} is the Bose distribution.

Equations (B.6)-(B.7) suggest that the maximum scattering rate due to LO phonons is found for $E_{ij} = \hbar\omega_{\text{LO}}$. This is schematized in Fig. B.2: if the energy difference between subbands 1 and 2 (E_{12}) is larger than the phonon energy $\hbar\omega_{\text{LO}}$, it is possible for the system to emit a phonon while conserving the total energy (left panel). The maximum efficiency for the LO-phonon emission process is however found for $E_{12} = \hbar\omega_{\text{LO}}$ (right panel), in which case the transition can be vertical (see also Fig. 1.13).

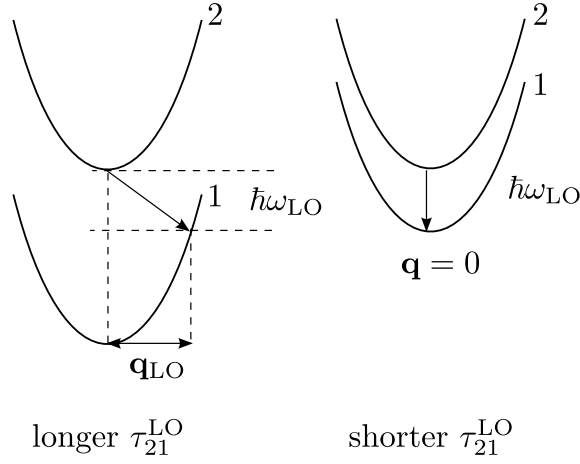


Figure B.2: Comparison of the LO-phonon emission process when $E_{12} > \hbar\omega_{\text{LO}}$ (left panel) and $E_{12} = \hbar\omega_{\text{LO}}$ (right panel).

B.5. Material parameters

We summarize in Table B.1 the parameters used in this work in the calculation of the band structure and the scattering times described above.

	GaAs/Al _{0.33} Ga _{0.67} As	GaInAs/AlInAs
m_b	0.086	0.076
m_w	0.067	0.0427
E_{g_w} (eV)	1.519	0.7518
V_b (eV)	0.295	0.520
$\Delta_{\text{so}w}$ (eV)	0.341	0.367
$\Delta_{\text{so}b}$ (eV)	0.334	0.337
$\hbar\omega_{\text{LO}}$ (meV)	36	32
Δ (Å)	1.5	1.2
Λ (Å)	60	90
V_w^{alloy} (eV)		0.6
V_b^{alloy} (eV)	0.8	1.4

Table B.1: Material parameters for the calculation of band structure and scattering times. The subscripts w and b indicate respectively wells and barriers.

C

Density matrix formalism for systems of multiple quantum wells

In principle, one could obtain the time evolution and phase coherence of the electrons in a multiple quantum well structure from the knowledge of all the single electron wavefunctions. In practice, a more efficient approach is the density matrix formalism (see for example Ref. [87]), which naturally accounts both for the quantum nature of the system and the statistical distribution of the quantum states. This statistical flavour is relevant in our case because of the very high number of particles involved.

The density matrix framework allows one to treat the properties of a large ensemble of electrons in a statistical way, without having to worry about the single electrons' wavefunctions.

C.1. Pure and mixed states

The standard description of a quantum state is the vector state representation:

$$|\psi\rangle = \sum_i c_i |u_i\rangle \quad (\text{C.1})$$

where $\{|u_i\rangle\}$ is an orthonormal basis, and c_i are the corresponding probability amplitudes, $c_i = \langle u_i | \psi \rangle$. When one writes the expression (C.1), it is implied that the state of the system is perfectly known: the probability of obtaining a particular result from a measurement can be calculated exactly. In this sense we say that $|\psi\rangle$ contains the maximal information about the quantum system [87]. States that can be described with a vector state are called *pure states*: see for example those represented in Fig. C.1(a).

An alternative representation to (C.1) is possible: the *density operator* associated with this pure state is defined as

$$\hat{\rho} = |\psi\rangle\langle\psi|$$

The matrix representation of $\hat{\rho}$ on the $\{u_i\}$ basis is the so-called *density matrix*, whose elements are

$$\rho_{ij} = \langle u_i | \hat{\rho} | u_j \rangle = c_i c_j^*$$

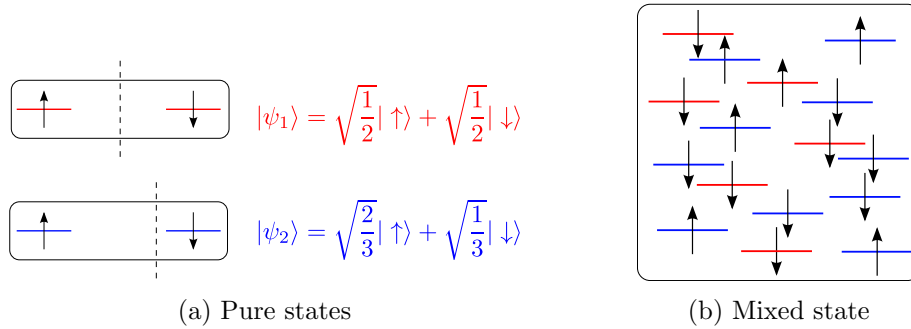


Figure C.1: Graphical representation of the difference between pure and mixed states.

It can be shown that the operator $\hat{\rho}$ completely characterizes the system, equivalently to the vector state representation. Indeed, all the properties of the vector state $|\psi\rangle$ have a counterpart in the density operator description [87]:

$$\text{Tr} [\hat{\rho}] = \sum_i^N \rho_{ii} = 1 \quad \text{normalization condition} \quad (\text{C.2})$$

$$\langle \hat{A} \rangle(t) = \text{Tr} [\hat{A} \hat{\rho}(t)] \quad \text{expectation value of an operator } A \quad (\text{C.3})$$

$$\frac{d}{dt} \hat{\rho}(t) = \frac{1}{i\hbar} [\hat{H}(t), \hat{\rho}(t)] \quad \text{time evolution equation} \quad (\text{C.4})$$

Let us now consider a more general system than the pure state described by $|\psi\rangle$ (C.1), like the one sketched in Fig. C.1(b). The state of this kind of system is known in a non-perfect, incomplete way: it might be either the state $|\psi_1\rangle$ with probability p_1 , or the state $|\psi_2\rangle$ with probability p_2 , etc.

Of course, we have:

$$p_1 + p_2 + \dots = \sum_k p_k = 1 \quad (\text{C.5})$$

The system under consideration is represented by a *statistical mix* of states $\{|\psi_1\rangle, |\psi_2\rangle, \dots\}$ with probabilities $\{p_1, p_2, \dots\}$. Note that probability enters at two levels: through quantum uncertainty (intrinsic) and through statistics, thus resulting in an incomplete knowledge of the system.

If the system was in the state $|\psi_k\rangle$, we could calculate the probability of obtaining a particular result from a measurement. As the occurrence of the state $|\psi_k\rangle$ has a probability p_k , the probabilities of the measurements must be weighted by p_k . The total probability of a measurement will correspond to the sum over k , that is to say the sum over the states of the statistical mix.

A mixed state has a straightforward representation in terms of density operator:

$$\hat{\rho} = \sum_k p_k \hat{\rho}_k \quad (\text{C.6})$$

where the $\hat{\rho}_k$ are the density operators corresponding to the pure states $|\psi_k\rangle$. Thanks to linearity, the properties (C.2)-(C.4) still hold.

C.1.1. Populations and coherences

What is the physical meaning of the density matrix elements? Let us start by considering the diagonal elements ρ_{ii} in the general case of a mixed state:

$$\rho_{ii} = \sum_k p_k [\rho_k]_{ii} = \sum_k p_k |c_i^{(k)}|^2 \quad (\text{C.7})$$

where we introduced $|\psi_k\rangle$ components on the $\{|u_i\rangle\}$ basis $c_i^{(k)} = \langle u_i | \psi_k \rangle$.

$|c_i^{(k)}|^2$ is a real positive number, whose physical meaning is the following: it is the probability, if the system is in the state $|\psi_k\rangle$, of finding, after a measurement, the system in the state $|u_i\rangle$. So we can say that ρ_{ii} represents the average probability of finding the system in the state $|u_i\rangle$, considering the uncertainty of the state before the measurement. For this reason, ρ_{ii} is called *population* of the state $|u_i\rangle$: if the measurement is repeated a large number N of times, $N\rho_{ii}$ systems will be found in the state $|u_i\rangle$. ρ_{ii} is real and positive, and equal to zero just in the case in which all the $|c_i^{(k)}|^2$ are zero [see Eq. (C.7)].

Similarly, we can obtain for off-diagonal elements

$$\rho_{ij} = \sum_k p_k c_i^{(k)} c_j^{(k)*}$$

The cross term $c_i^{(k)} c_j^{(k)*}$ translates the interference effects between states $|u_i\rangle$ and $|u_j\rangle$ that can arise just if $|\psi_k\rangle$ is a linear and coherent superposition of these two states. ρ_{ij} is the weighted average of these cross terms on all the possible states of the statistical mix. Differently from ρ_{ii} , ρ_{ij} can be zero even if none of the cross terms $c_i^{(k)} c_j^{(k)*}$ is. If $\rho_{ij} = 0$, it is because the average (C.1.1) cancels all the interference effects between $|u_i\rangle$ and $|u_j\rangle$; on the other hand, if $\rho_{ij} \neq 0$, a certain amount of coherence still exists between the two states. This is the reason why the off-diagonal elements in the density matrix are called *coherences*.

We will describe the quantum cascade structure with a mixed state in the density matrix representation, on the basis of the electronic wavefunctions. The diagonal part of ρ will then contain the populations of the levels, and the off-diagonal part the coherences between these levels, as schematized in Fig. C.2. The effect of dephasing can be seen as the scrambling of phase of some electrons in one of the pure state ensembles that compose the mixed state. In this picture, dephasing causes electrons to be removed from their original pure state, and then added back with a new phase unrelated to the original one. This has no direct effect on the populations ρ_{ii} , but just on the coherences [37].

$$\rho = \begin{pmatrix} \rho_{11} & \rho_{12} & \cdots & \rho_{1n} \\ \rho_{21} & \rho_{22} & \cdots & \\ \vdots & & \ddots & \vdots \\ \rho_{n1} & \rho_{n2} & \cdots & \rho_{nn} \end{pmatrix}$$

subband populations
coherences

Figure C.2: Density matrix representation of electronic levels.

C.2. Simplified density matrix model for mid- and far-infrared QCLs

We present in this section a simplified model of electron transport in quantum cascade structures based on the density matrix formalism.

The method is based on the observation that the active region of a QCL can be divided in sub-models, corresponding to the light-emitting and injection/extraction regions [37, 92, 94]. It will be assumed that the inter-module transport is dominated by tunnelling through barriers, and the intra-region transport by incoherent relaxation. This approach is justified by the fact that the barriers limiting the modules (injection and extraction barriers) are the thickest in the structure. This results in the inter-module tunnel couplings being considerably smaller than the intra-module tunnel couplings. The intermodule interactions are then sensitive to dephasing, and are best treated by including explicitly tunnel coupling and dephasing, while a semiclassical description is adequate for the intra-module transport.

In this framework, we will make use of the localized basis approach introduced in §1.2. The advantage of writing the density matrix in such a basis is that this allows the inclusion of coherent tunnelling through the coupling frequencies Ω , as well as the inclusion of a dephasing time τ_{\parallel} by means of decay of the coherences associated with tunnel-coupled levels.

We want to be able to study systems involving an arbitrary number of levels: we look for a general method to solve Liouville equation of motion and determine the matrix elements of ρ , as in the two-level model proposed by Kazarinov and Suris [38] that we reviewed in §4.1.1. The possibility of extending the method to N levels comes from a matrix reformulation of this method.

C.2.1. Two-level system

Let us consider the of system discussed in §4.1.1, whose bandstructure is reported in Fig. C.3, and express it in a matrix form, appropriate for an extension to an arbitrary number of levels. We generalize the approach presented in [92, 94], based on analytical calculations and numerical diagonalization, in contrast to the simulations based on Monte

Carlo methods [37].

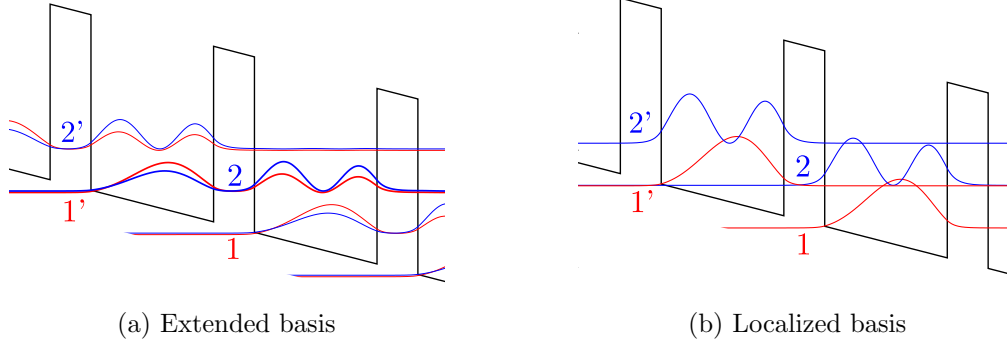


Figure C.3: Band structure and square moduli of wavefunctions in a GaAs/Al_{0.3}Ga_{0.7}As superlattice composed of 120 Å quantum wells coupled through 40 Å barriers. The applied field is 45 kV/cm.

We have shown in §4.1.1 that the current density flowing through the system can be expressed as:

$$j_z = -nei\Omega_{1'2}(z_{1'1'} - z_{22})(\rho_{1'2} - \rho_{21'}) \quad (\text{C.8})$$

The above expression depends on the difference between coherences ($\rho_{21'} - \rho_{1'2}$). We decompose the Liouville evolution equation with respect to sum and difference of coherences, and obtain from the evolution of the density matrix:

$$\begin{aligned} \frac{d\rho_{1'2}}{dt} + \frac{d\rho_{21'}}{dt} &= -i\frac{\Delta_{1'2}}{\hbar}(\rho_{1'2} - \rho_{21'}) - \frac{\rho_{1'2} + \rho_{21'}}{\tau_{\parallel 1'2}} \\ \frac{d\rho_{1'2}}{dt} - \frac{d\rho_{21'}}{dt} &= -i\frac{\Delta_{1'2}}{\hbar}(\rho_{1'2} + \rho_{21'}) - \frac{\rho_{1'2} - \rho_{21'}}{\tau_{\parallel 1'2}} + 2i\Omega_{1'2}(\rho_{1'1'} - \rho_{22}) \end{aligned} \quad (\text{C.9})$$

and

$$\begin{aligned} \frac{d\rho_{1'1'}}{dt} &= i\Omega_{1'2}(\rho_{1'2} - \rho_{21'}) + \frac{\rho_{22}}{\tau_{21}} \\ \frac{d\rho_{22}}{dt} &= -i\Omega_{1'2}(\rho_{1'2} - \rho_{21'}) - \frac{\rho_{22}}{\tau_{21}} \end{aligned} \quad (\text{C.10})$$

We translate Eqs. (C.9)-(C.10) in steady state conditions in a matrix form:

$$[D]_{2 \times 2} \cdot \begin{pmatrix} \rho_{1'2} - \rho_{21'} \\ \rho_{1'2} + \rho_{21'} \end{pmatrix} = [C]_{2 \times 2} \cdot \begin{pmatrix} \rho_{1'1'} \\ \rho_{22} \end{pmatrix} \quad (\text{C.11})$$

$$[E]_{2 \times 1} \cdot (\rho_{1'2} - \rho_{21'}) = [F]_{2 \times 2} \cdot \begin{pmatrix} \rho_{1'1'} \\ \rho_{22} \end{pmatrix} \quad (\text{C.12})$$

where

$$C = \begin{pmatrix} 0 & 0 \\ 2i\Omega_{1'2} & -2i\Omega_{1'2} \end{pmatrix} \quad D = \begin{pmatrix} i\frac{\Delta_{1'2}}{\hbar} & \frac{1}{\tau_{\parallel 1'2}} \\ \frac{1}{\tau_{\parallel 1'2}} & i\frac{\Delta_{1'2}}{\hbar} \end{pmatrix} \quad E = \begin{pmatrix} -i\Omega_{1'2} \\ i\Omega_{1'2} \end{pmatrix} \quad F = \begin{pmatrix} 0 & \frac{1}{\tau_{21}} \\ 0 & -\frac{1}{\tau_{21}} \end{pmatrix}$$

We can rewrite Eq. (C.11) as

$$\begin{pmatrix} \rho_{1'2} + \rho_{21'} \\ \rho_{1'2} - \rho_{21'} \end{pmatrix} = [D^{-1} \cdot C]_{2 \times 2} \cdot \begin{pmatrix} \rho_{1'1'} \\ \rho_{22} \end{pmatrix}$$

and consequently consider just the difference term

$$(\rho_{1'2} - \rho_{21'}) = [D^{-1} \cdot C]_{1 \times 2}^{\text{reduced}} \cdot \begin{pmatrix} \rho_{1'1'} \\ \rho_{22} \end{pmatrix} = [Y]_{1 \times 2} \begin{pmatrix} \rho_{1'1'} \\ \rho_{22} \end{pmatrix}$$

which allows us to express Eq. (C.12) as

$$[E]_{2 \times 1} \cdot [Y]_{1 \times 2} \begin{pmatrix} \rho_{1'1'} \\ \rho_{22} \end{pmatrix} = [F]_{2 \times 2} \cdot \begin{pmatrix} \rho_{1'1'} \\ \rho_{22} \end{pmatrix}$$

Using the normalization condition $\sum_i \rho_{ii} = 1$, we can obtain

$$\begin{pmatrix} \rho_{1'1'} \\ \rho_{22} \end{pmatrix} = [E \cdot Y - F]^{-1} \cdot \begin{pmatrix} 0 \\ 1 \end{pmatrix} \quad (\text{C.13})$$

$$(\rho_{1'2} - \rho_{21'}) = [Y] \cdot [E \cdot Y - F]^{-1} \cdot \begin{pmatrix} 0 \\ 1 \end{pmatrix} \quad (\text{C.14})$$

From Eq. (C.13) we can derive the populations $\rho_{1'1'}$ and ρ_{22} , and from Eq. (C.14) the difference between coherences, and therefore the current density through Eq. (C.8). This provides the same result as Eq. (4.7), and the two formulations of the problem are completely equivalent.

C.2.2. Four-level system

We give here the details of the calculations performed in relation to the results discussed in §4.1.2, as an application of the density matrix formalism to a THz quantum cascade laser [42, 92]. We report in Fig. C.4 the active region bandstructure for convenience.

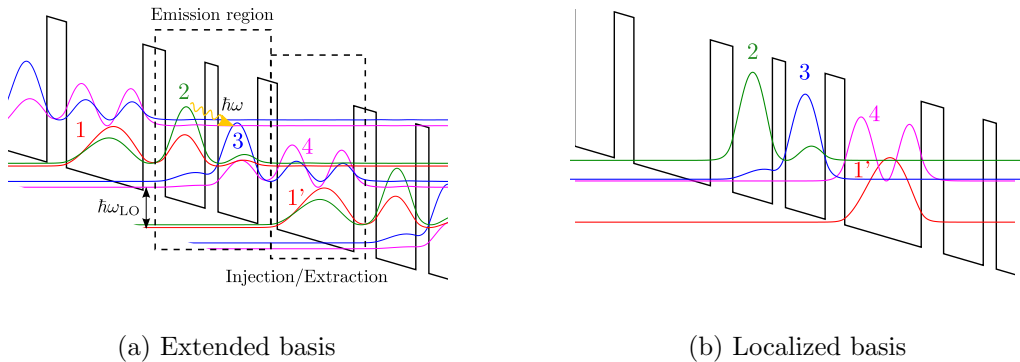


Figure C.4: Band structure and square moduli of wavefunctions in the THz structure of Ref. [42]. Starting from the injector barrier, the layer thicknesses in Å are: 48/85/28/85/42/164. The external electric field is 12.5 kV/cm.

In this system, Eqs (C.11) and (C.12) are extended to the form

$$[D]_{12 \times 12} \cdot \underbrace{\begin{pmatrix} \rho_{12} - \rho_{21} \\ \rho_{13} - \rho_{31} \\ \rho_{14} - \rho_{41} \\ \rho_{23} - \rho_{32} \\ \rho_{24} - \rho_{42} \\ \rho_{34} - \rho_{43} \\ \rho_{12} + \rho_{21} \\ \rho_{13} + \rho_{31} \\ \rho_{14} + \rho_{41} \\ \rho_{23} + \rho_{32} \\ \rho_{24} + \rho_{42} \\ \rho_{34} + \rho_{43} \end{pmatrix}}_{[\Delta\rho_{ij}^{\pm}]_{12 \times 1}} = [C]_{12 \times 4} \cdot \underbrace{\begin{pmatrix} \rho_{11} \\ \rho_{22} \\ \rho_{33} \\ \rho_{44} \end{pmatrix}}_{[\rho_{ii}]_{4 \times 1}}$$

$$[E]_{4 \times 6} \cdot \underbrace{\begin{pmatrix} \rho_{12} - \rho_{21} \\ \rho_{13} - \rho_{31} \\ \rho_{14} - \rho_{41} \\ \rho_{23} - \rho_{32} \\ \rho_{24} - \rho_{42} \\ \rho_{34} - \rho_{43} \end{pmatrix}}_{[\Delta\rho_{ij}^{-}]_{6 \times 1}} = [F]_{4 \times 4} \cdot \underbrace{\begin{pmatrix} \rho_{11} \\ \rho_{22} \\ \rho_{33} \\ \rho_{44} \end{pmatrix}}_{[\rho_{ii}]_{4 \times 1}}$$

where

$$C = 2i \begin{pmatrix} 0 & 0 & 0 & 0 \\ 0 & 0 & 0 & 0 \\ 0 & 0 & 0 & 0 \\ 0 & 0 & 0 & 0 \\ 0 & 0 & 0 & 0 \\ 0 & 0 & 0 & 0 \\ -\Omega_{12} & \Omega_{12} & 0 & 0 \\ -\Omega_{13} & 0 & \Omega_{13} & 0 \\ -\Omega_{14} & 0 & 0 & \Omega_{14} \\ 0 & -\Omega_{23} & \Omega_{23} & 0 \\ 0 & -\Omega_{24} & 0 & \Omega_{24} \\ 0 & 0 & -\Omega_{34} & \Omega_{34} \end{pmatrix}_{12 \times 4}$$

$$D = i \begin{pmatrix} \frac{\Delta_{12}}{\hbar} & -\Omega_{23} & -\Omega_{24} & -\Omega_{13} & -\Omega_{14} & 0 & \frac{-i}{\tau_{\parallel 12}} & 0 & 0 & 0 & 0 & 0 \\ -\Omega_{23} & \frac{\Delta_{13}}{\hbar} & -\Omega_{34} & \Omega_{12} & 0 & -\Omega_{14} & 0 & \frac{-i}{\tau_{\parallel 13}} & 0 & 0 & 0 & 0 \\ -\Omega_{24} & -\Omega_{34} & \frac{\Delta_{14}}{\hbar} & 0 & \Omega_{12} & \Omega_{13} & 0 & 0 & \frac{-i}{\tau_{\parallel 14}} & 0 & 0 & 0 \\ \Omega_{13} & \Omega_{12} & 0 & \frac{\Delta_{23}}{\hbar} & -\Omega_{34} & -\Omega_{24} & 0 & 0 & 0 & \frac{-i}{\tau_{\parallel 23}} & 0 & 0 \\ \Omega_{14} & 0 & \Omega_{12} & -\Omega_{34} & \frac{\Delta_{24}}{\hbar} & \Omega_{23} & 0 & 0 & 0 & 0 & \frac{-i}{\tau_{\parallel 24}} & 0 \\ 0 & \Omega_{14} & \Omega_{13} & \Omega_{24} & \Omega_{23} & \frac{\Delta_{34}}{\hbar} & 0 & 0 & 0 & 0 & 0 & \frac{-i}{\tau_{\parallel 34}} \\ \frac{-i}{\tau_{\parallel 12}} & 0 & 0 & 0 & 0 & 0 & \frac{\Delta_{12}}{\hbar} & -\Omega_{23} & -\Omega_{24} & \Omega_{13} & \Omega_{14} & 0 \\ 0 & \frac{-i}{\tau_{\parallel 13}} & 0 & 0 & 0 & 0 & -\Omega_{23} & \frac{\Delta_{13}}{\hbar} & -\Omega_{34} & \Omega_{12} & 0 & \Omega_{14} \\ 0 & 0 & \frac{-i}{\tau_{\parallel 14}} & 0 & 0 & 0 & -\Omega_{24} & -\Omega_{34} & \frac{\Delta_{14}}{\hbar} & 0 & \Omega_{12} & \Omega_{13} \\ 0 & 0 & 0 & \frac{-i}{\tau_{\parallel 23}} & 0 & 0 & -\Omega_{13} & \Omega_{12} & 0 & \frac{\Delta_{23}}{\hbar} & -\Omega_{34} & \Omega_{24} \\ 0 & 0 & 0 & 0 & \frac{-i}{\tau_{\parallel 24}} & 0 & -\Omega_{14} & 0 & \Omega_{12} & -\Omega_{34} & \frac{\Delta_{24}}{\hbar} & \Omega_{23} \\ 0 & 0 & 0 & 0 & 0 & \frac{-i}{\tau_{\parallel 34}} & 0 & -\Omega_{14} & \Omega_{13} & -\Omega_{24} & \Omega_{23} & \frac{\Delta_{34}}{\hbar} \end{pmatrix}_{12 \times 12}$$

$$E = i \begin{pmatrix} -\Omega_{12} & -\Omega_{13} & -\Omega_{14} & 0 & 0 & 0 \\ \Omega_{12} & 0 & 0 & -\Omega_{23} & -\Omega_{24} & 0 \\ 0 & \Omega_{13} & 0 & \Omega_{23} & 0 & -\Omega_{34} \\ 0 & 0 & \Omega_{14} & 0 & \Omega_{24} & \Omega_{34} \end{pmatrix}_{4 \times 6}$$

$$F = \begin{pmatrix} -\frac{1}{\tau_1} & 0 & 0 & \frac{1}{\tau_4} \\ 0 & -\frac{1}{\tau_2} - \frac{1}{\tau_{st}} & \frac{1}{\tau_3} + \frac{1}{\tau_{st}} & 0 \\ 0 & \frac{1}{\tau_2} + \frac{1}{\tau_{st}} & -\frac{1}{\tau_3} - \frac{1}{\tau_{st}} & 0 \\ \frac{1}{\tau_1} & 0 & 0 & -\frac{1}{\tau_4} \end{pmatrix}_{4 \times 4}$$

$$Y = [D^{-1} \cdot C]_{6 \times 12}^{\text{reduced}} \quad (\text{just the upper half matrix})$$

The above matrices allow the determination of populations $[\rho_{ii}]$ and the coherence differences $[\Delta\rho_{ij}^-]$:

$$\begin{aligned} [\rho_{ii}] &= \begin{pmatrix} \rho_{11} \\ \rho_{22} \\ \rho_{33} \\ \rho_{44} \end{pmatrix} = [E \cdot Y - F]^{-1} \cdot \begin{pmatrix} 0 \\ 0 \\ 0 \\ 1 \end{pmatrix} \\ [\Delta\rho_{ij}^-] &= \begin{pmatrix} \rho_{12} - \rho_{21} \\ \rho_{13} - \rho_{31} \\ \rho_{14} - \rho_{41} \\ \rho_{23} - \rho_{32} \\ \rho_{24} - \rho_{42} \\ \rho_{34} - \rho_{43} \end{pmatrix} = [Y] \cdot [E \cdot Y - F]^{-1} \cdot \begin{pmatrix} 0 \\ 0 \\ 0 \\ 0 \\ 0 \\ 1 \end{pmatrix} \end{aligned}$$

where all the elements in the last row of matrix $[E \cdot Y - F]^{-1}$ are set to 1 to respect charge conservation.

We define the matrix

$$U = \frac{1}{\hbar} [H_{\text{sp}}, z]$$

whose elements can be shown to be

$$U_{ij} = \frac{\Delta_{ij}}{\hbar} z_{ij} + \Omega_{ij} (z_{jj} - z_{ii}) + \sum_{k \neq i,j}^4 (\Omega_{ik} z_{jk} - \Omega_{jk} z_{ik})$$

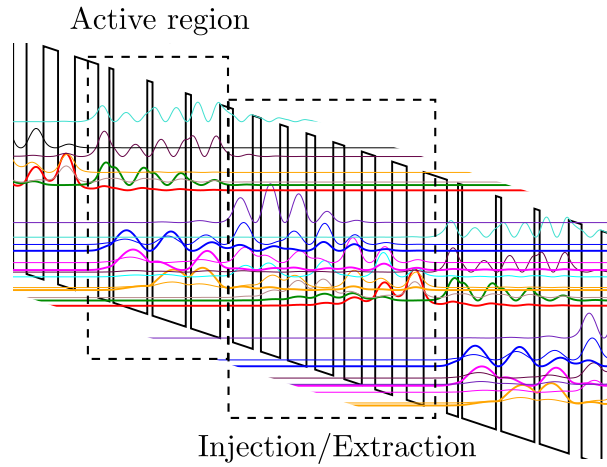
The current density is finally expressed in terms of matrices U and ρ as

$$J = -nei \sum_{i < j}^4 U_{ij} (\rho_{ij} - \rho_{ji})$$

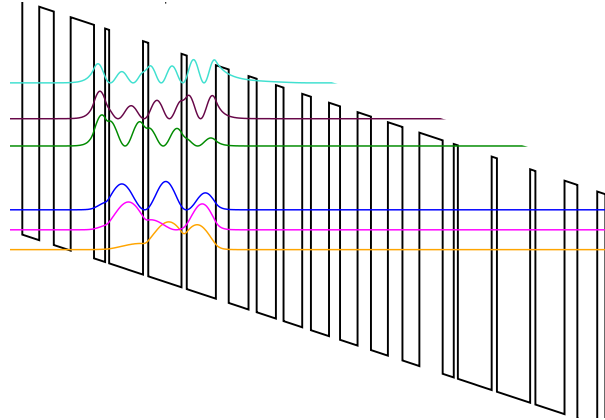
C.2.3. N -level system

The formulation of the current density calculation in matrix form is suitable for a generalization of the procedure to an arbitrary number of levels. Consider for instance a mid-IR QCL structure [39], with 13 electronic levels per period, as shown in Fig. C.5(a). This real QCL structure is way more complex than the simple 2 and 4-level picture we just introduced. However, we can again treat the system by identifying two modules, one corresponding to the active region [Fig. C.5(b)] and one to the injection and extraction region [Fig. C.5(c)].

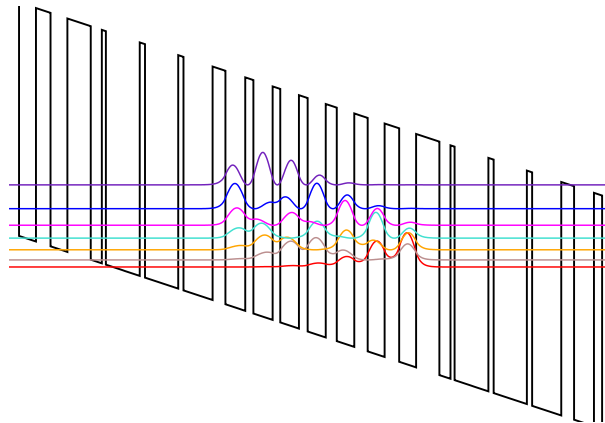
In addition to the N electronic levels constituting one period, we will have to consider also some 'interface levels', with the role of ensuring the transport of electrons from one period to the following, in analogy to the role of the injector (level 1) in the four-level calculation.



(a) Extended basis



(b) Localized basis: active region



(c) Localized basis: injection/extraction region

Figure C.5: Band structure and square moduli of wavefunctions in the mid-IR structure of Ref. [39]. Starting from the injector barrier, the layer thicknesses in \AA are: **40/19/7/58/9/57/9/50/22/34/14/33/13/32/15/31/19/30/23/29/25/29**. The external electric field is 43 kV/cm.

In the case of N levels

$$\begin{aligned} [D]_{2M \times 2M} \cdot [\Delta\rho_{ij}^{\pm}]_{2M \times 1} &= [C]_{2M \times N} \cdot [\rho_{ii}]_{N \times 1} \\ [E]_{N \times M} \cdot [\Delta\rho_{ij}^-]_{M \times 1} &= [F]_{N \times N} \cdot [\rho_{ii}]_{N \times 1} \end{aligned}$$

where $M = \binom{N}{2}$ is the number of possible level pairings.

In order to generalize matrices C, D, E, F , we use a greek index to denote transitions, i.e. $\alpha \equiv (\alpha_i, \alpha_j)$, $1 \leq \alpha \leq M$, and keep on using latin indices to indicate levels, $1 \leq i, j \leq N$. With this notation, we write matrix C as:

$$C = \begin{pmatrix} [0]_{M \times N} \\ [C]_{M \times N}^{\text{lower}} \end{pmatrix}$$

and the elements of the lower matrix are given by

$$C_{\alpha j}^{\text{lower}} = 2i \begin{cases} -\Omega_{\alpha_i \alpha_j} & \text{if } j = \alpha_i \\ \Omega_{\alpha_i \alpha_j} & \text{if } j = \alpha_j \\ 0 & \text{otherwise} \end{cases}$$

For the D matrix we have:

$$D = \left(\begin{array}{c|c} [D]_{M \times M}^{\text{diag}_1} & [D]_{M \times M}^{\text{off-diag}} \\ \hline [D]_{M \times M}^{\text{off-diag}} & [D]_{M \times M}^{\text{diag}_2} \end{array} \right)$$

$$D_{\alpha\beta}^{\text{diag}_1} = i \begin{cases} \frac{\Delta_\alpha}{\hbar} & \text{if } \alpha = \beta \\ -\Omega_{\alpha_j \beta_j} & \text{if } \alpha_i = \beta_i, \alpha_j \neq \beta_j \\ \Omega_{\alpha_j \beta_i} & \text{if } \alpha_i = \beta_j, \alpha_j \neq \beta_i \\ -\Omega_{\alpha_i \beta_j} & \text{if } \alpha_j = \beta_i, \alpha_i \neq \beta_j \\ \Omega_{\alpha_i \beta_i} & \text{if } \alpha_j = \beta_j, \alpha_i \neq \beta_i \\ 0 & \text{otherwise} \end{cases} \quad D_{\alpha\beta}^{\text{diag}_2} = i \begin{cases} \frac{\Delta_\alpha}{\hbar} & \text{if } \alpha = \beta \\ -\Omega_{\alpha_j \beta_j} & \text{if } \alpha_i = \beta_i, \alpha_j \neq \beta_j \\ -\Omega_{\alpha_j \beta_i} & \text{if } \alpha_i = \beta_j, \alpha_j \neq \beta_i \\ \Omega_{\alpha_i \beta_j} & \text{if } \alpha_j = \beta_i, \alpha_i \neq \beta_j \\ \Omega_{\alpha_i \beta_i} & \text{if } \alpha_j = \beta_j, \alpha_i \neq \beta_i \\ 0 & \text{otherwise} \end{cases}$$

$$D_{\alpha\beta}^{\text{off-diag}} = \begin{cases} \frac{1}{\tau_{\parallel\alpha}} & \text{if } \alpha = \beta \\ 0 & \text{otherwise} \end{cases}$$

Matrix E :

$$E_{i\beta} = i \begin{cases} -\Omega_{\beta_i \beta_j} & \text{if } i = \beta_i \\ \Omega_{\beta_i \beta_j} & \text{if } i = \beta_j \\ 0 & \text{otherwise} \end{cases}$$

Matrix F contains relaxation times. We divide it in two parts, $F = F^0 + F^1$. F^0 contains the relaxation times within localized regions:

$$F_{ij}^0 = \begin{cases} -\frac{1}{\tau_i} = -\sum_{k \neq i} \frac{1}{\tau_{ik}} & \text{if } i = j \\ \frac{1}{\tau_{ji}} & \text{if } i \neq j, (i, j) \in \text{same region} \\ 0 & \text{otherwise} \end{cases}$$

F^1 contains the relaxation due to interface levels. Suppose these are listed in a set $\{\text{interface levels}\}$. The only non-zero elements of F^1 are then

$$F_{ij}^1 = \begin{cases} -\frac{1}{\tau_i} = -\sum_{k \neq i, k \in \{\text{i.levs.}\}} \frac{1}{\tau_{ik}} & \text{if } i = j \\ \frac{1}{\tau_{ji'}} & \text{if } i \neq j, i \in \{\text{interface levels}\} \\ \frac{1}{\tau_{j'i}} & \text{if } i \neq j, j \in \{\text{interface levels}\} \end{cases}$$

where the primed indices i', j' represent the levels i, j in the previous (injectors) or following (extractors) period.

As in the previous cases, we can use these matrices to determine populations $[\rho_{ii}]$ and the coherence differences $[\Delta\rho_{ij}^-]$:

$$[\rho_{ii}] = \begin{pmatrix} \rho_{11} \\ \rho_{22} \\ \vdots \\ \rho_{NN} \end{pmatrix} = [E \cdot Y - F]^{-1} \cdot \begin{pmatrix} 0 \\ 0 \\ \vdots \\ 1 \end{pmatrix}$$

$$[\Delta\rho_{ij}^-] = \begin{pmatrix} \rho_{12} - \rho_{21} \\ \rho_{13} - \rho_{31} \\ \vdots \\ \rho_{N-1,N} - \rho_{N,N-1} \end{pmatrix} = [Y] \cdot [E \cdot Y - F]^{-1} \cdot \begin{pmatrix} 0 \\ 0 \\ \vdots \\ 1 \end{pmatrix}$$

where again all the elements in the last row of matrix $[E \cdot Y - F]^{-1}$ are set to 1 for the conservation of charge. The elements of the generalized matrix U are

$$U_{ij} = \frac{\Delta_{ij}}{\hbar} z_{ij} + \Omega_{ij}(z_{jj} - z_{ii}) + \sum_{k \neq i, j}^N (\Omega_{ik} z_{jk} - \Omega_{jk} z_{ik})$$

and the current density can be finally calculated as

$$J = -nei \sum_{i < j}^N U_{ij} (\rho_{ij} - \rho_{ji})$$

D

Mid-infrared quantum cascade lasers: from TEM measurements to electron transport modeling

The formulation of the current density calculation in matrix form is suitable for a generalization of the procedure to an arbitrary number of levels, to apply in the case of any quantum cascade laser structure, as detailed in Appendix C.

In this section, we apply our method to a post-growth study of a MOCVD- (MetalOrganic Chemical Vapour Deposition) grown QCL, fabricated at the Laboratoire de Photonique et de Nanostructures (LPN) by Isabelle Sagnes and Grégoire Beaudoin. This systematic study has been done in close collaboration with Ariane Calvar and Maria Amanti, who have performed the processing and experimental characterization of the device.

After their experimental demonstration in 1994 [2], all the first successful QCLs were grown by Molecular Beam Epitaxy (MBE), a technique based on the sequential deposition of thin layers of semiconductors of high crystalline quality.

MOCVD is a growth technique based on chemical reactions rather than physical deposition. The first MOCVD-grown active region was reported in 2003 [117]. Compared to MBE, MOCVD offers higher deposition rates ($\approx 2 \mu\text{m}$ per hour) and the possibility to grow on several substrates during the same run. In addition, MOCVD does not need an ultra vacuum environment. These features make MOCVD more suitable for industrial purposes of QCL-mass-production. However, the chemical nature of the process is more prone to deviations from the ideal growth. While shutters on the effusion cells allow for a good control of the MBE deposition, gas flows and mixtures in the MOCVD growth can generate residual doping and less abrupt interfaces.

We consider here an MOCVD-grown AlInAs/GaInAs//InP QCL (sample InP969) based on a two-phonon extraction design [39], conceived for a $9\text{-}\mu\text{m}$ emission. Its nominal band structure is shown in Fig. D.2(a). In the following, we present the post-growth TEM measurements (performed by Gilles Patriarche at LPN) and experimental characterization on this device, which we will then interpret with a theoretical analysis within the density-matrix transport model.

D.1. HAADF-STEM tomography measures

It is possible to analyze the composition and thickness of the semiconductors layers using a Scanning Transmission Electron Microscope (STEM). In this microscopy technique, a focussed electron beam scans the surface of a thin sample, interacting with it when passing through. Thanks to this interaction, an image with electronic resolution is formed.

If used in the bright field mode, the contrast of a STEM image comes from the absorbance of the electrons in the sample, and is observed in the transmission of the main beam. On the contrary, in dark field imaging the main beam is avoided, and just electrons scattered above a certain angle are collected. In this case the contrast comes from electron scattering, mainly due to strong Coulomb interaction between the electrons of the beam and the nuclei of the sample. A measure performed using an annular dark field detector to collect the scattered beam at high angle (HAADF) is highly sensitive to variations in the atomic number of atoms. One can thus obtain images where the contrast is proportional to the atomic number Z .

The result of an HAADF-STEM measurement on the QCL structure under consideration is presented in Fig. D.1. Panel (a) presents the image of one period of the active region. The darker layers correspond to AlInAs barriers ($Z_{\text{Al}} = 13$), and the lighter zones to InGaAs wells ($Z_{\text{Ga}} = 39$). The contrast profile deduced from this image is presented on panel (b). Here, the solid black lines indicate the contrast limits expected for lattice-matched ternaries $\text{In}_{0.53}\text{Ga}_{0.47}\text{As}/\text{In}_{0.52}\text{Al}_{0.48}\text{As}$, extrapolated from the values of the thicker layers. Deviations in the peaks height or dips compared to these lines represent variations in the layer compositions from the nominal ones. In addition to this, Fig. D.1(c) shows that the interfaces between the different semiconductor epilayers are not monolayer abrupt.

The results of the HAADF contrast profile are summarized in Table D.1, which reports the nominal values of the layer thicknesses along with their measured values. In the case of InGaAs wells, the main deviation from the nominal design is the layer thicknesses, with an average absolute deviation of 6%. In terms of material composition, all the wells result to be really composed of a ternary InGaAs, except for one (labeled 15 in the table), which contains 7.6% of Al.

The differences from the nominal design are more substantial for AlInAs barriers, especially in the active region, where the thinnest barriers are found in the design. The thickness difference between expected and measured values ranges from 5% to 56%. Only the two thickest barriers contain the nominal 48% Al concentration: all the other barriers are composed of quaternary materials, with a finite content of Ga.

D.2. Modeling

In order to model a structure closer to the STEM measurements characterization, we consider the modified thicknesses and compositions of the layers, and change the confining potential accordingly. The height of the barriers can be modified proportionally to the measured percentage of Al content (see Ref. [118]).

The nominal (left panel) and modified (right panel) band structure are shown in

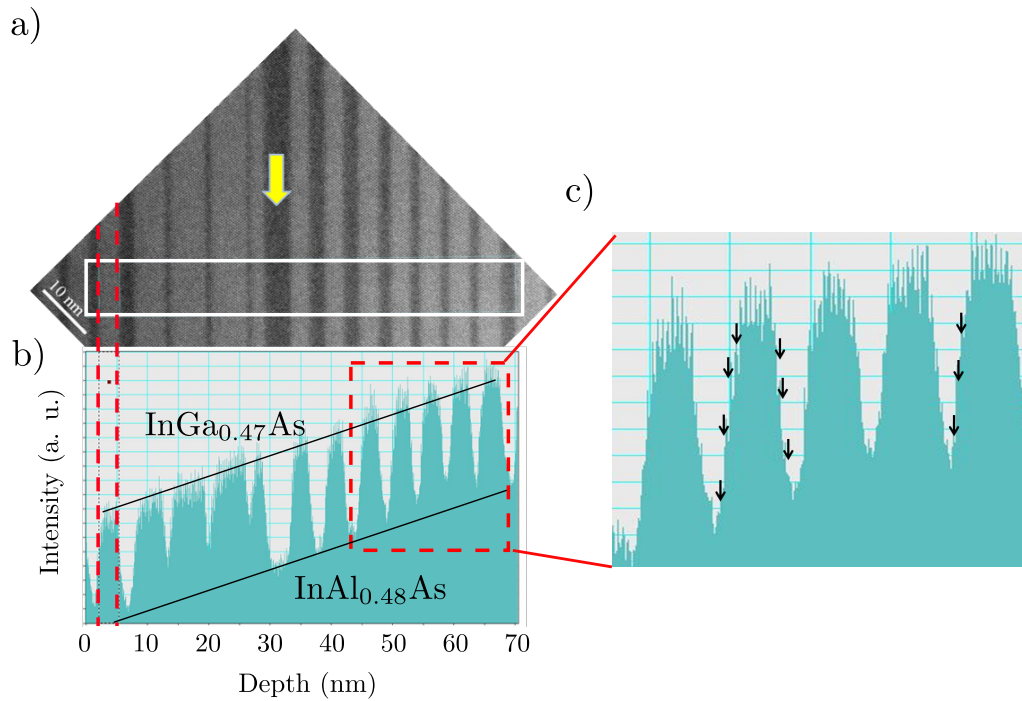


Figure D.1: a) HAADF-STEM image of one period in the active region of the sample InP969, obtained with a TEM/STEM JEOL 2200 FS with a spherical aberration correction and a resolution of ≈ 2 nm. The contrast between the layers corresponds to the different chemical composition of the InAlAs barriers and InGaAs wells. The yellow arrow indicates the thickest InAlAs layer for which the nominal composition is supposed to be respected. b) HAADF contrast profile obtained from the STEM image. The black lines correspond to the lattice matched ternary alloys. c) Close up of the wells and barriers in the injection/relaxation region. The interfaces between the two are not abrupt. (Courtesy of I. Sagnes and G. Beaudoin).

	Layer	Thickness (Å)		InAlAs			InGaAs			
		Nominal (Å)	TEM (Å)	%In	%Al	%Ga	%In	%Ga	%Al	
× 36	Injection/Extraction region									
	1	InGaAs	34.0	33.3				53	47	-
	2	InAlAs	14.0	17.2	52	45.5	2.5			
	3	InGaAs	33.0	31				53	47	-
	4	InAlAs	13.0	14.3	52	41.7	6.3			
	5	InGaAs	32.0	31				53	47	-
	6	InAlAs	15.0	16.6	52	43	5			
	7	InGaAs	31.0	28.7				53	47	-
	8	InAlAs	19.0	20.1	52	43	5			
	9	InGaAs	30.0	31				53	47	-
	10	InAlAs	23.0	24.1	52	45.5	2.5			
	11	InGaAs	29.0	28.1				53	47	-
	12	InAlAs	25.0	26.4	52	48	-			
	13	InGaAs	29.0	29.9				53	47	-
	Active region									
	14	InAlAs	40.0	41.9	52	48	-			
	15	InGaAs	19	17.2				53	39.4	7.6
	16	InAlAs	7.0	10.9	52	22.8	25.2			
	17	InGaAs	58	49.9				53	47	-
	18	InAlAs	9.0	11.4	52	29	19			
	19	InGaAs	57	50.5				53	47	-
	20	InAlAs	9.0	13.8	52	31.6	16.4			
21	InGaAs	50.0	47.6				53	47	-	
22	InAlAs	22.0	24.7	52	44.3	3.7				

Table D.1: Chemical composition and thickness of the different layers of one period of the sample InP969 based on the analysis of the HAADF contrast profile of Fig. D.1. The nominal and lattice-matched composition is $\text{In}_{0.53}\text{Ga}_{0.47}\text{As}/\text{In}_{0.52}\text{Al}_{0.48}\text{As}$. The InAlAs layer highlighted in orange (14) corresponds to the one on Fig. D.1(b) for which the nominal composition is respected. The InGaAs layer highlighted in blue (15) corresponds to the only well for which nominal composition is not attained.

The error on these values is related to the analysis of the contrast profile, and estimated to be $\pm 10\%$ on the Al concentration, and $\pm 3 \text{ \AA}$ on the thicknesses. (Courtesy of I. Sagnes and G. Beaudoin).

	Nominal	Grown
Transition energy (meV)	136 - 145	130 - 135
z_{23} (Å)	33.0 - 33.2	29.7 - 30.5
τ_{exc} (ps)	0.6 - 0.9	0.2 - 0.3
$2\hbar\Omega_{12}$ (meV)	7	6.5
$2\hbar\Omega_{\text{extraction}}$ (meV)	3 - 10	5 - 11

Table D.2: Value range of some relevant parameters in InP969 structure, for electric fields between 30 kV/cm and 55 kV/cm.

Fig. D.2¹. Some of the relevant parameters in the comparison of the two structures are reported in Table D.2.

The changes in the potential and in the wavefunctions appear quite impressive, especially in the active region, where the height of the barriers is strongly reduced. This has the immediate consequence of making the transition from excited (level 2) to ground state (level 3) much less diagonal, as well as less energetic (from ≈ 140 meV to ≈ 130 meV). Moreover, this verticality causes higher values of the dipole z_{32} , and shorter lifetimes of the excited state. Overall, the upper wavefunctions in the active region are badly confined due to the lowered heights of the barriers.

As a result, the two structures present a different alignment field for the coupling between the main injector (level 1) and the excited state (level 2): in the nominal design, this happens around ≈ 45 kV/cm, while in the grown structure this value rises to ≈ 50 kV/cm.

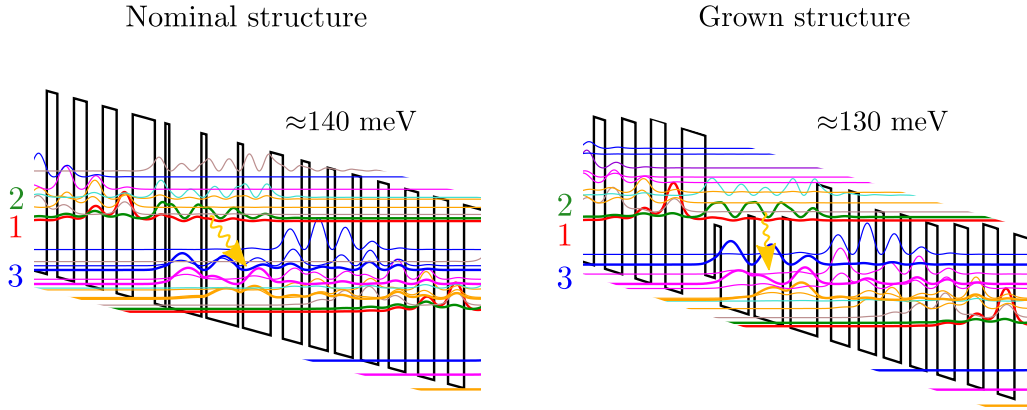


Figure D.2: Band structure and squared moduli of wavefunctions for the nominal design (left panel) and for the actual structure deduced from the TEM measurements summarized in Table D.1. The most relevant changes affect the active region, resulting in a less diagonal and less energetic radiative transition.

¹In the following, we label as 'nominal' the ideal design, and 'grown' the structure calculated accounting for STEM measurements.

Finally, we apply to the nominal and grown structure the generalized density matrix calculation presented in §C.2.3. We use for our calculation the value of the doping which has been measured post-growth, and found to be equal to $N_V = 1.5 \times 10^{16} \text{cm}^{-3}$ [119].

In the mid-IR frequency range, the pure dephasing time T_2 (see Eq. (1.26) and corresponding footnote) is expected to be well approximated by the interface roughness intrasubband scattering time (see §B.1) [111]. The dashed lines in Fig. D.3 present the calculated VI characteristics for the nominal (a) and grown (b) structure, where all the dephasing times have been calculated considering as sources of pure dephasing the interface roughness scattering. The appearance of the two curves is not smooth, especially in the case of Fig. D.3(a). This effect can be attributed to the variation of the overlap between wavefunctions with the electric field. We choose to smoothen the curves by setting a common τ_{\parallel} which preserves the predicted value of maximum current. The result of this approximation is represented by the solid lines in Fig. D.3. We use $\tau_{\parallel}=0.15$ ps for the nominal structure, and $\tau_{\parallel}=0.10$ ps for the grown structure, both parameters being included in the range of the τ_{\parallel} calculated from interface roughness.

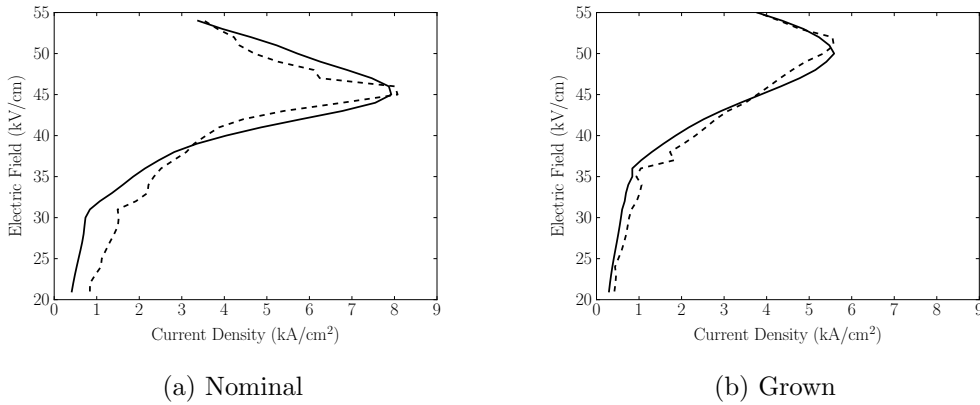


Figure D.3: Calculated VI (accounting for stimulated emission) for the InP969 structures of Fig. D.2. Dashed lines: dephasing time τ_{\parallel} calculated from interface roughness. Solid lines: dephasing time τ_{\parallel} set to an average value.

Comparison between the two curves in Fig. D.3 confirms that the alignment voltage of the grown structure is higher. A slightly lower maximum current is calculated for the latter. This can be understood in terms of a reduced injection coupling, due to the increased thickness of the injection barrier, and of a lower extraction efficiency.

The calculated gain spectra are shown in Fig. D.4(b). The peak of the gain spectra of the grown structure is much less variable in energy than what expected for the nominal structure, as the main transition is much less diagonal in the grown rather than in the nominal structure.

The calculated LVI curves [Fig. D.4(c)] show that even if deeply changed, the design can still sustain current and operate as a laser. This is a proof of the robustness of this

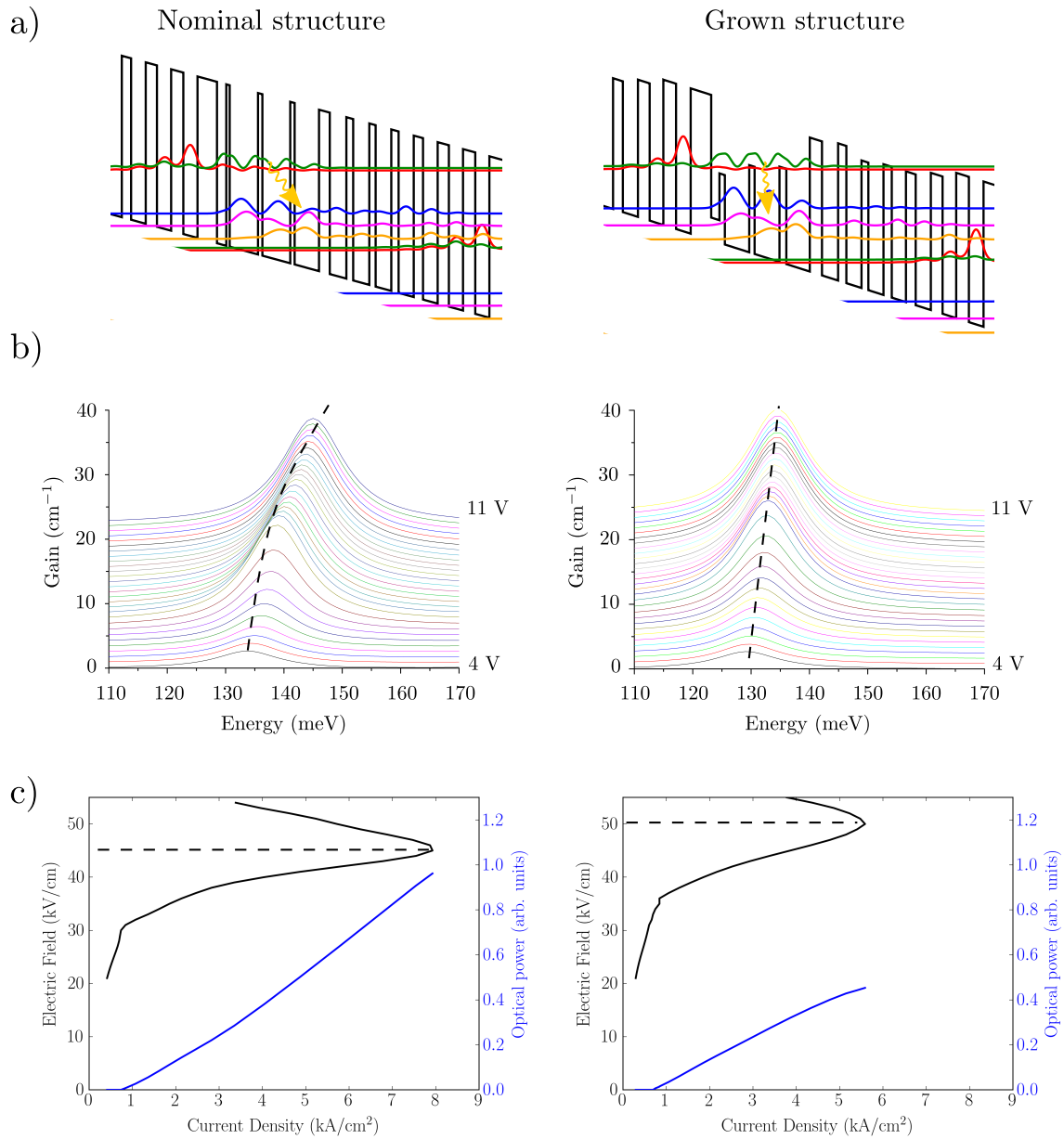


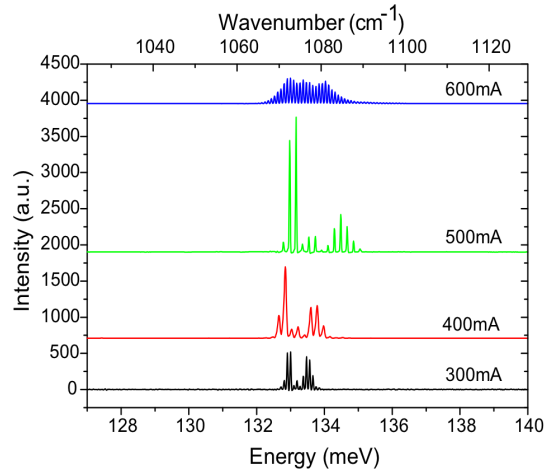
Figure D.4: a) Band structure and potential as in Fig. D.2, just most relevant levels plotted. b) Calculated gain spectra for nominal and grown structure presented in Fig. D.2 and Table D.1. c) Calculated LVI, $\alpha_{\text{tot}} = 14 \text{ cm}^{-1}$.

QCL design. The emitted power of the grown structure is expected to be lower (due to the reduced dynamic range), while the threshold remains comparable.

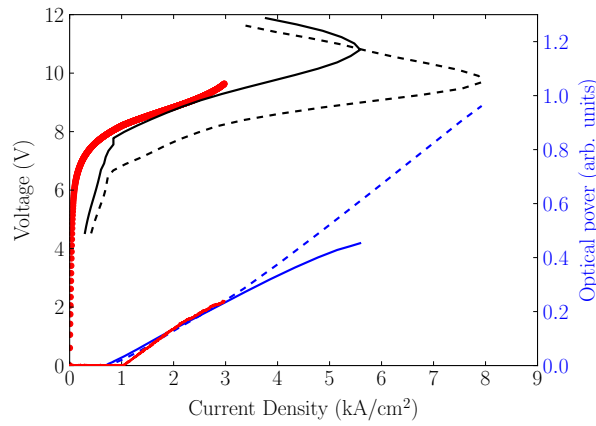
The experimental characterization of this structure is presented in Fig. D.5 [119]. The device is composed of 36 repetitions of the active region, processed into a typical uncoated Fabry-Perot device, 1.9 mm long and 12.7 μm wide.

The laser emission spectra of Fig. D.5(a) is centered between 132 and 137 meV. It shows a small variation while sweeping the voltage, in agreement with the calculated behaviour of the gain spectrum. Lastly, comparison between measured and calculated VI [Fig. D.5(b)] shows a better agreement with the LVI characteristics of the grown structure.

Thanks to the present study and to a combined effort between the LPN and our team, the growth of the 9- μm structure has been optimized in order to reproduce the nominal design more accurately. The optimized structure has been eventually exploited in the demonstration of high-frequency modulated QCLs [119].



(a) Laser emission spectra of the sample as a function of the operating voltage at 77K [cf. Fig. D.4(b)].



(b) Comparison between the calculated LVI for the nominal (dashed line) and grown (solid line) structure and the experimental data (red dots), CW operation, 77 K.

Figure D.5: Comparison with experimental data for InP969 [119].

Bibliography

- [1] F. Capasso and S. Datta. Quantum electron devices. *Physics Today*, 43:74–82, 1990.
- [2] J. Faist, F. Capasso, D. L. Sivco, C. Sirtori, A. L. Hutchinson, and A. Y. Cho. Quantum cascade laser. *Science*, 264(5158):553–556, 1994.
- [3] J. Faist. *Quantum Cascade Lasers*. Oxford University Press, 2013.
- [4] F. K. Tittel, D. Richter, and A. Fried. Mid-infrared laser applications in spectroscopy. In *Solid-State Mid-Infrared Laser Sources*, pages 458–529. Springer, 2003.
- [5] P. Jouy, M. Mangold, B. Tuzson, L. Emmenegger, Y. C.i Chang, L. Hvozda, H. P. Herzig, P. Wägli, A. Homsy, N. F. de Rooij, Wirthmueller A., D. Hofstetter, H. Looser, and J. Faist. Mid-infrared spectroscopy for gases and liquids based on quantum cascade technologies. *Analyst*, 139(9):2039–2046, 2014.
- [6] For example, see Daylight Solutions, whose core technology are quantum cascade lasers. <http://www.daylightsolutions.com>. Accessed: 2014-10-20.
- [7] D. Dini, R. Köhler, A. Tredicucci, G. Biasiol, and L. Sorba. Microcavity polariton splitting of intersubband transitions. *Phys. Rev. Lett.*, 90:116401, 2003.
- [8] Y. Todorov, A. M. Andrews, R. Colombelli, S. De Liberato, C. Ciuti, P. Klang, G. Strasser, and C. Sirtori. Ultrastrong light-matter coupling regime with polariton dots. *Phys. Rev. Lett.*, 105:196402, 2010.
- [9] R. H. Dicke. Coherence in spontaneous radiation processes. *Phys. Rev.*, 93:99–110, 1954.
- [10] M. Gross and S. Haroche. Superradiance: An essay on the theory of collective spontaneous emission. *Physics Reports*, 93(5):301 – 396, 1982.
- [11] M. Scheibner, T. Schmidt, L. Worschech, A. Forchel, G. Bacher, T. Passow, and D. Hommel. Superradiance of quantum dots. *Nature Physics*, 3(2):106–110, 2007.
- [12] T. V. Teperik and A. Degiron. Superradiant optical emitters coupled to an array of nanosize metallic antennas. *Phys. Rev. Lett.*, 108:147401, Apr 2012.

- [13] Marlan O. Scully and Anatoly A. Svidzinsky. The super of superradiance. *Science*, 325(5947):1510–1511, 2009. doi: 10.1126/science.1176695.
- [14] A. Delteil, A. Vasanelli, Y. Todorov, C. Feuillet Palma, M. Renaudat St. Jean, G. Beaudoin, I. Sagnes, and C. Sirtori. Charge-induced coherence between intersubband plasmons in a quantum structure. *Phys. Rev. Lett.*, 109:246808, 2012.
- [15] T. Laurent, Y. Todorov, A. Vasanelli, A. Delteil, I. Sagnes, G. Beaudoin, and C. Sirtori. Superradiant electroluminescence from a collective excitation in a semiconductor. *Unpublished*.
- [16] G. Pegolotti, A. Vasanelli, Y. Todorov, and C. Sirtori. Quantum model of coupled intersubband plasmons. *Phys. Rev. B*, 90:035305, 2014.
- [17] M. Kira and S. W. Koch. *Semiconductor Quantum Optics*. Cambridge University Press, 2011.
- [18] P. Y. Yu and M. Cardona. *Fundamentals of Semiconductors: Physics And Materials Properties, Volume 3*. Springer, 2005.
- [19] M. L. Cohen and J. Chelikowsky. *Electronic Structure and Optical Properties of Semiconductors*. Springer, Berlin, Heidelberg, 1989.
- [20] N. W. Ashcroft and N.D. Mermin. *Solid State Physics*. Thomson Learning, 1976.
- [21] G. Bastard. *Wave mechanics applied to semiconductor heterostructures*. Les Éditions de physique, France, 1988.
- [22] E. Rosencher and B. Vinter. *Optoelectronics*. Cambridge University Press, 2002.
- [23] E. O. Kane. Band structure of indium antimonide. *J. Phys. Chem. Solids*, 1:249–261, 1957.
- [24] M. Helm. The basic physics of intersubband transitions. In H. C. Liu and F. Capasso, editors, *Intersubband Transitions in Quantum Wells, Physics and Device Applications I*. Academic, Boston, 2000.
- [25] J. H. Davies. *The Physics of Low-Dimensional Semiconductors*. Cambridge University Press, 1997.
- [26] C. Sirtori, F. Capasso, J. Faist, and S. Scandolo. Nonparabolicity and a sum rule associated with bound-to-bound and bound-to-continuum intersubband transitions in quantum wells. *Phys. Rev. B*, 50:8663–8674, 1994.
- [27] P. Harrison. *Quantum well, wires and dots - Theoretical and computational physics*. Wiley, 2000.
- [28] W. H. Press, S. A. Teukolsky, W. T. Vetterling, and B. P. Flannery. *Numerical recipes in C: the art of scientific computing*. Cambridge University Press, 1992.

- [29] M. Fox. *Optical Properties of Solids*. Oxford University Press, 2010.
- [30] T. Ando, A. B. Fowler, and F. Stern. Electronic properties of two dimensional systems. *Rev. Mod. Phys.*, 54(2):437, 1982.
- [31] R. Loudon. *The Quantum Theory of Light*. Oxford University Press, 1983.
- [32] T. Ando. Line width of inter-subband absorption in inversion layers: Scattering from charged ions. *Journal of the Physical Society of Japan*, 54(7):2671–2675, 1985.
- [33] T. Unuma, M. Yoshita, T. Noda, H-Sakaki, and H. Akiyama. Intersubband absorption linewidth in GaAs quantum wells due to scattering by interface roughness, phonons, alloy disorder, and impurities. *J. Appl. Phys.*, 93(3):1586–1597, 2003.
- [34] T. Ando. Broadening of Inter-Subband Transitions in Image-Potential-Induced Surface States outside Liquid Helium. *Journal of the Physical Society of Japan*, 44(3):765–773, 1978.
- [35] R. L. Terazzi. *Transport in quantum cascade lasers*. PhD thesis, ETH Zurich, 2012.
- [36] T. Unuma, T. Takahashi, T. Noda, M. Yoshita, H. Sakaki, M. Baba, and H. Akiyama. Effects of interface roughness and phonon scattering on intersubband absorption linewidth in a gaas quantum well. *Appl. Phys. Lett.*, 78(22):3448–3450, 2001.
- [37] H. Callebaut and Q. Hu. Importance of coherence for electron transport in terahertz quantum cascade lasers. *Journal of Applied Physics*, 98(10):104505, 2005.
- [38] R. F. Kazarinov and R. A. Suris. Possibility of the amplification of electromagnetic waves in a semiconductor with a superlattice. *Sov. Phys. Semicond.*, 5(4):707–709, 1971.
- [39] M. Beck, D. Hofstetter, T. Aellen, J. Faist, U. Oesterle, M. Ilegems, E. Gini, and H. Melchior. Continuous Wave Operation of a Mid-Infrared Semiconductor Laser at Room Temperature. *Science*, 295(5553):301–305, 2002.
- [40] Y. Yao, A. J. Hoffman, and C. F. Gmachl. Mid-infrared quantum cascade lasers. *Nat. Photon.*, 6(7):432–439, 2012.
- [41] R. Köhler, A. Tredicucci, F. Beltram, H. E Beere, E. H. Linfield, A. G. Davies, D. A Ritchie, R. C Iotti, and F. Rossi. Terahertz semiconductor-heterostructure laser. *Nature*, 417(6885):156–159, 2002.
- [42] S. Kumar, Q. Hu, and J. L. Reno. 186 K operation of terahertz quantum-cascade lasers based on a diagonal design. *Appl. Phys. Lett.*, 94(13):131105, 2009.
- [43] S. Fatholouloumi, E. Dupont, C.W.I. Chan, Z.R. Wasilewski, S.R. Laframboise, D. Ban, A. Mátyás, C. Jirauschek, Q. Hu, and H. C. Liu. Terahertz quantum cascade lasers operating up to ~ 200 K with optimized oscillator strength and improved injection tunneling. *Opt. Express*, 20(4):3866–3876, 2012.

- [44] C. Sirtori and R. Teissier. Quantum cascade lasers: Overview of basic principles of operation and state of the art. In R. Paiella, editor, *Intersubband Transitions in Quantum Structures*. McGraw-Hill, New York, 2006.
- [45] Q. J. Wang, C. Pflügl, L. Diehl, F. Capasso, T. Edamura, S. Furuta, M. Yamanishi, and H. Kan. High performance quantum cascade lasers based on three-phonon-resonance design. *Appl. Phys. Lett.*, 94(1):011103, 2009.
- [46] B. Vinter. Effect of the Electron-Electron Interaction on the Excitation Energies of an n -Inversion Layer on Si. *Phys. Rev. Lett.*, 35:598–601, 1975.
- [47] S. J. Allen Jr, D. C. Tsui, and B. Vinter. On the absorption of infrared radiation by electrons in semiconductor inversion layers. *Solid State Commun.*, 20:425–428, 1976.
- [48] A. Pinczuk, S. Schmitt-Rink, G. Danan, J. P. Valladares, L. N. Pfeiffer, and K. W. West. Large exchange interactions in the electron gas of GaAs quantum wells. *Phys. Rev. Lett.*, 63:1633–1636, 1989.
- [49] S. L. Chuang, M. S. C. Luo, S. Schmitt-Rink, and A. Pinczuk. Many-body effects on intersubband transitions in semiconductor quantum-well structures. *Phys. Rev. B*, 46:1897–1900, 1992.
- [50] M. Zaluzny. On the intersubband absorption line width in semiconductor quantum wells. *Solid State Commun.*, 8(7):565 – 567, 1992.
- [51] L. Wendler and E. Kandler. Intra- and Intersubband Plasmon-Polaritons in Semiconductor Quantum Wells. *Phys. Status Solidi (b)*, 177:9, 1993.
- [52] R. J. Warburton, C. Gauer, A. Wixforth, J. P. Kotthaus, B. Brar, and H. Kroemer. Intersubband resonances in InAs/AlSb quantum wells: Selection rules, matrix elements, and the depolarization field. *Phys. Rev. B*, 53:7903–7910, 1996.
- [53] K. Craig, B. Galdrikian, J. N. Heyman, A. G. Markelz, J. B. Williams, M. S. Sherwin, K. Campman, P. F. Hopkins, and A. C. Gossard. Undressing a collective intersubband excitation in a quantum well. *Phys. Rev. Lett.*, 76:2382–2385, 1996.
- [54] D. E. Nikonov, A. Imamoglu, L. V. Butov, and H. Schmidt. Collective Intersubband Excitations in Quantum Wells: Coulomb Interaction versus Subband Dispersion. *Phys. Rev. Lett.*, 79(23):4633, 1997.
- [55] R. J. Warburton, K. Weilhammer, J. P. Kotthaus, M. Thomas, and H. Kroemer. Influence of collective effects on the linewidth of intersubband resonance. *Phys. Rev. Lett.*, 80:2185–2188, 1998.
- [56] D. E. Nikonov, A. Imamoglu, and M. O. Scully. Fano interference of collective excitations in semiconductor quantum wells and lasing without inversion. *Phys. Rev. B*, 59:12212–12215, 1999.

- [57] S. Luin, V. Pellegrini, F. Beltram, X. Marcadet, and C. Sirtori. Interplay between disorder and intersubband collective excitations in the two-dimensional electron gas. *Phys. Rev. B*, 64:041306, 2001.
- [58] S. Graf, H. Sigg, K. Köhler, and W. Bächtold. Direct observation of depolarization shift of the intersubband resonance. *Phys. Rev. Lett.*, 84:2686–2689, 2000.
- [59] J. Li and C. Z. Ning. Interplay of collective excitations in quantum-well intersubband resonances. *Phys. Rev. Lett.*, 91:097401, 2003.
- [60] X. G. Guo, R. Zhang, H. C. Liu, A. J. SpringThorpe, and J. C. Cao. Photocurrent spectra of heavily doped terahertz quantum well photodetectors. *Appl. Phys. Lett.*, 97(2):021114, 2010.
- [61] H. C. Liu. Quantum well infrared photodetector physics and novel devices. In H. C. Liu and F. Capasso, editors, *Intersubband Transitions in Quantum Wells, Physics and Device Applications I*. Academic, Boston, 2000.
- [62] H. Haug and S.W.Koch. *Quantum Theory of the Optical and Electronic Properties of Semiconductors*. World Scientific, 2004.
- [63] E. Scholl, editor. *Theory of Transport Properties of Semiconductor Nanostructures*. Chapman and Hall, 1998.
- [64] A. Delteil, A. Vasanelli, Y. Todorov, B. Paulillo, G. Biasiol, L. Sorba, and C. Sirtori. Gate controlled coupling of intersubband plasmons. *Appl. Phys. Lett.*, 102(3):031102, 2013.
- [65] A. Delteil. *Exaltation multicorps du couplage lumière-matière*. PhD thesis, Université Paris Diderot - Paris 7, 2012.
- [66] G. Onida, L. Reining, and A. Rubio. Electronic excitations: density-functional versus many-body Green's-function approaches. *Rev. Mod. Phys.*, 74:601–659, 2002.
- [67] B. Askenazi, A. Vasanelli, A. Delteil, Y. Todorov, L. C. Andreani, G. Beaudoin, I. Sagnes, and C. Sirtori. Ultra-strong light-matter coupling for designer reststrahlen band. *New J. Phys.*, 16(4):043029, 2014.
- [68] Y. Todorov and C. Sirtori. Intersubband polaritons in the electrical dipole gauge. *Phys. Rev. B*, 85:045304, 2012.
- [69] Y. Todorov, L. Toso, A. Delteil, A. Vasanelli, and C. Sirtori. Polaritonic spectroscopy of intersubband transitions. *Phys. Rev. B*, 86:125314, 2012.
- [70] C. Cohen-Tannoudji, J. Dupont-Roc, and G. Grynberg. *Photons et Atomes*. EDP Sciences, Paris, 2001.
- [71] S. S. Scheel, L. Knoll, , and D.-G. Welsch. *Coherence and Statistics of Photons and Atoms*. Wiley, New York, 2001.

- [72] C. Ciuti, G. Bastard, and I. Carusotto. Quantum vacuum properties of the inter-subband cavity polariton field. *Phys. Rev. B*, 72:115303, 2005.
- [73] R. Resta. Electrical polarization and orbital magnetization: the modern theories. *Journal of Physics: Condensed Matter*, 22(12):123201, 2010.
- [74] B. Vinter. Many-body effects in *n*-type Si inversion layers. II. Excitations to higher subbands. *Phys. Rev. B*, 15(8):3947, 1977.
- [75] J. Hopfield. Theory of the contribution of excitons to the complex dielectric constant of crystals. *Phys. Rev.*, 112(5):1555, 1958.
- [76] F. Wooten. *Optical Properties of Solids*. Academic, New York, 1972.
- [77] S.H. Autler and C.H. Townes. Stark effect in rapidly varying fields. *Phys. Rev.*, 100:703, 1955.
- [78] C. Cohen-Tannoudji. *The Autler-Townes effect revisited*, volume Amazing Light. Springer, 1996.
- [79] B. Harbecke, B. Heinz, and P. Grosse. Optical properties of thin films and the Berreman effect. *Applied Physics A*, 38(4):263–267, 1985.
- [80] M. Fleischhauer, A. Imamoglu, and J. P. Marangos. Electromagnetically induced transparency: Optics in coherent media. *Rev. Mod. Phys.*, 77:633–673, 2005.
- [81] W. Hong-wei, M. Xian-wu, H. Yong-gang, and S. Ke-hui. Autler-Townes splitting and quantum confined stark effect of sideband peak in asymmetric double quantum wells. *Journal of Applied Physics*, 113(4):043105, 2013.
- [82] M. Wagner, H. Schneider, D. Stehr, S. Winnerl, A. M. Andrews, S. Schartner, G. Strasser, and M. Helm. Observation of the intraexciton Autler-Townes effect in GaAs/AlGaAs semiconductor quantum wells. *Phys. Rev. Lett.*, 105:167401, 2010.
- [83] C. Cohen-Tannoudji, J. Dupont-Roc, and G. Grynberg. *Processus d'interaction entre photons et atomes*. EDP Sciences, Paris, 2001.
- [84] K. Kempa, E. Gornik, K. Unterrainer, M. Kast, and G. Strasser. Resonant tunneling mediated by resonant emission of intersubband plasmons. *Phys. Rev. Lett.*, 86:2850–2853, 2001.
- [85] M. Coquelin, G. Strasser, E. Gornik, P. Bakshi, and M. Ciftan. Controlled generation of resonant electron-electron scattering induced current in quantum well structures. *Appl. Phys. Lett.*, 95(17):172108, 2009.
- [86] H. Callebaut. *Analysis of the Electron Transport Properties in Quantum Cascade Lasers*. PhD thesis, Massachusetts Institute of Technology, 2006.
- [87] C. C. Tannoudji, B. Diu, and F. Laloë. *Mécanique Quantique I*. Hermann, Paris, 1973.

- [88] C. Sirtori, F. Capasso, J. Faist, A.L. Hutchinson, D. L. Sivco, and A. Y. Cho. Resonant tunneling in quantum cascade lasers. *Quantum Electronics, IEEE Journal of*, 34(9):1722–1729, 1998.
- [89] H. Willenberg, G. H. Döhler, and J. Faist. Intersubband gain in a bloch oscillator and quantum cascade laser. *Phys. Rev. B*, 67:085315, 2003.
- [90] R. C. Iotti and F. Rossi. Nature of Charge Transport in Quantum-Cascade Lasers. *Phys. Rev. Lett.*, 87:146603, 2001.
- [91] J. B. Khurgin, Y. Dikmelik, P. Q. Liu, A. J. Hoffman, M. D. Escarra, K. J. Franz, and C. F. Gmachl. Role of interface roughness in the transport and lasing characteristics of quantum-cascade lasers. *Appl. Phys. Lett.*, 94(9):091101, 2009.
- [92] S. Kumar and Q. Hu. Coherence of resonant-tunneling transport in terahertz quantum-cascade lasers. *Phys. Rev. B*, 80:245316, 2009.
- [93] R. Terazzi and J. Faist. A density matrix model of transport and radiation in quantum cascade lasers. *New Journal of Physics*, 12:033045, 2010.
- [94] E. Dupont, S. Fatholouloumi, and H. C. Liu. Simplified density-matrix model applied to three-well terahertz quantum cascade lasers. *Phys. Rev. B*, 81:205311, 2010.
- [95] A. Bismuto, R. Terazzi, B. Hinkov, M. Beck, and J. Faist. Fully automatized quantum cascade laser design by genetic optimization. *Appl. Phys. Lett.*, 101(2):021103, 2012.
- [96] C. Jirauschek and T. Kubis. Modeling techniques for quantum cascade lasers. *Applied Physics Reviews*, 1(1):011307, 2014.
- [97] H. Haug and A.-P. Jauho, editors. *Quantum Kinetics in Transport and Optics of Semiconductors*. Springer, 1996.
- [98] D.J. Fisher, C. Zhang, S.M. Stewart, W. Xu, M.L.F. Lerch, A.D. Martin, and L. Eaves. Effect of frequency dependent electron-electron interaction on resonant tunneling. *Superlattices microst.*, 18(3):239, 1995.
- [99] S. De Liberato and C. Ciuti. Quantum theory of intersubband polarons. *Phys. Rev. B*, 85:125302, 2012.
- [100] X. W. Mi, J. C. Cao, C. Zhang, and F.B. Meng. Effects of collective excitations on the quantum well intersubband absorption. *J. Appl. Phys.*, 98:103530, 2005.
- [101] S. De Liberato and C. Ciuti. Quantum model of microcavity intersubband electro-luminescent devices. *Phys. Rev. B*, 77:155321, 2008.
- [102] T. Kuhn. Density matrix theory of coherent ultrafast dynamics. In E. Scholl, editor, *Theory of Transport Properties of Semiconductor Nanostructures*. Chapman and Hall, 1998.

- [103] M. Klymenko, O. Shulika, and I. Sukhoivanov. Electron transport effect on optical response of quantum-cascade structures. In Jan Grym, editor, *Semiconductor Technologies*. InTech, 2010.
- [104] T. Liu, K. E. Lee, and Q. J. Wang. Microscopic density matrix model for optical gain of terahertz quantum cascade lasers: Many-body, nonparabolicity, and resonant tunneling effects. *Phys. Rev. B*, 86:235306, 2012.
- [105] J. Fricke. Transport equations including many-particle correlations for an arbitrary quantum system. general formalism. *Ann. Phys.*, 252(479), 1996.
- [106] F. Alpeggiani and L. C. Andreani. Semiclassical theory of multisubband plasmons: Nonlocal electrodynamics and radiative effects. *Phys. Rev. B*, 90:115311, 2014.
- [107] M. Kociak and O. Stephan. Mapping plasmons at the nanometer scale in an electron microscope. *Chem. Soc. Rev.*, 43:3865–3883, 2014.
- [108] T. Ando. Inter-subband optical absorption in space-charge layers on semiconductor surfaces. *Zeitschrift fur Physik B Condensed Matter*, 26(3):263–272, 1977.
- [109] R. Ferreira and G. Bastard. Evaluation of some scattering times for electrons in unbiased and biased single- and multiple-quantum-well structures. *Phys. Rev. B*, 40:1074–1086, 1989.
- [110] A. Leuliet. *Simulation du transport dans les lasers à cascade quantique*. PhD thesis, Université Paris Diderot, 2007.
- [111] S. Tsujino, A. Borak, E. Muller, M. Scheinert, C. V. Falub, H. Sigg, D. Grutzmacher, M. Giovannini, and J. Faist. Interface-roughness-induced broadening of intersubband electroluminescence in p-SiGe and n-GaInAs-AlInAs quantum-cascade structures. *Appl. Phys. Lett.*, 86(6):062113, 2005.
- [112] A. Vasanelli, A. Leuliet, C. Sirtori, A. Wade, G. Fedorov, D. Smirnov, G. Bastard, B. Vinter, M. Giovannini, and J. Faist. Role of elastic scattering mechanisms in GaInAs/AlInAs quantum cascade lasers. *Appl. Phys. Lett.*, 89(17), 2006.
- [113] P. K. Basu and Keya Bhattacharya. Alloy scattering limited mobility of two-dimensional electron gas in quaternary alloy semiconductors. *Journal of Applied Physics*, 59(3):992–994, 1986.
- [114] J. H. Smet, C. G. Fonstad, and Q. Hu. Intrawell and interwell intersubband transitions in multiple quantum wells for far-infrared sources. *Journal of Applied Physics*, 79(12):9305–9320, 1996.
- [115] S.-C. Lee and I. Galbraith. Intersubband and intrasubband electronic scattering rates in semiconductor quantum wells. *Phys. Rev. B*, 59:15796–15805, 1999.
- [116] H. Fröhlich. Electrons in lattice fields. *Advances in Physics*, 3:325–361, 1954.

-
- [117] J. S. Roberts, R. P. Green, L. R. Wilson, E. A. Zibik, D. G. Revin, J. W. Cockburn, and R. J. Airey. Quantum cascade lasers grown by metalorganic vapor phase epitaxy. *Appl. Phys. Lett.*, 82(24):4221–4223, 2003.
- [118] I. Vurgaftman, J. R. Meyer, and L. R. Ram-Mohan. Band parameters for iii–v compound semiconductors and their alloys. *J. Appl. Phys.*, 89(11):5815–5875, 2001.
- [119] A. Calvar. *Design, engineering and processing of QC Lasers for high frequency modulation*. PhD thesis, Université Paris Diderot - Paris 7, 2013.